Fabrication and characterisation of poled ferroelectric optical crystals

Benjamin F. Johnston

BTech Optoelectronics (Hons.)

MQ Photonics Research Centre
Department of Physics
Division of Information and Communication Sciences
Macquarie University
North Ryde, NSW 2109, AUSTRALIA
Email: benjamin@ics.mq.edu.au
Telephone: (61-2) 9850 8975, Facsimile: (61-2) 9850 8115
June 2008

The research presented in this thesis is affiliated with the Centre of Ultrahigh-bandwidth Devices for Optical Systems (CUDOS), an Australian Research Council Centre of Excellence.

This thesis is presented for the degree of Doctor of Philosophy

Contents

Abstract

Lithium niobate is a prolific optoelectronic material. It continues to be utilized in devices ranging from surface acoustics wave (SAW) filters and modulators in electronics to electro-optic modulators, q-switches and frequency conversion in optics. Domain engineering (poling) for frequency conversion is an area of lithium niobate technology where there continues to be innovation and the transition from laboratory research to commercial products is still ongoing. What makes lithium niobate such an attractive material platform is its large piezoelectric, electro-optic and nonlinear optical properties. Domain engineering of the crystal structure allows extra degrees of freedom for the production of useful devices based on these properties. Periodically poled lithium niobate (PPLN) has become an increasingly popular second order nonlinear material since its realisation in the early 1990's. Poling in optical crystals enables quasi-phase-matching (QPM) of nonlinear optical interactions with the advantages of accessing large optical nonlinearities and the ability to tailor the domain pattern to the target optical interaction.

This thesis explores the fabrication of (PPLN) with laser micro-machined topographical electrode patterning. This direct write technique, used in conjunction with the now mature electric field poling method, offers the advantages of being highly versatile, fast, and devoid of lithographic or wet processing steps. There are three key topic areas looked at within this dissertation; laser micro-machining of lithium niobate with nanosecond and femtosecond laser systems, electric field poling of lithium niobate wafers patterned by laser machining and quasi-phase-matched nonlinear optics. The focus of the laser machining studies is both fundamental and practical in nature. Nanosecond and femtosecond ablation of lithium niobate and silicon are compared, and clear differences in the ablation characteristics for the different laser sources and materials are identified and discussed. Laser machining of surface structures suitable for electric field poling are then presented, and control over the geometry of these structures via laser parameters is demonstrated. The electric field studies deal with both modelling of the electrostatics which arise from poling with topographical electrodes and the field dependant domain kinetics which govern domain inversion and spreading. Frequency conversion using PPLN devices produced using laser machined electrode structures is demonstrated. The frequency conversion processes featured in this thesis both demonstrate the utility for rapid prototyping and highlights a novel optical interaction which simultaneously phase-matches two different second harmonic generation (SHG) processes. This interaction results in a cascading of optical energy between orthogonally polarised laser beams. The implications and potential applications of this interaction are discussed.

Statement of Candidate

The original concept of using laser machining to produce electrode structures for poling appeared in the literature in 1998[i] and investigations into this technique were initiated at Macquarie University with my supervisor, Dr. Michael Withford[ii] in 2002. The concepts for the cascaded nonlinear optics investigated herein were motivated by Professor Solomon Saltiel[iii] during visits to Macquarie University in 2006. I acknowledge Professor Yuri Kivshar's[iv] generous support of my collaborative work with Professor Saltiel.

I have developed all computer simulations of electrostatic fields and nonlinear optical interactions contained herein within the Matlab programming environment. I have independently operated all experimental apparatus utilized during my candidature and all original experimental data presented herein is my own. I acknowledge the contributions of Dr. Graham Marshall for overseeing the operation and maintenance the Spectra Physics Hurricane laser system utilized for laser machining, and the contribution of Dr Peter Dekker for construction and instruction of a lab built Q-switched 1.064μm laser used for frequency doubling experiments. During my candidature I have installed an electric field poling apparatus based on the Trek 20/20C high voltage amplifier, developed the apparatus and software for automated recording of temperature detuning curves in frequency doubling experiments and undertaken all manual tasks and measurements including crystal handling, laser micromachining, microscopy and profilometry.

This thesis is submitted in fulfillment of the requirements of the degree of Doctor of Philosophy at Macquarie University and has not been submitted for a higher degree to any other university or institution. I certify that to the best of my knowledge, all sources used and assistance received in the preparation of this thesis has been acknowledged. This thesis does not contain any material which is defamatory of any person, form or corporation and is not in breach of copyright or breach of other rights which shall give rise to any action at Common Law or under Statute.

_____

Benjamin F. Johnston

_____

[i] Reich *et al,* Opt. Lett. **23** (23), 1817-1819 (1998).
[ii] Dr. Michael Withford, Macquarie University, withford@ics.mq.edu.au
[iii] Prof. Solomon Saltiel, University of Sofia, saltiel@phys.uni-sofia.bg
[iv] Prof. Yuri Kivshar, Australian National University, ysk124@rsphysse.anu.edu.au

Acknowledgements

Thanks to Mick, Jim, Dave B and Linda H for giving me the earliest possible opportunity to get in the lab and try my hand. It has set me on a path which has quickly become a life choice and hopefully a fruitful carreer ☺. Special thanks to Mick for your patience, and the faith you have shown in the way I go about things. I hope we can continue to share in the odd 'win' in the future.

On the work front, thanks must go to Pete and Graham. Our group has grown and transformed itself for the good over the past few years and mostly because of your elbow grease and the knowledge and wisdom you guys bring to work each day. Thanks also to Rich and Russ, your advice on and off the field is also worth listening too. Thanks to those magical people, the office ladies, that make humble students feel like real people too. Linda H, Carol, Christine, Jackie and of course Kali.

To all the academic staff, especially Peter B, Judith, Ewa, Deb and Dave C, it is your tireless efforts in presenting lecture material which is interesting, technical and cool all at the same time which keeps students like me in the race. Physics at Macquarie is special because of this.

To the guys and girl(s) with whom I have shared my time in the PhD pit, Andy, Marty, Doug, Luke, Josh, Nem, Aaron, Tom, Hamo, Chris, Coeus, Mark, Alanna and Joyce, thanks for your friendship, the laughs, the moments of insanity, Origin nights, FA cup nights, Friday footy, Thursday trivia…Im sure we did some decent work in amongst these somewhere.

Finally, thanks to my family, Mum and Dad for your unending support, my grandparents with whom I lived with when I first came to the 'big smoke' to do the uni thing. To the old school friends from Wello who keep me smiling. And to Sharon, I love you…but it's your turn now Miss Muffett.

Chapter 1. Introduction

"The important thing in science is not so much to obtain new facts as to discover new ways of thinking about them."

-Sir William Henry Bragg

"You can't change the world singing songs, believe me, but you can offer people an alternative perspective, even on their own situations."

-Billy Bragg

1.1 Lithium niobate: material and devices

1.1.1 Introduction

Lithium niobate ($LiNbO_3$) is a prolific material in the electronics and optoelectronics industries. The current global production of lithium niobate is substantial and it is available as a relatively cheap and mature material with various grades, crystal cuts, stoichiometries and dopings available to suit a range of applications. It is a piezoelectric, ferroelectric, electro-optic and nonlinear optical material. Its most common application is as the substrate material for surface acoustic wave (SAW) devices where its piezoelectric properties are utilized. SAW devices have numerous applications in analogue and digital electronics and are an important circuit element in transceivers in most cell phones and wireless devices. Lithium niobate is also important for optical communications, as it is a key material for many types of electro-optic modulators. The nonlinear optical properties of lithium niobate have also made it an increasingly popular material for optical frequency conversion. The development of periodic poling of lithium niobate – and other ferroelectric optical crystals such as lithium tantalate and potassium titanium oxide phosphate (KTP) - has enabled innovation in visible laser sources, optical parametric oscillators, optical signal processing devices, and is also a leading contender as a nonlinear material for laser display technologies.

This dissertation looks at a novel technique for the electrode patterning step in the fabrication of periodically poled lithium niobate (PPLN). This technique involves laser micro-machined topographical electrode patterning of the crystal surface, used in conjunction with the now mature electric field poling method. This technique offers the advantages of being highly

versatile, fast, and devoid of lithographic or wet processing steps, though it also has limitations which will be discussed over the course of this thesis. Frequency conversion with PPLN fabricated using this technique has been demonstrated for type-I (d_{31}) and 3rd order type-0 (d_{33}) second harmonic generation. In addition a novel optical interaction which simultaneously phase-matches two different second harmonic generation (SHG) processes is demonstrated. This interaction results in a cascading of optical energy between orthogonally polarised laser beams.

This introductory chapter is arranged in four sections. The remainder of this opening section looks at some of the properties of lithium niobate, as well as the basic principles of some common lithium niobate devices. Section 1.2 reviews the major milestones in the development of periodically poled lithium niobate, as well as highlighting recent innovations in alternative methods for controlled periodic poling. Section 1.3 outlines the motivation for the investigations carried out over the course of this project and section 1.4 explains the arrangement of the following chapters within this dissertation.

1.1.2 Properties of lithium niobate

There are several reference texts available on lithium niobate, for example see refs [1,2 & 3]. An often cited summary of lithium niobate's structure and properties was also published by Weis and Gaylord in 1985[4]. Lithium niobate is a crystal with *3m* point symmetry which can be considered as having hexagonal and rhombic unit cells. The orientation and properties of lithium niobate can often be described with respect to a set of Cartesian *(x,y,z)* coordinates with the *z*-axis corresponding the crystallographic *c*-axis of the crystal, which is also the ferroelectric and optical axis of the crystal. In this dissertation the *(x,y,z)* notation will be used in reference to the crystal orientation and properties. This subsection now reviews some of the useful properties of lithium niobate that are exploited in a variety of optoelectronic devices.

Optical transmission

Optical grade lithium niobate has many desirable properties that make it a good candidate for many linear and nonlinear optical applications. It has a broad transmission window, extending from the blue end of the visible spectrum out to the mid-infrared. The measured transmission in the 200nm-2200nm wavelength range, taken with a Cary Spectrophotometer through a 0.5mm wafer of congruent composition lithium niobate is shown in Figure 1.1. As shown on the right of Figure 1.1, the UV edge in lithium niobate begins at ~350 nm. This signifies the lower limit of wavelengths that are compatible with lithium niobate devices. It also indicates the onset of UV

absorption that is sufficient for conventional laser micro-machining, which will be discussed further in chapter 3.

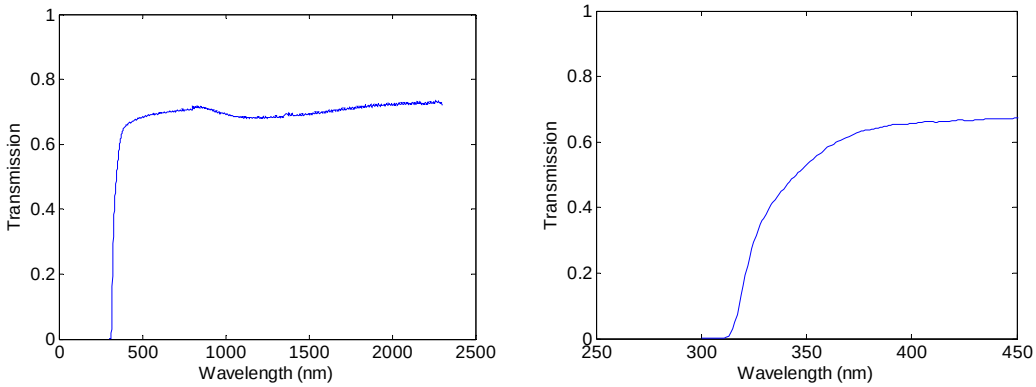

Figure 1.1 Left: transmission in congruent composition lithium niobate in the 200-2200nm range. Right: UV absorption edge.

Refractive indices

Lithium niobate is a uniaxial material, i.e. the directional dependence of its refractive indices can be described by an ellipsoid - or indicatrix – with single axial symmetry described by two primary refractive indices, often referred to as the ordinary, n_o, and extraordinary, n_e, refractive indices. Further more lithium niobate is a negative uniaxial material with $n_e<n_o$.

$$\frac{x^2}{n_o^2}+\frac{y^2}{n_o^2}+\frac{z^2}{n_e^2}=1 \qquad (1.1)$$

The coordinates in the indicatrix refer to the projection of an incident beam's electric field polarisation onto the primary crystal axes. For uniaxial crystals with the indicatrix given in Eq. (1.1), this means light propagating down the *z*-axis of the crystal with polarizations in the *xy* plane will experience a uniform refractive index of n_o, independent of polarization. When the propagation direction moves away from the z-axis the refractive index becomes polarisation dependant, for example light propagation along the *x*-axis with a polarisation in the *yz* plane will experience a refractive index of n_o for the component of polarisation projected onto the y-axis and a refractive index of n_e for the component of polarisation projected onto the z-axis. In optical materials the refractive indices' dependence on wavelength and temperature can often be described by Sellmeier relations. Sellmeier relations for lithium niobate used throughout this dissertation were taken from ref [5], and will be given explicitly in chapter 2 where they are important in various calculations for nonlinear optics.

Electro-optic properties

The electro-optic effect describes changes in the optical properties of a material with the application of an electric field. The linear electro-optic, or Pockels effect, is a change in the refractive indices which has a linear dependence on the electric field applied across the material. The Pokels effect is mathematically described as a deformation, (Δ), of the generalised indicatrix, which for a uniaxial material can be written as,

$$\left(\frac{1}{n_o^2}+\Delta_1\right)x^2+\left(\frac{1}{n_o^2}+\Delta_2\right)y^2+\left(\frac{1}{n_e^2}+\Delta_3\right)z^2+2\Delta_4 yz+2\Delta_5 xz+2\Delta_6 xy=1 \qquad (1.2)$$

The deformation values, $\Delta_{1\times6}$, for an applied electric field given as $\left(E_x, E_y, E_z\right)$ are found from the tensor expression,

$$\Delta_{1\times6}=r_{6\times3}\begin{pmatrix}E_x\\E_y\\E_z\end{pmatrix} \qquad (1.3)$$

where r is the 6×3 linear electro-optic tensor. For lithium niobate, which belongs to the *3m* crystal symmetry group, the non-zero electro-optic coefficients are r_{51}, r_{22}, r_{13}, r_{33}, $r_{61}=-r_{22}$, $r_{21}=-r_{22}$, $r_{42}=r_{51}$ and $r_{23}=r_{13}$. Typical values of the electro-optic coefficients in lithium niobate are,

r_{51}	28 pm/V
r_{22}	3.4 pm/V
r_{13}	8.6 pm/V
r_{33}	30.8 pm/V

Table 1.1 Typical electro-optic coefficients for the Pockels effect in lithium niobate.

The electro-optic coefficients show dependence on both the wavelength of light and modulation frequency of the applied electric field. Lithium niobate's electro-optic coefficients are some of the largest that are available in crystalline optical materials. As such it is a popular material for electro-optic devices, some of which will be discussed in the following subsection.

Piezoelectric properties

The piezoelectric effect describes the relationship between stress, strain and the applied or produced electric field (or charge displacement) that is exhibited in some materials. The piezoelectric effect in crystals can be described by a pair of tensor equations for the strain and the electric field, often referred to as the direct and inverse relations,

$$D = \varepsilon E_{3\times1} = e_{3\times6} ST_{6\times1} + \left[\varepsilon^{ST_0} \right]_{3\times3} E_{3\times1}$$
$$S_{6\times1} = [s^{E_0}]_{6\times6} ST_{6\times1} + e^{t}{}_{6\times3} E_{3\times1} \quad (1.4)$$

In these equations, E are the electric fields components, ST is the matrix of stress (elastic compliance) coefficients , e is the piezoelectric tensor, ε is the matrix of linear dielectric permitivities , and S is the vector describing the piezoelectric induced strain. The superscripts E_0 and ST_0 indicate the strain and permittivity associated with ambient (zero) electric field and stress respectively. The relationships between stress and strain properties are also often referred to as the 'elasticity' of a material. Recent appraisals of lithium niobate's piezoelectric and elastic properties have been publish by Ogi *et al*[6,7]. For crystals with *3m* symmetry the non-zero piezoelectric coefficients are, e_{15}, $e_{16} = -e_{22}$, $e_{21} = -e_{22}$, e_{22}, $e_{24} = -e_{15}$, e_{31} , and $e_{32} = e_{32}$. Depending on the formulation of the piezoelectric effect, the piezoelectric coefficients can be defined in a number of ways. If the piezoelectric charge or voltage is considered in relation to the actual deformation (stress) of the crystal then the coefficients take on units of *V/m* or C/m^2. Alternatively if the charge is considered in relation to the amount of force applied to the crystal the coefficients may take on units of *C/N*.

Coefficient	C/m^2	C/N (10^{-12})
e_{15}	3.65	78
e_{22}	2.39	19.2
e_{31}	0.31	1.3
e_{33}	1.72	18.9

Table 1.2 Typical piezoelectric coefficients for lithium niobate.

Ferroelectric/pyroelectric properties

The ferroelectric and pyroelectric properties are perhaps the most important properties to be aware of during fabrication of poled lithium niobate. Ferroelectricity and pyroelectricity are closely related properties in materials such as lithium niobate, as they both arise from the distribution of ions within the crystal lattice. Ferroelectricity arises from a stable arrangement of aligned dipoles in a material, giving rise to a spontaneous internal polarisation. This internal polarisation is susceptible to being reversed by an external electric field applied in the opposite direction to the internal dipoles. This reversal corresponds to an inversion the crystal orientation, with regions of a particular crystal orientation referred to as a 'domain'. The magnitude of the

electric field required to produce reversal is called the coercive field, E_c. Ferroelectric properties are also susceptible to temperature changes. Heating a ferroelectric causes it to become 'less ferroelectric', resulting in a reduction of the spontaneous polarisation. The change in spontaneous polarisation results in an accumulation of compensating charges on the crystal surfaces, in turn giving rise to the pyroelectric effect. Heating also acts to reduce the coercive field required for domain reversal. At a sufficeintly high temperature ferroelectrics become completely depolarised and move to a 'paraelectric' phase. The temperature that marks this transition is referred to as the Curie temperature, T_c. Thermal cycling during fabrication steps of lithium niobate devices needs to be managed carefully. Thermal shock can result in inadvertently causing 'defect' domain inversions due to the simultaneous actions of coercive field reduction and charging. In the worst case wafers can crack and even shatter due to the rapid charging, thermal expansion and piezoelectric stress that a rapid temperature change brings about. The ferroelectric properties of congruent composition lithium niobate and lithium tantalate are given below, though it should be noted that these values can vary substantial with crystal composition and from supplier to supplier. These properties will be elaborated on further in chapter 4 in the context of electric field poling.

Parameter	**Lithium niobate**	**Lithium tantalate**
Melting point	~1250 °C	~1650 °C
Curie temperature	~1140 °C	~610 °C
Coercive field	~20-24 kV/mm	~21 kV/mm
Spontaneous polarisation	72 μC/cm^2	55 μC/cm^2

Table 1.3 Typical values of characteristic ferroelectric properties of lithium niobate and lithium tantalate.

Nonlinear optical properties

Lithium niobate has relatively large quadratic susceptibilities. That is, the polarisation induced in the crystal that is proportional to the product of two incident field components is substantial, especially at optical high powers. For *3m* crystals the second order nonlinear polarisation is given by,

$$P = \chi^{(2)} E^2 = 2\varepsilon_o \begin{pmatrix} 0 & 0 & 0 & 0 & d_{31} & -d_{22} \\ -d_{22} & d_{22} & 0 & d_{31} & 0 & 0 \\ d_{31} & d_{31} & d_{33} & 0 & 0 & 0 \end{pmatrix} \begin{pmatrix} E_x^2 \\ E_y^2 \\ E_z^2 \\ 2E_yE_z \\ 2E_xE_z \\ 2E_xE_y \end{pmatrix}^{(\omega_x,\omega_y,\omega_z)} \quad (1.5)$$

Here $\chi^{(2)}$ is the second order susceptibly tensor, which can be expressed in terms of the nonlinear coefficients d_{mn}. Values of the second order susceptibilities for lithium niobate and lithium tantalate are shown below, along with some other common nonlinear materials. It is seen that the nonlinear coefficients of lithium niobate and lithium tantalate, especially the d_{33} coefficients, are substantial compared to other materials.

$LiNbO_3$ (pm/V)	$LiTaO_3$ (pm/V)	LBO (pm/V)	KDP (pm/V)	KTP (pm/V)	BBO (pm/V)
d_{22}=2.7	d_{22}=2.0	d_{31}=0.85	d_{36}=0.44	d_{15}=1.91	d_{22}=2.2
d_{31}=4.5	d_{31}=1	d_{32}=-0.67		d_{24}=3.64	d_{15}=0.03
d_{33}≈27-30	d_{33}=21	d_{33}=0.04		d_{31}=2.54	d_{31}=0.04
				d_{32}=4.35	d_{33}=0.04
				d_{33}=16.9	

Table 1.4 Nonlinear coefficients for lithium niobate and lithium tantalate along with other common nonlinear crystals.

The following subsection now reviews some of the devices which exploit the various favourable properties of lithium niobate.

1.1.3 Lithium niobate based devices

SAW devices

As mention in the introduction, lithium niobate SAW devices are a key component in many electrical circuits used for signal processing applications. SAW devices utilise the piezoelectric properties of a substrate material to convert an electrical signal into an acoustic signal which propagates on the material surface and is then coverted then back to an electrical signal. There are several reasons for doing this, for instance conversion to an acoustic signal creates a delay in the signal travel time as the propagation of the acoustic wave depends on the speed of 'sound' on

the substrate. The most common application is as band-pass filters in devices such as radios and cell phones. A diagram of the basic layout of a SAW device is shown in Figure 1.2.

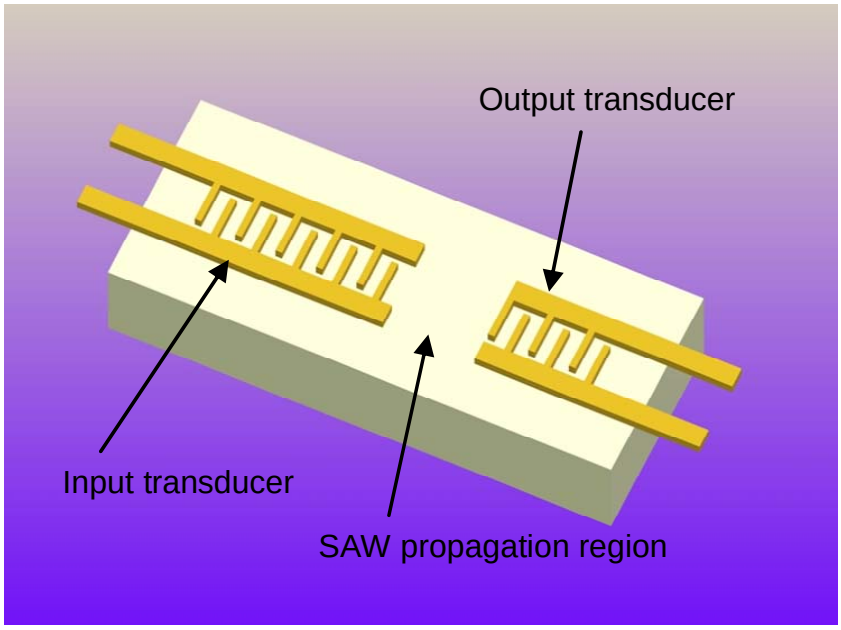

Figure 1.2 Diagram of a basic SAW device.

Electro-optic devices

The electro-optic properties of lithium niobate are used in a variety of devices to change the polarisation of light or to modulate the amplitude or phase of light for signaling applications. A diagram of a basic lithium niobate electro-optic device is shown in Figure 1.3. Free space electro-optic modulation can be carried out in either z-cut or x-cut orientations in lithium niobate. X-cut crystals are preferred in some cases as there is no birefringence at zero applied electric field. Some bulk electro-optic modulators also consist of two or more pieces of crystal with different cuts to manage the birefringence. Bulk electro-optic devices are often characterised by their half-wave voltage or V_π, which is the voltage which is need electro-optically change the retardance between orthogonal field components by $\pi/2$, for some orientation in the crystal. This results in a polarisation rotation of 90° for a linearly polarised input. A basic electro-optic modulator (also referred to as a Pockels cell) consists of an electro-optic crystal in tandem with crossed linear polarisers at the input and output. This enables amplitude modulation of light in free-space controlled by the electrical signal delivered to the Pockels cell. The electro-optic properties of lithium niobate are also the basis of integrated optical modulators for communications and signal processing applications. One common implementation of an integrated electro-optic modulator is based on a Mach-Zehnder waveguide configuration. A

diagram of a basic Mach-Zehnder electro-optic modulator is shown in Figure 1.4. Electro-optic modulation of one arm of the Mach-Zehnder waveguide interferometer produces an amplitude modulated output. With careful design of the waveguide and electrode geometries, reliable modulation frequencies of 40 Gbit/s have been achieved[8].

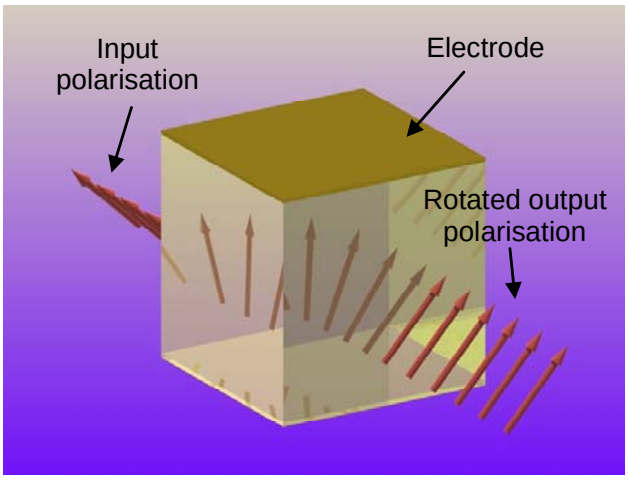

Figure 1.3 Diagram of a basic lithium niobate electro-optic device.

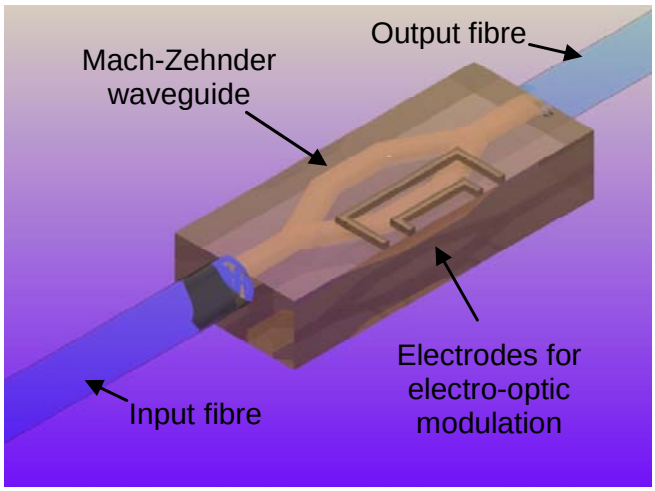

Figure 1.4 Diagram of a basic lithium niobate integrated electro-optic modulator based on a Mach-Zehnder configuration.

Periodically poled lithium niobate (PPLN)

Due to its high nonlinearity, broad transparency window and readily engineered domain structure, PPLN has become a popular nonlinear material. Periodic reversal of the crystal domain structure produced by poling is accompanied by spatial modulation of the crystal's nonlinear response. Periodic poling with the correct period can be used to compensate for the group velocity walk off between the pump and generated waves in a nonlinear interation that comes about because of dispersion. This process is called quasi-phase-matching and was suggested in a famous paper

from Armstrong and Bloembergen in 1962[9]. The following is the excerpt from this paper where they devise that crystals of KDP with a particular thicknesses with their optical axes orientated at 180˚ will preserve the phase-matching in second harmonic generation;

VIII. APPLICATIONS OF THE THEORY TO EXPERIMENTAL SITUATIONS

A. Harmonic and Subharmonic Generation

The most studied nonlinear effect is, thus far, second-harmonic generation. The analysis of Sec. V shows that it is possible, in principle, to convert all incident power into the second harmonic. Since χ_{zyz}^{NL} is about 10^{-11} esu for KDP,[14] the interaction length l [Eq. (5.13)] has the order of magnitude of 10^3 cm for an incident amplitude $\rho_1(0)=30$ kV/cm. For phase matching over a path $z=1$ cm, only about one part in 10^8 of the incident power is converted. It is possible to increase the peak power considerably, and field strengths of up to 10^6 V/cm may be attainable. Even then the required phase matching over the interaction length will certainly not be achieved for all rays in the solid angle of the beam. It will be necessary to apply phase correction schemes after the waves have traveled a distance $d=\pi(\Delta k)^{-1}$.

A phase shift of 180° in $\theta=\Delta kz+2\phi_1-\phi_2$ can be obtained in several ways. One can pass the waves through a dispersive linear dielectric phase correcting plate. It is more expedient from an experimental point of view to pass the light waves into another crystal of KDP, whose crystalline orientation is obtained by inversion of the first crystal, cf. Fig. 10. The sign of the third-order tensor, and therefore, of the interaction constant, is inverted in the inverted crystal. This can be repeated after each thickness d. An even simpler way to obtain the same result is to reflect both light waves after they have traversed a distance d. They each undergo an 180° phase shift on reflection and, therefore, $\Delta\theta=2\Delta\phi_1-\Delta\phi_2$ changes by 180°. In this case, the light waves, rather than the crystal, are inverted in space.

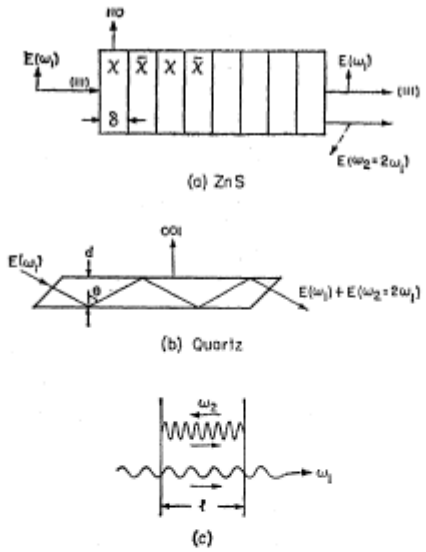

FIG. 10. Three experimental arrangements to provide phase correction, if the phase velocities of the fundamental and second harmonic are not perfectly matched. (a) After a distance $\delta = \pi(k_2 - 2k_1)^{-1}$ the crystal is replaced by its inversion image. The nonlinear susceptibility χ_{xyz} changes sign. The linear optical properties remain the same. This scheme can, of course, also be used in noncubic piezoelectric crystals. (b) Both fundamental and second harmonic undergo multiple total reflections in a crystal of thickness $d = (k_2 - 2k_1)^{-1}\pi \cos\theta$. On each reflection E_1 and E_2 undergo a 180° phase shift, the product $E_2E_1^2$ changes sign. (c) The traveling wave at ω_1 pumps the interferometer cavity, which contains a nonlinear dielectric and is resonant at ω_2, $l = n\lambda_2/2 < (k_2 - 2k_1)^{-1}\pi$. The backward harmonic wave does not interact with the pump. On each forward pass it has the correct phase for amplification.

The implementation of quasi-phase-matched nonlinear optics will be elaborated on theoretically in Chapter 2 and experimentally in Chapter 5. This approach to optical frequency conversion in PPLN has lead to the demonstration of many promising devices. First and foremost, it is a convenient material for extra-cavity frequency doubling of readily available infrared solid-state and semiconductor lasers into the visible. This approach has been especially useful for frequency doubling of fibre lasers and semiconductor lasers such as vertical cavity surface emitting lasers (VCSEL), where intra-cavity frequency doubling is challenging. The efficiency, flexibility and tunability of PPLN based optical parametric oscillators and amplifiers (OPOs and OPAs) has enabled significant innovations in spectroscopic light sources for laboratory and remote sensing applications. There has also been promising implementations of frequency conversion devices for carrying out some useful functions in optical communications, such as shifting and swapping a data channel's wavelength, optically controlled multiplexing and signal regeneration. A conceptual diagram of optical frequency conversion is shown in Figure 1.5.

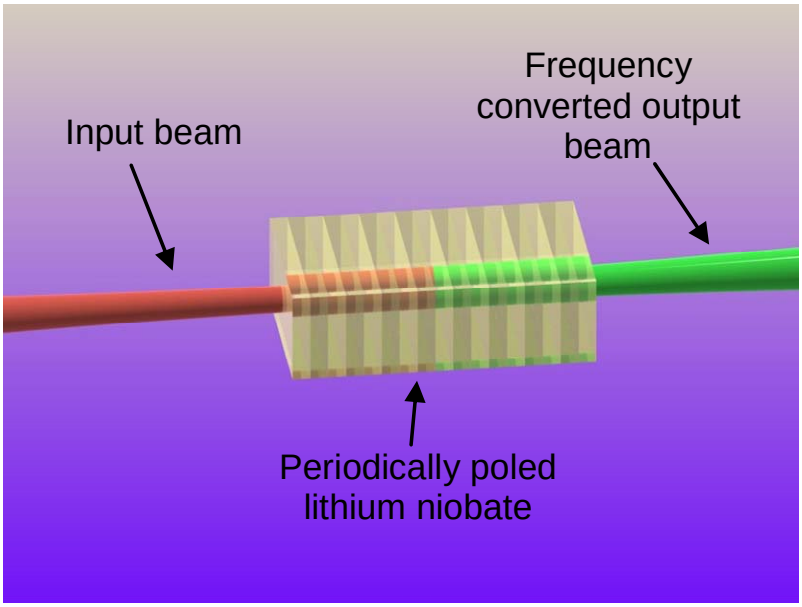

Figure 1.5 Conceptual diagram of optical frequency conversion in periodically poled lithium niobate.

Another application of periodically poled crystals is for Solc-type filters. Solc filters behave as strongly wavelength dependant wave-plates, which when implemented with cross polarised input and output filters form a wavelength selective transmission filter. The advantage of PPLN based Solc filters over simple in-fibre Bragg gratings is that they are electroptically and thermally tuneable, although but they also are limited to applications where the loss of the wavelengths that are not transmitted is not an issue. Solc filters work on the principal of spectrally dependant polarisation rotation through a stack of birefringent wave-plates with alternating orientations. The domain inversions in PPLN resemble such a stack, and the same advantages of domain engineering and good electro-optic response exploited in PPLN and lithium niobate electro-optic devices can be exploited for Solc filters.

The following section now provides an historical and technical overview of the development of PPLN fabrication technologies, as well as some ongoing innovations in methods of domain engineering.

1.2 Overview of PPLN development

1.2.1 Introduction

Lithium niobate was once thought of as permanent or 'frozen' ferroelectric, a material with such a large coercive field under ambient conditions that the application of an external electric field would result in dielectric breakdown before ferroelectric domain inversion could be achieved. With the improvements in crystal growing technologies, and increasing demand, the quality of lithium niobate has improved and techniques for successfully poling bulk quantities of lithium niobate for optical devices have been developed. Today high quality, single domain, lithium niobate is grown with various compositions by many manufacturers using the Czochralski technique. There are still technical challenges when working with lithium niobate and lithium tantalate - high coercive fields limit the thicknesses of crystals which are practical to pole, and photorefractive damage and green induced infrared absorption (GRIIA) limit the power handling and lifetime attributes of devices intended for visible applications. Recent advances in crystal growth techniques have allowed near stoichiometric lithium niobate and lithium tantalate (50% lithium and 50% niobium or tantalate ions) crystals to be fabricated, and techniques such as vapour transport equilibration have been demonstrated to further improve the quality and stoichiometry of available materials. Doping lithium niobate and lithium tantalate with magnesium oxide (MgO) has also been an important advancement in creating resilient devices operating in the visible. Improving stoichiometry and doping crystals with MgO has had a twofold advantage, namely lowering of the coercive field and improving resilience of the material to photorefractive damage. Parallel to the improvement in materials is the maturing of electric field poling techniques for fabrication of high quality periodically poled crystals. The following subsections provide an overview of the important milestones in the literature which have contributed to the development of periodic poling technology. This is followed by a review of some of the recent innovative techniques for control of domain inversion during electric field poling.

1.2.2 Review of the development of poling techniques

An early observation of domain inversion being produced during lithium niobate device fabrication came from Miyazawa in 1979[10]. Miyazawa found that high temperature titanium indiffusion on the +z face of lithium niobate resulted in reversal of the domain structure. The

purpose of the titanium indiffusion in Miyazawa's work was for the fabrication of electro-optic waveguide devices, so domain inversion was actually a nuisance. Accordingly Miyazawa's conclusion was that titanium indiffusion was best carried out on the *–z* face in order to avoid domain inversion. Deliberate fabrication of a laminar domain structure was reported by Feng *et al* in 1980[11]. Growth of small sections of periodically reversed lithium niobate via controlled temperature fluctuations during Czochralski growth was demonstrated, along with a demonstration of improved frequency conversion with crystals grown in this way. This sparked interest in the fabrication of singular crystals with engineered domain structures for nonlinear optics, and signified an improved approach to QPM which had previously been investigated using crystal plates manually stacked with varying orientations[12,13]. The influence of electric fields on the growth of periodic domain structures was investigated by Feisst and Koidl in 1985[14]. They reported the growth of periodic domains in chromium doped lithium niobate under the influence of an electric field during Czochralski growth. Magel *et al*[15] and Jundt *et al*[16] also reported the controlled formation of periodic domains during Czochralski growth, with the added innovation of using modulated laser heating to produce the reversals in crystal structure.

Despite these early successes in the growing of periodic crystals of lithium niobate, post-growth engineering of single domain crystals is the approach which has become popular.
Fabrication of patterned domain structures produced in single crystal lithium niobate was first demonstrated by Lim *et al* in 1989[17]. The same domain inversion mechanism noted by Miyazawa was exploited by periodically patterning the deposited titanium on the +z face prior to indiffusion. This resulted in a periodic orientation of domains near the crystal surface, suitable for quasi-phase-matching in proton exchanged waveguides, which were included after the metal indiffusion step. In initial investigations, Lim *et al* demonstrated green light generation by 3rd order SHG of 1064 nm, with generation of blue light via 3rd order QPM[18] and infrared generation by difference frequency generation[19] following soon after.

One of the first reports of external field poling through the entire crystal substrate comes from Matsumoto *et al* in 1991[20] who reported periodic poling of lithium tantalate. This was achieved by patterning aluminium electrodes onto the +z face, heating to temperatures in the vicinity of the Curie temperature and then applying a potential (~1.4V) to the electrodes as the crystal cooled, reversing the crystal domain orientation at the electrodes. This advancement was followed by Yamada *et al* in 1992[21] who reported external electric field poling of lithium niobate via patterned aluminium electrodes at room temperatures. Yamada *et al* avoided the onset of

dielectric breakdown by poling thinned substrates so that the coercive field was exceeded before breakdown occurred. Yamada *et al's* reported results of achieving a poling period of 2.8 μm and a conversion efficiency of 600%/W still stand in good stead with today's PPLN capabilities. Burns *et al*[22] also reported on room temperature PPLN fabrication by poling with metal electrodes while submerged in an oil bath. The higher dielectric strength of the oil compared to air allowed pulsed electric field poling of 250 μm thick lithium niobate.

Perhaps the first implementation of liquid electrode poling with resist patterned crystals comes from Webjorn and colleagues at the University of Southampton in 1994[23]. They reported fabrication of PPLN using a 1 μm thick layer of patterned photoresist as an insulating layer. Uniform electrical contact was then achieved by a filter paper soaked in LiCl solution. In 1995 Myers and colleagues at the Ginzton laboratory at Stanford published their now highly cited publications on the fabrication and applications of PPLN[24, 25]. Their technique involved lithographic patterning and then poling via immersion in a liquid electrolyte. The fabrication method established by Myers and colleagues has evolved into the technique of choice for fabricating PPLN. Further improvements of this technique, and the development of models to describe the electrostatics and domain kinetics, was undertaken by Miller[26]. The outcome of Miller's work was wafer scale fabrication of PPLN periods suitable for green generation by first order QPM-SHG (6.5μm) in 500μm thick crystals. Miller and colleagues reported 42% conversion efficiency from a 53 mm length of PPLN with 6.5 W of CW input[27]. SHG at blue wavelengths requires poling periods on the order of 3-5μm. Reliably producing PPLN with these periods is still technically challenging. A promising approach for the fabrication of shorter periods was suggested by Batchko *et al* in 1999[28], who reported on the spatial multiplication of domains compared to the electrode patterning by controlled back-switching. This type of domain engineering is performed by abruptly dropping the applied potential during the poling pulse. This causes a back-switch of domains at the electrode edges. Using this technique Batchko *et al* have demonstrated the fabrication of 4 μm period PPLN over 5 cm lengths.

The field poling method has proved to be reliable for 500 μm thick wafers of which there are now several commercial suppliers. There have been several recent endeavours to develop methods for periodic poling thicker samples to improve the available clear aperture. Diffusion bonding several 0.5 mm or 1 mm thick substrates of PPLN has been demonstrated by Missey *et al*[29], but aligning the domains between stacks and achieving a high quality optical bond is technically challenging. It has recently been demonstrated that electric field poling can be

achieved through substrates of 3 mm[30,31] and even 5 mm[32] thicknesses. MgO doped and near stoichiometric crystals have been target of these demonstrations as their lower coercive fields compared to congruent composition crystals are more compatible with moving to thicker substrates. Furthermore, poling was performed at elevated temperatures to reduce the effective coercive field to a manageable level.

The fabrication, characterisation and implementation of PPLN based devices continues to be a very active field of research, with an increasing emphasis on devices with commercial potential. The citation rates for three of the most widely cited milestone publications are shown in Figure 1.6 (data from ISI Web of Science). There has been a steady citation rate of these papers rate since 1998, and it interesting to note that 2007 (the year prior to the submission of this dissertation) saw the highest citation rates for Myers *et al* and Yamada *et al*. It is apparent that PPLN related research is still a fertile ground for fundamental and commercial orientated research. The follow subsection reviews some of the recent innovations for controlling domain inversion during electric field poling.

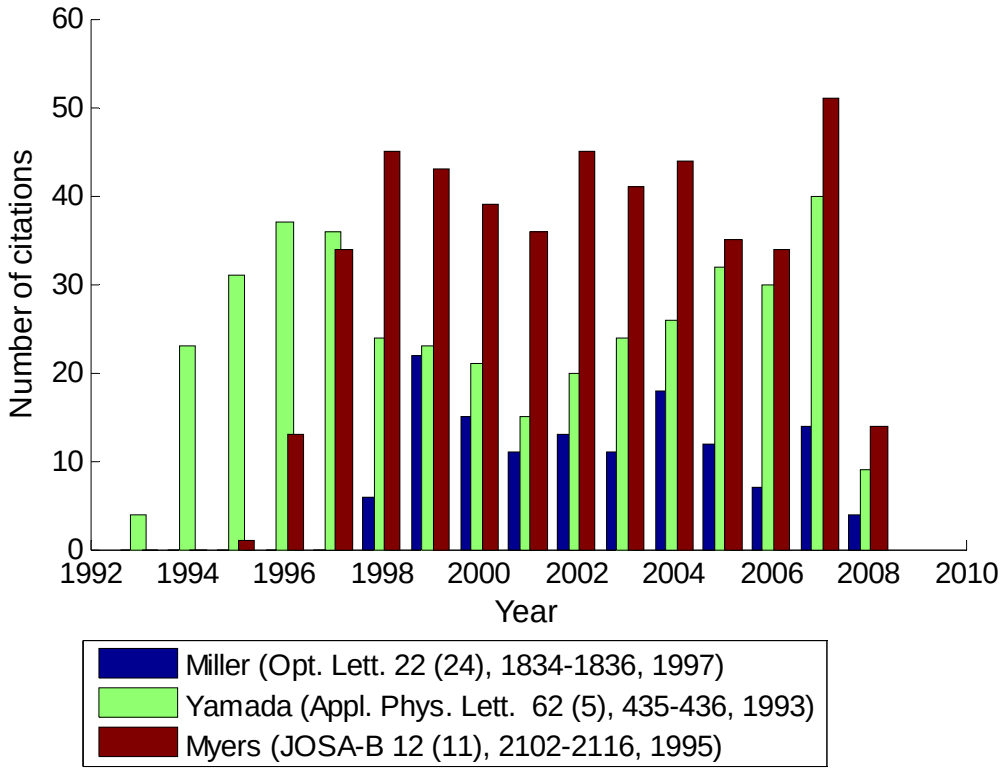

Figure 1.6 Citation rates of some milestone papers in the development of PPLN.

1.2.3 Recent innovations in periodic poling

Whilst periodic poling with patterned photoresist electrodes in a liquid electrolyte cell is a proven and mature method for PPLN fabrication, alternative methods for domain engineering has been, and continues to be, an active research area. For example, e-beam writing of domain inversions was reported by Ito *et al* in 1991[33] and has been revisited by many other authors since. In 1995 Houe and Townsend[34] looked at thermally assisted field poling of lithium niobate, using a YAG laser to locally raise the temperature and invert the crystal at the laser heated zone. This raised the possibility of laser guided poling in a direct write fashion. Harada and Nihi[35] reported promising results of poling of MgO doped lithium niobate by a novel corona discharge method, though poling MgO doped crystals with liquid electrodes is now also common place.

There have also been several recent investigations of alternative domain pattern techniques for ranging from chemical processing to optically induced domain growth. Grilli *et al*[36] have demonstrated that patterned proton exchange layers produce a change in the ferroelectric properties of lithium niobate sufficient to prevent domains merging. This is illustrated in the reproduced images in Figure 1.7.

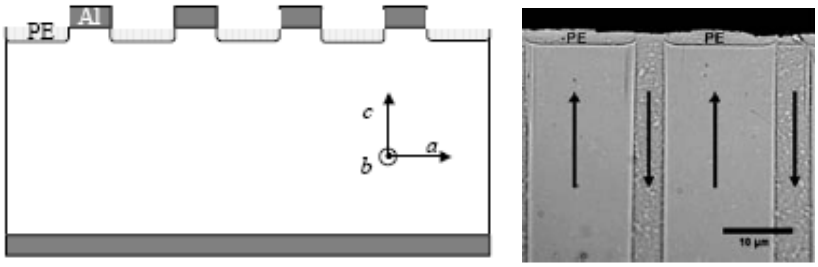

Figure 1.7 Proton exchange assisted domain engineering from the recent work of Grilli *et al*[36]. Left: patterning of the substrate prior to poling with aluminium electrodes in tandem with proton exchange regions. Right: experimental sample showing no domain inversion underneath the proton exchanged regions.

There is also a growing interest in light induced domain reversal. The basic idea is to hold the substrate at a potential that is just shy of the bulk coercive field and then selectively reduce the local coercive field by irradiating with a short wavelength laser. The influence of light on the coercive field during poling was initially investigated in lithium tantalate by Chao[37,38] *et al* in 1995, with domain patterning optical interference patterns also reported by Brown *et al*[39] in 1999. This effect has recently been demonstrated for patterning of congruent and MgO doped lithium niobate by authors such as Fujimura *et al*[40], Muller *et al*[41], Wengler *et al*[42,43], Sones *et al*[44,45,46],

and Dierwolf *et al*[47]. A basic layout of the poling apparatus for producing light induced domain inversion is reproduced from Muller *et al* in Figure 1.8. By introducing a phase-mask or other interferometric modulation of the incident laser radiation, patterned domain reversal is possible though not ideal, and investigations on improving this method are on going.

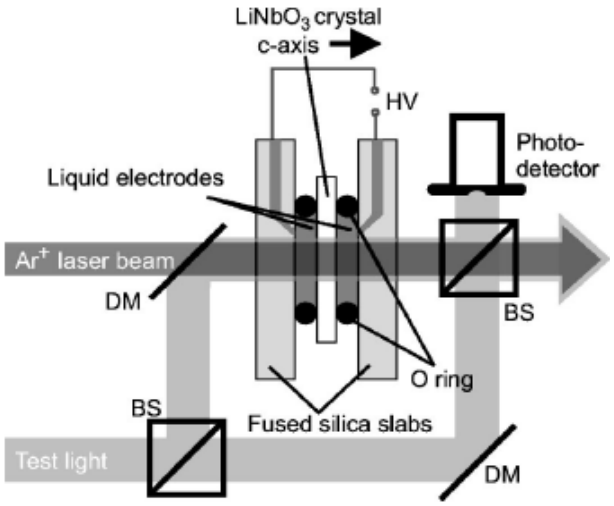

Figure 1.8 Poling apparatus for light induced domain reversal from Muller *et al*[41].

Another novel direct-write poling technique has been reported by Mohageg *et al*[48] who demonstrated 'calligraphic' writing of domains using a high voltage probe in the form of a tungsten needle. A schematic of the setup is reproduced in Figure 1.9. While this is not a convenient technique for large scale fabrication, it has the benefits of precise control of domain placement and patterning.

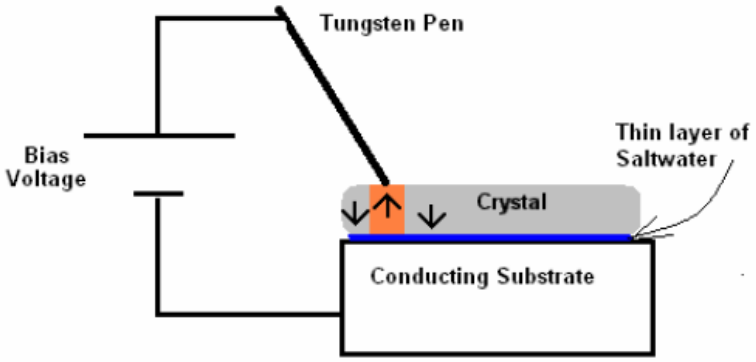

Figure 1.9 Apparatus for calligraphic poling of lithium niobate for Mohageg[48].

The technique underpinning the work in this thesis comes from Reich *et al*[49]. They demonstrated that laser machined surface features can define the electric fields required for electric field poling,

without requiring any lithographic patterning steps. A cross-section of the PPLN produced with this technique is reproduced in Figure 1.10. The motivations for pursuing this research direction are detailed in the following section.

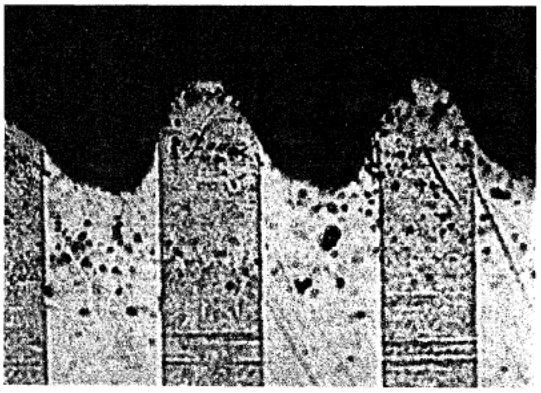

Figure 1.10 Periodic poling produced by laser machined electrodes from Reich *et al*[49]

1.3 Motivation

This thesis further explores the potential of utilising laser machined topographical electrodes for fabricating PPLN. The motivation for pursuing this technique is threefold – 1) the type of laser machining to be employed is 'direct write' in nature which allows for easy fabrication of various domain patterns without the requirement for lithography masks or a clean room environment. 2) Being able to quickly laser machine arbitrary electrode patterns for electric field poling provides an avenue for fast prototyping of domain engineered devices. 3) Since the investigations of Reich there have been no further reports, to my knowledge, of using this technique for domain engineering of optical crystals. A systematic study of the laser machining, electrostatics and domain kinetics pertinent to this fabrication method will provide further insight into the potential and limitations of this electrode patterning technique.

There are three key topic areas explored in this thesis – laser micromachining, electric field poling and quasi-phase matched nonlinear optics.

- The laser machining study investigates the ablation characteristics of lithium niobate. Laser processing with UV nanosecond lasers and 800 nm ultrafast (femtosecond lasers) has been looked at, with the goal of establishing optimal parameters for fabrication of surface features for poling.

- The electric field poling investigations look at the electrostatics and domain kinetics associated with poling with topographical surface electrodes, with the goal of establishing the limitations and identifying the subtleties associated with this technique.
- The quasi-phase-matched nonlinear optics presented in this thesis investigates both straight forward measurements of frequency conversion in laser fabricated PPLN crystals, but also looks at a novel nonlinear process which involves domain engineering to achieve simultaneous phase-matching of two different nonlinear processes. This simultaneous phase-matching results in a cascaded interaction, the likes of which have been of great interest for optical processing.

The layout of these topics within the thesis is elaborated upon in the following section.

1.4 Thesis arrangement

This dissertation has been set out in six chapters covering the three key topic areas within the project mentioned above. Since these three topics are quite different in nature they are each set-out within self contained chapters that deal with the background physics and literature, any modelling that has been undertaken, the experimental equipment, procedures and the results. In this way any future readers of this dissertation with a particular interest in one or other of these subject areas may refer to the appropriate chapter alone. The content of the chapters is arranged as follows;

Chapter 2 provides a review of nonlinear optics specific to quasi-phase-matching. Various implementations of domain engineering for nonlinear optics are reviewed including aperiodic, two dimensional and random domain patterns. The results of some numerical simulations developed during this project to aid in explaining the effects of domain imperfections on the nonlinear performance are included.

Chapter 3 looks at laser machining of lithium niobate from both fundamental and fabrication perspectives. An investigation of the ablation characteristics of lithium niobate with UV nanosecond lasers and 800 nm ultrafast lasers, along with a parallel comparative study of silicon will be presented. The laser machining of grooves in the surface of lithium niobate suitable for poling is also demonstrated, and the influence of laser and motion control parameters is investigated.

Chapter 4 looks at the electric field poling of lithium niobate with laser machined topographical electrodes. Finite element modelling of Laplace's equation is used to give an

indication of the electric field distributions needed to produce domain reversal. Particular attention has been paid to the influence of the geometry of the surface features on the electric field distribution and contrast with the background field. The domain kinetics and control of domain reversal when using topographical electrodes are investigated, and the limitations of domain sizes and periods are discussed.

Chapter 5 looks at the experimental nonlinear optics undertaken during this project. In particular 3rd order type-0 (d_{33}) as well as type-I (d_{31}) quasi-phase-matched second harmonic generation, with a variety of periods and domain patterns, is presented. A scheme to simultaneously phase-matched type-0 and type-I interactions in a single PPLN crystal is also proposed and demonstrated experimentally. As mention above, this interaction results in a cascaded interaction the likes of which have been of great interest for optical processing.

Chapter 6 concludes the dissertation with a summary of the key findings and suggestions for future implementations of laser written electrodes for electric field poling.

Chapter 2. Quasi-phase-matched nonlinear optics.

"It is also a good rule not to put overmuch confidence
in the observational results that are put forward
until they are confirmed by theory."
-Arthur Eddington

"Books are but waste paper unless we spend in action
the wisdom we get from thought"
-W.B. Yeats

2.1 Introduction

Nonlinear optics is an important and progressive field of research, which is integral to the development of modern laser technology, photonics, biophotonics, optical sensing and spectroscopy. It is of increasing interest in the field of photonics, as future all-optical communications systems will need to make use of nonlinear optical processes to achieve a level of functionality analogous to current electrical systems. Current optical communications systems use the wavelength of light to define data channels in fibre based wavelength division multiplexed (WDM) systems. Filtering of these channels is then carried out using passive resonant devices such as fibre Bragg gratings. Routing of the data to the end users, especially in local networks, is still predominantly carried out via electronic means. The push towards all-optical networks, which will need to be integrated with existing long haul optical communication systems, may utilise the wavelength and intensity of light for routing and switching as well as multiplexing. Wavelength conversion of light may be important for routing operations, where exchanging or sharing data streams across several wavelength dependent channels may be necessary. Quasi-phase-matching (QPM) materials offer an extremely versatile platform for implementing single or multiple 2^{nd} order nonlinear processes. These materials can be engineered to accommodate specific wavelengths and processes, and offer some of the higher 2^{nd} order nonlinearities available in mature solid-state materials. The family of ferroelectric crystals used for QPM includes lithium niobate, lithium tantalate and potassium titanium oxide phosphate (KTP), all of which have established waveguide technologies which allow for integration into fibre based networks. To date there have been several demonstrations of integrated QPM devices carrying out operations such as wavelength shifting[50,51,52,53,54], optical time division multiplexing (TDM)[55,56], optical code division multiple access (CDMA)[57,58], format conversion[59] and optical

gating[60,61,62]. These applications for photonics continue to motivate experimental and entrepreneurial activities based on QPM in materials such as PPLN.

The trend towards compact all-solid-state lasers sources, covering large regions of the visible and IR, is also a driving force behind improvements and innovations in nonlinear optics. There is particular interest in QPM materials for realising many of these laser sources, again due to the efficiency and versatility that they offer. Many popular solid-state and semi-conductor laser materials emit around 0.8-0.9μm (diodes, Ti: Sapphire, and the 946 nm Nd line), 1 μm (diodes, Nd, Yb), 1.3 μm (diodes, Nd), 1.5 μm (diodes, Er) and 2 μm (Tm, Ho). Frequency conversion of these commonly available laser sources via nonlinear optical elements has diversified the application range of these laser systems. A key advantage of QPM materials is they can be engineered for second-order frequency conversion of almost all of the currently available laser sources operating in the near to mid IR. To illustrate, there has been wide spread implementation of optical-parametric-oscillators (OPOs) based on QPM materials for spectroscopy and sensing where the tunability of the nonlinear element is a convenient means for tuning the source radiation in a well controlled manner[63,64,65]. The development of tuneable terahertz sources has also benefited from sources based on optical rectification, optical-parametric-generation (OPG) and optical-parametric-amplification (OPA) in QPM materials[66,67,68]. Highly compact and efficient solid-state visible sources have long been sought after for display applications, and the high efficiency offered by QPM materials allows for chip scale implementation of nonlinear optical elements, suitable for either fibre or semi-conductor based sources. Laser based projection units and displays resulting from this technology are expected to come to market within the next year (2008).

The goal of this chapter is to provide a theoretical and developmental overview of QPM nonlinear optics. This chapter is comprised of four subsequent sections. Section 2.2 deals with the basic theory of second order nonlinear optics pertinent to this dissertation, especially QPM in lithium niobate crystals. Section 2.3 will review some of the advanced approaches in QPM which include aperiodic, phase-reversed and two dimensional domain patterns. Section 2.4 will look at the effects that fabrication errors in crystal domain structures can have on the performance and tuning of QPM crystals. This will include the development of a numerical approach for modelling such errors, complimentary to previous analytical approaches in the literature.

2.2 Quasi-phase-matching

2.2.1 Basics of 2nd order nonlinear optics

The physical origin of 2nd order nonlinear optical processes lies in the polarisation that an incident electric field (such as light) can induce in a transparent material. For a dielectric optical crystal this polarisation is expressed in tensor form as,

$$P_i = P_i^0 + \sum \chi_{ij}^{(1)} E_j^{\omega} + \sum \chi_{ijk}^{(2)} E_j^{\omega_1} E_k^{\omega_2} + \sum \chi_{ijkl}^{(3)} E_j^{\omega_1} E_k^{\omega_2} E_l^{\omega_3} + \ldots \qquad (2.1)$$

where P_i is the polarisation induced in the *i* direction, P_i^o is the spontaneous polarisation of the material with no external electric field, E_m^{ω} are the incident electric field components with frequencies ω and polarised in the *m* direction, $\chi_{ij}^{(1)}$ is the linear (1st order) susceptibility tensor and $\chi_{ijk}^{(2)}$ is the second-order susceptibility tensor. There are higher order terms in the polarisation such as $\chi_{ijkl}^{(3)}$ which contribute to processes such as Kerr nonlinearities, four-wave-mixing and Raman scattering, but it is the $\chi_{ijk}^{(2)}$ term in non-centrosymmetric materials that we are interested in for the 2nd order nonlinear optics discussed hereafter. In order to refine the discussion further we will consider the $\chi_{ijk}^{(2)}$ tensor for optical crystals belonging to the *3m* point group, which includes lithium niobate, the material of most interest in this dissertation. For these crystals the second order term for the polarisation becomes,

$$\begin{pmatrix} p_x \\ p_y \\ p_z \end{pmatrix}^{(2)} = \sum_{j,k} \chi_{ijk}^{(2)} E_j^{\omega_1} E_k^{\omega_2} = 2\varepsilon_o \begin{pmatrix} 0 & 0 & 0 & 0 & d_{15} & -d_{16} \\ -d_{21} & d_{22} & 0 & d_{24} & 0 & 0 \\ d_{31} & d_{32} & d_{33} & 0 & 0 & 0 \end{pmatrix} \begin{pmatrix} E_x^2 \\ E_y^2 \\ E_z^2 \\ 2E_yE_z \\ 2E_xE_z \\ 2E_xE_y \end{pmatrix} \qquad (2.2)$$

where the *x,y* and *z* subscripts indicate the field polarisations with respect to an orthogonal set of crystallographic axes, ε_o is the permittivity of free-space and d_{mn} are the nonlinear coefficients of the crystal ascribable to the electric field components with suitable polarisation. It can be seen above that the second order polarisation is induced by products of the incident electric field components. For the mixing of co-propagating plane waves this product results in,

$$E_1E_2 = \left(A_1 e^{i(\omega_1 t - k_1 z)} + cc\right)\left(A_2 e^{i(\omega_2 t - k_2 z)} + cc\right) = A_1A_2 e^{i((\omega_1+\omega_2)t-(k_1+k_2)z)} + A_1A_2 e^{i((\omega_1-\omega_2)t+(k_1-k_2)z)} + \ldots \qquad (2.3)$$

The nonlinear polarisation, $P^{(2)}$, thus contains sum and difference frequency components of the incident electric fields, which can be re-radiated at these sum and difference frequencies. The particulars of arriving at the field equations which describe light waves propagating in a second order medium are well understood and can be found in many texts on optics (Davis[69] and Boyd[70] were used for reference for this dissertation). Suffice to say that by considering the electrical displacement, $D = \varepsilon_0 E + P$, in the context of Eq. (2.2) and assuming no free charges (lossless and optical media with negligible permeability) the decoupling of Maxwell's equations bring us to the modified wave equation,

$$\nabla^2 E = \mu\varepsilon_0\varepsilon_r \frac{\partial^2 E}{\partial t^2} + \mu \frac{\partial^2}{\partial t^2} P_{NL} \qquad (2.4)$$

For illustrative purposes sum-frequency-generation (SFG) and second-harmonic-generation (SHG), which are the simplest, prototypical processes, will be looked at. SFG occurs when the incident fields are at frequencies ω_1 and ω_2 so that a term in the second order polarisation is at the sum frequency,

$$\omega_3 = \omega_1 + \omega_2 \qquad (2.5)$$

thus we have a three-wave mixing process. Considering plane waves propagating collinearly in the *z* direction, with polarisations in the *x,y* plane, we have

$$\begin{aligned} E_{1i}^{\omega_1}(z,t) &= \frac{1}{2}\left[E_{1i}(z) e^{i(\omega t - k_1 z)} + cc \right] \\ E_{2j}^{\omega_2}(z,t) &= \frac{1}{2}\left[E_{2j}(z) e^{i(\omega t - k_2 z)} + cc \right] \\ E_{3k}^{\omega_3}(z,t) &= \frac{1}{2}\left[E_{3k}(z) e^{i(\omega t - k_3 z)} + cc \right] \end{aligned} \qquad (2.6)$$

(*cc* – is the complex conjugate). Treating the equations from (2.6) with the wave-equation in (2.4), using Eq (2.2) to infer the P_{NL} term, and using the slowly varying amplitude approximation, $\frac{d^2 E}{dz^2} \approx 0$, the propagation of the three waves can be derived as a set of coupled equations which describe the parametric interaction of the waves at the three frequencies,

$$\frac{dE_{\omega_1 i}}{dz} = -\frac{i\omega_1 d_{eff}}{4n_1 c} E_{\omega_3 k} E^*_{\omega_2 j} e^{-i\Delta kz}$$
$$\frac{dE_{\omega_2 j}}{dz} = -\frac{i\omega_2 d_{eff}}{4n_2 c} E_{\omega_3 k} E^*_{\omega_1 j} e^{-i\Delta kz} \qquad (2.7)$$
$$\frac{dE_{\omega_3 k}}{dz} = -\frac{i\omega_3 d_{eff}}{4n_3 c} E_{\omega_1 i} E_{\omega_2 j} e^{i\Delta kz}$$

In these equations the field subscripts *ijk* denote the polarisations for the three fields, d_{eff} is the effective nonlinear coefficient found by considering Eq (2.2) and the propagation direction in the material. $k_{1,2,3}$ are the wave-numbers for the particular fields given by

$$k = \frac{2\pi n}{\lambda} = \frac{\omega n}{c} \qquad (2.8)$$

and Δk is the wave-number or phase-mismatch between the waves given by

$$\Delta k = k_3 - k_2 - k_1 \qquad (2.9)$$

In general the goal is to start with input fields E_1 and E_2 and generate the third field E_3. In (2.7) it can be seen that the change in E_1, E_2, and E_3 as the waves propagate will be oscillatory in nature, ($e^{\pm i\Delta kz}$) unless,

$$\Delta k = k_3 - k_2 - k_1 = 0 \qquad (2.10)$$

The condition in (2.10), which will be dealt with extensively in the following section, is called the phase-matching condition, and is of vital importance to obtaiing efficient 2nd order nonlinear processes. If the low conversion approximation is considered, i.e. when E_1 and E_2 remain relatively unchanged so we can ignore depletion, we can look at solving for the generated field, E_3, by simple integration along the interaction length. From (2.7), considering propagation over a length L we have,

$$E_3(L) = \frac{-i\omega_3 d}{4n_3 c} E_{1k} E_{2j} \int_0^L e^{i\Delta kz} dz \qquad (2.11)$$

which is evaluated as,

$$E_3(L) = \frac{-i\omega_3 d}{4n_3 c} E_{1k} E_{2j} \left[\frac{e^{i\Delta kL} - 1}{i\Delta k} \right]$$
$$= \frac{-\omega_3 d}{4n_3 c} E_{1k} E_{2j} \frac{L}{2} e^{i\Delta kL/2} \left[\frac{e^{i\Delta kL/2} - e^{-i\Delta kL/2}}{\Delta kL/2} \right]$$
$$= \frac{-i\omega_3 d}{4n_3 c} E_{1k} E_{2j} L e^{i\Delta kL/2} \left[\frac{\sin(\Delta kL/2)}{\Delta kL/2} \right]$$

Looking at the irradiance of the generated field we have,

$$I_3 = \frac{E_3 E_3^*}{2Z_3} = \frac{1}{2Z_3}\frac{\omega_3^{\,2} d_{eff}^{\,2}}{16 n_3^2 c^2} I_1 2Z_1 I_2 2Z_2 L^2 \left[\frac{\sin(\Delta kL/2)}{\Delta kL/2}\right]^2$$

$$I_3 = \sqrt{\frac{\varepsilon_3\varepsilon_0}{\mu}}\frac{\omega_3^{\,2} d_{eff}^{\,2}}{16 n_3^2 c^2} I_1 I_2 4\sqrt{\frac{\mu}{\varepsilon_1\varepsilon_0}}\sqrt{\frac{\mu}{\varepsilon_2\varepsilon_0}} L^2 \left[\frac{\sin(\Delta kL/2)}{\Delta kL/2}\right]^2 \qquad (2.12)$$

$$I_3 = \frac{\omega_3^{\,2} d_{eff}^{\,2}}{4 n_3 n_1 n_2 \varepsilon_0 c^3} I_1 I_2 L^2 \left[\frac{\sin(\Delta kL/2)}{\Delta kL/2}\right]^2$$

where the irradiance has been introduced for each field as

$$I = \frac{E^* E}{2Z} \qquad (2.13)$$

with Z being the impedance of the material for the particular field given as.

$$Z = \sqrt{\frac{\mu}{\varepsilon_r\varepsilon_0}} = \frac{1}{n\varepsilon_0 c} \qquad (2.14)$$

From (2.12) we see that the irradiance of the generated field has a quadratic dependence on the input fields and interaction length, and a *sinc²* dependence on the term $\Delta kL/2$. For the generated field to grow steadily as the fields propagate, the *sinc²* function needs to tend to unity, i.e. its argument needs to tend to zero. This occurs when the phase-matching condition in (2.10) is satisfied. In the case of second-harmonic-generation $E_1=E_2$ and equations 2.8 and 2.10 simplify to

$$\Delta k = k_{2\omega} - 2k_{\omega} = n_{2\omega} - n_{\omega} = 0 \qquad (2.15)$$

$$I_{2\omega} = \frac{\omega^2 d_{eff}^2}{n_{\omega}^2 n_{2\omega} \varepsilon_0 c^3} I_{\omega}^2 L^2 \left[\frac{\sin(\Delta kL/2)}{\Delta kL/2}\right]^2 \qquad (2.16)$$

Equation (2.16) is a well known equation for describing small-signal SHG, with the efficiency being proportional to the fundamental irradiance and the square of the interaction length,

$$\eta = \frac{I_{2\omega}}{I_{\omega}} \propto I_{\omega} L^2 \qquad (2.17)$$

For efficient processes where the fundamental is being noticeably depleted the SHG process is more precisely described by a Jacobi elliptical *sn* function[71], which retains the *sinc²* phase-matching behaviour for low efficiencies, but becomes narrower with larger secondary lobes for highly efficient conversion, as illustrated in Figure 2.1. The SH field grows quadratically when

phase-matched with low efficiency, and then tends the $tanh(\Gamma L)^2$ form when depletion is appreciable, as shown in Figure 2.2.

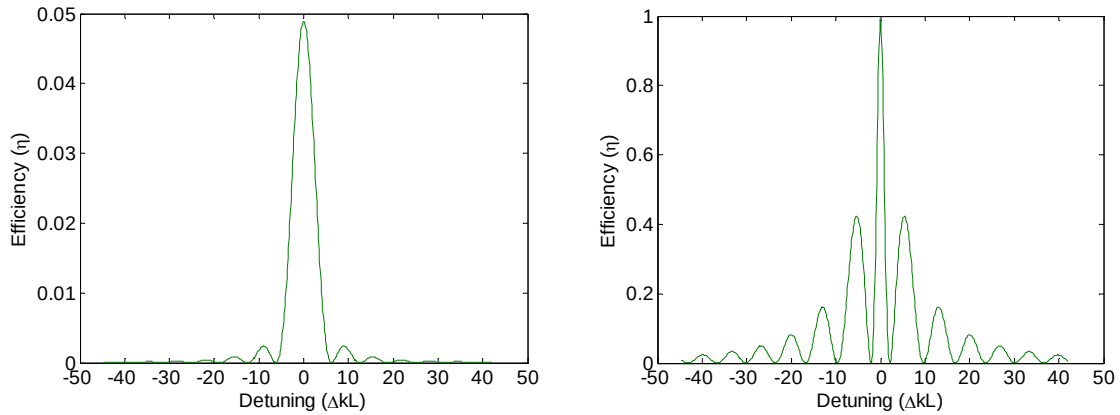

Figure 2.1 Phase-matching curves for SHG. Left: negligible depletion regime. Right: Strong depletion regime.

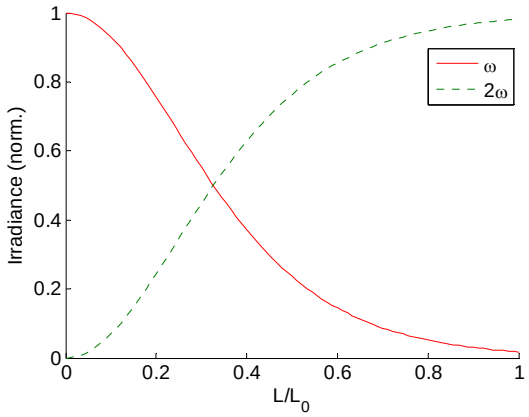

Figure 2.2 Evolution of the irradiances for phase-matched second-harmonic-generation.

To demonstrate the effect of the phase-matching condition (Eq.(2.15)) when propagating through a nonlinear material, consider the case of collinear plane-waves with all fields polarised in the same direction. Due to natural dispersion Eq. (2.15) will not generally be satisfied, as the refractive indices for the fundamental and its second-harmonic field are usually quite different. With a non-zero Δk the intensity of the second-harmonic builds and decays periodically as the fields propagate, and the maximum intensity that the second harmonic can reach is very low compared the fundamental. The period of this dephasing of the second-harmonic and the fundamental is the nonlinear coherence length of the process,

$$l_c = \frac{\pi}{\Delta k} \tag{2.18}$$

Phase-matching seeks to compensate for, or make this coherence length as long as possible. Figure 2.3 shows an example of the evolution of a phase-matched and non-phase-matched SHG process. The phase-matched process grows quadratically while the non-phase-matched SHG grows and decays with the nonlinear coherence length. Methods for achieving phase-matched processes are reviewed in the following section.

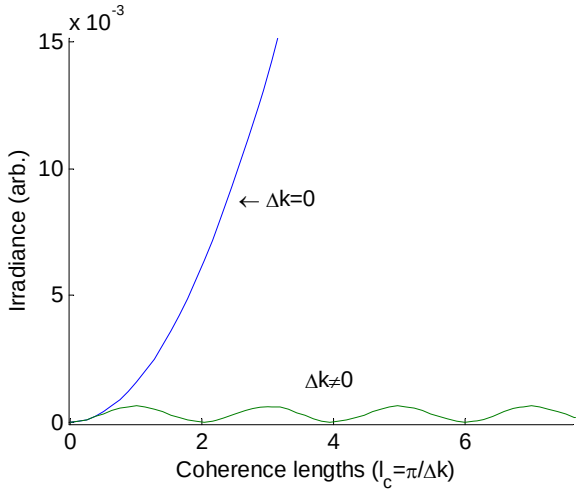

Figure 2.3 Evolution of a phase-matched and a non-phase-matched SHG process

2.2.2 Methods of phase-matching

Birefringent phase matching.

The most common method of phase-matching is to make use of the birefringence in uniaxial and biaxial optical crystals. The tensor nature of the coupling of the incident electric fields to the nonlinear polarisation, along with the directional dependence of the refractive indices in these materials can be used to satisfy equation (2.10) and (2.15). Here we will concentrate on uniaxial crystals, and particularly on negative uniaxial crystals such as lithium niobate. In uniaxial crystals there are two well designated refractive index components called the ordinary and extraordinary indices (or fast and slow indices respectively for a negative uniaxial crystal such as lithium niobate). These are shown geometrically in Figure 2.4

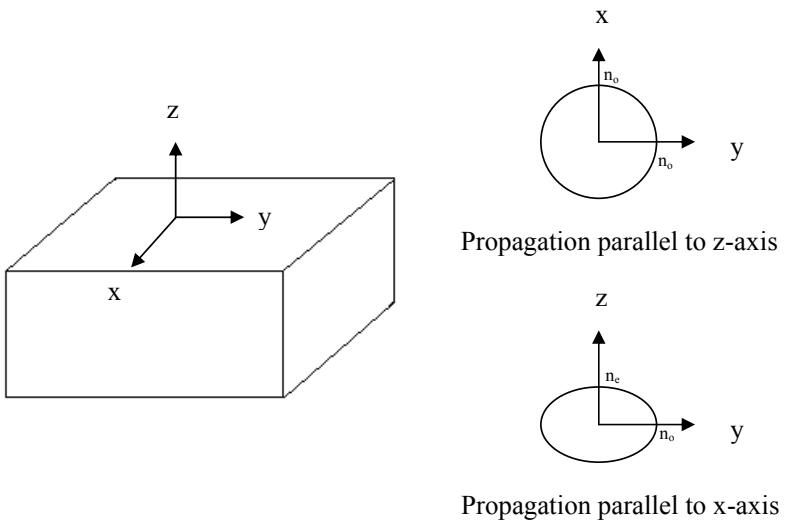

Figure 2.4. Refractive indices seen by fields propagating parallel to the z and x–axes in a negative uniaxial crystal.

The refractive index is also a function of the frequency and wavelength of the light in the material. This can be visualised by changes in the radii of the refractive index ellipses shown in Figure 2.4. When you overlay the set of the refractive index curves for the fundamental and second harmonic frequencies, certain propagation angles may be found where the phase-matching condition in Eq. (2.15) is satisfied, indicated by the phase matching angle θ_{pm} in Figure 2.5. At this propagation direction in the crystal the differently polarised fundamental and second harmonic components will see the same refractive indices so that the phase-matching condition is satisfied.

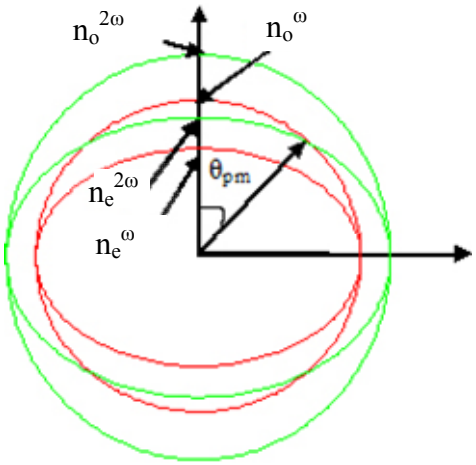

Figure 2.5 Phase -matching diagram for a negative uniaxial crystal. The red curves indicate the refractive indices for the fundamental fields and the green curves indicate the refractive indices for the second harmonic fields.

From Eq. (2.2) it can be seen that in *3m* group crystals an electric field polarised along the *x* or *y* axes will produce a nonlinear polarisation along the *z* axis via the d_{31} nonlinear coefficient. The incident and generated field utilize the ordinary and extraordinary refractive indices respectively, allowing for birefringent phase-matching if Eq. (2.15) can be satisfied. The nonlinear coefficient associated with an arbitrary birefringent process is refererd to as the effective nonlinear coefficient, d_{eff}, and is generally a geometric combination of the principal nonlinear coefficients in Eq. (2.2). Concentrating on the *3m* class of crystals, the value of d_{eff} for birefringent phase matching can be found using the relation

$$d_{eff} = d_{31}\sin\varphi - d_{22}\cos\varphi\sin 3\phi \qquad (2.19)$$

where φ and ϕ describe the propagation direction of the fields with respect to the crystal axis i.e. φ is the declination angle from the optical axis (z-axis) and ϕ is the angle from the x-axis in the *xy* plane. The birefringent phase-matching approach can have disadvantages such as Poynting vector walk-off, where the energy flow associated with the electrical displacement in the crystal is in a slightly different direction to the propagating fields. Restrictive angular, temperature and wavelength acceptances may also be a problem, as well as identifying crystals suitable for the particular wavelengths. A solution to the phase-matching problem, which avoids some of the disadvantages inherent in bulk single crystals, is quasi-phase-matching in domain engineered materials.

Quasi-phase-matching.

Quasi-phase-matching was suggested by Armstrong and Bloembergen in 1962[9]. Rather than letting nature dictate suitable conditions in birefringent crystals, QPM requires modulation of the crystal structure in a pattern that provides a net compensation for the phase-mismatch between the interacting waves. In lithium niobate this involves modulation of the crystal's ferroelectric axis which also corresponds to inversions in the $\chi^{(2)}$ tensor. This modulation introduces extra complexity to the coupled field equations. For example the d_{33} coefficient (and also the d_{31} and d_{22} coefficients) changes its relative sign with each inversion of the crystal structure. Mathematically we describe these inversions of the nonlinear coefficient with a Fourier series for the appropriate pattern of the modulation. The most common implementation is to use periodic inversions, which introduces the nonlinear coefficient as a rectangular wave Fourier series into the coupled field equations. That is, for a periodically poled crystal the nonlinear coefficient can be represented by a Fourier series in the form;

$$d(z) = d_{eff} \sum_{m=-\infty}^{+\infty} g_m e^{iG_m z} \tag{2.20}$$

where the g_m terms are the Fourier coefficients and the G_m terms are the series of inverse lattice vectors, or spatial frequencies, which are harmonics of the primary spatial frequency, related to the period of inversions, Λ, by,

$$G_m = \frac{2\pi m}{\Lambda} \tag{2.21}$$

This Fourier series can then be introduced into the field equations where, mathematically, the exponents can be combined with other exponential terms including the phase-mismatch term $i\Delta kz$. For the second-harmonic field equation (see Eq. (2.7)) we arrive at,

$$\begin{aligned} \frac{dE_{2\omega}}{dz} &= -\frac{i2\omega}{4n_{2\omega}c} d_{eff} \sum_{m=-\infty}^{+\infty} g_m e^{iG_m z} E_\omega^2 e^{i\Delta kz} \\ &= -\frac{i2\omega}{4n_{2\omega}c} E_\omega^2 d_{eff} \sum_{m=-\infty}^{+\infty} g_m e^{i(G_m+\Delta k)z} \end{aligned} \tag{2.22}$$

The key to achieving a growing level of SHG as the fields propagate is to end up with a constant (linear) term from the series in Eq (2.22), so that the second harmonic has a steady (non-oscillating) component in its derivative. This is now realized by satisfying the **quasi-phase-matching** condition

$$\Delta k + G_m = \Delta k_Q = 0 \tag{2.23}$$

for one of the G_m*'s* in the series. For rectangular-type modulation of the crystal structure we introduce the rectangular-wave Fourier series as,

$$d_Q = d_{eff} \sum_{m=-\infty}^{\infty} g_m e^{iG_m z} = 2d_{eff} \sum_{\substack{m=-\infty \\ m\neq 0}}^{\infty} \frac{\sin(D\pi m)}{\pi m} e^{iG_m z} \tag{2.24}$$

where D is the duty cycle (similar to grating mark-space ratio) of the inversions. From (2.21) it can be seen that the poling period required to satisfy the quasi-phase-matching condition in (2.23) is,

$$\Lambda = \frac{2\pi m}{\Delta k} \tag{2.25}$$

Here the sign of Δk is not important as G_m will have alternatively signed (±) spatial components from the series in (2.24), and a frequency conversion processes with a negative Δk that would

otherwise fall beyond the noncritical phase-matching point in birefringent media can still be quasi-phase-matched. In the case of SHG the required period is simply derived as,

$$\Lambda = \frac{m\lambda}{2(n_{2\omega} - n_{\omega})} \tag{2.26}$$

One important aspect of QPM is the effect of the poling duty cycle on the effective nonlinearity. As seen in (2.24) both the order of the grating component, m, and the duty cycle, D, determine the strength of the nonlinear coefficient compared to the materials maximum possible value of d_{eff}. In the ideal case of a 1st order grating component and a 50% duty cycle the effective nonlinear coefficient of the QPM is maximized, and in comparison to d_{eff} will be,

$$d_Q = \frac{2d_{eff}}{\pi} \tag{2.27}$$

Note that for a 50% duty cycle square-wave poling function, nonlinear gain exists only for odd values of the QPM order m (refer again to Eq. (2.24)). In general the nonlinear gain sees a sinusoidal dependence on D, which for higher order QPM m>1 results in several suitable duty-cycles for achieving the optimal nonlinear gain for the particular QPM order. The even order QPM orders can also be utilized by poling patterns with the appropriate duty-cycles. The nonlinear gain dependence on duty cycle is shown for the odd and even QPM orders is shown in Figure 2.6 and Figure 2.7 respectively. The optimum duty cycle(s) for a given order of phase-matching can be found as,

$$D = \frac{n + 1/2}{m}, \quad n : 0 \to m - 1 \tag{2.28}$$

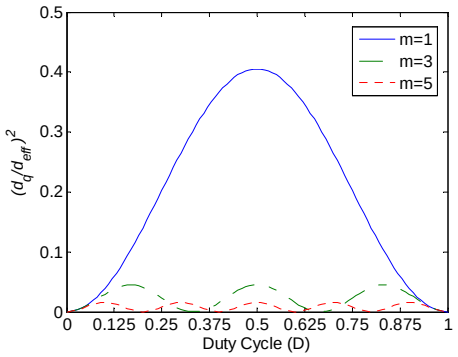

Figure 2.6. Dependence of the nonlinear gain on the poling duty cycle for odd-order QPM.

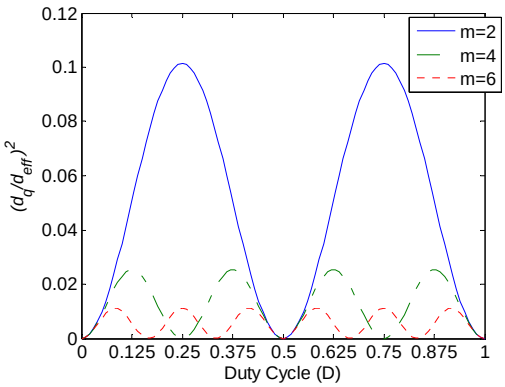

Figure 2.7. Dependence of the nonlinear gain on the poling duty cycle for even-order QPM.

The growth of quasi-phase-matched SHG can be found by integrating (2.22), in a similar fashion to the genaral case shown in (2.11). Considering just the dominant term from the series for d_Q term, where the QPM condition in (2.23) is satisfied, we have an approximate form for the small-signal second harmonic irradiance that is similar to the general case,

$$I_{2\omega} = \frac{\omega^2 d_Q^2}{n_\omega^2 n_{2\omega} \varepsilon_0 c^3} I_\omega^2 L^2 \left[\frac{\sin\left(\Delta k_Q L/2\right)}{\Delta k_Q L/2} \right]^2 \qquad (2.29)$$

The other terms from (2.22) do contribute to the evolution of the SH irradiance by giving an undulating appearance to the irradiance as it grows along the interaction length. The evolution of the SHG irradiance phase-matched with the *m=1,2,3* QPM orders is shown in Figure 2.8.

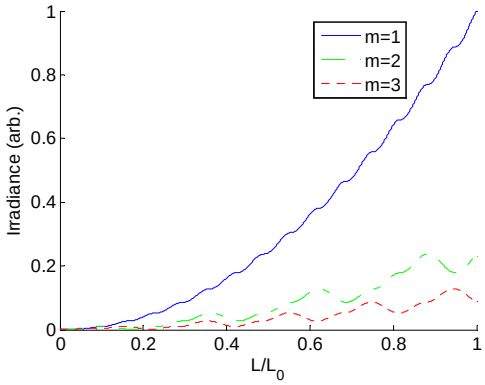

Figure 2.8. Evolution of the irradiance of QPH SHG for 1st, 2nd and 3rd order QPM.

One of the advantages of QPM in materials such as lithium niobate and tantalate is access to the large d_{33} nonlinear coefficient. The d_{33} nonlinear coefficient cannot be accessed by birefringent phase-matching as all fields need to be co-polarised along the z-axis of the crystal. In negative

uniaxial crystals this is an '*eee*' process as all fields propagate as extraordinary waves when polarised along the z-axis. Type-I interactions on the d_{31} nonlinear coefficient (where the fundamental components are polarised orthogonally to the second harmonic) can also be quasi-phase-matched. In negative uniaxial crystals type-I phase-matching is an '*ooe*' interaction where the fundamental propagates as an ordinary wave and the second harmonic as an extraordinary wave. Although $d_{31} < d_{33}$ in these crystals, the '*ooe*' process, which will be looked at experimentally in this dissertation, can be easier to quasi-phase-match under some conditions, as the required poling period can longer (especially in the 1-1.3μm region) resulting in more reliable fabrication of suitable crystals.

Some performance considerations when phase-matching, either birefringently or by QPM methods, are the wavelength and temperature acceptance of the interaction being implemented. The wavelength and temperature acceptance for QPM can be determined from the $sinc^2(\Delta k_Q L/2)$ term in (2.29) and the Sellmeier relations, which relate the refractive indices to the crystal temperature and wavelength of the incident light. Typical Sellmeier equations for congruent composition lithium niobate[5] are given below in equations (2.30) and (2.31), where the wavelength is in μm and the temperature in Kelvin (the zero point temperature for these particular equations is 297.5K, hence the T^2-88506.25 terms).

$$n_o^2 = 4.9048 + 2.1429\times10^{-8}(T^2 - 88506.25) + \frac{0.11775 + 2.2314\times10^{-8}(T^2 - 88506.25)}{\lambda^2 - (0.21802 - 2.9671\times10^{-8}(T^2 - 88506.25))^2} - 0.027153\lambda^2 \tag{2.30}$$

$$n_e^2 = 4.5820 + 2.2971\times10^{-7}(T^2 - 88506.25) + \frac{0.09921 + 5.716\times10^{-8}(T^2 - 88506.25)}{\lambda^2 - (0.21090 - 4.9143\times10^{-8}(T^2 - 88506.25))^2} - 0.02194\lambda^2 \tag{2.31}$$

The calculated temperature and wavelength curves for type-0 and type-I QPM SHG, from a 1064 nm source laser and a temperature near 450 K, in a 5 mm long length of lithium niobate are shown in Figure 2.9 and Figure 2.10 respectively. It is apparent that while the type-0 case has a broader temperature acceptance bandwidth than the type-I case, its wavelength acceptance is narrower. There are QPM grating design techniques which address issues such as wavelength and temperature acceptances when using QPM which will be addressed in the follow section.

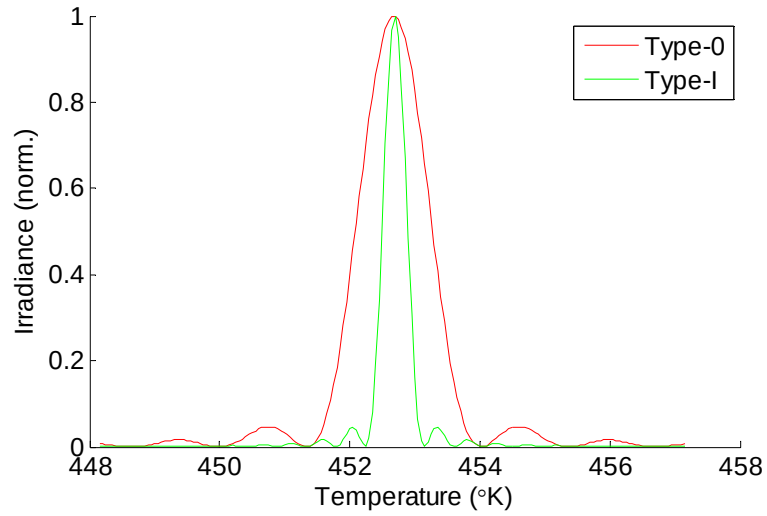

Figure 2.9. Temperature acceptance curves for type-0 and type-I QPM SHG in a 5mm section of lithium niobate.

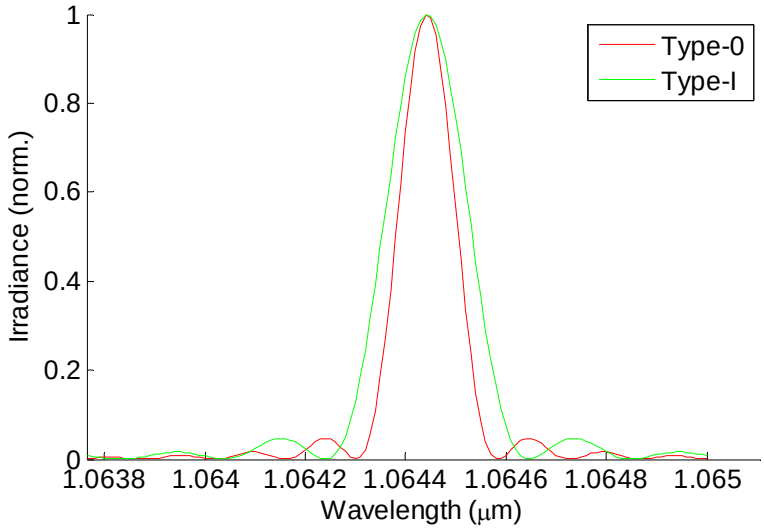

Figure 2.10. Wavelength acceptance curves for type-0 and type-I QPM SHG in a 5mm section of lithium niobate.

2.3 Advanced structures

2.3.1 Overview.

QPM in domain engineered materials is by no means limited to a single three-wave-mixing process per QPM grating, and is amenable to many of the tricks and traits of the Fourier toolbox used in other grating based devices. That said, when moving to multiple or broadband QPM gratings there will be a trade-off against the nonlinear efficiency of the crystal, as the nonlinear

gain will be distributed amongst the interactions it has been designed to phase-match. For broadband or multi-wavelength systems, the use of advanced QPM can be beneficial and even necessary for the performance and functionality of the optical system. Longitudinally varying gratings (1D), which are compatible with waveguides and are the most commonly implemented. More exotic approaches to QPM have also been explored using fabricated and naturally occurring 2D and 3D domain structures. In this section various QPM gratings which allow for broadband, multi-wavelength and cascaded phase-matchings will be reviewed, along with some of the recent results in 2D and 3D QPM.

2.3.2 Multiple, sequential and fan-out QPM gratings.

The simplest way to realise tuneable or multiple QPM structures is to use sequential or spatially varying QPM gratings. Placing several gratings in the same crystal with varying periods, either adjacent each other or in a longitudinal sequence, is a simple way of producing multipurpose QPM crystals. Multiple adjacent QPM gratings, typically with 0.1-0.5μm steps in period and with 5 or more gratings fabricated in a single crystal, are commercially available and are used in tuneable OPO configurations. The selection of grating period, in conjunction with temperature and cavity tuning, allows for continuous tuneability across range of wavelengths[72]. Fan-out grating designs have also been demonstrated as useful structures for continuous spectral tuning of the phase-matching condition[73]. In these structures the period is slowly ramped from one edge of the crystal to the other, presenting a continuous transversely varying period, allowing tuning of the phase-matching by translating the crystal through the pump beam as shown in Figure 2.11. Longitudinally sequential gratings can be used in a similar manner for some applications where lateral translation of the crystal is undesirable. This of course limits the available crystal length that each grating period can occupy limiting the efficiency. Sequential gratings can however be useful for cascaded processes such as third harmonic generation or multi-step processes such as SHG/SFG-DFG, where different gratings can be placed sequentially to phase-match first one then subsequent processes. An attractive alternative is to use more complicated, aperiodic gratings which provide distributed phase-matching to several interactions. This approach can provide increased efficiency and control over the acceptance bandwidths compared to simple periodic gratings.

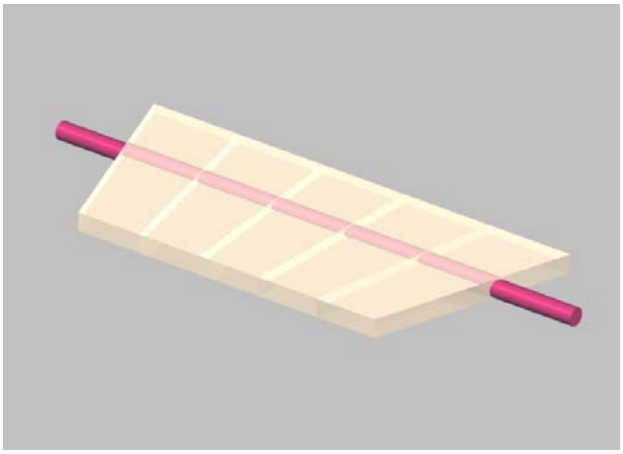

Figure 2.11 Fan out grating geometry

2.3.3 Chirped and apodized gratings

A common technique to improve the bandwidth in many grating based technologies is to implement chirped and apodized gratings. Such techniques are used in fibre Bragg gratings (FBGs) to produce broadband resonant filters for WDM, gain flattening filters for EDFAs etc. In the case of QPM the goal is to ensure phase-matching across the optical bandwidth a laser source of interest. Chirp and apodization in QPM gratings[74,75,76] allow for this and can even lead to temporal compression and modification of the converted pulses, similar to the chromatic dispersion compensation properties of chirped FBGs. The basic mathematical form of chirp is a continuous or quasi-continuous change in the periodicity of the structure as some function of the length. For a linearly chirped structure the periodicity can simply be described by

$$\Lambda(z) = \Lambda_0 / (1 \pm rz) \qquad (2.32)$$

where Λ_0 is the initial period and r represents the rate of chirp. Because the chirped structure has a continuous band of periods across the grating, it will have an increased phase-matching acceptance in both the wavelength and temperature tuning regimes. Figure 2.12 shows an exaggerated example of a grating with an increasing linear chirp across its length.

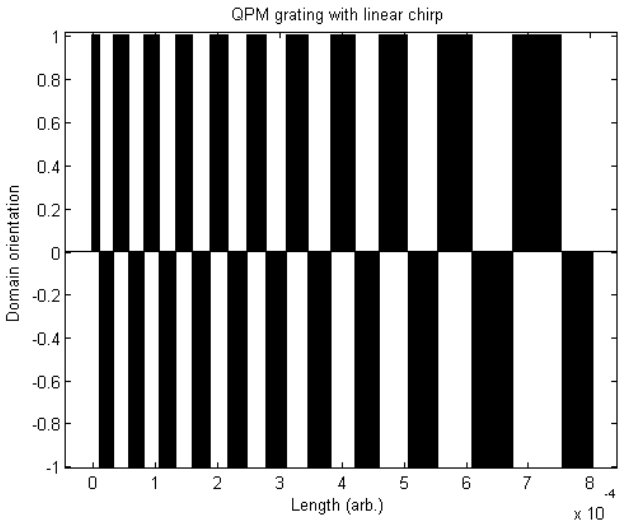

Figure 2.12 QPM grating with linear chirp.

One of the issues of using a purely chirped grating becomes apparent when considering the Fourier spectrum of such a grating. The nonlinear gain across the phase-matching bandwidth will not be flat, especially at the edges of the acceptance band. This will be reflected in the phase-matching performance by producing a markedly more efficient frequency conversion at the edges of the bandwidth provided by the chirp. This is shown in Figure 2.13, along with the spectrum of an un-chirped grating for comparison.

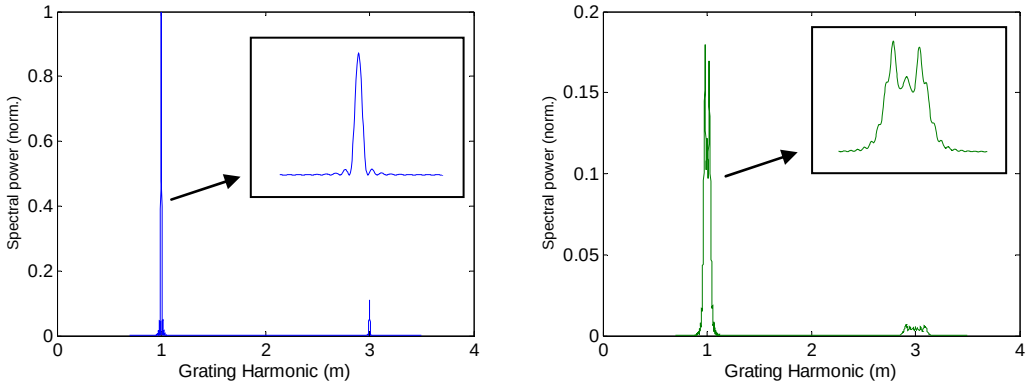

Figure 2.13 Left: Power spectrum of a periodic square wave grating. Right: Power spectrum of a linearly chirped grating. Insets show expanded view of the 1st order grating component.

Flattening the phase-matching bandwidth of a chirped grating is performed by apodizing the grating. Typically apodization is performed by modulating the contrast of the grating, e.g. the refractive index contrast is modulated in apodized FBGs to produce flat-top stop-band filters. In QPM structures it is the local duty cycle which is modulated to control the relative efficiency of the nonlinear conversion across the phase-matching bandwidth. The local duty cycle influences

the nonlinear gain as suggested by Eq. (2.24). For a linear chirp the major feature of the QPM spectrum which needs to be modified is the enhanced efficiency at the band edges. To remove these peaks the duty cycle needs to follow a function which reduces the efficiency at the maximum and minimum periods in the chirped structure. A simple approach to this is a centered *tanh* function,

$$D(z) = D_0 \tanh\left(\frac{2az}{L}\right), \quad 0 \le z \le L/2$$
$$D(z) = D_0 \tanh\left(\frac{2a(L-z)}{L}\right), \quad L/2 \le z \le L \tag{2.33}$$

where a is a parameter which varies the rate of apodization across the length of the crystal. A plot of an apodization profile and the corresponding grating with chirp is shown in Figure 2.14.

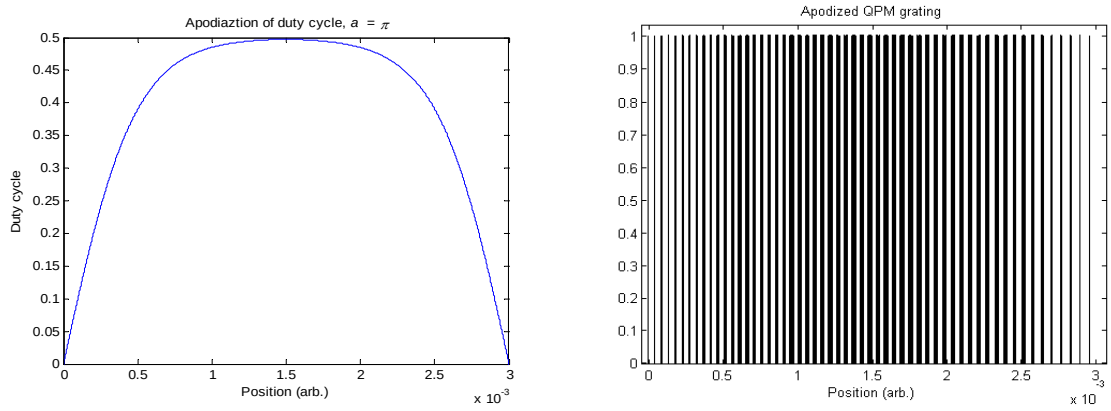

Figure 2.14 Left Apodization profile of the duty as a function of the crystal length. Right: Chirped and apodized grating for broadband applications.

Such an apodization profile smooths the phase-matching curve, providing similar nonlinear gain across the phase-matching bandwidth and removing the peaks at the band edges, as shown in figure Figure 2.15.

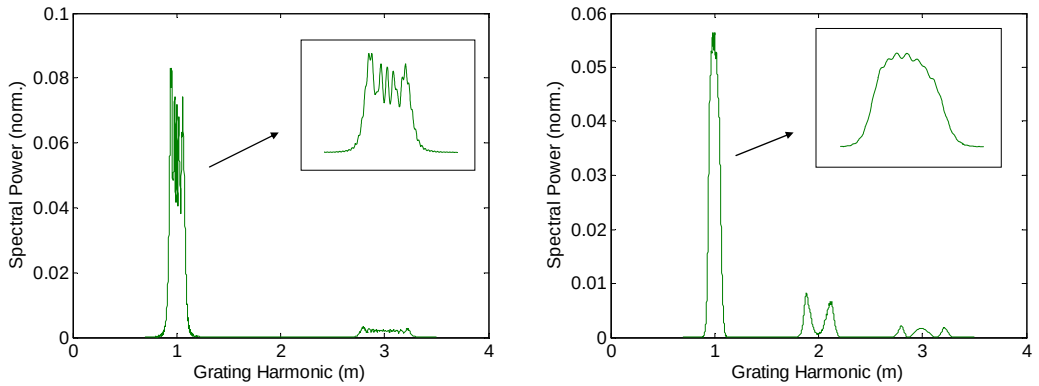

Figure 2.15 Power spectrum of an un-apodized (left) and apodized (right) chirped grating.

2.3.4 Aperiodic and phase-reversed

The chirped and apodized gratings reviewed in the previous section allow for phase-matching of broadband laser light, but for simultaneously phase-matching multiple processes, which may have substantially different wavelengths, other approaches need to be considered. Aperiodic and quasi-periodic domain structures, sometimes referred to as optical super-lattices, can be used to achieve this. These are QPM gratings which contain several grating vectors (spatial frequencies) suitable for phase-matching several processes at the same time. There are several approaches to designing such structures which will be reviewed here, including Fibonacci sequence based gratings, phase-reversed gratings and summed Fourier component gratings. The general goal is to diversify the Fourier spectrum of the grating structure to provide the appropriate spatial frequencies to allow for multiple phase-matching conditions to be satisfied.

Fibonacci series lattices

In the case of the Fibonacci series approach[77] two or more grating building blocks, which are determined by the phase-matching conditions, are arranged according to the Fibonacci series,

$$S_{j+1} = S_j + S_{j-1} \tag{2.34}$$

Looking at the case of two phase-matched processes, say a SHG and then SFG between the fundamental and second-harmonic to get to the third harmonic, the grating can be made up of two building blocks, *A* and *B*. Each block has a positive and negative domain orientation with a particular width of the positive and negative domain orientations for each block. Determining the construction of these blocks is based around finding a good approximation to the relationship

$$l = sl_{C1} = \Phi^n l_{C2} \tag{2.35}$$

where l_{C1} and l_{C2} are the nonlinear coherence lengths (2.18) of the two processes, s is an odd integer and $\Phi=(1+\sqrt{5})/2 \approx 1.618$ is the golden ratio. The blocks *A* and *B*, illustrated in Figure 2.16, are then constructed on the principle that one of the domain orientations in each block is of the characteristic length l, $l_{A1}=l_{B1}=l$ and the other orientation is a weighted distribution of this length given as,

$$\begin{aligned} l_{A2} &= l(1+\eta) \\ l_{B2} &= l(1-\Phi\eta) \end{aligned} \tag{2.36}$$

Here η is a weighting parameter which controls the relative distribution of the nonlinearity between the coupled processes, which in this case is important for achieving optimal conversion to the third harmonic. The construction of the Fibonacci sequence then follows (2.34), such that $S_0 = A$, $S_1 = B$, $S_2 = AB$, $S_3 = BAB$ etc, so that the sequence $S_0S_1S_2S_3\ldots \rightarrow ABABBAB\ldots$

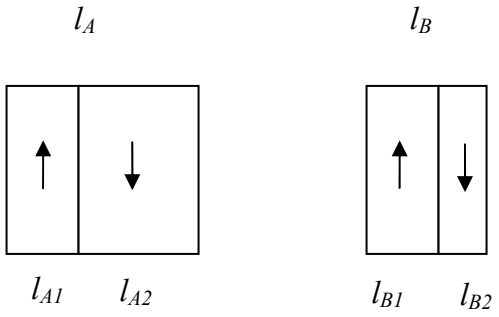

Figure 2.16. Building blocks A and B for a Fibonacci quasi-periodic-grating.

The lattice vectors that such a grating contains are determined by,

$$G_{m,n} = \frac{2\pi}{l'}\left(m + \Phi n\right) \tag{2.37}$$

where $l' = \left(\Phi l_A + l_B\right)$ is the average structural parameter. It is these lattice vectors which need to correspond the phase-mismatches of the two processes involved for some m and n. Fibonacci sequence gratings are however somewhat limited in their versatility as there is a reliance on nature to provide suitable wavelengths and temperatures so that Eq. (2.35) can be satisfied.

As an example of a Fibonacci series grating consider third harmonic generation of 1.662 μm laser light in $LiNbO_3$. The coherence lengths of the SHG and SFG processes at 200 ºC are approximately 10.54 μm and 4.03 μm (individual poling periods of 21.084 μm and 8.053μm) respectively, which approximately corresponds to $l = l_{shg} = \Phi^2 l_{sfg}$. The grating blocks are thus, $l_{A1} = l_{B1} = 10.54\mu m$, and with $\eta = 0.3$ (near optimal of THG) we have $l_{A2} = 13.7\mu m$ and $l_{B2} = 5.42\mu m$. A section of the grating and its frequency spectrum are shown in Figure 2.17. Spatial frequencies corresponding to the poling periods for the individual processes appear in the frequency spectrum, as required for phase-matching. The evolution of the three fields as they propagate through the aperiodic QPM grating are shown in Figure 2.18. Zhu *et al* showed that such an approach offers ~8 times the efficiency of sequential gratings for the same process[77].

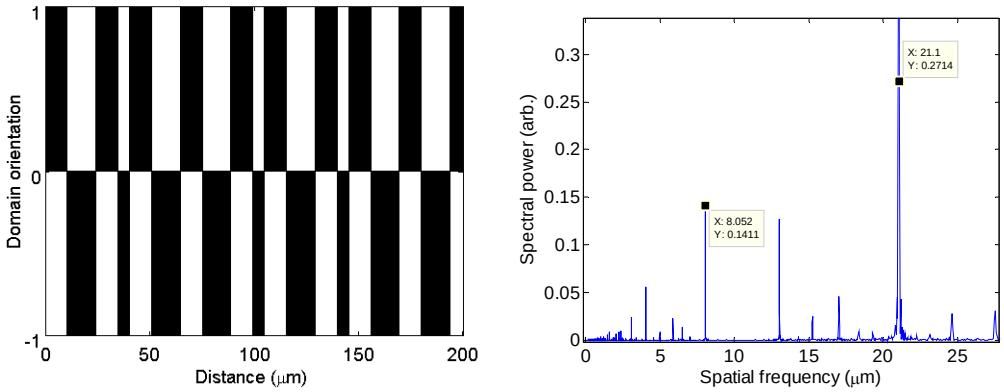

Figure 2.17 Domain pattern and frequency spectrum for an aperiodic optical lattice based on the Fibonacci sequence.

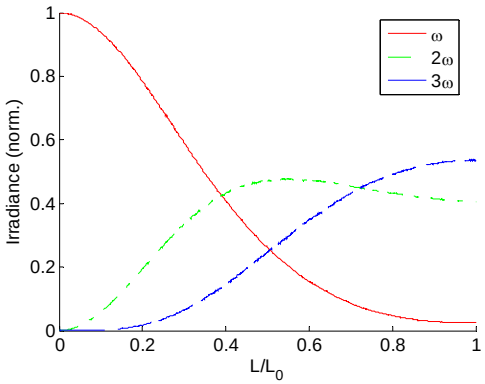

Figure 2.18. Third harmonic generation in an aperiodic optical lattice based on the Fibonacci sequence.

Phase-reversed gratings

Phase-reversed gratings are another quasi-periodic approach for achieving multiple phase-matching conditions in the same grating[78]. For the case of two phase-matched processes with phase-matching conditions $\Delta k_1 - G_1 = 0$ and $\Delta k_2 - G_2 = 0$ we construct a quasi-periodic grating such that the grating parameters are found as,

$$G_1 = \frac{2\pi}{\Lambda_Q} p_1 + \frac{2\pi}{\Lambda_{ph}} q_1 , \; G_2 = \frac{2\pi}{\Lambda_Q} p_2 + \frac{2\pi}{\Lambda_{ph}} q_2 \qquad (2.38)$$

Here Λ_Q is the primary period of the domain structure so that the unit size of the domain inversions is $\Lambda_Q/2$. The phase of the grating is reversed with a period Λ_{ph}. The parameters p and q are integers which indicate orders of the periodic and phase-reversal components. For 50% duty cycle grating components these need to be odd integers for the resulting grating to provide non-zero spatial frequency components at the required phase-mismatches. To ensure a fixed base

domain size as the building block for the grating we need to operate the crystal at wavelengths and temperatures that satisfy the additional constraint that

$$\Lambda_{ph} / 2\Lambda_Q = m \tag{2.39}$$

for some integer *m* so that the phase reversals happen modulo $\Lambda_Q/2$. Solving (2.38) for the periods that are used for fabrication we have

$$\Lambda_Q = \frac{2\pi(p_1 q_2 - p_2 q_1)}{G_1 q_2 - G_2 q_1}, \quad \Lambda_{ph} = \frac{2\pi(p_1 q_2 - p_2 q_1)}{G_1 p_2 - G_1 p_1} \tag{2.40}$$

along with the corresponding inverse vectors $G_{Q,ph} = 2\pi / \Lambda_{Q,ph}$. The phase-matching conditions for the two target processes are then satisfied by,

$$\Delta k_1 - G_Q p_1 - G_{ph} q_1 = 0, \ \Delta k_2 - G_Q p_2 - G_{ph} q_2 = 0 \tag{2.41}$$

A functional form of the uniform domain structure of the phase-reversed grating is,

$$d_{pr}(z) = d_{eff} sign(\sin(G_Q z)\sin(G_{ph} z)) \tag{2.42}$$

The practical composition of these gratings is illustrated in Figure 2.19.

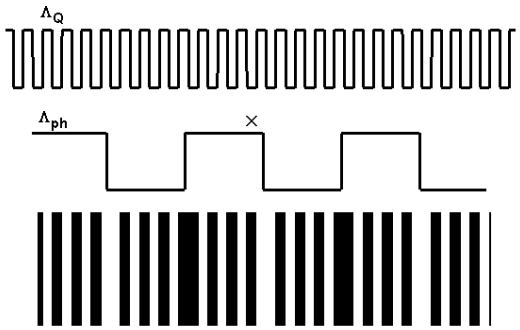

Figure 2.19 Composition of a phase-reversed grating. A primary grating period, Λ_Q, is modulated by a phase-reversal period, Λ_{ph}, resulting in quasi-periodic domain pattern as shown on the bottom of the figure.

Similar to Fibonacci gratings, with phase-reversed gratings we are again bound by nature in finding situations where (2.39) can be realized for reasonable selections of *p* and *q* parameters. Phase-reversed gratings are also analogous to sample gratings in FBGs and can be used in a similar fashion. Rather than targeting a particular pair of processes by finding periods and temperatures where Eqs. (2.40), (2.39) and (2.41) can be used, multiple 'channel' devices can be

created in an ad-hoc fashion by modulating a periodic grating with an arbitrary phase-reversal grating. There are still two design considerations with this approach.

- Firstly, for fabrication purposes it is convenient to have the phase-reversal period be an integer multiple of the periodic grating so a constant domain width can be used.
- Secondly, for the two initial sideband channels to have an equal nonlinear gain the phase-reversal period should an integer multiple of $\Lambda_Q / 2\pi$ which is not arbitrarily an integer multiple of Λ_Q. The best approximations to this is to use integers which are approximately integer multiples of 2π (50≈8×2π, 69≈11×2π etc.)

A 50% duty cycle phase-reversal introduces two channels either side of the primary frequency. Adjusting the duty-cycle of the phase-reversal grating introduces more channels into the Fourier spectrum of the grating. As an example, consider a primary grating period of 19 μm which is suitable for SHG of 1550 nm light at 304 K in congruent PPLN. Introducing a phase-reversal grating envelope with a period of 50×19 μm (50≈8×2π) produces two similar amplitude sidebands. The spectrum of such a phase reversed grating, 300 periods (5.7 mm) long, is shown along with the spectrum for the pure frequency grating in Figure 2.20. Phase-reversal gratings can also be stacked, i.e. multiple phase-reversal modulations can be applied sequentially to the grating design, multiplying the number of sidebands. Example spectra of gratings with an increased number of channels is shown in Figure 2.21.

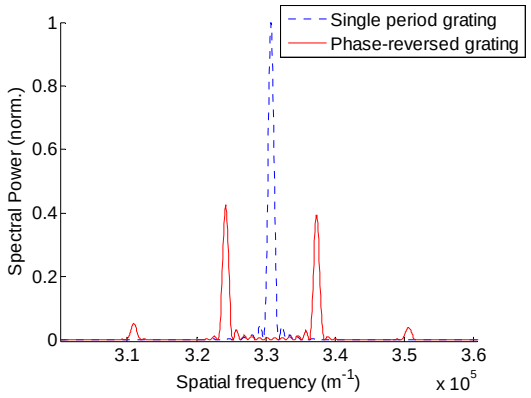

Figure 2.20 Spectrum of a phase reversed grating with $\Lambda_{ph}=50\Lambda_Q$, 300 periods long.

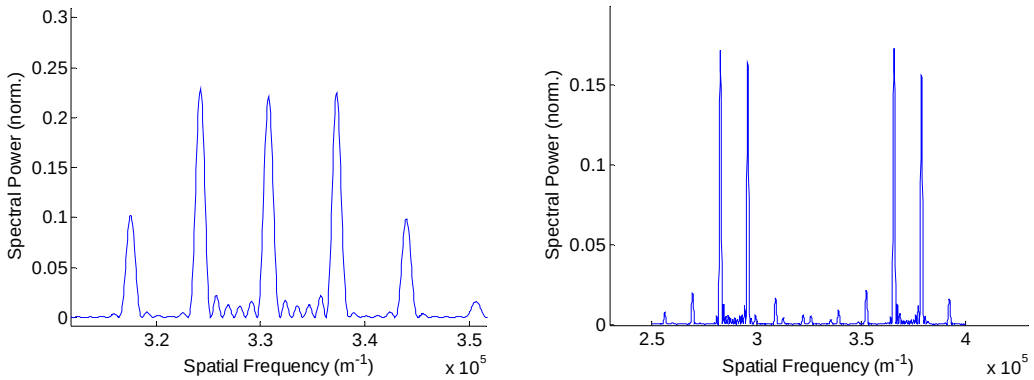

Figure 2.21 Spectra of multi-channel phase-reversed gratings. Left: 3 channels produced via duty cycle adjustment of the phase-reversal modulation. Right: 4 channels produced by stacking 2 phase-reversal modulations.

Periodically Chirping (frequency modulation)

A variation on the phase-reversed approach is to use a periodic chirping of the grating. Rather than modulating the phase of the grating the period is modulated periodically according to,

$$\Lambda = \Lambda_Q + \varepsilon \cos(2\pi z / \Lambda_{pc}) \qquad (2.43)$$

where ε is the degree to which the period is chirped (a small fraction of the primary period) and Λ_{pc} is the period of the chirping. The composition of a periodically chirped grating is illustrated in Figure 2.22.

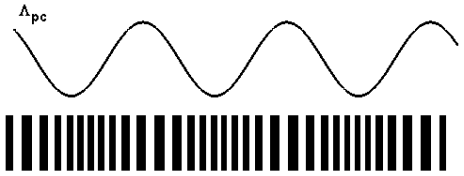

Figure 2.22 Periodically chirped grating.

Finding the appropriate values for the primary and chirping periods to achieve phase-matching for two interactions is the same as for the phase-reversed case (see Eq. (2.40)). As an example of an ad-hoc approach to periodic chirping we can consider the same 19 μm period grating as for the phase-reversed case. For a periodically chirped grating the chirping period, Λ_{pc}, determines the sideband spacing and the degree of chirp, ε, determines the number and amplitude of the sidebands. The primary frequency remains the dominant spectral feature in these gratings as opposed to phase-reversed gratings whereas it is suppressed. The spectrum of a periodically chirped grating with $L = 300\Lambda_Q$, $\Lambda_{pc} = 20\Lambda_Q$, and $\varepsilon = 0.15\%\Lambda_Q$ is shown in Figure 2.23.

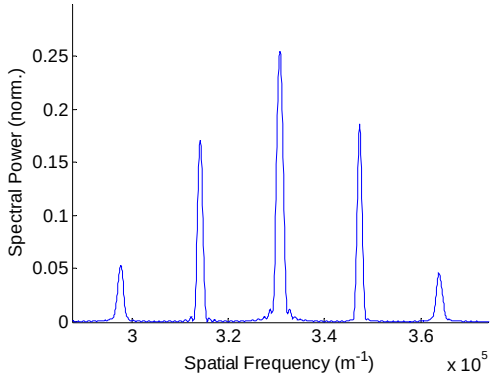

Figure 2.23 Spectrum of a periodically chirped grating with $\Lambda_{pc} = 20\Lambda_Q$ and $\varepsilon = 0.15\%\Lambda_Q$.

Phase and frequency modulation can be used in a similar way to diversify the grating spectrum. The poling function for frequency modulated grating with a single modulation tone determined by Λ_{fm} can be written as,

$$p(z) = sign\left\{\sin\left[(2\pi/\Lambda_Q)z + A\sin((2\pi/\Lambda_{fm})z\right]\right\} \tag{2.44}$$

The spectrum of such a grating is determined by the modulation period (spacing of sidebands) and modulation amplitude (number and amplitudes of the sidebands).

Summed component aperiodic gratings

A more direct method of diversifying the frequency components in a QPM grating is to construct it directly from the required lattice vectors[79]. This method is much more versatile as the grating design can target arbitrary wavelengths, temperatures, and weightings of the nonlinear gain. The problem is that the resulting design can be very difficult to fabricate as there will be a large range of domain sizes and spacings in such aperiodic structures. The basic form of the poling function for such gratings satisfying *n* different phase-matching conditions requiring the lattice vectors G_n is

$$d(z) = d_{eff}\, sign\sum_n w_n \cos(G_n z) \tag{2.45}$$

The *w* parameters allow for weighting of the nonlinearity between the processes, which as mentioned previously is important for processes such as cascaded THG. As an example consider THG of a 1550 nm laser source in lithium niobate at 289 K. The required lattice vectors to phase-match the SHG and SFG are $G_{SHG} = 3.552\times10^5\, m^{-1}$ and $G_{SFG} = 1.021\times10^6\, m^{-1}$. We construct a grating according to Eq. (2.45), and use the optimal weightings for THG[80],

$w_{SHG} = 1,\ w_{SFG} = 0.88$. A section of the grating and the evolution of the irradiance are shown in Figure 2.24.

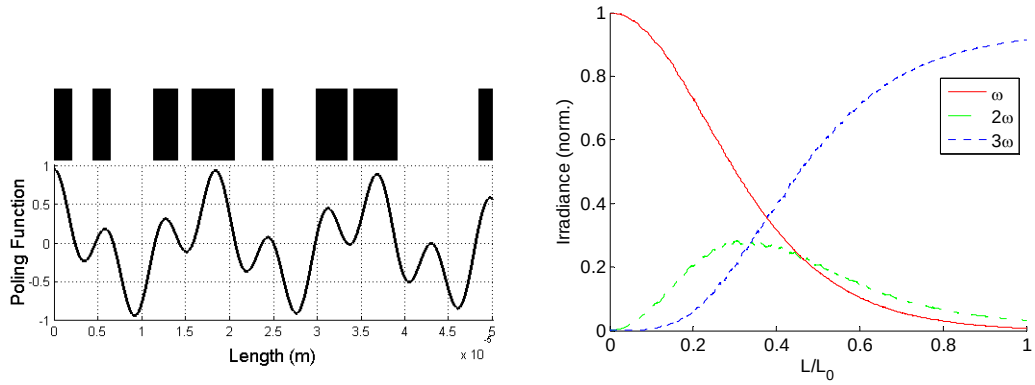

Figure 2.24. Left: Aperiodic grating for THG. Right: Evolution of the irradiances in an aperiodic grating optimised for THG.

In summary, there are several approaches to designing QPM gratings suitable for phase-matching broadband, multiple and cascaded processes. Simulated annealing[81] and genetic algorithms[82] are also useful techniques for designing QPM gratings with arbitrary profiles. While these advanced grating structures may generally be difficult to fabricate, several arbitrary phase-matching conditions can be considered simultaneously. Several authors to date have made use of these techniques, perhaps most markedly in multi-channel c-band frequency conversion and also with crystals capable of simultaneous red-green-blue generation for display applications[83,84,85] . Fabrication and performance of some of these QPM structures will be discussed and demonstrated in Chapter 5.

2.3.5 QPM with 2D domain structures

Advanced approaches to QPM are not only limited to 1D longitudinally varying domain patterns, but can also be realised in transverse and 2D geometries. Broderick *et al*[86], and other groups since, have reported the fabrication of hexagonally poled lithium niobate, as shown in Figure 2.25, which can provide multiple phase-matching conditions at different angles through the hexagonal lattice of domain inversions. 2D structures fabricated with more generalised lattice vectors also show promise as a means for achieving efficient cascaded processes, such as 3rd and 4th harmonics[87 88]. For example the 2D poling pattern and focusing geometry for third harmonic generation in the recent experiments from Fujioka *et al*[87]. are shown in Figure 2.26. In certain geometries the targeted higher order process can be generated collinearly with the pump beam

while the intermediate processes are non-collinearly phase-matched in the 2D lattice[89]. Other geometries can influence the spatial and temporal qualities of the QPM output, either in bulk crystals or waveguides. Examples of 'slit' and beam shaping QPM structures from Kurz[90] and Imeshev[91] are shown in Figure 2.27. QPM conversion of particular modal distributions in waveguides can also be managed by similar approaches[92].

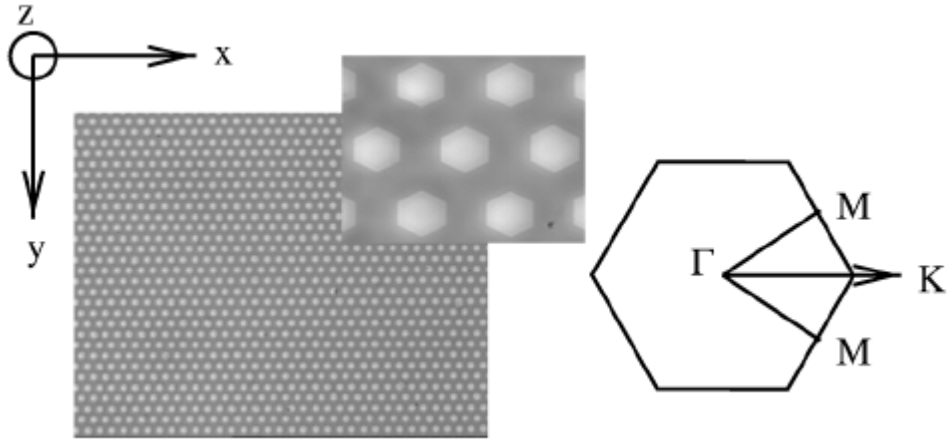

Figure 2.25 Hexagonally poled lithium niobate, reproduced from Broderick *et al*[86].

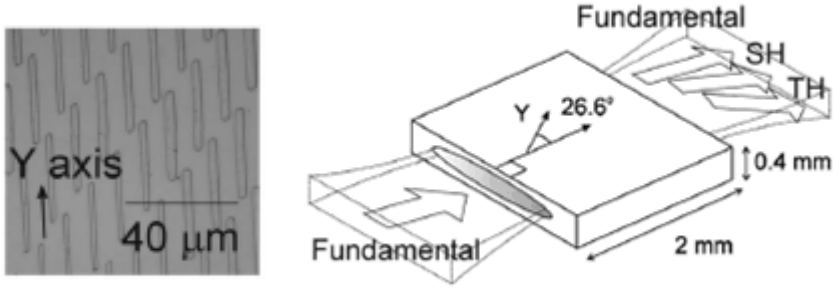

Figure 2.26 2D poling pattern and focusing geometry for third harmonic generation, reproduced from Fujioka *et al*[87].

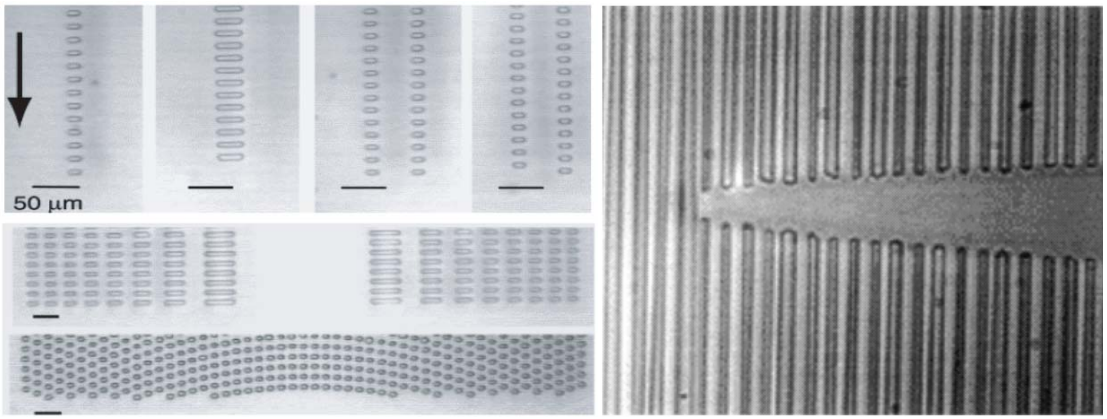

Figure 2.27 QPM optics. Left: From Kurz. Right: From Imeshev *et al*

Randomly arranged 2D domain patterns can provide a continuum of phase-matching conditions for broadband light and produce some interesting beam shaping phenomena[93]. Materials such as strontium barium niobate (SBN) and zinc selenide (ZnSe) can be grown with a randomly orientated nano-domain structure. Second-harmonic generation into Bessel beams[94], ultra-short pulse measurements with counter propagating pulses[95], and broadband 'white-light' second-harmonic generation with preservation of spectral content, have recently been demonstrated in SBN. Fabricated, μm scale, 2D pseudo-random domain structures have also been demonstrated for broadband (continuum) phase-matching . The domain structure and two propagation geometries in SBN, and an example of a 2D pseudo-random domain structure from the work of Sheng *et al*[96] are shown in Figure 2.28.

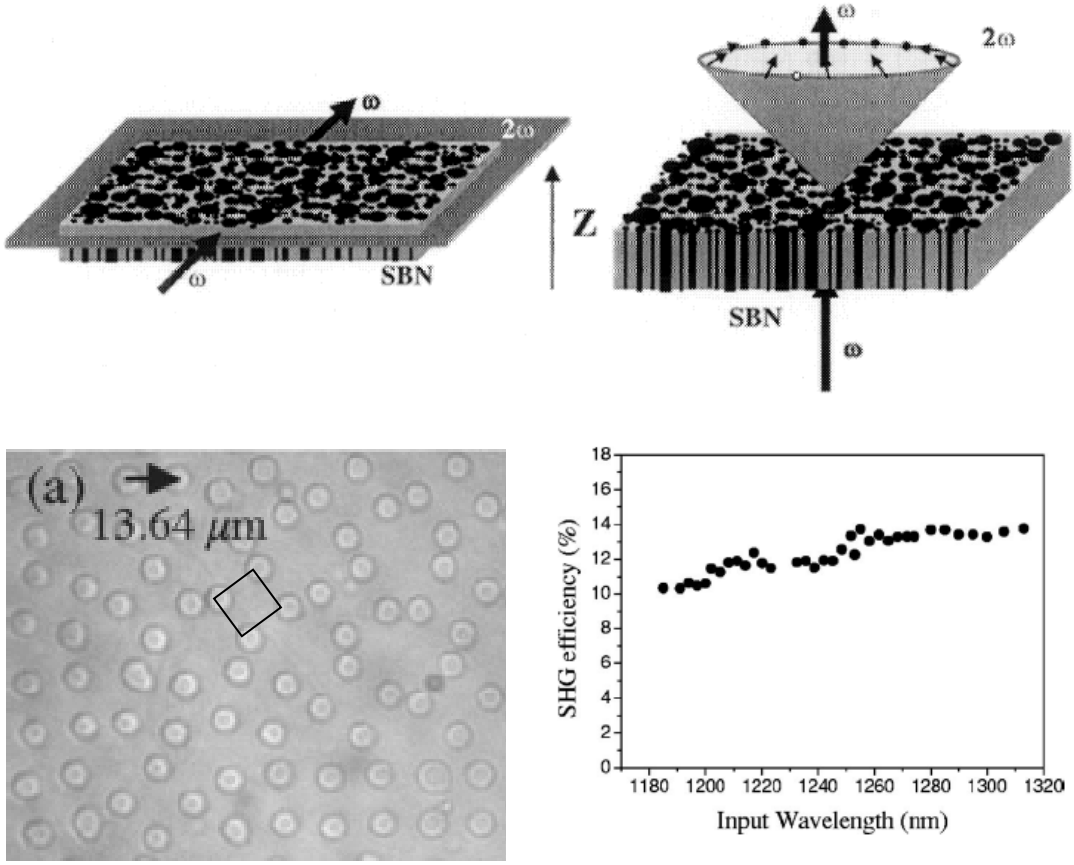

Figure 2.28 Top: illustration of the random domain structure in an SBN crystal and the propagation geometries give rise to either a planar continum of phase-matching vectors or a conical output. Bottom: pseudo random 2D domain pattern based on random orientations of a square unit cell as shown. The SHG from such a crytsal phase-matches a continuum of wavelengths.

The direct-write fabrication technique under study in this dissertation is well suited to the prototyping of some 2D QPM patterns, and examples of this will be shown in Chapter 5.

2.4 Fabrication errors

2.4.1 The effects of errors in QPM gratings.

Domain inversion in ferroelectrics is rarely a perfect process, and a perfect domain pattern with ideal periodicity and duty cycle can be difficult to achieve. Fabrication errors in QPM gratings result in nonlinear efficiency penalties and can also change the spectral content of the gratings. The nonlinear performance and tuning behaviour of a QPM crystal can be a good diagnostic as to the type of fabrication errors which are present. In this section the QPM behaviour of crystals with stochastic grating errors will be looked at numerically using Fourier analysis. There are three major geometric errors which arise when considering one-dimensional periodic structures; fluctuations in the local periodicity of the grating, fluctuations in the duty cycle of the inverted domains and missing periods or inversions.

Periodicity fluctuations

Periodicity fluctuations can occur when a domain forms asymmetrically around the electrode structure. There may also be resolution and roundup errors during fabrication of the electrode pattern which contribute a more systematic error. Periodicity fluctuations are of particular concern when using direct write methods such as described in this dissertation. These errors are brought about by drift in the position of translation stages when writing each electrode period, or round-up errors when working near the resolution of the positioning system. Fluctuations in the grating period generally act to broaden and deform the phase-matching tuning curves, and in doing so reduce the available nonlinear gain to a narrowband process. These fluctuations can cause strong perturbations in the tuning and performance of higher order QPM as it is the higher spectral frequencies of the grating which are perturbed most by small fluctuations in periodicity.

Duty Cycle Fluctuations

Duty cycle fluctuations can originate from defects in the crystal, adhesion of electrode materials and variations in electrode width, the field distribution inside the poling cell and cleanliness of the substrate. Duty cycle fluctuations chiefly affect the efficiency of the process, but for higher order processes where there are several optimum duty cycles, even moderate duty cycle fluctuations can cause deformation of the phase matching curves and act to broaden it as well as reducing the efficiency.

Missing inversions

Missing inversions are often caused by adhesion issues of electrode materials during or after lithography, crystal defects, or debris on the crystal surface which produces shielding during poling. Missing inversions in otherwise ideal odd order periodic gratings simply correspond to a reduction in the effective length of the crystal, but for aperiodic or even order gratings the results can be more detrimental.

2.4.1 Numerical modelling of errors in 1D QPM gratings.

Background

The influence of errors in QPM gratings has been looked at by Fejer *et al* in the highly cited article *"Quasi-phase-matching: tuning and tolerances"*[97] (1992). In this section the goal is to offer some additional empirical insight into errors in domain structures and the effect they have on nonlinear performance and tuning behaviour. The approach will be numerical in nature and will address the three primary fabrication errors discussed above. Such errors were analysed by Fejer *et al* by considering the accumulated errors in domain boundary positions and phase-mismatches. This approach defines the error in the k^{th} boundary position (with the z coordinate as the position) as $\delta z_k = z_k - z_{k,ideal}$ and the deviation from the expected phase-mismatch at this point as $\delta\Delta k = \Delta k_{actual} - \Delta k_{ideal}$. The exact integral in equation (2.11) is now modified to include these accumulated errors within a phase term ϕ_k,

$$E_{2\omega} = \frac{i2\Gamma g_1 d_{eff}}{\Delta k}\left[\sum_{k=1}^{N} e^{-i\phi_k} + 1\right] \tag{2.46}$$

where Γ represents the constant terms and g_1 is the initial domain orientation. The summation term contains the contributions from the imperfections in the domain structure, where the phase error from the k^{th} domain is contained in the term,

$$\phi_k = \Delta k_{actual} z_k - \Delta k_{ideal} z_{k,ideal} \approx \Delta k_{actual}\delta z_k + \delta\Delta k z_{k,ideal} \tag{2.47}$$

Here Δk_{actual} and z_k is the actual phase-mismatch and position at the k^{th} domain boundary and Δk_{ideal} and $z_{k,ideal}$ are the design (ideal) phase-mismatch and domain position at the k^{th} boundary. Ideally all the terms in equation (2.47) will be zero, in which case the sum in (2.46) is simply $N+1 \approx N$ with N being the number of domains, which in an ideal structure with length L

corresponds to an integer number of coherence lengths in the crystal such that $N = L/ml_c = L\Delta k/m\pi$ and (2.46) becomes

$$E_{2\omega,ideal} = i\Gamma g_1 \frac{2d_{eff}}{m\pi} L \tag{2.48}$$

which is consistent with the ideal case in Eq. (2.27). An integral approach to the problem can be arrived at by treating the term in Eq. (2.47) as a continuous function so that the departure from the ideal case can be expressed as

$$\frac{E_{2\omega}}{E_{2\omega,ideal}} = \frac{1}{L}\int_0^L e^{-i\phi(z)}dz \tag{2.49}$$

In reality $\phi(z)$ is rarely a completely know equation, except when considering cases such as unintentional but well defined chirp, stitching error or positional round-up error. In order to gain insight into the stochastic nature of domain errors and to compare such results to those found in practice, a numerical approach has been developed, which is somewhat analogous to dealing with Eq. (2.49) in a discrete fashion.

Numerical modelling of stochastic domain errors

The field equation for the quasi-phase-matched second harmonic in the low conversion regime can be written as ((2.22), (2.24))

$$E_{2\omega} = -\int_0^L i\Gamma d_{eff} g_n(z) \sum_{\substack{m=-\infty \\ m\neq 0}}^{+\infty} \frac{2\sin\left(D(z)\pi m\right)}{\pi m} e^{i(\Delta k(T,\lambda)+2\pi m/\Lambda(z))}dz \tag{2.50}$$

Here we have written the Fourier series for the domain pattern to include the common fluctuations that can occur during fabrication, $g_n(z)$ missing inversions, $D(z)$ duty-cycle, and $\Lambda(z)$ periodicity. For Fourier analysis it is mainly the poling function *p(z,T)* which encapsulates the geometric structure of the poled medium which is of interest.

$$p(z) = g_n(z) \sum_{\substack{m=-\infty \\ m\neq 0}}^{+\infty} \frac{2\sin\left(D(z)\pi m\right)}{\pi m} e^{i(2\pi m/\Lambda(z))} \tag{2.51}$$

This complete equation, (2.50), can be integrated numerically using Runge-Kutta or similar techniques, made easy in software such as Matlab or Maple. Insight into the phase-matching behaviour and efficiency penalties that such errors cause can also be obtained by looking at the numerical fast Fourier transform (FFT) of the poling function, (2.51). The power spectrum of the poling function gives a good approximation of the QPM tuning behaviour and relative efficiency.

The FFT for a square-wave grating of 100 periods is shown in Figure 2.29 along with the power spectrum in Figure 2.30. The FFT and power spectrum have been normalised to the magnitude of the first order peak, and the spatial frequency has been plotted in units of G/G_0 where $G_0 = 2\pi/\Lambda$. For a square wave grating this results in spectral peaks at the odd harmonics, $G/G_0 = 1,3,5...$ as expected from the square Fourier series. The neighbourhood of the dominant spatial frequencies in the power spectrum resemble the *sinc*^{2} function commonly associated with phase-matching tuning behaviour. The relationship between the FFT of the spatial modulation in the nonlinear medium and the actual QPM tuning curves is. This holds as long as Δk changes in an approximately linear fashion with temperature and wavelength, which is usually the case within the acceptance bandwidths of most phase-matched processes. The bandwidth of the frequency peaks in the FFT reflects the length of the crystal considered, i.e. the number of periods computed. Stochastic or systematic errors in the QPM grating can be assembled into the poling function *p(z)*, prior to integration or FFT calculation. In order to look at stochastic errors in the numerical modelling, a degree of randomness is introduced into the parameter under investigation using a random number generator from the software. The approaches for describing each type of error in the poling function and the results from Fourier analysis are presented below.

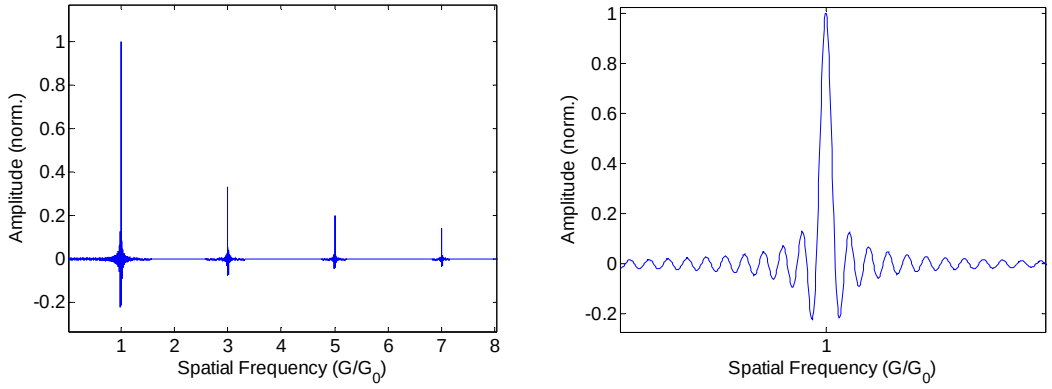

Figure 2.29 Fast Fourier transform of a square-wave function. Note only odd order harmonics are non-zero for a 50% duty cycle (square) waveform.

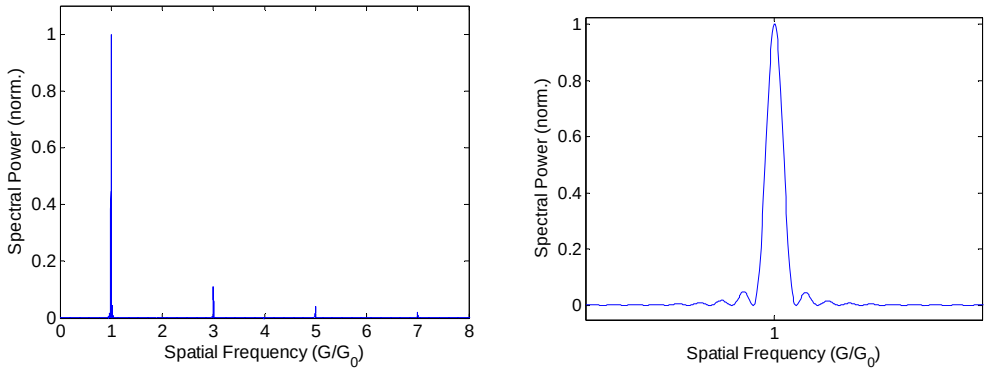

Figure 2.30 Power spectrum of a square-wave function. The region around the 1st order peak has been magnified on the right to show the characteristic *sinc*^{2} form that is indicative of the QPM tuning behaviour.

The effect of periodicity

A practical example of local periodicity error is shown in Figure 2.31 where a domain has formed asymmetrically about a topographical electrode. Errors in lithography or crystal defects can also produce local periodicity error in QPM crystals.

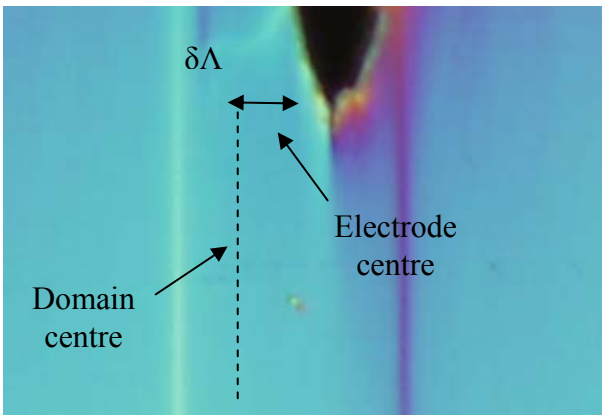

Figure 2.31 Domain formation occurring asymmetrically around electrode structures can result in local periodicity errors. An example of a domain forming asymmetrically around a topographical groove is shown.

Stochastic fluctuations around the design period Λ_0 can be introduced into the poling function, (2.51), as

$$\Lambda(z) = \Lambda_0 + 2\Lambda_0 q\left(\frac{1}{2} - rand(z)\right) \tag{2.52}$$

where the parameter q gives the maximum spread around the design period (typically much less than 1-2% for reasonable crystals) and *rand* is a changing random number from a distribution between 0-1. To see the effects of these perturbations the numerical resolution of the poling

function should be $< q\Lambda_0$, with the local periodicity $\Lambda(z)$ being updated either continuously so that the periodicity error becomes a like a round up error or periodically, i.e. modulo Λ_0, so as to move the local position of each inversion but to produce the same total length as for the ideal crystal. $\Lambda(z)$ can also include other regular profiles, such as chirp, which may be influencing the periodicity of the grating. The neighbourhood of the 1st order spatial frequency for some sample gratings with various degrees of stochastic periodicity error, are shown in Figure 2.32. The shape of the spectrum becomes perturbed from the ideal $sinc^2$ and the peak magnitude or 'efficiency' of the spectrum is reduced as the degree of error is increased. The efficiency penalty in relation to the extent of the periodicity errors is in illustrated in Figure 2.33. Here 10 sample gratings with stochastic periodicity errors have been analysed for each of value of the maximum deviation (q).

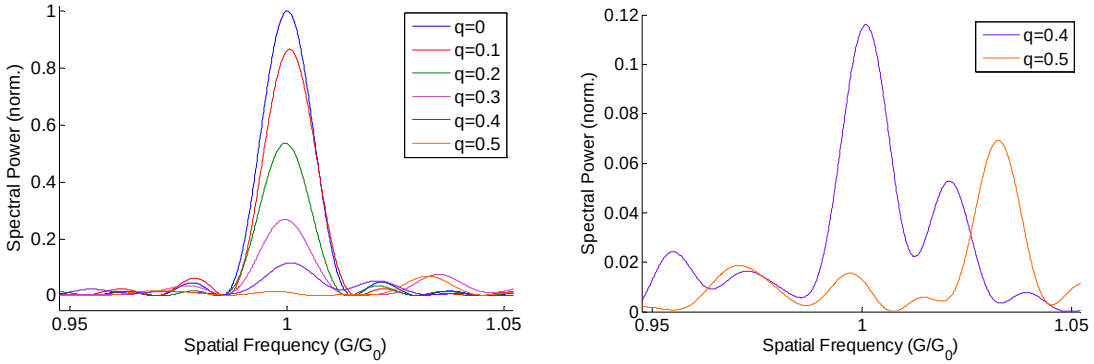

Figure 2.32. Spatial frequency curves in the neighbourhood of the 1st order spatial component of a square wave grating, with stochastic local periodicity errors. These curves approximate the phase-matching curves of 1st order QPM with such gratings. The left graph shows the curves from extremely poor gratings which have departed from the expected $sinc^2$ form.

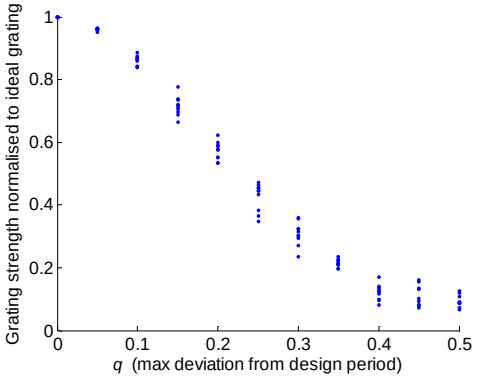

Figure 2.33 Peak of the 1st order spatial frequency component in relation to the grating quality in terms of periodicity errors. A sample of 10 gratings per q value is shown.

Duty Cycle

Duty cycle fluctuations can be significant, even in QPM crystals provided by commercial sellers as seen in the left of Figure 2.34. If the crystal is otherwise periodic the tuning behaviour (shape) of the 1st order phase-matching remains unperturbed but a significant loss of efficiency may be present. Large discrepancies in the apparent nonlinear efficiency of a crystal compared with that expected can reveal that the duty cycle fluctuations are significantly affecting the nonlinear performance.

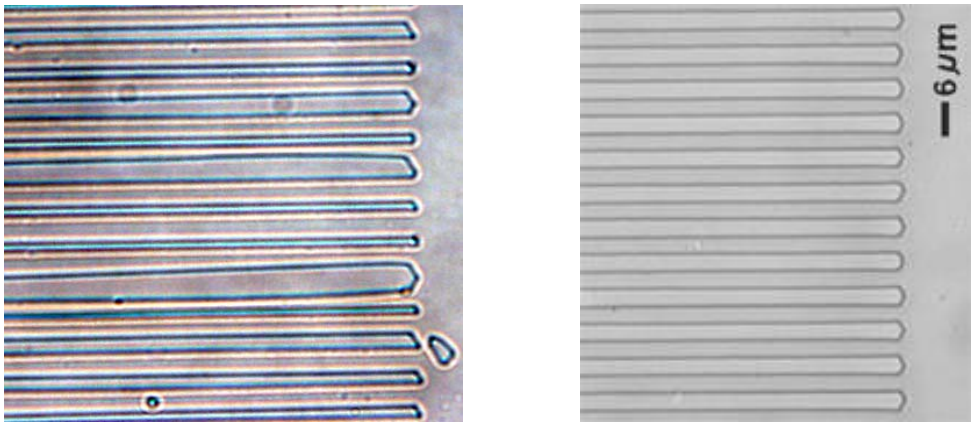

Figure 2.34. Left:~7μm period PPSLT (stoichiometric lithium tantalate) from a commercial seller, showing quite large variations in the domain duty cycle. Right: ~7μm period PPLN research sample from a leading university research group in the field, showing excellent domain uniformity.

Stochastic duty cycle fluctuations can be introduced in a similar fashion to the periodicity as,

$$D(z) = D_0 + 2D_0 q\left(\frac{1}{2} - rand(z)\right) \tag{2.53}$$

Here q determines the maximum deviation from the design duty cycle. As each domain inversion only needs one particular value of duty cycle to describe its width, duty cycle fluctuations are also updated modulo Λ_0. D(z) can also include regular profiles in domain sizes such as chirped or apodised duty cycle. Pure duty cycle errors primarily produce efficiency penalties for 1st order QPM gratings. The shape of the 1st order QPM tuning curves remains relatively unperturbed as the primary periodic content of the grating is not changed by changing the duty cycle. Figure 2.35 shows the spectral curves and grating strengths of some sample 1st order gratings with stochastic duty cycle errors. The trend of the efficiency penalty, in relation to the allowed deviation, corresponds well with the idea of an 'average' duty cycle affecting the efficiency of the grating, $\eta \propto \sin^2(\pi D_{ave})$, as suggested by (2.24). When the duty cycle is allowed to fluctuate

by 25% (a worst case average duty cycle of 25% or 75%, which are equivalent for the 1st order case) we see the grating strength has fallen by approximately 50%.

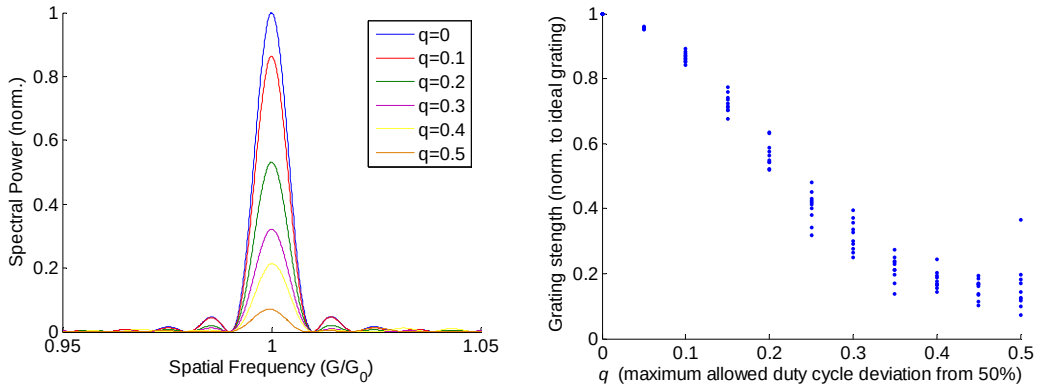

Figure 2.35. Spectral curves and grating strengths for random duty cycle errors in gratings for 1st order QPM. In this case the quality factor sets the allowed deviation from the ideal duty cycle of 50%

Missing Inversions

Missing periods are introduced by flipping the parameter g_n in (2.51) from 1 to -1 for particular inversion locations, resulting in no actual inversion at all. The frequency at which this occurs gives an indication of the fabrication quality and can be controlled using random number generation and Boolean logic to control the probability of having missing domains. The missing domain function is also updated modulo Λ_0 to flip only what would otherwise be the inverted section. Missing periods in an otherwise ideal 1st order grating simply results in a reduction in the effective length of the crystal. Since we are working with a second order process the efficiency of the process has a quadratic dependence on the interaction length. As such the effect of missing domains is quadratic on the grating strength, as shown on the right of Figure 2.36. An example of a poled sample which has some regions of missing domains is shown in Figure 2.37.

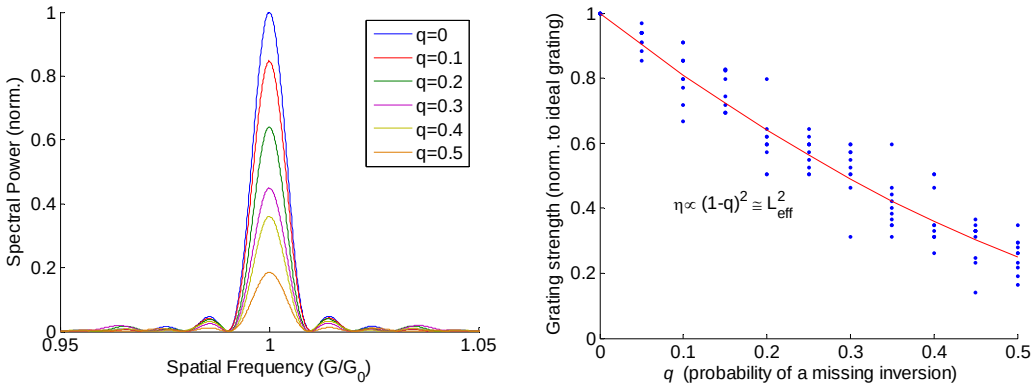

Figure 2.36 Spectral curves and grating strengths for random missing inversions errors in gratings for 1st order QPM. Here the quality factor indicates the probability of the domain inversion missing. This results in the loss of effective length of the crystal, upon which the efficiency has a quadratic dependence.

Figure 2.37 Example of PPLN with good periodicity but with some duty cycle errors and missing inversions in some regions.

Stochastic domain errors in higher order spatial frequencies

For some applications it can be appealing to move to higher order QPM, where longer and more easily fabricated periods can be used (especially for visible applications). QPM gratings utilising higher order components for phase-matching still rely on the grating reversals to occur regularly with respect to the nonlinear coherence length of the process being phase-matched. Practically this means the relative tolerances on domain errors become more stringent as the QPM order increases. That is, while the primary frequency component of a grating may not be severely affected by small errors, the perturbations in the grating will predominantly influence the higher order spatial frequencies. Thus the phase-matching curves for the higher order QPM can become deformed from the ideal $sinc^2$ form easily, as well as suffering from efficiency penalties as has been explored for 1st order QPM. Periodicity errors are the major culprit when it comes to producing asymmetric tuning curves in the higher QPM orders, whereas a pure duty cycle error may retain some symmetry in its tuning behaviour but may be catastrophic to the efficiency of the process. Figure 2.38 and Figure 2.39 show sample gratings and spectra for gratings for mild

periodicity errors and duty cycle errors respectively. The spectral power for each order has been normalized to the peak value for that order in a perfect grating.

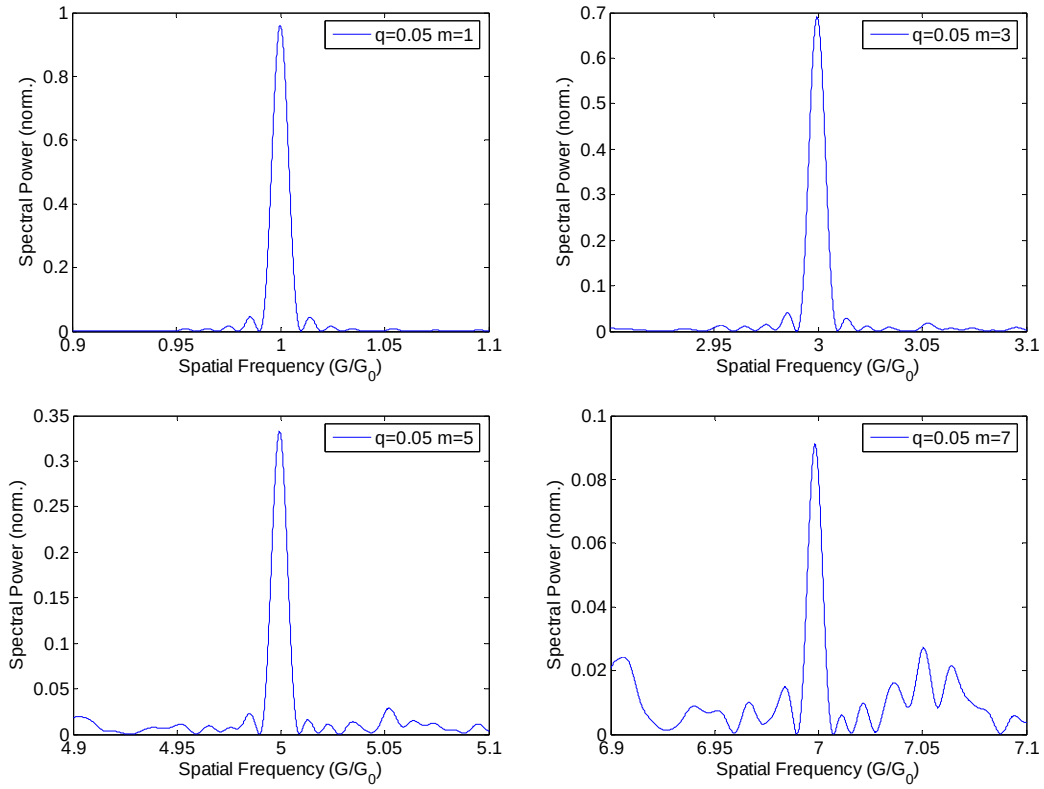

Figure 2.38 Spectra of the 1st, 3rd, 5th and 7th order peaks of a grating with a stochastic periodicity of up to 5% deviation from the design period. Normalized to a perfect grating, note the changing vertical scales.

For the 5% periodicity error introduced in the sample grating spectra in Figure 2.38 we see only a few percent penalty in the magnitude of the 1st order spatial frequency, but >90% penalty in the 7th order component. The distortion in the shape of the higher order curves is also more apparent. We see a similar case for a sample grating with 5% duty-cycle fluctuations, with the 5th and 7th orders experiencing a penalty of ~70% and ~96% respectively. This approach to predicting the effect of fabrication errors can also be used diagnostically. Fourier analysis of microscope images or profilometry data of the domain patterns in periodically poled crystals will give a good indication of the performance and tuning behaviour which can be expected.

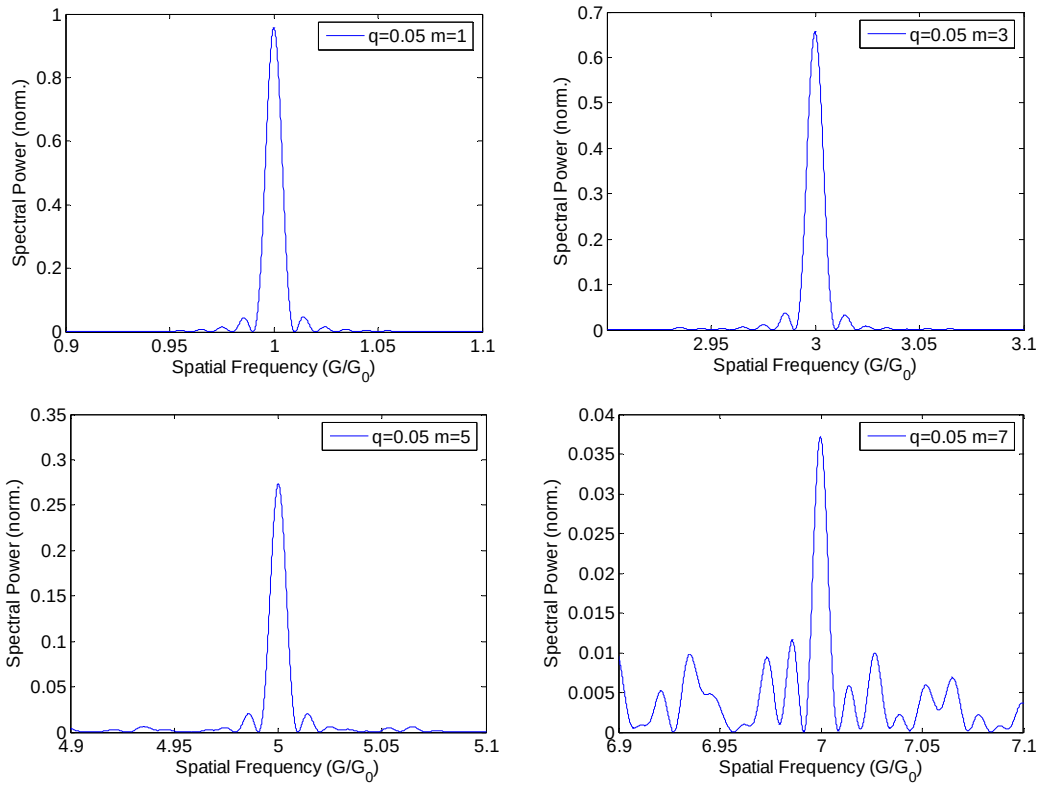

Figure 2.39 Spectra of the 1st, 3rd, 5th and 7th order peaks of a grating with a stochastic duty cycle error of up to 5% deviation from the ideal duty cycle of 50%.

External factors

Irregular tuning behaviour and performance factors which cannot be attributed solely to the domain pattern can arise in certain situations. Often the common observation of distorted tuning curves can be attributed to a phase-mismatch which is not constant through the length of crystal. This can be due to a variety of reasons ranging from inhomogeneous temperatures, to material inconsistencies and photorefractive profiles in the medium. A linear, polynomial or exponential phase-mismatch (Δk) over the length of the crystal gives rise to distinct modifications in the measured tuning curves. A functional form for a polynomial distribution of Δk across the length of the crystal with a maximum deviation δΔk from the intended mismatch of Δk_0 can be given as,

$$\Delta k(x) = \Delta k_0 \left(1 \pm \left(\frac{2}{L} \right)^n \frac{\delta \Delta k}{\Delta k_0} \left(x - L/2 \right)^n \right) \text{ (centred)} \qquad (2.54)$$

$$\Delta k(x) = \Delta k_0 \left(1 \pm \frac{\delta \Delta k}{\Delta k_0} \frac{x}{L^n}^n \right) \text{ (increasing/decreasing)} \qquad (2.55)$$

Such a distribution of Δk causes an asymmetry to appear in the measured tuning curves, namely the secondary peaks of SHG irradiance appear towards one side of the phase-matching peak and also have an increase relative efficiency. Examples of a phase-mismatch with a centered quadratic profiles across a 5 mm section of crystal are shown in Figure 2.40. A deviation of 500 m^{-1} (wave-numbers) from the expected phase-mismatch of 9.6266×10^5 m^{-1} (the mismatch corresponding to type-0 SHG at 1064 nm in PPLN) has been used for quadratic profiles with positive and negative deviations from the expected phase-mismatch. The temperature detuning curves can in practice be used to indicate the type of phase-mismatch profile in the crystal. For the centred quadratic profiles in Figure 2.40 the side-lobes in the detuning curves appear to the higher side of the temperature detuning curves for a negative deviation in the phase-mismatch profile and to the lower side for a positive deviation. The difference between a centred phase-mismatch profile and an increasing/decreasing profile is also apparent. For these profiles the detuning curves remain more symmetric but shift slightly to higher or lower temperature detuning. An example of this is shown in Figure 2.41. In summary there are a variety of fabrication errors, material and environmental factors which can reduce the efficiency and alter the tuning behaviour of quasi-phase-matched interactions. By knowing what to look for in the detuning behaviour of these processes some of the most likely causes of nonlinear performance loss can be diagnosed.

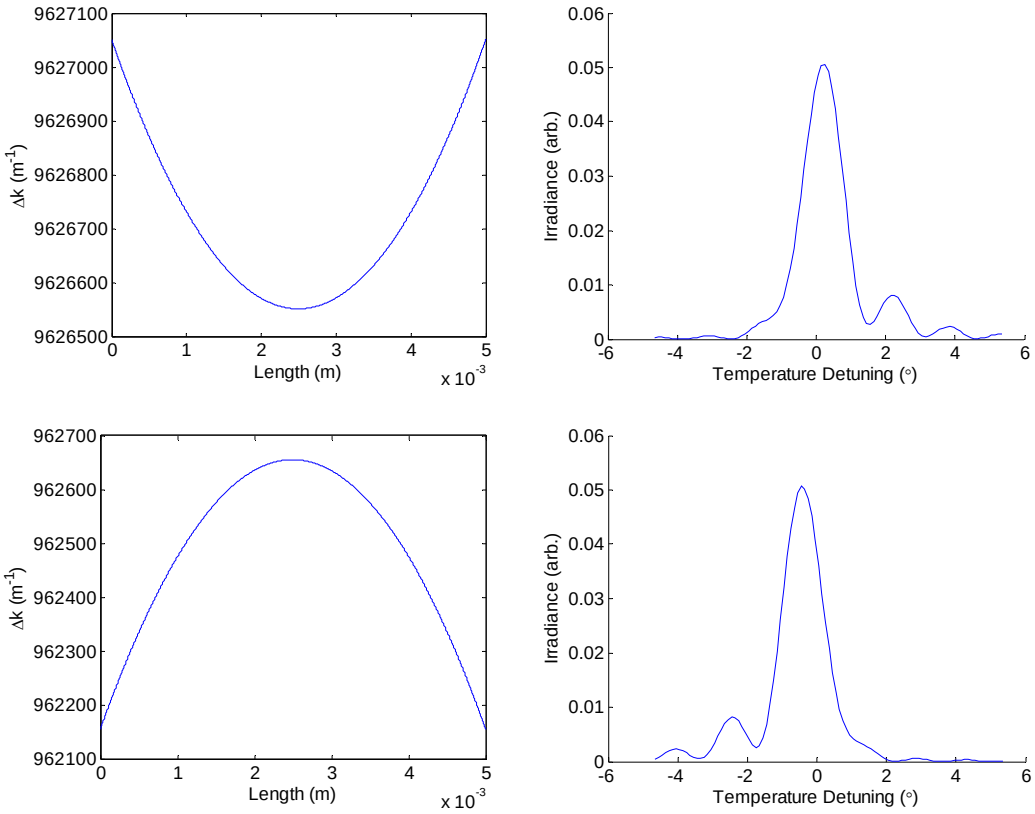

Figure 2.40 An example of a centred quadratic phase-mismatch profile and corresponding detuning curves for 500m^{-1} deviation through a 5mm length of crystal. Top plots: negative deviation from the expected phase-mismatch, bottom plots: positive deviation from the expected phase-mismatch.

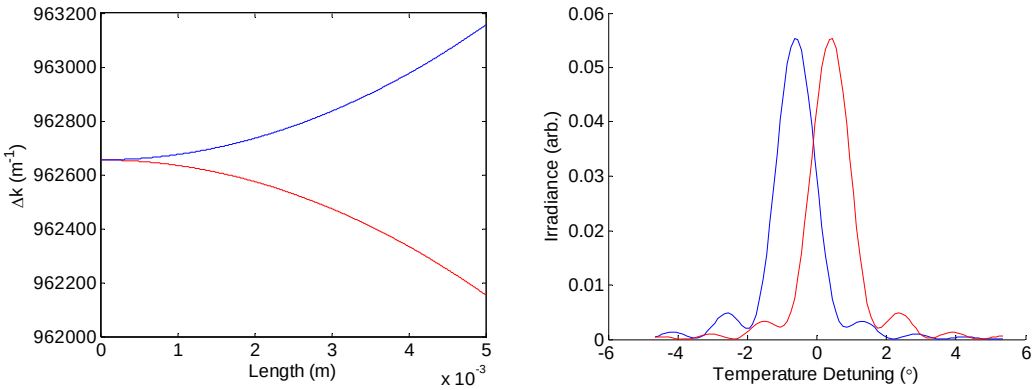

Figure 2.41 An example increase/decreasing quadratic phase-match profiles and detuning curves.

2.5 Summary of Chapter 2

In this chapter the background theory of nonlinear optics which applies to phase-matching and quasi-phase-matching in uniaxial ferroelectric materials such as lithium niobate has been introduced and reviewed. The spatial and Fourier characteristics of QPM in domain engineered materials has been explored by reviewing advanced grating designs which allow for multiple and broadband phase-matchings as well as 2D and non-collinear phase-matching geometries. In a similar fashion, some of the issues which arise due to imperfect fabrication of domain engineered materials have been reviewed and numerical simulations of the effects of stochastic and systematic errors in the domain structure on the phase-matching behaviour have been carried out by numerical Fourier analysis as well numerical integration of the coupled-wave equations for a 'real' system. Finally a brief overview of the inclusion of waveguides to the nonlinear medium is presented with a view to the practical implementation and characterization of such structures. Experimental results pertaining to elements of the topics presented here will be presented in chapter 5 of this dissertation. The domain quality and fabrication issues will be discussed further in chapter 4, where electric field poling to produce QPM gratings is presented. The following chapter now turns to the laser materials processing elements of this project.

Chapter 3. Laser machining

"For a successful technology, reality must take precedence over public relations, for nature cannot be fooled."

-Richard Feynman

"*I don't pretend we have all the answers. But the questions are certainly worth thinking about."*

-Arthur C. Clarke

3.1 Introduction

Materials processing is one of the major applications of modern laser technology. While lasers have revolutionised cutting and welding in the steel and automotive industries, they remain key research tools in the areas of micro and nano-technology due to their ability to modify and machine materials on scales where mechanical methods become unfeasible. Photonics is one such area of technology where there is a growing interest in micro and nano-scale material processing to make devices for the control of light. Photonic band-gap materials, waveguides and gratings have all been fabricated using laser processing methods, whether through ablative laser machining or non-destructive material modification. In this project laser machining is of interest for the fabrication of topographical structures in the surface of lithium niobate. These structures can then be used for electric field poling of ferroelectric domain patterns, the results of which will be presented in Chapter 4. This chapter looks at laser machining with pulsed UV (266 nm) nanosecond lasers and near IR (800 nm) femtosecond lasers. The ablation properties of lithium niobate and have been investigated with the goal to establishing optimal parameters for producing well defined topographical features of the desired geometry with minimal damage or modification to the nearby crystal structure. A parallel and comparative investigation of the ablation characteristics of silicon has also been carried out. Laser processing of silicon has been looked at extensively in the literature, so it is a good material with which to compare the present experimental results with. It is also a markedly different material compared to lithium niobate in terms of its thermal and electrical conductivity and optical absorption. This has facilitated a fundamental study comparing the dominant ablation mechanisms for different classes of materials, in particular semi-conductors and dielectrics.

Section 3.2 looks at the theoretical concerns of laser machining, and contrasts the nanosecond and femtosecond ablation regimes. The results of fundamental ablation studies will

be presented in section 3.3. Ablation thresholds for the laser sources used during these experiments will be estimated from the theory and compared to what is found experimentally. Section 3.4 will look at experimental material removal rates and geometry of the produced features when machining grooves into the surface of lithium niobate.

3.2 Laser ablation theory

3.2.1 Overview

There are many fields of applied physics which deal with interactions between light and matter, and laser induced material removal, generally referred to as ablation, is one of the most diverse. One of the difficulties in this area of research is that there have been many models and experimental studies describing different material removal regimes and each model and experimental investigation needs to be taken into context. Key aspects of any laser ablation model that are of interest from a practical viewpoint include the material removal rate in terms of pulse numbers and pulse energies, threshold fluence - i.e. the minimum amount of deposited optical energy required for material removal, the dominant ablation mechanism, be it thermal, chemical or ionising in nature, and ultimately size and quality of the features produced. The dominant ablation mechanism at work can also have a strong dependence on the laser wavelength, pulse energy, pulse duration, peak power and pulse repetition rate. In this section an overview of the theory relevant to the laser machining in this project will be presented. One of the key areas of interest is the difference between the nanosecond and femtosecond pulse regimes, both for fundamental and fabrication quality reasons. For instance, nanosecond UV lasers have wavelengths shorter than the UV absorption cut off of lithium niobate and are also readily absorbed by silicon. For both materials the laser energy is strongly absorbed with a thin layer of material at the surface. The duration of the pulses are long enough to produce a significant temperature rise and thermal loading of the laser affected volume, resulting in melting, vaporization and plasma formation. On the other hand, Ti:Sapphire femtosecond lasers produce wavelengths in the 750-850 nm range which are within the optical transmission window of lithium niobate, but still absorbed in silicon. Absorption of 800 nm light in lithium niobate, and other transparent materials, is predominantly a nonlinear process with defects and free carriers playing a role in some cases. Efficient nonlinear absorption is facilitated by the high peak irradiances typical of ultrafast laser pulses from commercial systems. Pulse durations on the

order of picoseconds and below can also lead to ablation mechanisms which are distinct from the photo-thermal and photo-chemical processes commonly attributed to nanosecond, and longer, pulsed laser ablation. This is due to the pulse durations being shorter than the timescales of typical thermal processes with the target materials. Consequently sub-picosecond laser ablation is often suggested to be athermal in nature, though this is not necessarily the full picture for all materials. The initial photon-electron interaction can thermally couple energy to the material lattice in the post pulse time frame, resulting in a temperature rise sufficient for melting and vaporisation. This especially the case in conductive materials where there is a significant free carrier density to absorb, diffuse and collisionally transfer energy. Ultrafast ablation of conductive materials is often described by the two temperature model, which treats the electron ensemble and the atomic lattice as two distinct but coupled systems. For dielectric materials with low thermal conductivity, multi-photon absorption and ionization followed by avalanche ionization has been suggested as the dominant mechanism for ablation. High quality laser processing attributed to ultrafast and athermal ablation mechanisms has been widely reported for many organics, dielectrics and semi-conductor materials. In practice these ablation mechanisms can also be accompanied by acoustic and mechanical processes. Stresses and fractures, detrimental to the quality of produced features, can be produced in and surrounding the ablated features, especially at high incident pulse energies well above threshold. Sensible selection of laser parameters aided by empirical and visual inspection of the ablated features is required for optimal results.

A comprehensive reference text on laser-materials interactions is *Laser Processing and Chemistry 3rd edition (*Bauerle, 2000)[98]. Definitions, symbols and units of parameters frequently referred to in this section are shown below in Table 3.1. The following sub-sections will deal with some aspects of the physics of ablation that are important to the experimental results presented in subsequent sections. In particular section 3.2.2 will look at UV nanosecond ablation and section 3.2.3 will look at near IR femtosecond ablation. Section 3.2.4 will deal with Gaussian beam profiles, which are common to most solid state laser systems, and the implications when analysing ablated features produced with Gaussian beams.

Parameter	**Symbol**	**Definition**	**Units** Common (SI)
Irradiance	I	Optical power per unit area	W/cm^2 (W/m^2)
Fluence	ϕ	Optical energy per unit area	J/cm^2 (J/m^2)
Ablation threshold	I_{thres}, ϕ_{thres}	The minimum irradiance/fluence required to induce material removal from a target	W/cm^2, J/cm^2, $(W,J/m^2)$
Pulse duration	τ	Laser pulse duration	s
Linear absorption coefficient	α	Attenuation rate of laser power/energy in relation to distance of propagation is a linearly absorbing medium, as in the Beer-Lambert law, $I(z)=I_0e^{-\alpha z}$	cm^{-1} (m^{-1})
Optical penetration length	l_α	The distance over which the irradiance is reduced to 1/e in a linearly absorbing media, i.e. $l_\alpha=\alpha^{-1}$	cm, nm (m)
Optical skin depth	l_s	The generalised distance over which the irradiance is reduced to 1/e in an absorbing media. This can be the classical skin depth for conductors or more generally found from the Drude model of the dielectric function, $l_s = \frac{c}{\omega\varepsilon"}$ where $\varepsilon"$ is the imaginary (lossy) component of the dielectric function.	cm, nm (m)
Specific heat	C_p	Energy required to raise a unit mass of material through by a unit degree of temperature.	J/gK (J/kgK)
Mass density	ρ	The mass of a unit volume of material	g/cm^3 (kg/m^3)
Thermal conductivity	κ	The rate of energy transfer (power) per unit length of material per unit of temperature	W/cmK (W/mK)
Heat diffusivity	D	The heat diffusivity given by $D = \frac{\kappa}{\rho c_p}$	cm^2/s (m^2/s)
Heat of enthalpy	$\Delta H_{m,v,s}$	Energy absorbed during a change in physical state (melting, vaporisation or sublimination)	J/g, J/mol, J/cm^3, $(J/kg$, $J/atom)$
Thermal penetration length	$l_{thermal}$	The characteristic length of a laser induced thermal process found as $l_{thermal} = 2\sqrt{D\tau}$	cm, nm (m)
Gaussian beam waist diameter	w_0	The $1/e^2$ diameter of a symmetric Gaussian distribution, in particular Gaussian beam profiles.	cm, μm (m)

Table 3.1. Definitions and units of common parameters associated with laser processing.

3.2.2 UV nanosecond laser machining

For nanosecond processing of absorbing materials, thermal excitation is most often considered to be the initiator of material removal. In the simplest case the incident laser energy heats, melts and vaporises material from the surface of the target. There are in practice several other processes that can take place during ablation and the pulse energy, pulse duration and pulse repetition frequency can affect the type of ablation which proceeds during and after the pulse.

Ren *et al*[99], with their recent investigations of UV nanosecond ablation of silicon, have suggested that there are three distinct ablation regimes which can be identified; evaporation, plasma interactions and explosive boiling or 'phase-explosion'. Initially material removal is via thermal evaporation of atoms from the surface which creates a vapour plume near the surface, some of which will be in the beam path of the laser. In the low energy regime the density and temperature of the vapour plume being removed is fairly low and does not significantly interact with the laser beam. This thermal evaporation produced by 'gentle' laser heating from nanosecond and longer duration pulses can often be understood by considering the 1D heat equation. For the 1D heat equation the area of the laser treated volume is considered to be relatively large with respect to the depth of the affected material, so that the problem is considered primarily in a direction perpendicular with respect to the substrate (*z*-direction). Under these circumstances we can approximately assume thermal homogeneity in the *xy* plane so the problem can be treated as a 1D heat flow),

$$\rho C_p(T)\frac{\partial T}{\partial t} - \nabla[\kappa(T)\nabla T] + \rho C_p(T) v_s \Delta E = Q(z,t) \tag{3.1}$$

Here ρ is the mass density, C_p is the specific heat, κ is the thermal conductivity and v_s is the velocity of the substrate with respect to the heat source. *Q(z,t)* is the laser source term which is commonly given as,

$$Q(z,t) = (1-R) I_0(t) f(z) \tag{3.2}$$

where R is the reflectivity, *I(t)* is the temporal function describing the laser pulse in air/vacuum and *f(z)* describes the absorption of the laser energy in the material. In the linear absorption regime the energy absorption simply follows Beer's law,

$$f(z) = \alpha e^{-\alpha z} \tag{3.3}$$

where α is the absorption coefficient. The corresponding *1/e* optical penetration depth or 'skin' depth of the absorbing target is related at the absorption coefficient as $l_\alpha = \alpha^{-1}$. The absorbed energy per unit volume is simply αI. The absorption coefficient is in general temperature and physical state dependent, so using the absorption coefficient for the ambient bulk material can be a crude approximation.

In some cases, especially in metals, it is instructive to express the absorption in terms of the EM skin depth,

$$l_s = c/(2\pi\sigma\omega)^{1/2} \tag{3.4}$$

where σ is the frequency dependent AC conductivity. We can more generally consider parameters such as absorption and skin depth from the Drude formula, which has been invoked to aid in the description of laser interactions in both conductors and dielectrics where absorption of laser energy by existing or generated free carriers is taking place. The Drude formula describes the dielectric function of a material as,

$$\varepsilon = \varepsilon' + i\varepsilon'' = 1 - \frac{\omega_{pe}^2}{\omega^2 + \omega_{coll}^2} + i\frac{\omega_{coll}\omega_{pe}^2}{\omega\left(\omega^2 + \omega_{coll}^2\right)} \tag{3.5}$$

Here ε' refers to the real part of the dielectric function which relates to the refractive index of the material at the optical frequency ω, and ε'' is the decaying or 'lossy' part of the dielectric function which describes the absorption of the light by the free carriers in the material. ω_{pe} is the electron plasma frequency related to the electron charge (q_e), mass (m_e) and density (N_e),

$$\omega_{pe} = (4\pi q_e^{\,2} N_e / m_e)^{1/2} \tag{3.6}$$

and ω_{coll} is the collision frequency of electrons with the atoms/lattice. The skin depth is related to the 'lossy' part of the dielectric function as,

$$l_s = \frac{c}{\omega\sqrt{\varepsilon''}} \tag{3.7}$$

For the UV regime where the photon energy is in excess of the absorption bandgap of dielectrics (α is large), the skin depth of metals is very short (large ω in (3.4) or (3.5) produces a short skin depth), the skin depth may be well estimated as a delta function at the surface. This approximation is often made when considering thermal diffusion from the surface layer into the surrounding material. When a phase change occurs due to joule heating the enthalpies will also need to be considered. With some assumptions (see for example Gamaly *et al*[100]) the evolution of the temperature at the surface and into the material can be found explicitly. For a system where the absorption of the laser energy occurs in a thin layer and the laser pulses are approximated as a step like function with a pulse duration of t_p, the 1D heat equation, ignoring convection or evaporation, has an exact solution during the pulse of the form,

$$T(z,t) = \frac{1}{\kappa}\sqrt{\frac{D}{\pi}}\int_0^{t_p} \frac{I_\alpha(\tau)}{(t-\tau)^{1/2}} e^{-z^2/(2D(t-\tau))} d\tau \tag{3.8}$$

where z is the Cartesian coordinate pointing into (perpendicular) the surface of the material, with z=0 at the surface, and I_α is the absorbed laser irradiance. At the surface, z=0, the integral in (3.8) can be evaluated as,

$$T(z=0,t)=\frac{1}{\kappa}\sqrt{\frac{D}{\pi}}I_\alpha\int_0^{t_p}\frac{1}{(\tau-t)^{1/2}}d\tau=\frac{1}{\kappa}\sqrt{\frac{D}{\pi}}I_\alpha\left[-2(t-\tau)^{1/2}\right]_0^{t_p}$$

$$T(z=0,t)=\frac{1}{\kappa}\sqrt{\frac{D}{\pi}}I_\alpha\left[-2(t_p-t)^{1/2}+2t_p{}^{1/2}\right] \tag{3.9}$$

$$T(z=0,t_p)=\frac{2}{\sqrt{\pi}}\frac{I_\alpha\left(Dt_p\right)^{1/2}}{\kappa}$$

The average temperature through the volume of material is related to the surface temperature as,

$$\begin{aligned}\langle T\rangle&=\frac{1}{\left(Dt_p\right)^{1/2}}\int_0^\infty T(z,t_p)dz=\frac{1}{2^{1/2}}T(0,t_p)\\ \langle T\rangle&=\sqrt{\frac{2}{\pi}}\frac{I_\alpha\left(Dt_p\right)^{1/2}}{\kappa}\end{aligned} \tag{3.10}$$

In the case of optimal evaporation - which is the lower limit on the thermal ablation threshold - all the energy used in raising the temperature of the laser affected region is assumed to be transferred into the latent energy for fusion or atomisation (melting, vaporization or sublimination). Considering the specific heat and density of the material, the condition for optimal evaporation resulting from the deposition of energy ΔE and a corresponding temperature rise $\langle T\rangle$ is,

$$\Delta E=\langle T\rangle C_p\rho=\Delta H\rho \tag{3.11}$$

From (3.11) and (3.10) we can infer the ideal (minimum) intensity or fluence required for ablation as,

$$\begin{aligned}\Delta E&=\sqrt{\frac{2}{\pi}}\frac{I_\alpha\left(Dt_p\right)^{1/2}}{\kappa}C_p\rho=\Delta H\rho\\ \therefore I_\alpha^{\min}&=\sqrt{\frac{\pi}{2}}\frac{\kappa}{\left(Dt_p\right)^{1/2}C_p\rho}\Delta H\rho=\sqrt{\frac{\pi}{2}}\Delta H\rho\left(\frac{D}{t_p}\right)^{1/2}\end{aligned} \tag{3.12}$$

or alternatively for the minimum fluence as,

$$\phi_\alpha^{\min}=I_\alpha^{\min}t_p=\sqrt{\frac{\pi}{2}}\Delta H\rho\left(Dt_p\right)^{1/2} \tag{3.13}$$

For a surface temperature rise sufficient for evaporation (3.12) and (3.13) will be reduced by a factor of $1/\sqrt{2}$ as shown in Eq. (3.10), which is consistent with the 1D treatment of the heat equation found in Bauerle[98]. One of the features of this equation is the $t_p^{1/2}$ relation between the

pulse duration and the threshold fluence. This trend has been observed experimentally by several authors for pulses in the 50 ps-10 ns regime in both metals and dielectric materials. The application of the 1D heat equation to predicting the ablation thresholds is however limited to a range of time scales and energies. In the longer pulse regime volumetric heat conduction (3D) becomes important, and the ablation threshold tends to depart from the 1D case and take on a trend of t_p^n for ½<n<1, approaching n=1 for long pulses (t_p>1 us). This was demonstrated by Piglmayer *et al*[101] in polymide (Figure 3.1).

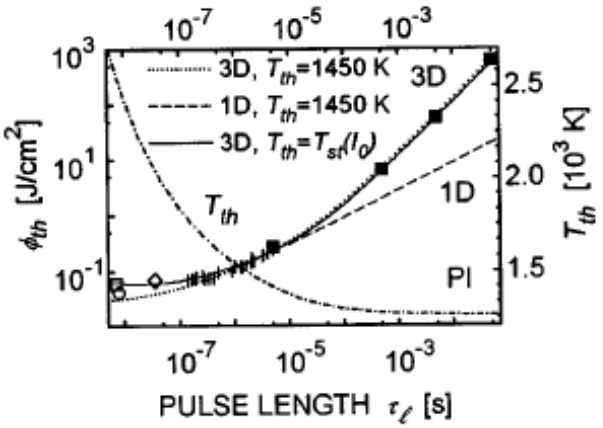

Figure 3.1. Ablation thresholds in polymide in relation to pulse duration (From Piglmayer[101]).

Once a temperature rise sufficient to produce evaporation from the surface is reached any additional laser energy from the pulse begins to go into the latent heat of evaporation, i.e. the excess laser energy goes into the term $\Delta E = \rho H_{s,v} v_s$ in Eq. (3.1) to accelerate the phase transition. When the energy going to convection and evaporation comes into equilibrium with the laser energy the temperature will saturate at the stationary temperature T_{st} and the conditions for stationary evaporation will be reached. For low powers near threshold, *equilibrium vaporization* (Anisimov[102]) has been demonstrated to yield good correlation with experiments. The result is that the surface receding velocity can be given as,

$$v_z(z=0) = \frac{(1-R)I}{\rho(H_{v,s} + 2.2k_B T_{st}(z=0)/M)} \tag{3.14}$$

where $H_{v,s}$ is the latent heat of vaporization or subliminination, k_B is the Boltzmann constant, M is the atomic mass, and $T_{st}(z=0)$ is the stationary surface temperature found from a more generic solution of (3.1). For these conditions the thickness of the layer evaporated from the surface can

be found as the integral of the surface receding velocity over the pulse duration, with a correction, δ, for and re-condensation of species or loss of energy via convection,

$$d = \int_{t_{start}}^{t_p} (1-\delta) v_z dt \qquad (3.15)$$

Ablation driven primarily by thermal evaporation is therefore expected to scale with both the incident irradiance and the pulse duration. However, increasing the pulse energy increases the density and temperature of the vapour plume and ions released from the surface or generated in the plume can begin to interact strongly with the incident laser beam. This causes a plasma to be produced in the vapour plume shortly after the pulse commences. The rest of the pulse energy then interacts with the plasma. This results in shielding of the substrate from the laser source, and saturation of the ablation rate may be observed, i.e. the ablation rate becomes independent of the pulse energy or duration over a range of parameters. This is referred to as 'plasma shielding' and has been identified in several experimental investigations. An example from the work of Ren[99] is reproduced in Figure 3.2.

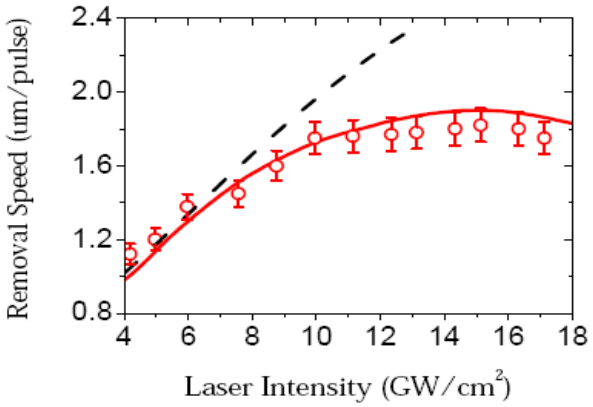

Figure 3.2 Observation of plasma shielding affecting the ablation rate in silicon (from Ren *et al*[99]). The dashed line shows the expected ablation rate if evaporative ablation were continuously scaling with irradiance.

The recoil shock from the expansion of the vapour plume and plasma can also result in displacement of molten material at the surface. Recent studies by Fishburn *et al*[103] involving pulsed ablation of aluminium have demonstrated that in some ablation regimes displaced melt can actually account for the majority of crater volume. An example of stylus profilometry data indicating the volume of displaced melt compared to the volume of the ablation crater is shown in Figure 3.3. A marked increase in the crater volume which is not accounted for by the melt displacement volume, can be seen at a fluence of 8 J/cm^2. This indicates the onset of the most

violent and effective ablation regime observed for nanosecond pulses referred to as phase-explosion or explosive boiling. While this ablation regime has been observed in several materials, there are still several different, but compelling, suggestions as to how it comes about. One of the intriguing characteristics of phase-explosion is that the explosive ejection of material usually occurs at a significant time after the laser pulse has interacted with the material. Experimental techniques such as fast-imaging (strobe imaging and laser shadowgraphy for example) and time resolved plume studies have provided empirical insights into the ablation time-line. An example of images captured by strobe light imaging from the work of Fishburn in aluminium is shown in Figure 3.4. The laser pulse duration in these experiments was 32 ns and the explosive materials ejection can be seen to be delayed until around 500 ns, with a relatively stationary plume of material above the crater persisting up to 20 µs after the pulse.

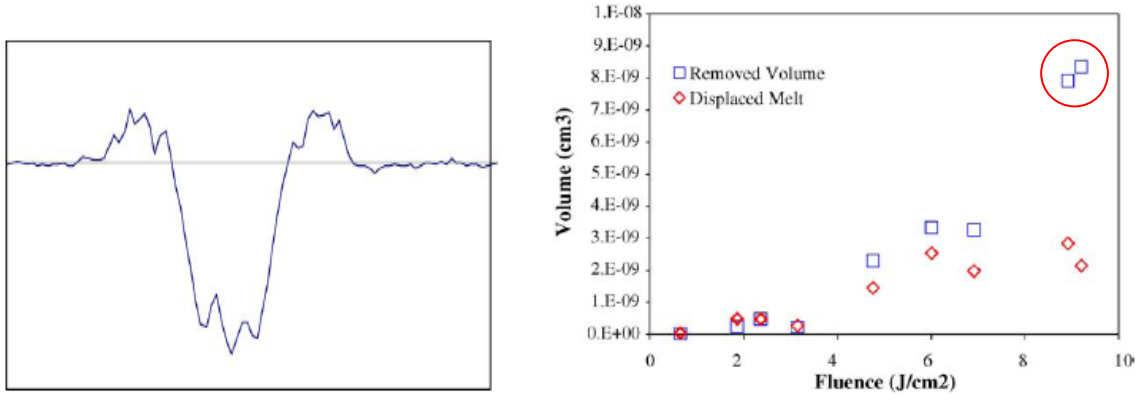

Figure 3.3 Top: Stylus profilometry of ablation craters in aluminum. Bottom: Comparison of crater volume and melt displacement showing that melt displacement is the dominant material removal mechanism at moderate fluences. The increase in removed volume at fluences in excess of 8 J/cm^2 (circled) is indicative of the onset of phase-explosion. (From Fishburn *et al*[103])

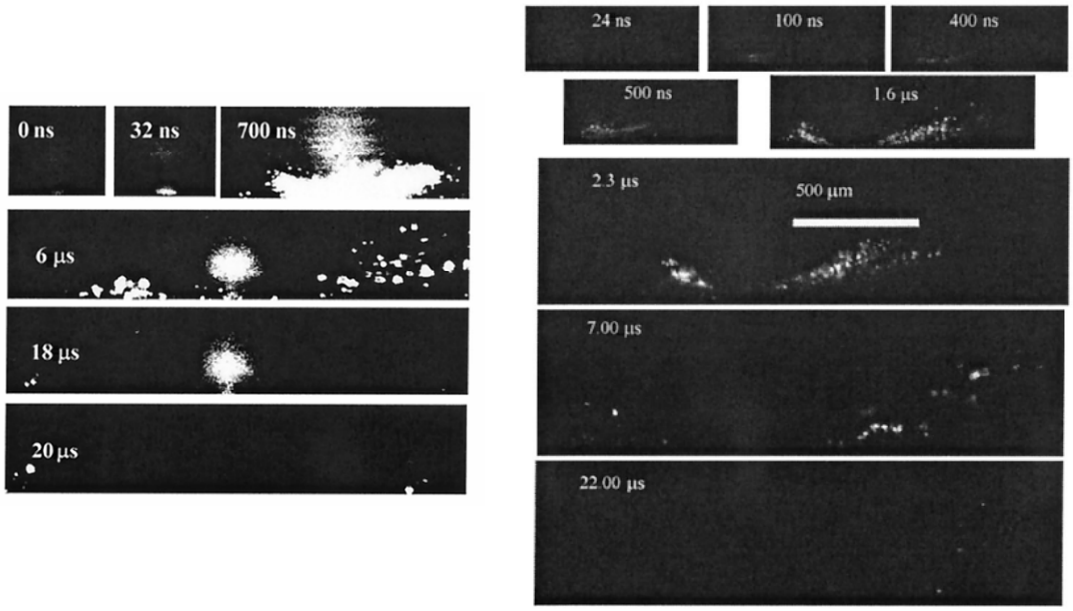

Figure 3.4 Laser strobe images capturing the plasma plume. Left: the plume can be seen to persist µs's after the pulse. Right: Explosive ejection of material occurs at ~500 ns after the pulse. (From Fishburn *et al*[104])

Ren *et al* have conducted analogous experiments based on plume transmission for silicon ablation with 355 nm, 5 ns pulses[105]. These experiments looked at the time dependent transmission of a HeNe beam directed across the surface of a silicon target. The estimated ablation rate in relation to the laser irradiance along with the plume transmission signals are reproduced in Figure 3.5. The silicon ablation rate shows three distinct trends; material removal attributed to evaporation up to irradiances of 10 GW/cm^2, saturation of the ablation rate attributed to plasma shielding between 10 and 20 GW/cm^2, the onset of further material removal, attributed to explosive ejection, beyond 20 GW/cm^2. The accompanying plume transmission signals show a delayed onset of the plume opacity, of the order of µs, in the higher irradiance ablation regime. This delayed dip in the transmission of the plume is attributed to explosive ejection occurring a significant time after the pulse. Earlier studies by Yoo *et al*[106] with 266 nm, 3 ns pulses also showed an abrupt change in the ablation rate at irradiances of ~20 GW/cm^2.

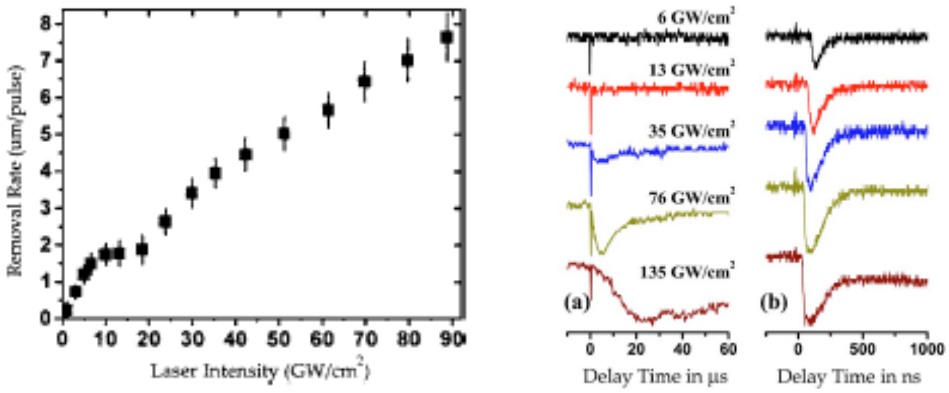

Figure 3.5 Ablation rates (left) and plume transmission dynamics (right) for ablation of silicon with 5ns pulses. (Ren *et al* 2006[105]).

A common suggestion for the physical process which gives rise to explosive ejection is the formation of a super-critical (metastable) liquid by intense laser heating. Such a metastable liquid state can persist within the laser affected volume for some time after the pulse before a rapid and explosive phase-change occurs. Ren *et al*[99] have also suggested that once sufficient laser pulse irradiances have been reached the plasma plays a role in storing and coupling energy to the substrate in the post pulse time frame, contributing to the delayed onset of phase-explosion. The onset of the rapid-phase change in a metastable liquid begins with nucleation vapour-phase pockets in the superheated liquid. The formation and coalescence of the vapour-phase pockets into rapidly expanding bubbles may occur over time scales longer than the laser pulse, which also explains the observation of delayed ejection of material in this ablation regime. A compelling overview of the theoretical basis for the formation of a metatable liquid and phase-explosion in laser heated silicon is can be found in the work of Yoo *et al*[106]. In summary, nanosecond ablation can have various dominant mechanisms depending on pulse energy and duration. Experimental endeavours such as those of Fishburn[107], Ren[105], Porneala[108] and others previously, have helped to identify the onset of these mechanisms and their contribution to material removal. Figure 3.6 shows the results of Fishburn's analysis using profilometry, recoil-momentum and laser shadowgraphy to de-convolve contributions from various ablation mechanisms. Good agreement between the measured crater volume and the sum of the volume removal attributed to the mechanisms shown was demonstrated.

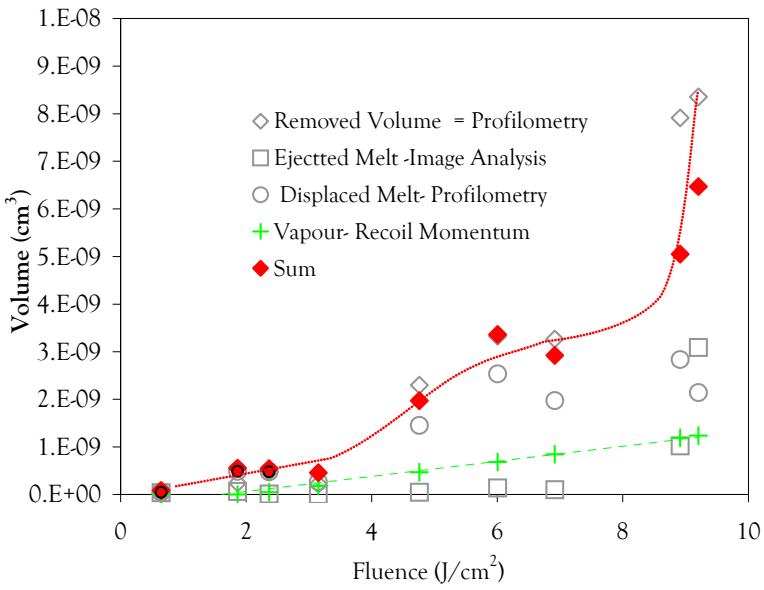

Figure 3.6. Measured ablation mechanisms which contribute to material removal at various fluences for nanosecond ablation of aluminium (from Fishburn *et al*[103]).

In regards to the material of specific interest in this dissertation, lithium niobate, nanosecond ablation studies have generally been carried out in an application specific manner. There is a fair body of work dealing with the ablation conditions suitable for pulse laser deposition of lithium niobate films. These studies pay attention to the chemistry of the liberated species, the environment and ablation conditions which optimize the fabrication of good quality films[109,110,111,112,113]. There are also studies which look at optimizing the ablation conditions to produce clean features for optoelectronic applications. Trimming and phase-correction of lithium niobate electro-optic modulators either by ablating the waveguide surface and surrounds or the electrode material[114,115,116] is one such application. Surface gratings[117] and alignment slots for optical fibres[118] have also been demonstrated. Most laser processing of lithium niobate in the nanosecond regime has been carried out with wavelengths near or below the UV absorption cut-off of the material (340-360 nm). These sources include nitrogen lasers (337 nm)[119], KrF excimer lasers (248 nm)[120,121], ArF excimer lasers, fluorine lasers (157 nm)[122] and frequency tripled (355 nm)[123] and quadrupled (266 nm) Nd lasers. A US patent specific to laser processing lithium niobate with 355 nm lasers is held by McCaughan and Staus[124]. Hybrid processes involving laser exposure and chemical etching[125,126] have also been demonstrated with the above sources as well as CW UV lasers such as frequency doubled argon-ion lasers and XeCl excimer

lasers (308 nm). The nanosecond machining in this dissertation will be carried out with a frequency quadrupled Nd:YAG (266 nm) system as detailed below in section 3.3.1.

The other system used during this project was an Ti:Sapphire 800 nm femtosecond system. With ultrashort pulses from such laser systems the ablation mechanisms begin to be driven by photon-electron and multiphoton processes rather than bulk thermal processes. This distinction has been demonstrated by Stuart *et al*[127] (Figure 3.7) as a departure from the $t^{1/2}$ dependence on the ablation threshold as pulse durations become shorter that ~10 ps. The ultrafast regime will be looked at further in the following section.

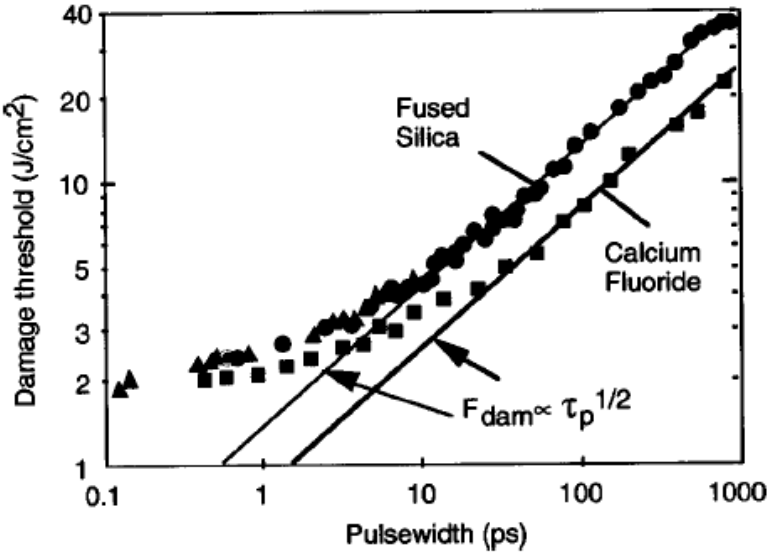

Figure 3.7. Ablation thresholds in relation to pulse durations from (Taken from Stuart *et al.*[128])

3.2.3 Ultra-fast laser machining

The development of short pulsed laser systems with pulse durations on the sub-picosecond time scale has brought about new areas of research and new opportunities for laser materials processing. Pulse durations of this scale are generally much shorter than the times scales of most thermal processes which occur in materials. This results in highly localised material interactions. The typical laser systems used for ultrafast material processing also have high peak irradiances compared to their nanosecond counterparts, typically in excess of 10^{12} W/cm^2. In transparent materials these intensities promote nonlinear processes such as multiphoton absorption, optical breakdown, ionization, and subsequent avalanche ionisation. Models of these phenomena in dielectrics have been developed in the literature by authors such as Perry, Stuart *et al*[127,129,130,131] at Laurence Livermore and also by Gamaly *et al*[132,133]. The experimental foundations of ultrafast

ablation of metals are often attributed to Preuss *et al*[134]. Several authors such as Anisimov *et al*[135,136,137], Stoain *et al*[138,139] and Quere *et al*[140,141] have since looked at a variety of theoretical and experimental aspects of ultrafast ablation. Earlier experimental investigations by authors such as Nolte *et al*[142,143] showed that some of the experimental characteristics of ultrafast ablation of metals can be understood by some straight forward physical models such as the two-temperature model (Anisimov *et al*[144]).

One of the laser-material interactions common to all these models is inverse Bremsstrahlung scattering which is the result of charged species oscillating in the laser field and accumulating large kinetic energies. In metals there is an ensemble of free electrons present in the target so that inverse Bremsstrahlung scattering can proceed at the onset of the pulse. However for dielectrics the electrons must first be freed from the host lattice. Suggested mechanisms for producing these free electrons include multiphoton absorption, which can resonantly or non-resonantly promote electrons to the conduction band and tunnelling ionisation caused by the large electric field distorting the electronic band structure of the material. Gamaly *et al*[132] suggest that a more generic optical breakdown process, which does not require the consideration of optical transitions, can take place. The large electric fields produced in the material by incident ultrafast pulses can cause the energy of the bound electrons oscillating in the laser field (electron quiver energy) to exceed ionization potential of the dielectric and escape from there parent molecules.

Freed electrons can then undergo inverse Bremsstrahlung scattering and obtain energies which allow them to ionize neighbouring atoms via impact ionisation, and the subsequent cascading of this process is referred to as avalanche ionisation. The suggested material removal mechanisms after the formation of this highly ionized volume of material are the expansion of critical density plasmas in the post pulse time frame, and the escaping of electrons which have exceeded the Fermi energy from the surface, which in turn pulls the ions from the surface via coulomb repulsion. An overview of the physics involved in some of these popular models is given below.

Multiphoton and avalanche ionization

For transparent dielectric materials Stuart, Perry *et al*[129,131] treat the electron subsystem of a material being irradiated with photons below the bandgap energy with the Fokker-Planck equation. Here the number density of electrons in the energy band $\varepsilon \to \varepsilon + d\varepsilon$ evolves according to,

$$\frac{\partial N_e(\varepsilon,t)}{\partial t}+\frac{\partial}{\partial \varepsilon}\left(VN_e(\varepsilon,t)-D\frac{\partial N_e(\varepsilon,t)}{\partial \varepsilon}\right)=S(\varepsilon,t) \tag{3.16}$$

where V accounts for the joule heating of electrons and losses due to collisions and D is the energy diffusion out of the energy band $\varepsilon \to \varepsilon + d\varepsilon$. The source term $S(\varepsilon,t)$ is often divided into two parts, the photon ionization and the subsequent impact ionizations.

$$S(\varepsilon,t)=S(\varepsilon,t)_{PI}+S(\varepsilon,t)_{IMP} \tag{3.17}$$

For straight forward multiphoton ionization the photo-ionization source term can be express in terms of the photon flux I_p (proportional to irradiance) and the probability cross-section of multiphoton ionization events for *m-photon* ionization σ_m,

$$S_{PI}=\sigma_m\left(\frac{I_p}{\hbar\omega}\right)^m \tag{3.18}$$

The impact ionization term is commonly described by the Keldysh impact treatment and the flux doubling assumption. In the limiting case an electron which has acquired kinetic energy equal to the ionisation potential of the material can collisionaly ionise a nearby atom producing two electrons with zero kinetic energy. In practice the evolution of the free-electron density due to photo and impact ionisation can be well approximated by the rate equation,

$$\frac{dN_e}{dt}=\alpha_{imp}N(t)I(t)+P(I) \tag{3.19}$$

where P is the photo-ionization term and $\alpha_{imp}NI$ is the impact/avalanche ionization term, which intuitively depends on the quantity of free electrons available at any particular time, *N(t),* and the laser field accelerating them *I(t).* An important end point in the production of electrons is when the electron density reaches a critical value of N_{cr}. This critical density is when the electron plasma frequency reaches the laser frequency, i.e. from Eq. (3.17) $\omega_{pe}=(4\pi q_e{}^2N_e/m_e)^{1/2}\to\omega_{laser}$ as $N_e \to N_{cr}$. Perry *et al* suggest and experimentally demonstrate that once a critical density plasma is produced the majority of the incident light will be reflected from the surface[131]. The strong reflectivity of the material surface when an electron plasma has been produced has also been observed in the pump-probe microscope imaging experiments of Sokolowski-Tinten *et al*[137]. An example of this is shown for near-threshold ablation of silicon in Figure 3.8. The bright region observed at 1 ps after the 120 fs pulse is due to strong reflection of probe radiation from the target.

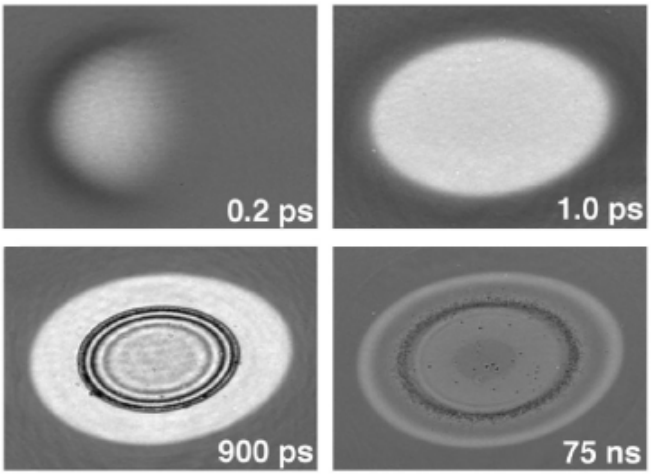

Figure 3.8 Pump-probe microscope imaging of femtosecond ablation of silicon (Sokolowski-Tinten[137], 1998).

Stuart *et al* imply that the threshold for laser damage corresponds with the generation of a critical density plasma, and consider the photo and impact ionisation as separable and sequential phenomena[129]. The generation of electrons due to photo-ionisation is assumed to peak and be almost complete by the peak of the pulse. For *m*-photon ionisation and a temporal pulse profile described by *I(t)* the electron population due to photo-ionisation can be estimated as,

$$n_0 = \int_{-\infty}^{\infty} N_s P(I) dt = N_s \int_{-\infty}^{\infty} \sigma_m \left(\frac{I(t)}{\hbar\omega} \right)^m dt \qquad (3.20)$$

where N_s is the atomic density of the material. The increase in the electron population due to impact ionization is then approximated from this value, but is only considered to be significant in the latter half of the pulse.

$$n_{tot} = n_0 \exp\left[\int_0^{\infty} \alpha_{imp} I(t) dt \right] \qquad (3.21)$$

As the pulse duration becomes shorter the generation of electrons becomes dominated by photo-ionisation which occurs relatively early in the pulse interaction. The photo-ionisation limit is the upper limit on the threshold for achieving a critical density plasma, i.e. when avalanche ionisation does not contribute to the electron density. For a Gaussian pulse with a FWHM of τ, evaluation of (3.20) suggests that generation of a critical density plasma via *m-photon* ionisation requires,

$$n_{cr} = N_s \sigma_m \left(\frac{I_0}{\hbar\omega} \right)^m \left(\frac{\pi}{\ln 2} \right)^{1/2} \frac{\tau}{4} \qquad (3.22)$$

Suggesting that the threshold fluence, $\phi_{th,photo} = \frac{I_0 \tau}{2}\left(\frac{\pi}{\ln 2}\right)^{1/2}$, for ablation via pure photo-ionisation is,

$$\phi_{th,photo} = \frac{\hbar\omega}{2^{(m-2)/m}} \tau^{(m-1)/m} \left(\frac{\pi}{\ln 2}\right)^{(m/2-1/2)/m} \left(\frac{n_{cr}}{N_s \sigma_m}\right)^{1/m} \tag{3.23}$$

When avalanche ionisation is contributing to the electron population the critical density may not be produced solely by photo-ionisation, instead the population produced in Eq. (3.22) acts as the seed electrons for the avalanche term in Eq. (3.21). For the Gaussian pulse this is evaluated as,

$$n_{cr} = n_0 \exp\left[\frac{\alpha_{imp} I_0 \tau}{4}\left(\frac{\pi}{\ln 2}\right)^{1/2}\right] \tag{3.24}$$

Resulting in a threshold fluence given by,

$$\phi_{th,photo+av} = \frac{2}{\alpha_{imp}} \ln\left(\frac{n_{cr}}{n_0}\right) \tag{3.25}$$

Note that n_0 is the electron population produced by photo-ionization.

Electron quiver ionization

Gamaly *et al*[132] have pointed out that the peak irradiances of a focused ultrafast pulse can exceed 10^{14} W/cm^2 at which point the electron quiver energy exceeds the ionising potential of most materials. The limiting ablation thresholds for this approach can be given in terms of material parameters for both metals and dielectrics as,

$$\phi_{thres}^{metal} = It_p = \frac{3}{4}(\varepsilon_b + \varphi)\frac{l_s n_e}{\alpha} \tag{3.26}$$

$$\phi_{thres}^{dielectric} = It_p = \frac{3}{4}(\varepsilon_b + J_i)\frac{l_s n_e}{\alpha} \tag{3.27}$$

where ε_b is the binding energy of ions to the lattice, φ is the work functions for metals, J_i is the ionization energy of dielectrics, and n_e is the electron density, which for singly ionized ions is equal to the atom density. One of the characteristics of this approach is that the ablation threshold scales with the skin-depth, which is inversely proportional to wavelength, and is chiefly independent of the pulse duration. While Gamaly *et al's* model is in agreement with the experimentally thresholds for gold found by Momma *et al*[145], the pulse duration dependence for fused silica found by Stuart, Perry *et al* cannot be reproduced well by Gamaly's proposition. This is because the pulse duration dependence of the ionisation processes in dielectrics, which are

considered in Stuart *et al'*s model, are not immediately apparent when using fixed material constants in Eqs. (3.26) and (3.27).

Dominant ablation mechanisms

For ablation with fluences well above threshold there is still some debate about what the dominant material removal mechanisms are. Various efforts using techniques such as time of flight mass spectroscopy[138,139] and pump-probe imaging and interferometry[140,141] have sought to identify the dominant ablation mechanisms. For example in ref [141] it was concluded from interferometry that multiphoton-ionization dominates plasma formation in dielectrics at high peak powers (10^{14} W/cm^2) with no evidence of avalanche ionisation when the pulse duration is less than 100 fs. The dominant material removal mechanism which proceeds after the pulse interaction in dielectrics has been suggested to be the pulling apart of the ionised material left at the surface after the electrons have been stripped from their parent atoms. This process has been termed *'coulomb explosion'*. In some materials this is not the whole story and despite the 'athermal' and 'cold' and 'clean' ablation characteristics often attributed to ultrafast pulses, there is strong evidence to suggest thermal vaporization and melting is be produced in some materials. The results of Stoain *et al*[139] demonstrated that there is a clear difference between the surface states of a dielectric and a conductive material under ultrafast pulse irradiation. This was confirmed by characterising the ion emission from the target in their pump-probe measurements. The suggested reason for this difference is quenching of the surface charge and also the formation of molten layers in conductive materials. The ultrafast formation of a molten layer in silicon was previously suggested by the imaging techniques used by Sokolowski-Tinten *et al*[137] (Figure 3.8), and the fast onset of molten states in ultrafast laser heated semi-conductors has been explained by Stampfli and Bennemann[146]. One must thus be aware that the assumption of *'cold'* ablation when using ultrafast pulses is not necessarily valid, especially in conductive materials. The onset of ablation regimes with thermal characteristics as opposed to coulomb explosion has also been observed in dielectrics under high power and multiple pulse ultrafast ablation[138]. Lee *et al*[147] have also found that a thermal ablation regime at higher fluences may also exist for UV femtosecond processing of some polymer materials.

Ablation rate scaling and the two temperature model

While many physical models have been developed to explain the ablation thresholds and material removal mechanisms associated with ultrafast laser processing, ablation rate scaling can often be characterised by simple consideration of the optical, electron heat and bulk thermal penetration of

the target. If the ablation is *'cold'* - relatively free from any diffusion processes - the extent of optical absorption in the target will define the ablated volume. If the initial absorption of the material does not change markedly as the pulse energy is increased the depth of the ablation crater as the pulse energy is increased will scale in a similar fashion to the way the optical energy scales with Beer-Lambert type absorption,

$$d = l_\alpha \ln\left(\frac{\phi}{\phi_{thres,optical}}\right) \tag{3.28}$$

The length scale l_α may be related to the linear or nonlinear absorption of the material, the skin depth in conductors, or a characteristic length associated with the electron heat penetration of the target. In materials where diffusion of the electron and lattice temperatures takes place, a single ablation rate scaling may not describe the ablation scaling across a large range of fluences. The two-temperature approach was previously used by authors such as Nolte/Chickov *et al*[142] to account for the different observed ablation rates and morphologies observed at different pulse energies. The two temperature model treats the lattice and the electron subsystem as two distinct but coupled energy systems, whose temperatures are governed by the heat equations (1D),

$$C_e \frac{\delta T_e}{\delta t} = \nabla.\left(\kappa_e \nabla T_e\right) - \Gamma(T_e - T_l) + Q \tag{3.29}$$

$$C_l \frac{\delta T_l}{\delta t} = \nabla.\left(\kappa_l \nabla T_l\right) + \Gamma(T_e - T_l) \approx \Gamma(T_e - T_l) \tag{3.30}$$

Here $C_{e,l}$ are the volumetric heat capacities, $\kappa_{e,l}$ are the thermal conductivities of the electron and lattice subsystems and Γ is coupling between them. Despite the considered pulse duration being of a much shorter duration than the typical thermal relaxation processes which occur in materials (and thus the thermal diffusion in the lattice is often ignored), the two temperature approach suggests that for conductive materials electron heating by the laser pulse can significantly coupled to the lattice in the post pulse time frame. This results in significant thermal evaporation when the lattice energy exceeds the energy of vaporization,

$$C_l T \geq \rho H_v \tag{3.31}$$

Nolte *et al* suggested a second logarithmic scaling to describe this thermal ablation regime. I.e. the thermal penetration of the target that results in ablation is assumed to decay exponentially into the target in an analogous fashion to the exponential decay of the optical field. The ablation rates for conductive materials have thus been well described by a pair of logarithmic equations, one for

the optical penetration and ionization regime at low fluences, and one for electron heating and thermal diffusion at higher fluences.

$$d = l_\alpha \ln\left(\frac{\phi}{\phi_{thres,optical}}\right),\ \phi < \phi_{thres,thermal} \tag{3.32}$$

$$d = l_{thermal} \ln\left(\frac{\phi}{\phi_{thres,thermal}}\right),\ \phi > \phi_{thres,thermal} \tag{3.33}$$

An example of experimental data which shows such trends is illustrated in the results of Nolte *et al* in Figure 3.9.

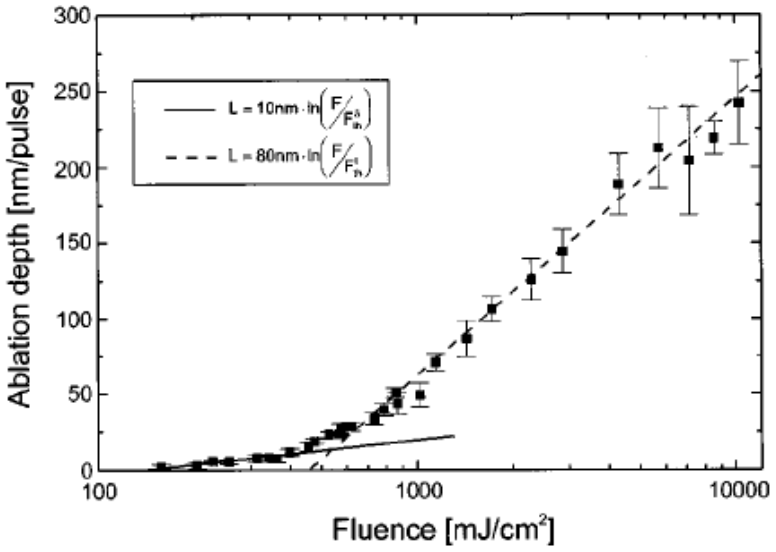

Figure 3.9. Ultrafast ablation rates for copper (150 fs pulses) from Nolte *et al*[148]. Two ablation regimes are apparent, and coincide well with optical penetration at low fluence and thermal penetration at higher fluences.

The characteristic length scale for the thermal ablation regime has been linked to the electron heat penetration length scale[142],

$$l_{thermal} = a_{at}(M_i / 3m_e)^{1/2} \tag{3.34}$$

where a_{at} is the average atomic spacing, M_i is the mass of the ions and m_e is the mass of the electrons. Bulk thermal transport also has a length scale which depends on the duration of the heat source, τ, in this case the laser pulse duration. This length scale is given as,

$$l_{thermal} = 2\sqrt{D\tau} = 2\sqrt{\frac{\kappa}{\rho c_p}\tau} \tag{3.35}$$

Christensen *et al*[149] have alternatively suggested, and found experimental evidence, that the thermal penetration occurs in a more linear fashion at higher fluences, with the energy deposited going into regular evaporation of the material so that the ablation depth scales as,

$$d = \sqrt{\frac{2}{\pi e}} \frac{\phi}{\rho H_v} \tag{3.36}$$

Previous studies of ultrafast ablation of lithium niobate

The body of literature associated with ultrafast laser processing of lithium niobate is relatively sparse compared to silicon and fused silica. Deshpande *et al*[150] and Chen *et al*[151] have carried out some fundamental studies based on lithium niobate ablation with 300 fs and 80 fs respectively from 800 nm Ti:Sapphire sources. Lithium niobate was also a material of interest in the dual pulse time-resolved investigations of Pruess *et al*[152] using 500 fs UV pulses. The suggested ablation thresholds for single shot ablation from Deshpande and Chen were 2.5 J/cm^2, 2.82 J/cm^2 respectively and as low as 0.05 J/cm^2 in the case of 248 nm 500 fs pulses from Pruess. Both Deshpende and Chen found that incubation via multi-pulse ablations lowers the ablation threshold in lithium niobate, a phenomenon which has be found for many materials[153]. Fabrication of structures in lithium niobate suitable for polaritonic optics[154] and periodically poling[49] have been demonstrated using ultrafast laser processing. There is also a growing interest in destructive and non-destructive laser induced internal modifications in lithium niobate for waveguides[155,156,157,158], photonic crystals[159] and data storage[160]. During the course of this project several previously reported structural and photo-refractive modifications where observed during ultrafast laser interactions with lithium niobate. The key areas of investigation in this project were the surface ablation characteristics and parameter optimisation for producing clean, well defined surface grooves for periodic poling.

3.2.4 Consideration of Gaussian beam profiles

Many laser systems have Gaussian irradiance profiles. This needs to be taken into account when considering the power distribution on target and the resulting profiles of the ablated features. The functional form of the irradiance profile for a symmetric Gaussian profile with peak irradiance I_0 is,

$$I(r) = I_0 e^{\left(\frac{-2r^2}{w_0^2}\right)} \text{ or } I(r) = I_0 e^{\left(\frac{-4\ln 2 r^2}{w_{fwhm}^2}\right)} \tag{3.37}$$

where w_0 is the $1/e^2$ radius (Gaussian half waist), or alternatively w_{fwhm} is the FWHM half width, of the intensity profile on target. The Gaussian profile needs to be considered when a measurement of average power or pulse energy is converted to the irradiance or energy distribution on target. From the integration of a Gaussian profile of irradiance or fluence we find that the peak irradiance/fluence, I_0/ϕ_{peak}, for a Gaussian half waist of w_0, is related to the total measured power/energy,

$$I_{total} = \int_{\phi[0,2\pi]} \int_{r[0,\infty]} I_0 e^{-2r^2/w_0^2} r dr d\phi = 2\pi I_0 \left[\frac{-w_0^2}{4} e^{-2r^2/w_o} \right]_0^\infty = \frac{w_0^2 \pi}{2} I_0 \qquad (3.38)$$

The peak laser fluence ϕ_{peak} (J/cm^2) or peak laser irradiance I_{peak} (W/cm^2) can thus be related to the measured pulse energy E_p or power I_{total} (respectively) as

$$\phi_{peak} = \frac{2E_p}{\pi w_0^2} \text{ or } I_0 = \frac{2I_{total}}{\pi w_0^2} \qquad (3.39)$$

Due the Gaussian distribution of energy across the beam, not all of the irradiated area will be above the ablation threshold. This is illustrated in Figure 3.10. The corresponding diameter of the ablation features depends on the incident fluence as related to the threshold fluence and the beam waist w_0,

$$D^2 = 2w_0^2 \ln \frac{\phi_{peak}}{\phi_{thres}} \qquad (3.40)$$

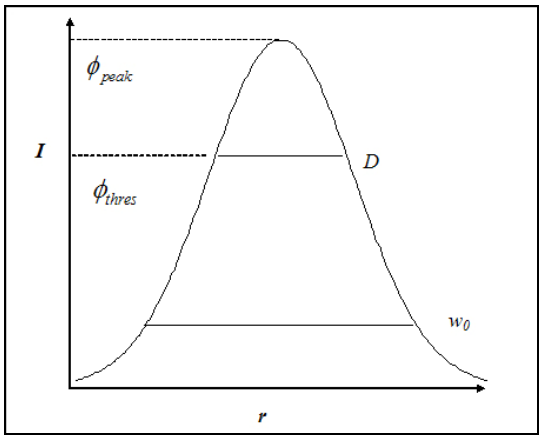

Figure 3.10 Gaussian irradiance profile, producing features of diameter D depending on the irradiance distribution which is above threshold

Eq (3.40) has been used by several authors as an empirical method for determining the beam waist from the slope of Eq (3.40) and the ablation threshold from the power where the extrapolated crater diameter goes to zero.

3.3 Experimental equipment and measurements

3.3.1 Laser systems

The two laser systems used in this investigation were a Light Wave Electronics Q201-HD (now owned by JDSU) and a SpectraPhysics Hurricane. A summary of the laser properties for these two systems is given inTable 3.2. The Q201-HD was external frequency doubled to 266 nm in by a single pass in a BBO crystal. This provided ~300μJ pulses for the UV nanosecond ablation studies presented below. A more detailed overview of the laser machining systems is provided in appendix A2.

	LWE Q201-HD	**SpectraPhysics Hurricane**
Description	Diode pumped, frequency doubled Q-switched Nd:YAG	Regeneratively amplified Ti:Sapphire femtosecond laser system.
Wavelength	532 nm	800 nm
Pulse duration	20 ns	100 fs
Repetition rate	100 Hz-20 kHz	1 Hz-1 kHz
Maximum pulse energy	3 mJ	1 mJ

Table 3.2 Laser parameters of the two systems used for ablation studies and machining during this project.

3.3.2 Characterisation

The characterisation of laser ablation of lithium niobate and silicon targets was carried out using differential interference contrast (DIC) microscopy with an Olympus BX-61 for qualitative inspection, and surface optical profilometry (SOP) with a modified optical profilometer from Veeco was to measure the geometry of ablated features. A more detailed overview of these characterisation systems is also provided in appendix A2. Figure 3.11 and Figure 3.12 show typical images and data collected from the Olympus BX-61 and Veeco SOP systems respectively.

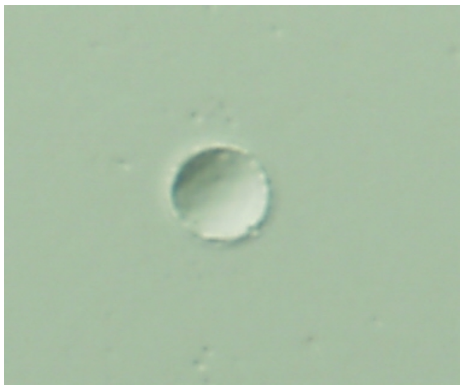

Figure 3.11 DIC microscope image of a single pulse ablation crater on silicon.

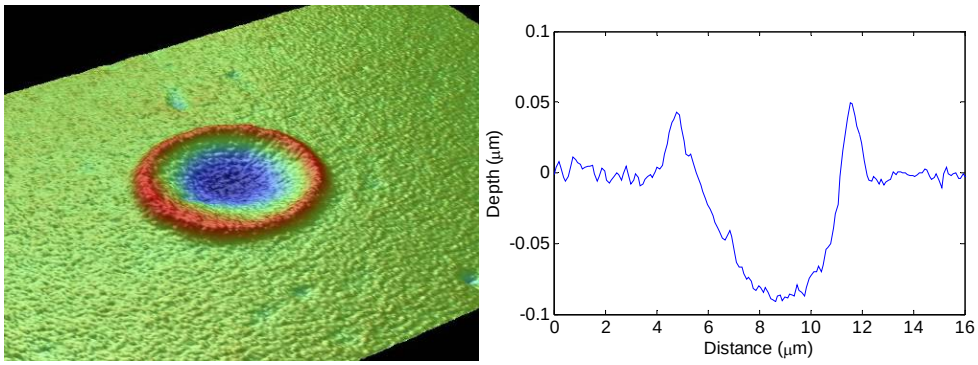

Figure 3.12 Surface optical profilometry data of the ablation crater shown above in Figure 3.11

3.4 Single shot ablation experiments

3.4.1 Experimental overview

Single shot ablation studies on silicon and lithium niobate targets was carried out by translating the targets through a focused laser beam at a feed rate sufficient to separate the individual pulses. The pulse energy was approximated by dividing the measured average power by the pulse repetition rate. The power incident on the target was adjusted using ND filters in the case of the LWE system and by rotating the waveplate/polariser pair in the case of the Hurricane. Microscope images of the ablation craters at various powers were taken, and the craters were then measured using optical profilometry. Ablation thresholds and ablation rate scaling were determined from the optical profilometry measurements as detailed below. Laser machining of scribes into the surface of lithium niobate is dealt with in the following section (3.5). The thermal properties of silicon and lithium, used in various calculations in this section, are given below in Table 3.3.

Parameter	Silicon	Lithium niobate
Density, ρ	2.33 g/cm^3	4.64 g/cm^3
Specific heat, C	0.71 J/gK	0.633 J/gK
Thermal conductivity, κ	1.49 W/cmK	0.042 W/cmK
Thermal diffusivity, D	0.808 cm^2/s	0.014 cm^2/s
Melting point, T_m	1412 °C	1240 °C
Enthalpy of atomization: ΔH_a Enthalpy of fusion: ΔH_m	439.3 kJ/mole (15.7 kJ/g) 46.44 kJ/mole (1.65 kJ/g)	

Table 3.3 Values of some thermal properties of silicon and lithium niobate.

3.4.2 Silicon ablation with the nanosecond DPSS system

Ablation studies with the LWE. DPSS nanosecond laser system was carried out with the following parameters;

- 3 mm beam diameter
- 1.5 kHz pulse repetition rate
- Feed rate of 2000mm/min (sufficient for pulse separation)
- 5x objective lens (OFR LMU 5x - 0.13 NA)

The spots size on target was ~5 μm. Microscope images of single shot ablation craters on silicon with fluences ranging from 5-100 J/cm^2 are shown in Figure 3.13. The threshold pulse energy for ablation of silicon with 20 ns 266 nm pulses was found to be ~0.8 μJ. An image of a crater produced with 0.8 μJ pulse is shown on the left of Figure 3.14. From optical profilometry data the square of the crater diameter in relation to the pulse logarithm of the incident pulse energy was plotted for pulse energies near threshold, as shown in Figure 3.15. The linear relationship between these two parameters can be related to Eq. (3.40) to determine the Gaussian half-waist of the incident beam and thus the threshold ablation threshold. I.e. $D^2 = 2w_0^2 \ln \frac{\phi_{peak}}{\phi_{thres}}$.

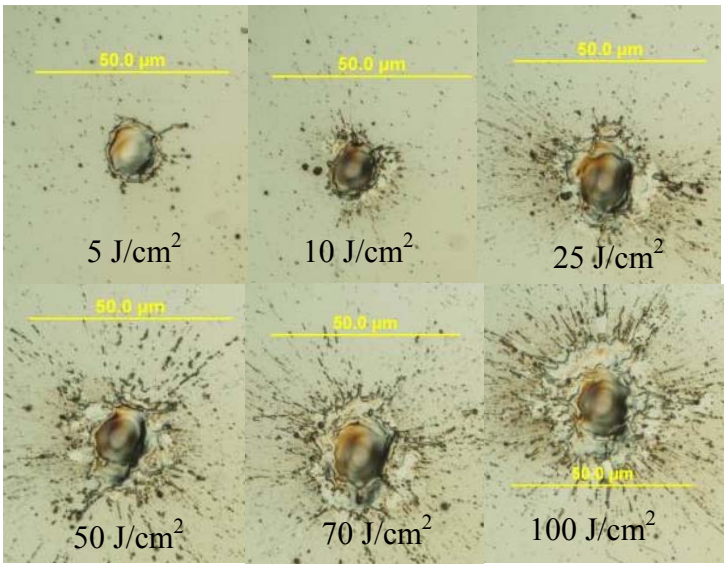

Figure 3.13 Single ablation shots in silicon with 266nm ~20ns pulses. Fluences from 5-100 J/cm^2

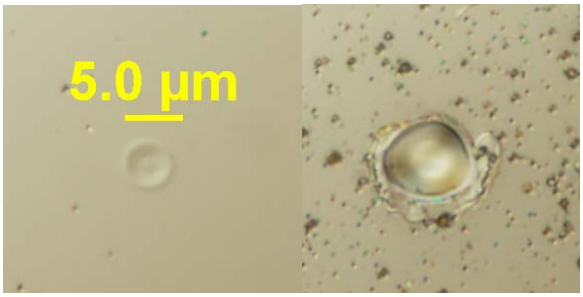

Figure 3.14 Left: Ablation crater in silicon near the ablation threshold (266nm 20ns pulses.) Right: crater produced with 7 J/cm^2.

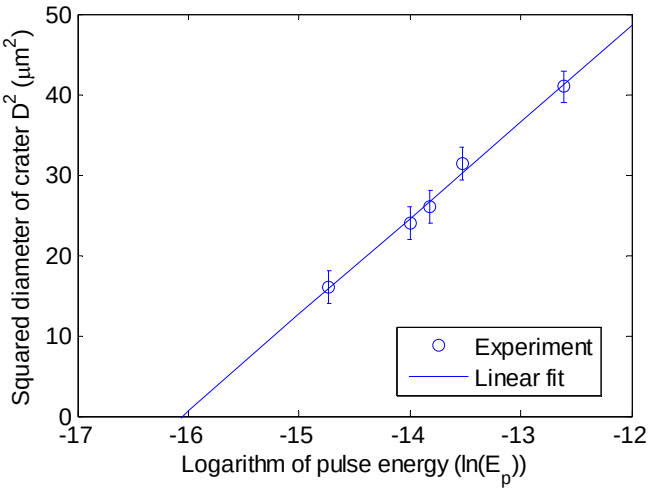

Figure 3.15 Evolution of crater diameter in relation to logarithm of the incident pulse energy.

From the linear fit in Figure 3.15, the Gaussian half-waist was determined as w_0=2.45 μm and the corresponding ablation threshold was 1.15 J/cm^2. The predicted ablation threshold for a 20 ns pulse from the approximate solution to the 1D heat equation,(Eq (3.13)), $\phi_\alpha^{\min} = I_\alpha^{\min} t_p = \sqrt{\frac{\pi}{2}} \Delta H \rho \left(D t_p \right)^{1/2}$) with the physical parameters for silicon, is 0.61 J/cm^2. Taking into account a silicon reflectivity of 50-60% in the UV, the predicted and experimental values of the ablation threshold fluence are in reasonable agreement. The ablation rate scaling for single shot ablation craters was investigated in the fluence range of 2-100 J/cm^2 the results of which are shown in Figure 3.16 with the fluence plotted on a logarithmic scale. Craters depths of almost 5 μm could be produced with single laser pulses at 100 J/cm^2 fluences. A logarithmic trend in the ablation rate scaling can be seen for fluences beyond 10 J/cm^2. As shown in Figure 3.13 there is significant splatter of material around the crater edges above fluences of 10 J/cm^2, suggesting that phase-explosion is taking place in this ablation regime. The observed length scale in this ablation regime, 1168 nm, is thus most likely associated with the extent of the superheating in the silicon which produces phase explosion. The thermal length scale for silicon with a 20 ns heat source and ambient thermal parameters is,

$$l_{thermal} = 2\sqrt{D\tau} = 2\sqrt{\frac{\kappa}{c_p \rho}\tau} = 2\sqrt{\frac{1.5}{0.8 \times 2.32} 20 \times 10^{-9}} \approx 2500 nm \qquad (3.41)$$

which is a approximately a factor of two larger than the length scale found from the experimental data. The discrepancy is most likely due to significant differences in the thermal properties of ambient and superheated silicon. At fluences below 10 J/cm^2 there was significantly less splatter around the ablation craters, as shown on the right of Figure 3.14. Whilst only a few data points were recorded at these lower fluences, a different ablation regime is still apparent from the ablation rate scaling. The apparent saturation of the ablation rate in the 5-10 J/cm^2 is somewhat consistent with the trend found in the investigations of Ren *et al*[99] who suggest that plasma shielding prior to the onset of phase-explosion..

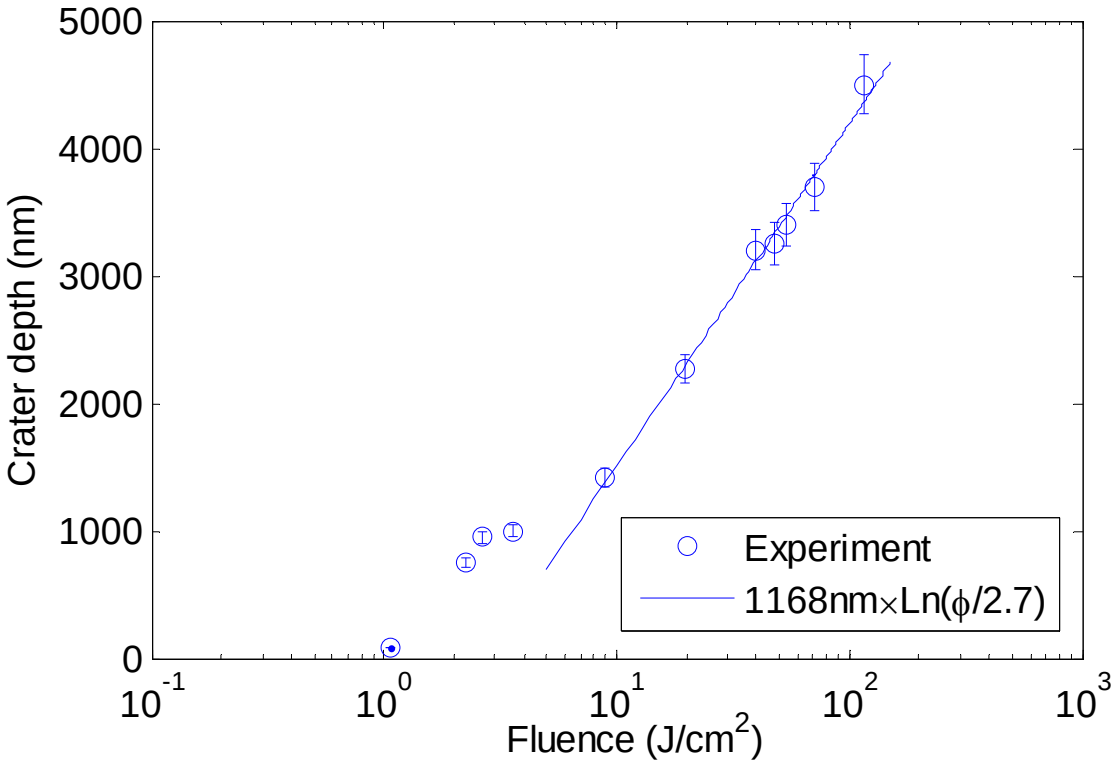

Figure 3.16 Ablation rate scaling for silicon (266 nm, 20 ns pulses.)

3.4.3 Lithium niobate ablation with the nanosecond DPSS system

Ablation studies of lithium niobate with the LWE laser system were carried out with the same parameters as used for the silicon targets described above. Microscope images of single shot ablation craters on lithium niobate with fluences of 5, 25 and 50 J/cm2 are shown in Figure 3.17. The experimental ablation rate scaling for lithium niobate is shown in Figure 3.18.

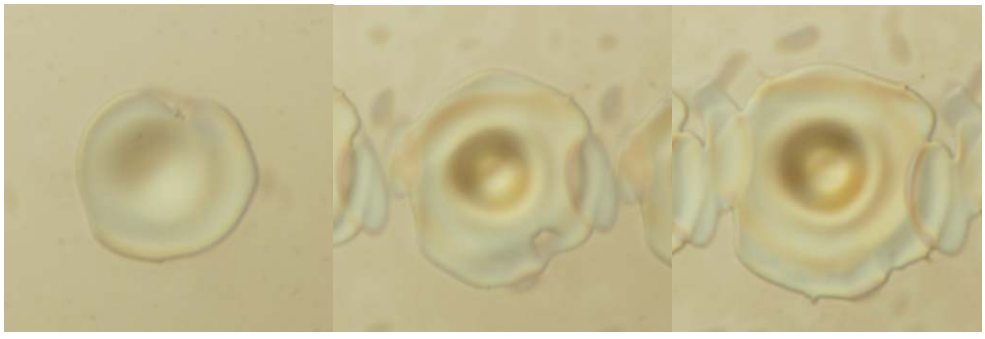

Figure 3.17 Single shot ablation craters on lithium niobate with 10, 25 and 50 J/cm (left to right).

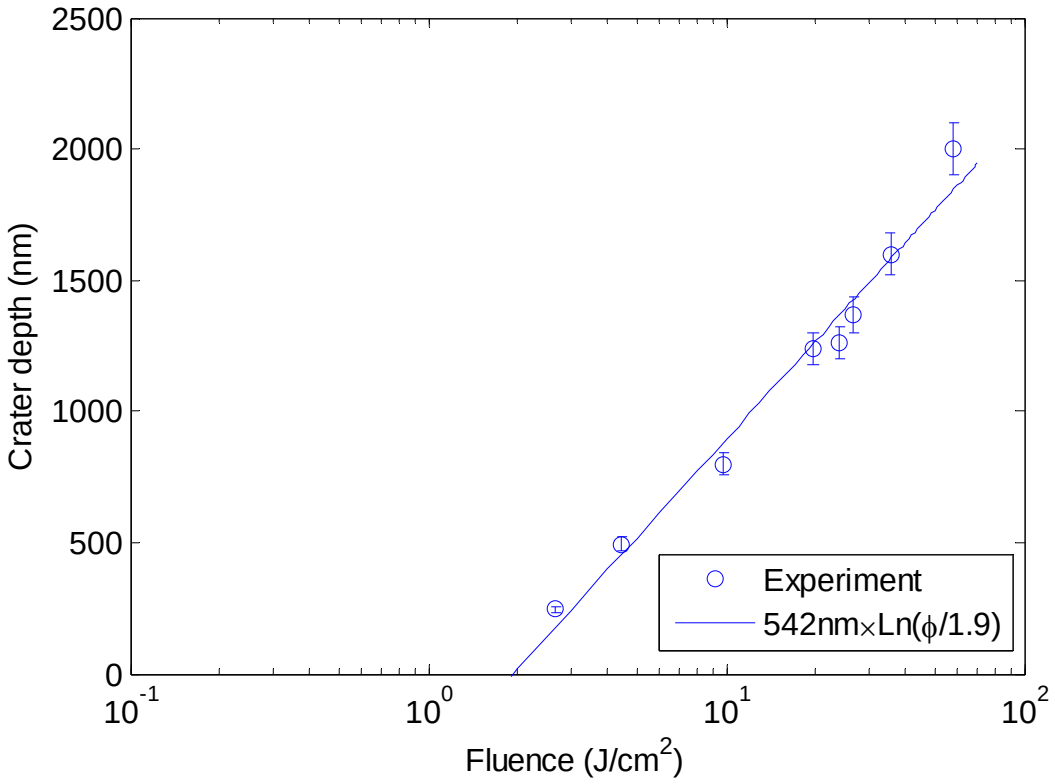

Figure 3.18 Ablation rate scaling for lithium niobate (266 nm, 20 ns pulses.)

The experimental ablation threshold for this regime was found by extrapolation to be 1.9 J/cm^2. This ablation threshold is towards the higher end of ablation thresholds previously reported in the literature for UV nanosecond lasers. A table of ablation thresholds from other similar studies is shown for comparison in Table 3.4. Based on common values of the ambient thermal properties of lithium niobate, D=0.014 cm^2/s, κ=0.042 W/cmK and a melting point of 1240°C, Eq (3.9) suggests a lower limit on the deposited energy required to begin melting the lithium niobate surface of, $\phi = \frac{\sqrt{\pi}}{2}\left(\frac{t_p}{D}\right)^{1/2} T_m \kappa \approx 0.05 J/cm^2$.

Author	Pulse duration, wavelength	Threshold fluence
Eyett[161]	11 ns, 308 nm (XeCl excimer)	0.9 J/cm^2
Chong[162]	20 ns, 248 nm (KrF excimer)	1 J/cm^2
Tomov[163]	25 ns, 248 nm (Krf excimer)	2.5 J/cm^2
Sones[45]	20 ns, 248 nm (KrF excimer)	0.5 J/cm^2
Chaos[164]	12 ns, 193 nm (ArF excimer)	0.4 J/cm^2
Rodenas[123]	12 ns, 355 nm (tripled Nd:YAG	0.85 J/cm^2
This dissertation	20 ns, 266 nm (quadrupled Nd:YAG)	1.9 J/cm^2

Table 3.4 Reported threshold fluences for UV nanosecond ablation of lithium niobate.

For lithium niobate a single logarithmic ablation scaling with a characteristic length scale of 542 nm was found. For a length scale which is hypothetically governed by the optical absorption of the target, the absorption coefficient is $\alpha=\sim 1.8\times10^5 cm^{-1}$. This large value is quite feasible as 266 nm is well below the UV absorption edge of lithium niobate. The early measurements of Redfield and Burke[165] suggest an absorption coefficient approaching $10^4 cm^{-1}$ for 4.4eV photons at 300K. 266 nm light has a photon energy of 4.66eV so an even larger absorption coefficient is to be expected. Alternatively the predicted thermal length scale (as in Eq. (3.35)) associated with a 20 ns heat source in lithium niobate (D=0.014 cm^2/s) is ~345 nm, significantly shorter than that found in these experiment. It is thus most probable that the ablation scaling for lithium niobate, within the range parameters investigated during these experiments, is chiefly governed by the extent of the optical absorption.

3.4.4 Silicon processed with the femtosecond Hurricane system

For the single shot investigations with the Hurricane system, the beam was apertured to produce a a circular beam profile. The aperture was placed in the beam in approximately 1.5 m from the focusing objective with its diameter adjusted so that a Gaussian beam profile without significant diffraction rings was seen on a beam profiling camera at the objective holder. The profile of the beam at the objective is shown in Figure 3.19. Due to the diffraction from the aperture the beam is not a perfect Gaussian and the first order diffraction rings could be seen in the ablated features at high fluences. However the central part of the beam still maintained a Gaussian intensity distribution, as shown by the fitting in Figure 3.20 and contained ~90% of the total power, so that using Eq. (3.39) still gives a good approximation of the peak fluence/irradiance on target.

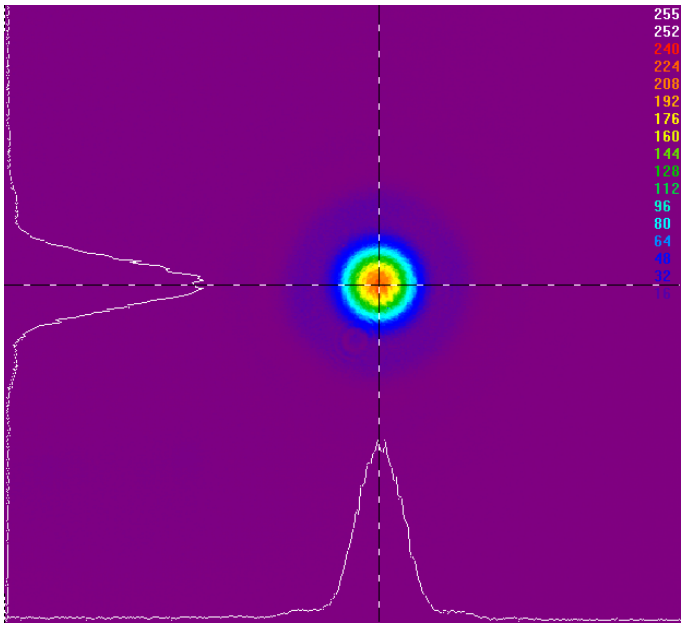

Figure 3.19. Spiricon image of the Hurricane beam at the objective lens holder after the beam has been irised near the laser output, 1.5 m from the objective holder.

For single shot experiments the repetition rate of the Hurricane output was reduced to 250 Hz from its default repetition rate of 1 kHz. The average power on target was adjusted between 0.1mW and 2.5mW, corresponding to pulse energies of 0.4-10μJ for the 250Hz pulse train. Microscope images of single ablation shots at various fluences are shown below in Figure 3.21.

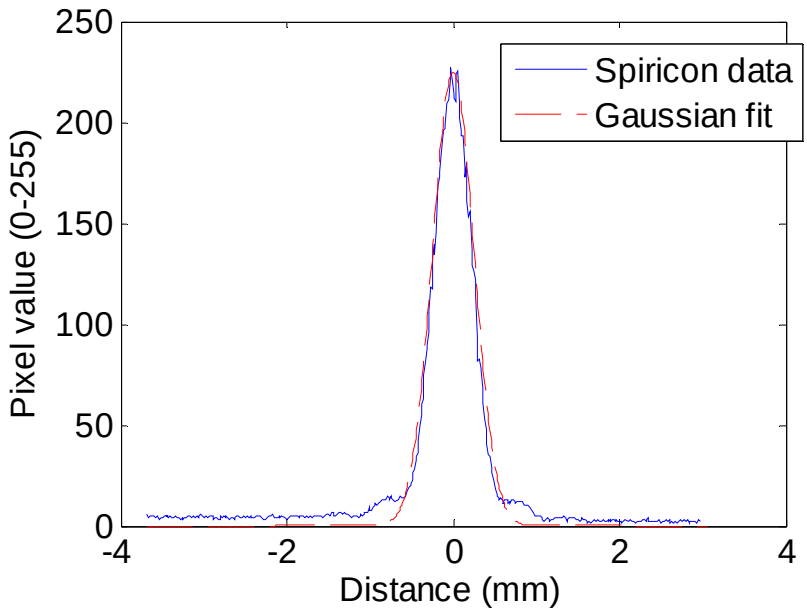

Figure 3.20 Gaussian fit to the apertured beam profile from the Hurricane laser system.

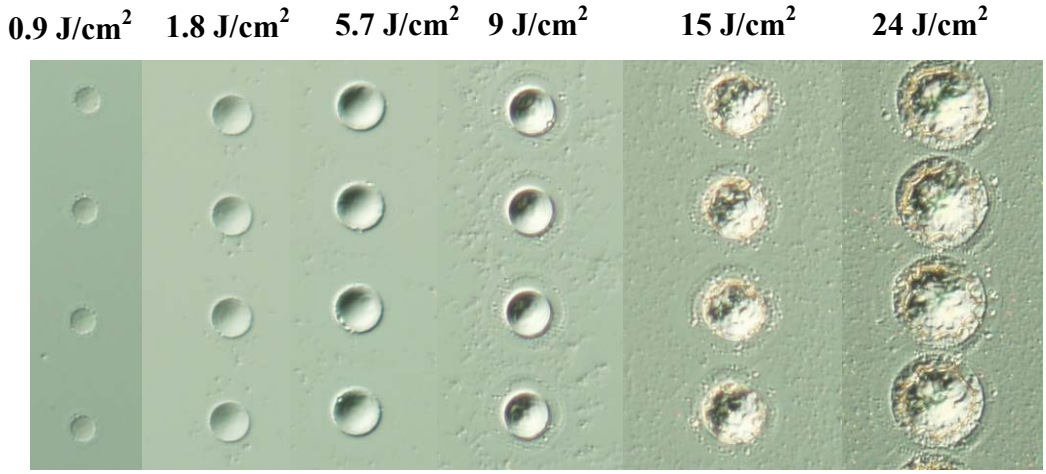

Figure 3.21 Single shot ablation craters in silicon at fluences of 1-25J/cm^2

Optical profilometry of the ablation craters was carried out to determine their depths and diameters. Increasing the pulse energy at low fluences, 0.9-5.7 J/cm^2, resulted in an increase in the crater diameter as indicated by the images in Figure 3.21. The square of the measured crater diameter was plotted against the logarithm of the estimated pulse energy, as suggest by Eq.(3.40). This is shown for four pulse energies near threshold in Figure 3.22. From the experimental data in Figure 3.22 a Gaussian half waist of w_0=4.6 μm and a threshold pulse energy of 0.214 μJ was determined. This corresponds to an experimental threshold fluence for silicon of 0.64 J/cm^2. This value does not take into account the reflection from the silicon surface, and is based purely on topographical modification. Bonse *et al*[166] have previously identified that different thresholds may exit for different degrees of modification of the silicon surface, with the experimental threshold for visibly modifying the material being about 0.21 J/cm^2 and the threshold for 'annealing' or displacing silicon being about 0.55 J/cm^2. Ablation thresholds from other authors point towards a lower limit on the ablation threshold of ~0.1-0.2 J/cm^2 for ~100 fs 800 nm pulses, though some of these experiments are based on multi-shot ablation where incubation aids in reducing the threshold, and others experiment identify the threshold fluence for atom and ion ejection from the target which occurs at lower fluences than for any appreciable topographic change. The result in this investigation is not dissimilar to that presented recently by Bonse *et al*[167], who found that surface modification (onset of melting) was apparent at fluences below 0.4 J/cm^2, but volume displacement and was not appreciable until fluences in excess of 0.64 J/cm^2 were applied. Recent results from Lee *et al*[168] also suggest a single shot ablation threshold of 0.63 J/cm^2, and are in general very similar to the overall results found during these

studies. A sample collation of experimental ablation thresholds for ultrafast ablation of silicon from the literature is shown in Table 3.5.

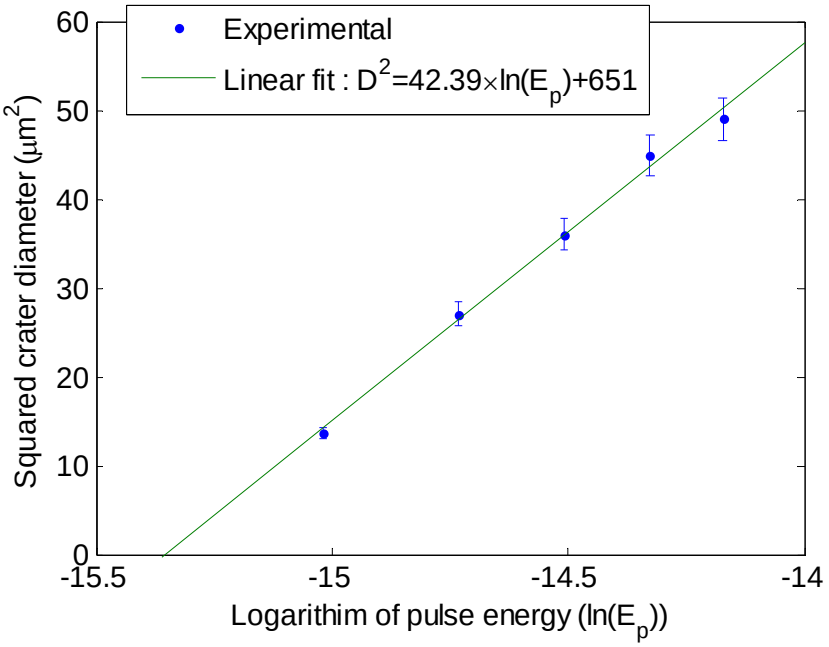

Figure 3.22. Increase in the square of the measured crater diameter in relation to the logarithm of the incident pulse energy as the pulse energy in increased above threshold.

Author	Pulse duration, wavelength	Threshold fluence
Bonse[166,167]	130 fs, 800 nm	0.27 J/cm^2 (0.55 J/cm^2 annealed region)
Borowiec[169]	130 fs, 790 nm	0.142 J/cm^2 (~25nJ with w_0=3.35μm)
Jeschke[170]	25 fs, 790 nm 400 fs, 790 nm	0.17 J/cm^2 0.28 J/cm^2
Cavalleri[171]	100 fs, 620 nm	0.3 J/cm^2
Lee[168]	150 fs, 775 nm	0.63 J/cm^2
Hwang[172]	83 fs, 800 nm	0.438 J/cm^2
This dissertation	100fs, 800nm	0.64 J/cm^2

Table 3.5 Experimental ablation thresholds for silicon with ultrafast pulses.

The ablation rate scaling for silicon was investigated by using optical profilometry measurements to determine the ablation crater depth in relation to the incident fluence. The results are shown in Figure 3.23. As in many previous investigations, the fluence has been plotted on a logarithmic

scale, as the ablation rate is initially expected to scale with the optical absorption as in Eq. (3.28). In these investigations the experimental results suggested two logarithmic ablation trends, one applicable below 5 J/cm^2 and a second ablation regime above 5 J/cm^2. A similar double logarithmic ablation rate scale for silicon has also observed by Crawford *et al*[173], Lee *et al*[168] and Barsch *et al*[174] (though the actual results of Barsch are vastly different to other authors). The logarithmic fits, as described in Eqs (3.32) and (3.33), have two parameters which provide insight into the ablation process, the threshold fluence where the extrapolated crater depth goes to zero, and a characteristic penetration length which indicates the ablation rate scaling with fluence.

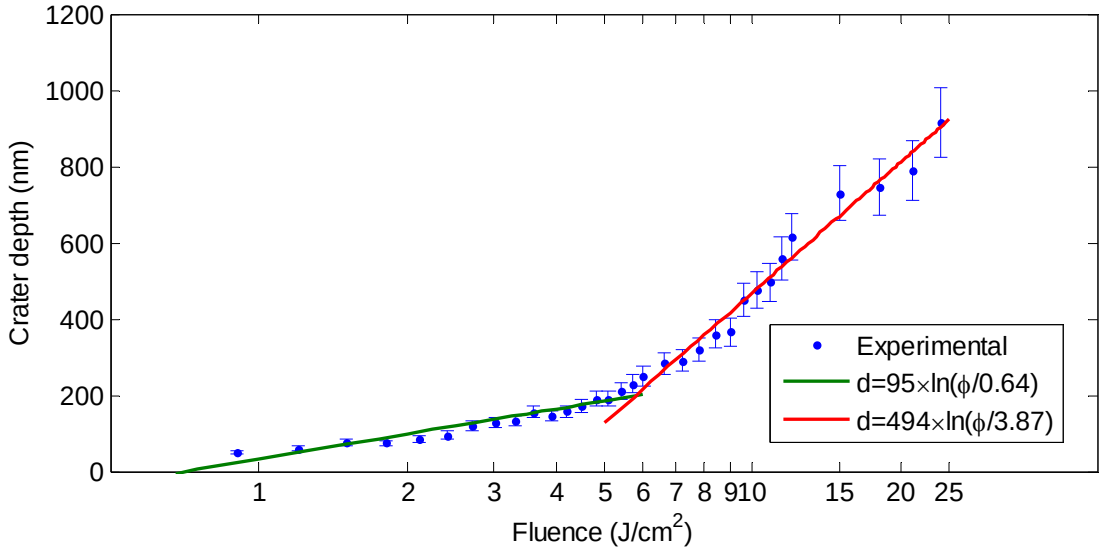

Figure 3.23 Measured crater depths in silicon in relation to the incident fluence for 100fs pulses.

As shown in Figure 3.23, the thresholds determined by the fittings to the experimental crater depth data, for the low and high fluence ablation regimes, were 0.64 J/cm^2 and 3.87 J/cm^2 respectively. The corresponding characteristic penetration lengths for the two regimes are 95 nm and 494 nm. The value of the ablation threshold arrived at by crater diameter and crater depth analysis is in agreement, suggesting that 0.64 J/cm^2 is an accurate assessment of the single pulse ablation threshold for appreciable topographic modification of silicon with these laser parameters. The characteristic penetration length scale of 95 nm for the lower fluences is of the order of the optical skin depth of silicon at 800 nm, but is also in fair agreement with the electron heat penetration length as suggested by Nolte *et al* for metals (Eq. (3.34). For silicon this is evaluated as $l_{thermal} = a_{at}(M_i / 3m_e)^{1/2} \approx 70nm$ for a lattice constant of a_{at}=5.431 Å and ion mass of 28 amu. Explanation of the double logarithmic trend in the ablation rate scaling of silicon lends itself well

to the two temperature model description as used by Nolte *et al*[142] to describe ultrafast ablation from metals. This is qualitatively explained by attributing the initial ablation regime to an ionization type ablation process (or at least an ablation regime defined by the optical absorption volume) and the onset of the higher fluence ablation regime when sufficient energy transferred is being transferred to the lattice to allow diffusion and melting beyond the laser heated volume. Evidence of a transition from an ionizing to a thermal ablation regime at higher powers is also apparent in the morphologies of the craters as shown in Figure 3.24. The smooth craters at low irradiance are suggestive of with ablation in an athermal/ionizing regime who's geometry closely resembles the optically affected volume, whereas craters produced with higher irradiance pulse appear to have been molten at some point during the ablative process and also have a marked increase of ejected particulates on the surrounding surface. The two extremes are illustrated in Figure 3.24.

The 494 nm characteristic penetration length for the higher fluence regime is most likely diffusive in origin but is much larger than the thermal length scale for a 100 fs pulse in silicon,

$$l_{thermal} = 2\sqrt{D\tau} = 2\sqrt{\frac{\kappa}{c_p \rho}\tau} = 2\sqrt{\frac{1.5}{0.8 \times 2.32} 100 \times 10^{-15}} \approx 5.70nm \qquad (3.42)$$

The observed length scale is likely an indication of the diffusion length of free carriers within the material which are energetic enough to collisionally heat the material lattice beyond its melting point. Lee *et al*[168] and Hwang *et al*[172] have both arrived at experimental penetration lengths of ~322 nm for the high fluence regime, however in both these investigations the fluence range was extended out to 1000 J/cm^2 where there was large variations in the measured ablation depths which affected the fitting. This is shown in the reproduced plots in Figure 3.25. If data from Lee and Hwang (especially Lee) is considered in the same fluence range as in this investigation, <30 J/cm^2, it is clear that the penetration length scale has been underestimated. The data from Lee's, Hwang's and the results present here all concur that an ablation depth of 1μm is produced by an incident fluence of ~20 J/cm^2.

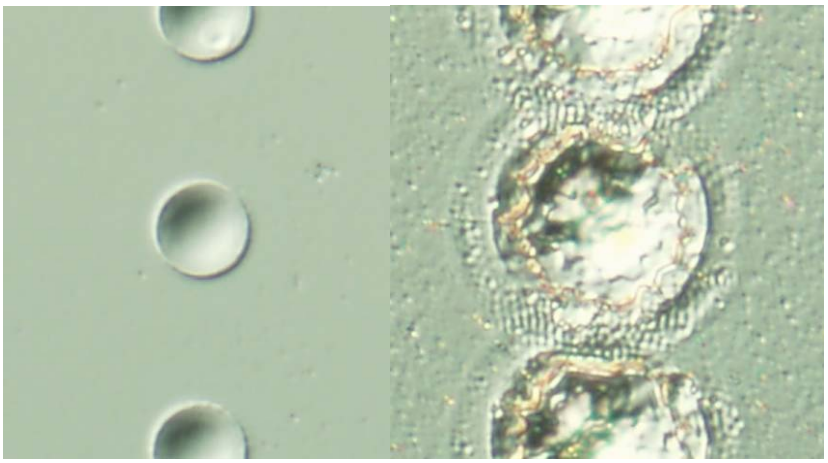

Figure 3.24 Ablation craters in silicon at 0.9 J/cm^2 and 24 J/cm^2.

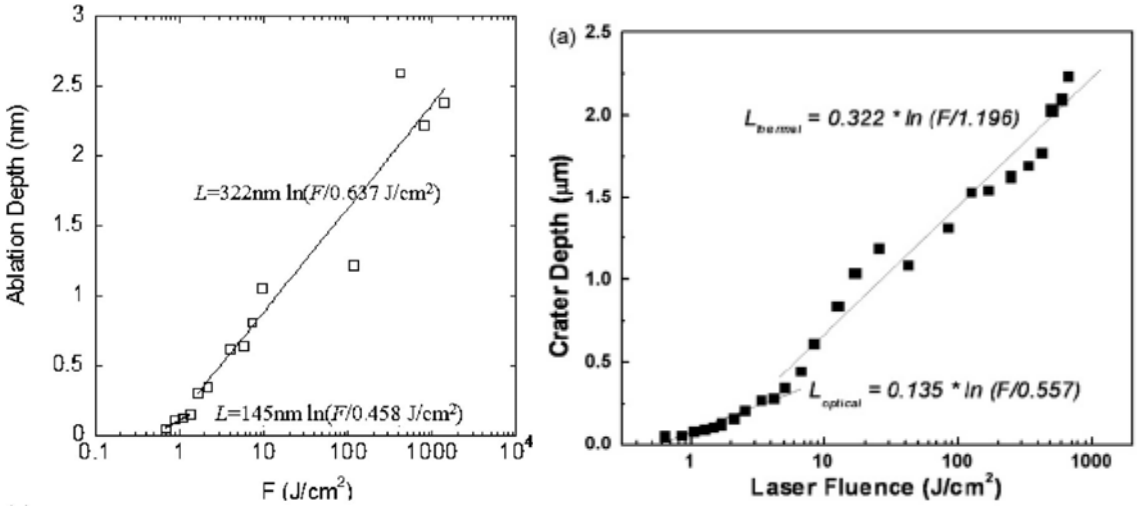

Figure 3.25 Left: Ablation rate scaling in silicon reproduced from Hwang *et al*[172].
Right: reproduced from Lee *et al*[168].

Another interesting and frequently observed feature which occurs when laser processing materials such as silicon is periodic ripples on the laser treated surface. An observation from this study was that the periodic ripples were observed at locations on the target which had been treated by only two pulses. The most apparent example of these ripples observed in these experiments is shown Figure 3.26. The ripples appear in regions which have been illuminated by the overlap of the diffracted light (from the aperture in the beam) from two subsequent pulses. The interpulse time of 4 ms in these experiments suggests that the mechanism that generates these features is quite long lived and that it is unlikely that plasma and optical interference from subsequent pulses play any role in their formation. The period of these ripples is ~760 nm approximately corresponding to the wavelength of the laser. A compelling explanation of the ripples observed in this investigation is the surface scattering and interference model proposed by

Guosheng *et al*[175] in 1982. The hypothesis behind model of Guosheng *et al* is that surface disturbances, in the form of either roughening, temperature or charge distributions, are initiated by the first pulse. These disturbances scatter some of the light from the subsequent pulses along the material surface, creating an interference pattern with the incident light. This interference tends to have a dominant spatial frequency component given by,

$$\Lambda = \lambda / (1 \pm \sin\theta) \tag{3.43}$$

where θ is the angle of incidence of the beam. The modulated irradiance on target gives rise to the periodic ablation ripples. This mechanism can be tested by confirming that the period of the ripples changes with the angle of beam incidence. It is perhaps surprising to see such obvious ripples appear after only two pulses, but further investigation into these structures is not within the current scope of this dissertation.

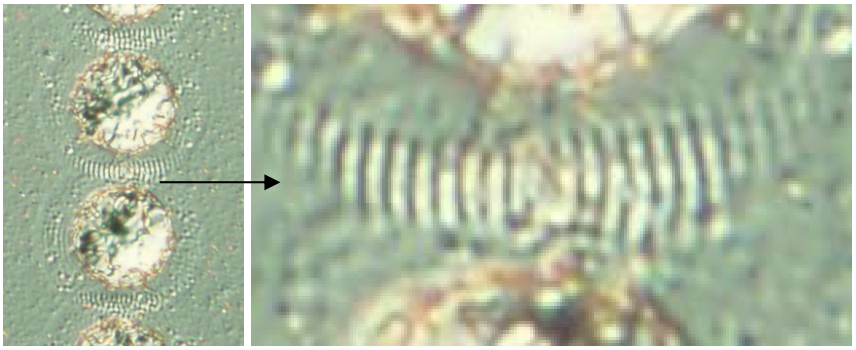

Figure 3.26 Surface ripples observed on regions of the silicon surface which have been irradiated by two pulses

3.4.5 Lithium niobate and lithium tantalate processed with the femtosecond Hurricane system.

Single shot processing of z-cut lithium niobate and lithium tantalate targets was carried out in a similar fashion to the silicon experiments described above, using the same laser and motion control settings. Single shot ablation craters for lithium niobate at various fluences are shown below in Figure 3.27. Optical profilometry was carried out to determined the crater depths and diameters, the results of which are shown in Figure 3.28 and Figure 3.29.

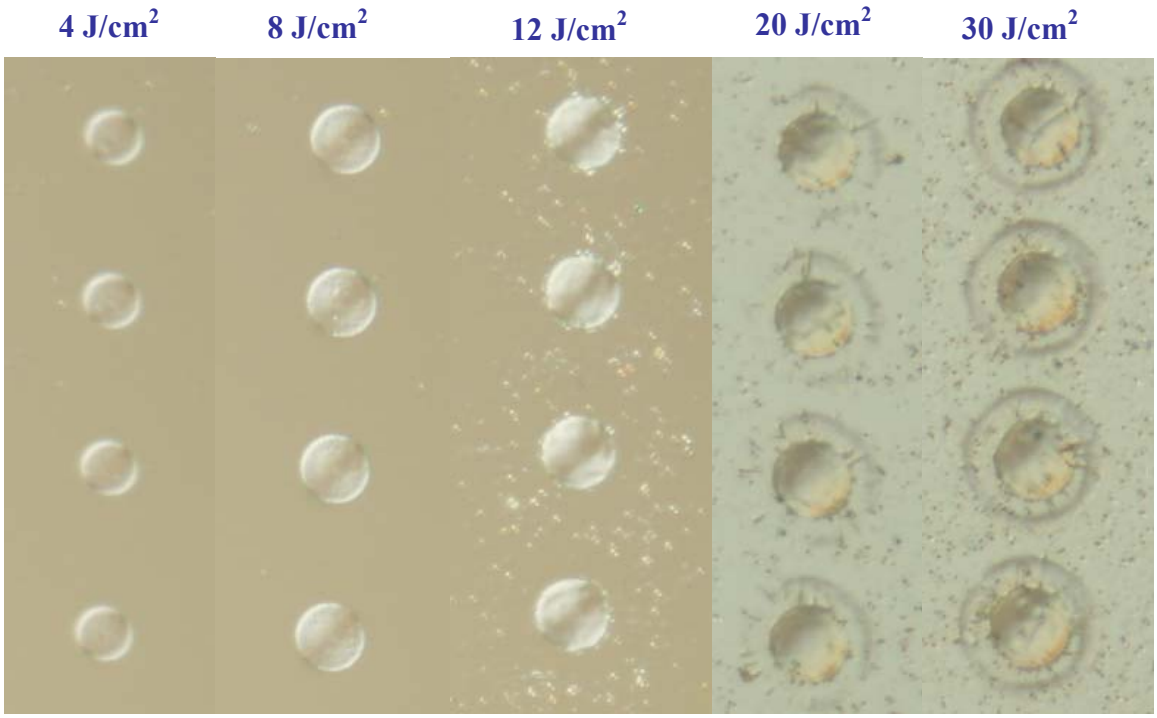

Figure 3.27 Single shot ablation in lithium niobate with fluences ranging from 4-30 J/cm^2

The evolution of the crater diameters for incident pulse energies near threshold are shown in Figure 3.28. From this data the experimental ablation thresholds for lithium niobate and lithium tantalate were found to be 1.46 J/cm^2 and 1.80 J/cm^2 respectively. Experimental ablation thresholds from previous investigations are shown for comparison in Table 3.6

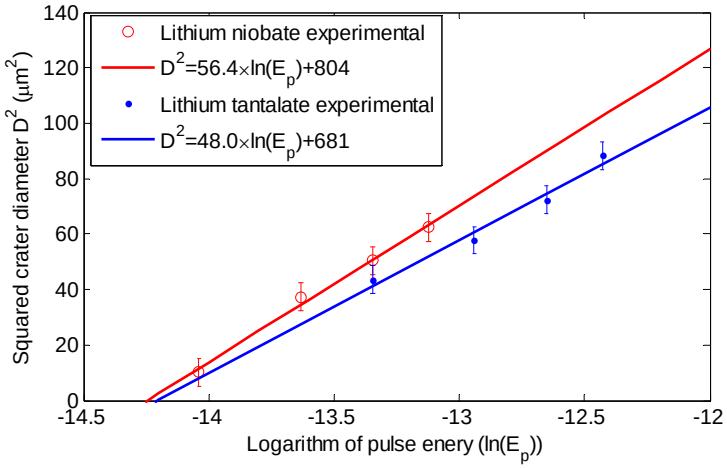

Figure 3.28 Square of the crater diameter in relation to the incident pulse energy for lithium niobate and lithium tantalate.

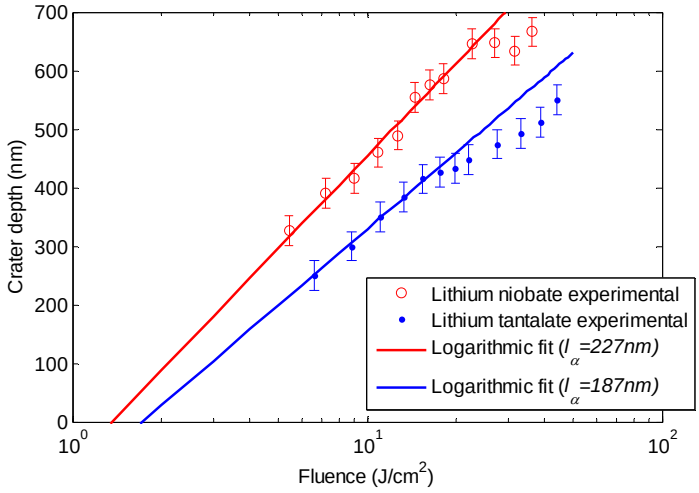

Figure 3.29 Measured crater depths in lithium niobate in relation to the incident irradiance of 85fs pulses from the Hurricane system.

The damage threshold for lithium niobate found in this investigation is markedly lower than that found by Deshpande[150] or Chen[151]. However the good agreement with the results of Zhang[176] for lithium tantalate suggest that the value determined in this investigation is valid. Lithium tantalate generally exhibits a higher optical damage threshold to that of lithium niobate, and as such is often used in preference to lithium niobate when poled materials are to be used for high power applications. With this reasoning, an ablation threshold of less than 1.8 J/cm^2 for lithium niobate is to be expected.

Author	Pulse duration/wavelength	Material	Threshold fluence
Zhang *et al*[176]	80 fs, 800 nm	$LiTaO_3$	1.84 J/cm^2
Deshpande *et al*[150]	300 fs, 800 nm	$LiNbO_3$	2.5 J/cm^2 (1 J/cm^2 multiple shots)
Chen *et al*[151]	80 fs, 800 nm	$LiNbO_3$	2.8 J/cm^2 (0.52 J/cm^2 multiple shots)
Yu *et al*[177]	50 fs, 800nm	$LiNbO_3$	2 J/cm^2 (0.8 J/cm^2 multiple shots)
This dissertation	100 fs, 800 nm	$LiNbO_3$ $LiTaO_3$	1.46 J/cm^2 1.80 J/cm^2

Table 3.6 Experimental ablation thresholds for lithium niobate and lithium tantalate from the literature.

The ablation rate scaling results, determined measuring the crater depth for various incident fluences are shown in above in Figure 3.29. In contrast to silicon, the lithium niobate and lithium

tantalate ablation rate scaling tends to follow a single logarithmic ablation trend over the fluence range investigated. The characteristic lengths for the logarithmic fits to the ablation data are 227 nm for lithium niobate and 187 nm for lithium tantalate. These results suggest that while the damage threshold of lithium tantalate is higher than lithium niobate, as found under many other optical conditions, the absorption mechanisms in lithium tantalate are more efficient than in lithium niobate, resulting in a shorter length scale. There is some evidence in the experimental results, especially for lithium tantalate, that the ablation rate tends to reduce as the fluence is increased beyond 20 J/cm^2. This may indicate the onset of shielding and reflection in the later stages of high energy pulses due to strong ionisation in the early stages of the pulse, or increased absorption in the target due to the nonlinear nature of multi-photon absorption becoming significant. Some investigations in picosecond ablation of dielectrics, such as those of Hermann *et al*[178], have found that a 'strong' ablation regime may be found at even higher fluences >50J/cm^2, but this regime was not investigated here as damage to the focusing objective lenses becomes an issue with ultrashort pulses. The absence of a second ablation regime with an increased ablation rate in the measured fluence range, is not surprising in light of the thermal and conductive properties of lithium niobate and lithium tantalate. The characteristic thermal diffusion length for lithium niobate with a 100 fs pulse is evaluated as,

$$l_{thermal} = 2\sqrt{D\tau} = 2\sqrt{\frac{\kappa}{c_p \rho}\tau} = 2\sqrt{\frac{0.042}{0.64 \times 4.46} 100 \times 10^{-15}} = 0.76nm \qquad (3.44)$$

Due to the low thermal and electrical conductivity of lithium niobate and lithium tantalate compared to the experimentally determined optical penetration length (227nm and 187nm respectively), diffusion of the energy beyond the laser heated volume is perhaps not expected to play a major role in the ablation rate scaling. We do however see a change in the crater morphology and an increase in the debris field around the ablation craters at higher fluences. The onset of a significant debris field occurs within a relatively well defined fluence range between 10-14 J/cm^2, as illustrated in Figure 3.30. The appearance of redeposited particles on the target within may be due to incomplete ionisation within the ablated volume leaving solid crystallites within the ablation plume which are heavy enough to fall back onto the substrate. Alternatively,the particles may be due to thermalisation and condensation within the ablation plume. The presence of thermal processes within the ablated volume is also evidenced by Figure 3.31. Not only is there a obvious debris field around the ablation craters, there is also tendril like

debris 'splattered' outwards from the crater edges. The tendrils like features are most likely due to the expansion of an ablation plume with some amount of molten material.

Figure 3.30 Single shot ablation craters on lithium niobate at fluences of 10 J/cm^2 (left) and 14 J/cm^2 showing the onset of particle ejection.

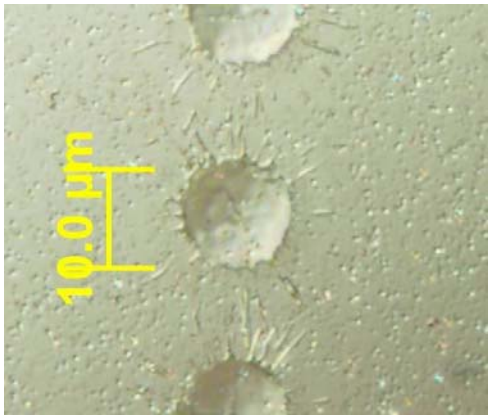

Figure 3.31 Single shot ablation craters on lithium niobate with an incident fluence of 30 J/cm^2.

The conclusions which may be made from these images are that despite thermal processes not significantly contributing to the ablation rate in these crystals, there is strong evidence to suggest that molten material is produced within the ablation plume, and that ultrafast ablation of lithium niobate is not an entirely athermal process, especially at fluences well above threshold.

3.4.6 Summary of findings

The ablation studies presented here have experimentally assessed the single shot ablation thresholds and ablation rates for silicon and lithium niobate for two different laser types; a UV nanosecond laser and a 800 nm ultrafast laser. The ablation thresholds found in this study are comparable with those presented previously in the literature. The ablation rate scaling for both

laser sources in all materials tended to have a logarithmic dependence on the incident fluence, i.e. the depth of the ablation craters depend on the incident fluence according to the `relation $d = l_{\alpha,t} Ln\left(\phi/\phi_{thres}\right)$. The measured ablation thresholds and ablation rate length scales are summarised in Table 3.7. A key result of this study was identifying a double logarithmic trend in the ultrafast ablation rate of silicon which was not present in lithium niobate or lithium tantalate over the same range of fluences. This observation points to a clear difference between the ultrafast ablation mechanisms at different fluences for semi-conductor materials and dielectrics. The relatively high thermal conductivity and electron mobility in semi-conductors leads to an ablation regime at high fluences which has diffusive and thermal characteristics, i.e. the ablation scaling length becomes larger than the optical penetration and there is a distinct change in the crater morphology. In dielectrics where diffusion processes are not a dominant factor in determining the extent of the ablation, a single length scale describes the ablation rate. Despite this, there is still evidence from the crater morphologies of lithium niobate that the material removed from the target can be heated to a molten state during ultrafast ablation.

Material	**Laser source**	**Threshold fluence ϕ_{thres}**	**Ablation scaling length $l_{\alpha,t}$**
Lithium niobate	266 nm , 20 ns pulses	1.9 J/cm^2	542 nm
	800 nm, 100 fs pulses	1.46 J/cm^2	227 nm
Lithium tantalate	800 nm, 100 fs pulses	1.8 J/cm^2	187 nm
Silicon	266 nm , 20 ns pulses	1.15 J/cm^2	1168 nm (ϕ>10 J/cm^2)
	800 nm, 100 fs pulses	0.64 J/cm^2	95 nm (ϕ<5 J/cm^2) 494nm (ϕ>5 J/cm^2

Table 3.7 Summary of experimental ablation thresholds and ablation scaling lengths

3.5 Laser machining of topographical structures for poling

3.5.1 Depth scaling with passes and feed rate

Pulsed laser machining of surface structures by direct writing (translating the sample with respect to a single stationary focused spot or vice versa) requires the laying down of many overlapping pulses from the source laser. The depth of such laser cut features is in practice controlled by the pulse energy, the number of passes made over the same area and the feed rate of the sample with respect to the laser beam. The effect of the laser pulse energy on single shot ablation has been

discussed in detail in the previous section. Ideally the ablation depth will be consistent from pulse to pulse and the depth of features with scale linearly with the number of passes. In reality there may be deviations from these trends as the morphology and chemistry of the laser treated surface changes and the evolving geometry of the machined affects the way the laser light interacts with the target. Changing the velocity of the sample with respect to the pulsed laser beam changes the pulse overlap and the spatial pulse rate on the surface. The shots per linear distance (and thus the deposited laser energy) intuitively scales inversely with the stage velocity;

$$Shots/mm = \frac{shots/s}{mm/s} \tag{3.45}$$

Plotted in the Aerotech control systems' native velocity units of mm/min , the shots/mm being deposited on a surface from a 1kHz pulse train is plotted in relation to the feed rate in Figure 3.32.

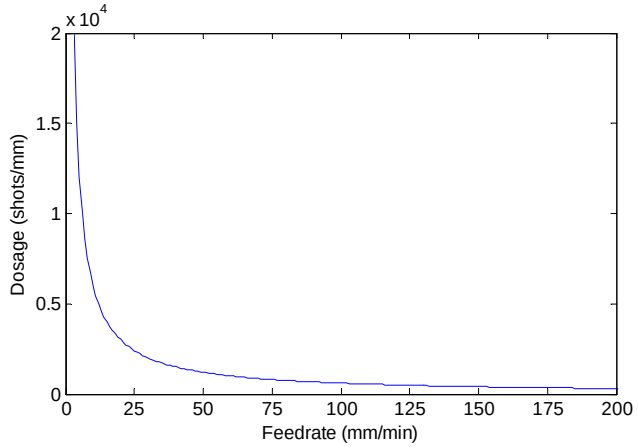

Figure 3.32 Laser shot rate per mm as a function of feedrate in mm/min

For features being machined with a pulse-to-pulse ablation rate which is consistent, the depth of features being machined can be expected to have a feed rate dependence similar to the hyperbolic trend shown in Figure 3.32.

The fabrication of grooves in lithium niobate using the LWE nanosecond and Hurricane femtosecond laser systems were investigated to establish some empirical relations between the laser parameters and the geometry of the features which were to be used for periodic poling.

3.5.2 UV nano-second laser machining

The machining of topographical electrodes into the lithium niobate surface for periodic poling was performed by ablating grooves in the +z face of the crystal, parallel to the y-axis of the crystal. The effect of the translation parameters on the produced features was investigated for the 266 nm quadrupled YAG system using laser parameters where the laser system maintained the

most stable output powers. This was at a repetition rate of 1.75 kHz with 200 mW average power (~115 µJ pulses) of 266 nm light. A 5x objective produced grooves with an opening width of ~15µm. Feed rates of 50, 100, 250, and 200 mm/min were used to machine grooves with 1-5 passes. Figure 3.33 shows a cross-sectional view of grooves machined at 50 mm/min with 1-5 passes shown from left to right. Figure 3.34 shows a similar set of grooves machined with a feed rate of 200 mm/min. The groove depth was measured from the calibrated microscope images and plotted as a function of feed rate and number of passes. It should be noted that laser machining was also used to dice lithium niobate wafers during this project. Using the high power visible output of the Q-201HD laser, reliable laser cleaving could be achieved. This is elaborated upon in appendix A3.

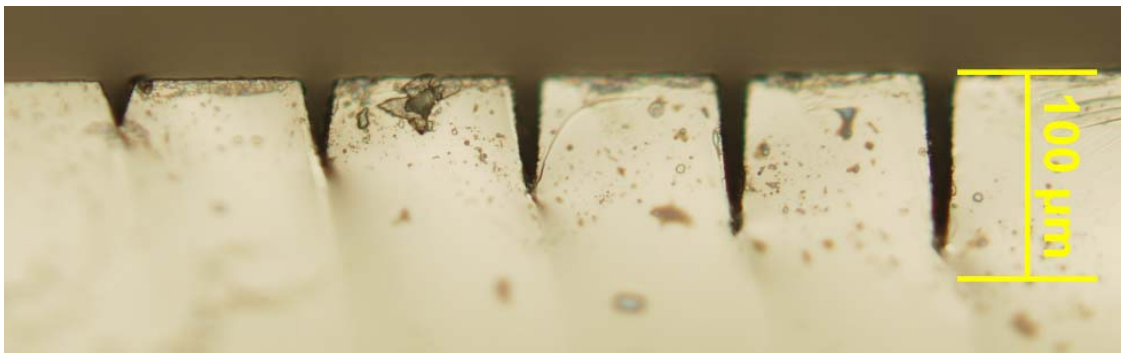

Figure 3.33. Cross-section of UV machined V-grooves, 50mm/min translation speed.

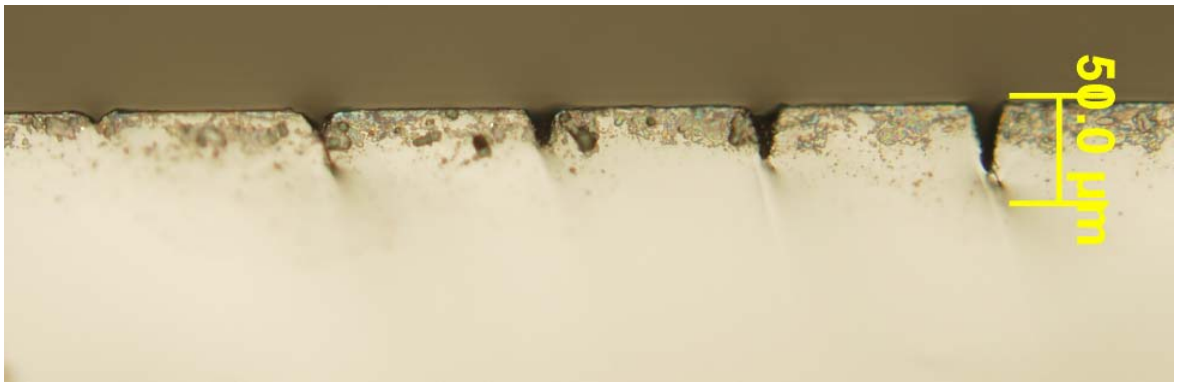

Figure 3.34 Cross-section of UV machined V-grooves 100mm/min translation speed.

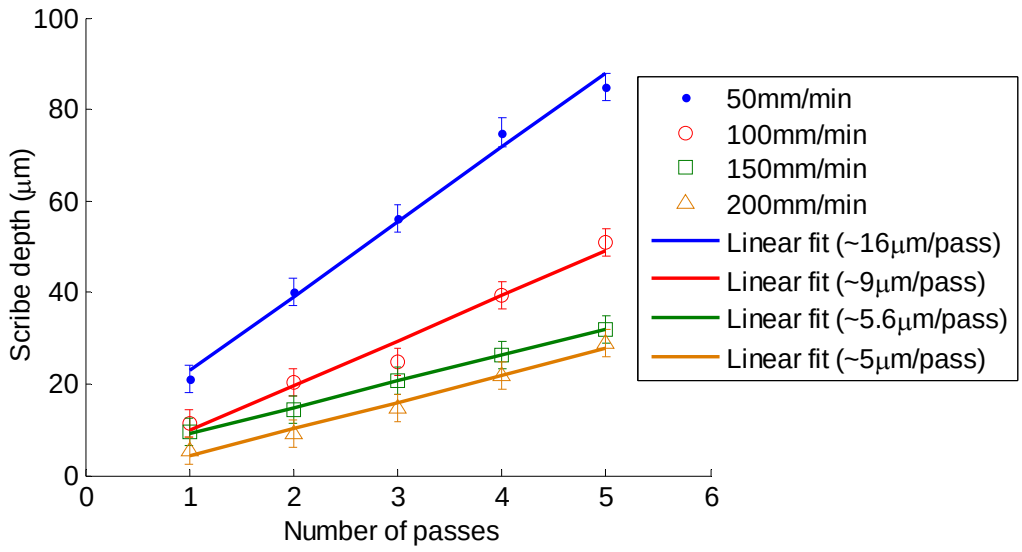

Figure 3.35 Depth of grooves in relation to the number of passes for 50-200mm/min feed rates

Figure 3.35 shows the measured depth of the grooves plotted in relation to the number of passes. A linear increase in depth as the number of passes is increased from 1-5 was observed across the four feed rates. The ablation depth per pass ranged from 16μm/pass for 50 mm/min feed rates to ~6μm/pass for 200 mm/min. It is instructive to re-plot the data as depths in relation to feed rate so comparisons to Eq (3.45) and Figure 3.32 can be made. This is shown in Figure 3.36. An empirical relationship between the depths, number of passes and feed rate can be written as,

$$d = nFRP(\phi)v^{\gamma} \tag{3.46}$$

where n is the number of passes, $FRP(\phi)$ is the feed rate scaling parameter (informal units of $\mu m.mm/min$) which depends on the incident fluence ϕ, and v is the feed rate. Ideally $FRP(\phi)$ will be constant for a particular pulse energy and $\gamma = -1$ for a consistent ablation rate per pulse. In practice there are deviations from this trend as the ablation conditions at the surface change. The conditions which undergo the least amount of surface processing are single pass scribes, and the fitting parameter was chosen according to experimental data for these grooves with $\gamma = -1$. Plotted in Figure 3.36 are the depths of the scribes in relation feed rate along with the fittings of Eq (3.46) with variable values of γ. The value of γ which corresponds to the best fit of Eq (3.46) progressively departs from its ideal value of $\gamma = -1$ as the number of passes increases. This indicates that the ablation becomes less efficient as the laser dosage on target and the depth

of the groove increases. The recorded data can still be used as a predictive indication as to the depth of features being produced with a particular set of laser parameters.

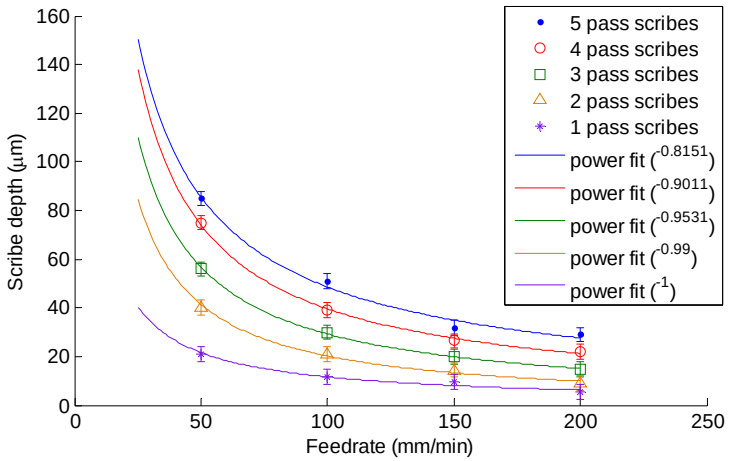

Figure 3.36 Depth of grooves in relation to feedrate with fitting based on Eq (3.46) for the single pass scribe depths. FRP=1100 µm.mm/min.

3.5.3 800nm ultrafast laser machining

Laser machining of lithium niobate with the femto-second Hurricane system was carried out in a similar fashion to the 266 nm Nd:YAG machining, with a few changes in the setup. A 10x objective lens was used to focus the pulses, and due to the lower pulse repetition rate and smaller spot size of the Hurricane system compared to the YAG system, feed rates of 25, 50, 75 and 100mm/min were used so that reasonable pulse overlap was maintained. Three incident pulse fluences of 3.14, 6.2 and 9.5 J/cm^2 were investigated for grooves fabricated with 1-5 passes. Figure 3.37 and Figure 3.38 show the cross-sections of grooves machined with 3.14 J/cm^2 pulses at 25mm/min and 100mm/min feed rates respectively.

Figure 3.37 Laser features machined in lithium niobate with 1-5 passes, 1µJ pulses at 1kHz, with a 25mm/min feedrate.

Figure 3.38 Laser features machined in lithium niobate with 1-5 passes, 1µJ pulses at 1kHz, with a 100mm/min feedrate.

The plots of groove depths in relation to the number of passes are shown in Figure 3.39. There was generally a linear relationship between the number of passes and the depths of the grooves, however a saturation of the groove depth at ~20 µm was seen for the higher number of passes at 9.5 J/cm^2. This saturation in the scribe depth is when the depth to spot-size aspect ratio of the grooves begins to exceed 2:1. At large aspect ratios a significant amount of the incident radiation is scattered off the roughened side walls, inhibiting the ablation efficiency. However, a decrease in the expected ablation efficiency was also observed for the lower incident fluence of 3.14J/cm^2 where the deepest groove was measured as ~12 µm for 5 passes at 25 mm/min. This points to a decrease in the ablation efficiency which depends on the amount of laser treatment the surface has received. The most likely cause of this is an increasing surface roughness as the laser dosage is increasing, scattering the incident laser light and reducing the ablation efficiency. The plots of groove depths in relation to feed rate are shown in Figure 3.40. The fittings for the scribe depths shown on the plots have the form $d = nFRP(\phi)v^{-1}$. The value for feed-rate scaling parameter for the three pulse fluences from the fittings shown above was FRP=180 for 9.5 J/cm^2, FRP=150 for 6.2 J/cm^2 and FRP=90 for 3.14 J/cm^2. The FRP in relation to the incident pulse fluence is plotted in Figure 3.41. A good logarithmic relationship between the three values of FRP and the incident fluences from the experimental findings can be seen. From this logarithmic relationship the threshold for laser machining (where the FRP goes to zero) is predicted to be 1.16 J/cm^2 which is in fair agreement with the single shot ablation threshold of 1.46 J/cm^2, especially since multi-pulse ablation is expected to exhibit lower thresholds due to incubation. The predictive capability of the fittings in Figure 3.40 can be seen to become poor for higher number of passes at low feed-rates where the laser dosage is relatively high.

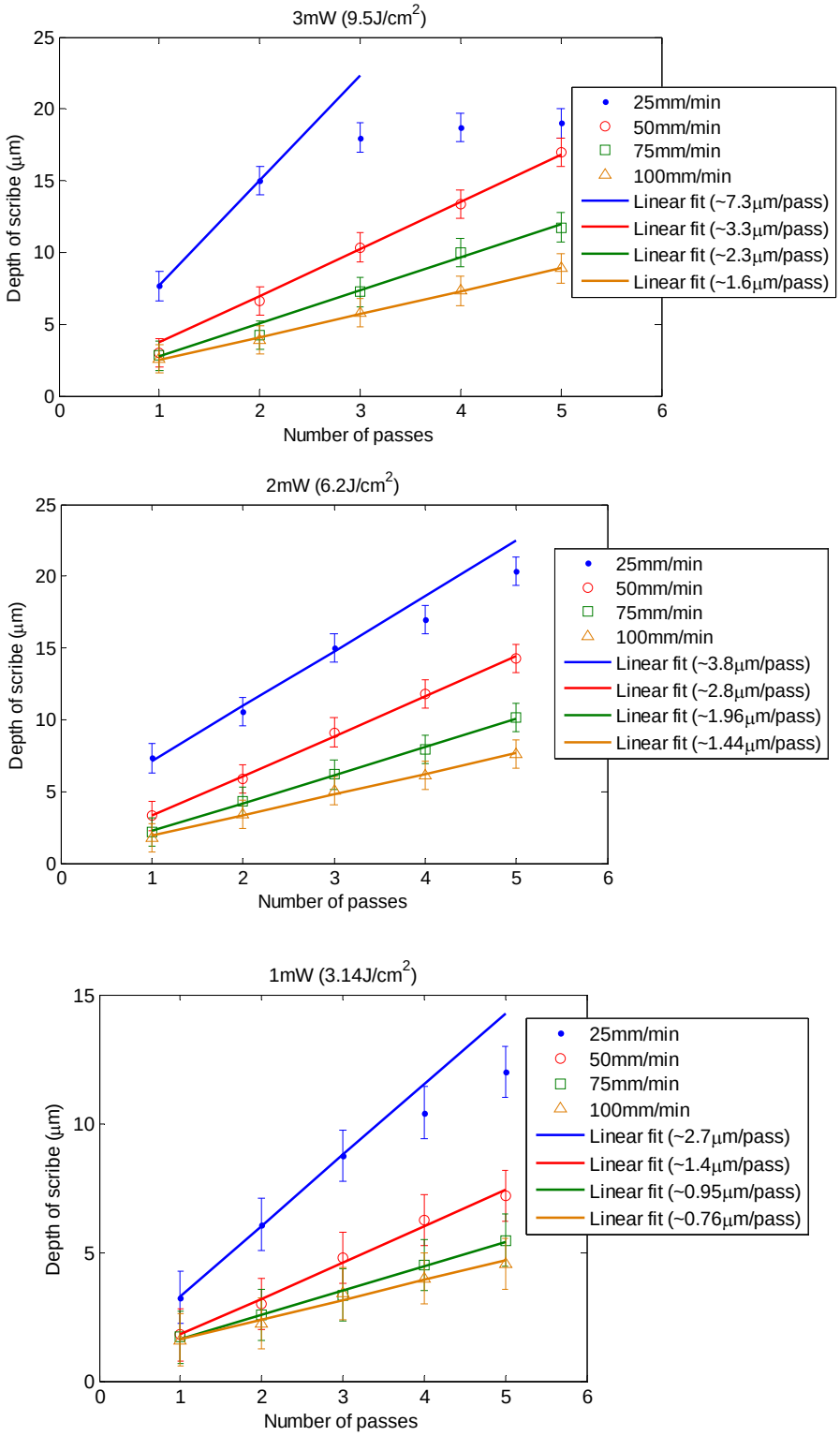

Figure 3.39 Scribe depths plotted in relation to the number of passes for feedrates of 25-100mm/min. Plots for fluences of 3.14, 6.2 and 9.5 J/cm^2 are shown.

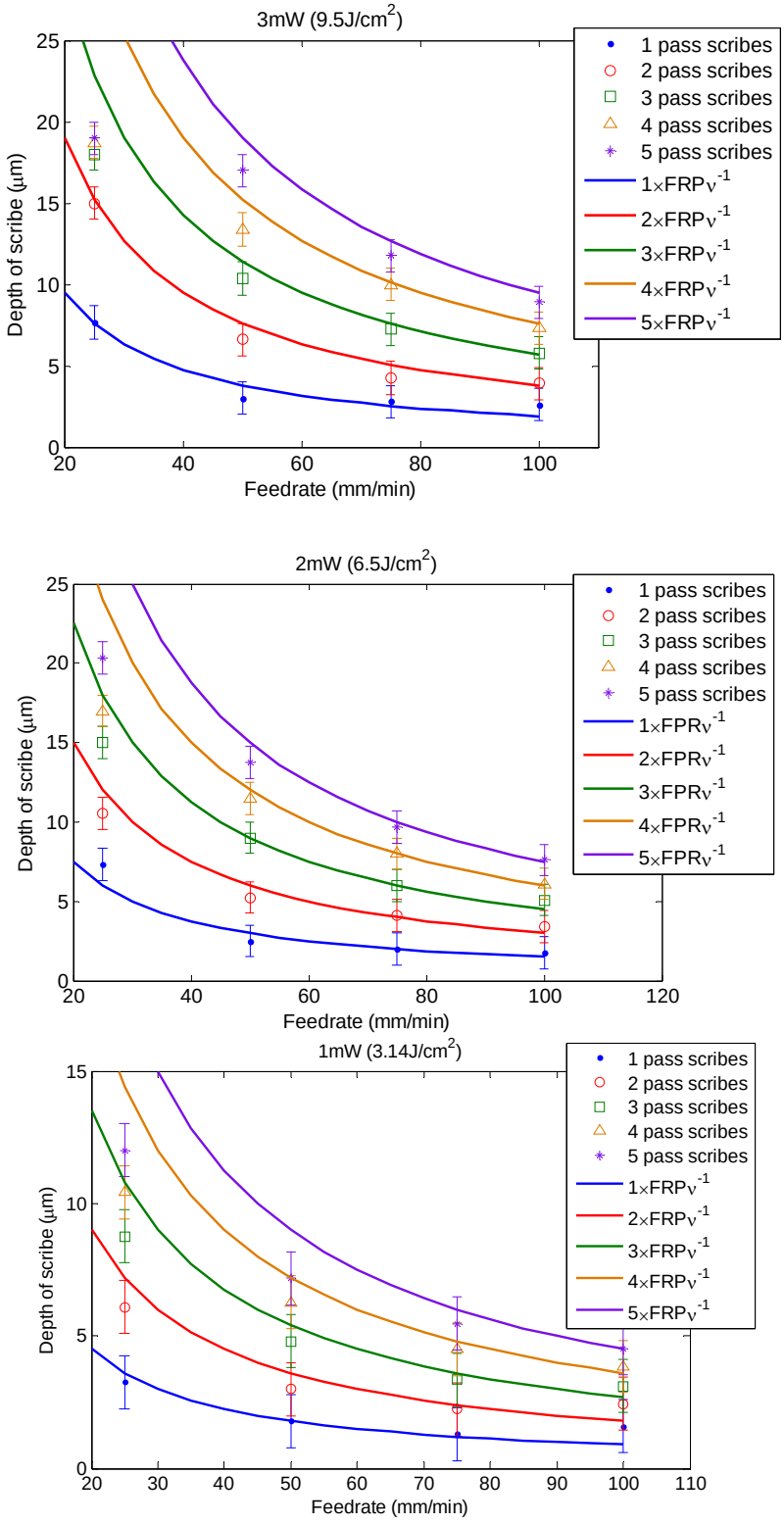

Figure 3.40 Scribe depths plotted in relation to feedrate for 1-5 passes. Plots for fluences of 3.14, 6.2 and 9.5 J/cm^2 are shown.

The empirical data in Figure 3.40 can still be used as a predictive guide for laser machining lithium niobate with the Hurricane laser system. As will be explored in the next chapter, the geometry of grooves in the surface of lithium niobate, most importantly the depth and aspect ratio, play an important role in the formation of domains when poling.

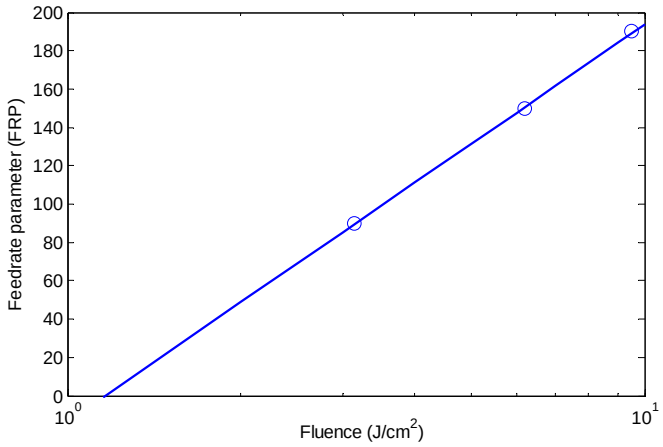

Figure 3.41 Feed rate parameter (FRP) plotted in relation to the incident pulse fluence.

3.5.4 Summary of findings

Machining of grooves in lithium niobate using a UV nanosecond laser system and a 800 nm ultrafast laser system has been experimentally assessed. Control of the depth of laser machined grooves has been demonstrated utilising the laser power, number of passes, and machine feed rate as the control parameters. An empirical relation that relates the depth of laser machined grooves to these parameters is $d = nFRP(\phi)v^{\gamma}$ where n is the number of passes, FRP is the fluence dependant fitting parameter which gives an indication of the ablation rate, v is the feed rate and γ indicates the effect the feed rate, with the ideal case of γ=-1 for a consistent pulse to pulse ablation depth. Some experimental values of the FRP fitting parameter are summarised in Table 3.8. There was no obvious difference between the quality of grooves machined with the nanosecond UV laser and the 800 nm ultrafast laser, although the superior beam quality and controllability of the ultrafast system makes it the laser system of choice for machining of fine features. Choosing suitable laser machining parameters to optimise the speed of machining and the quality of features is still an important consideration. Using excessive fluences can degrade the feature quality, especially in the case of the ultrafast laser system. Figure 3.42 shows two 20μm gratings machined in lithium niobate with fluences of 6.5 J/cm^2 and 12 J/cm^2. The higher

fluence results in a major degradation of the feature quality with severe chipping of the groove edges and a large amount of debris.

Laser	Fluence	FRP
LWE, λ=266 nm, t_p=20 ns, rep. rate=1.75kHz	~150 J/cm^2	1100 µm.mm/min.
Hurricane, λ=800 nm, t_p=100 fs, rep. rate=1 kHz	3.14 J/cm^2 6.5 J/cm^2 9.5 J/cm^2	90 µm.mm/min. 150 µm.mm/min. 180 µm.mm/min.

Table 3.8 Summary of experimental fitting parameters for laser machining grooves in lithium niobate.

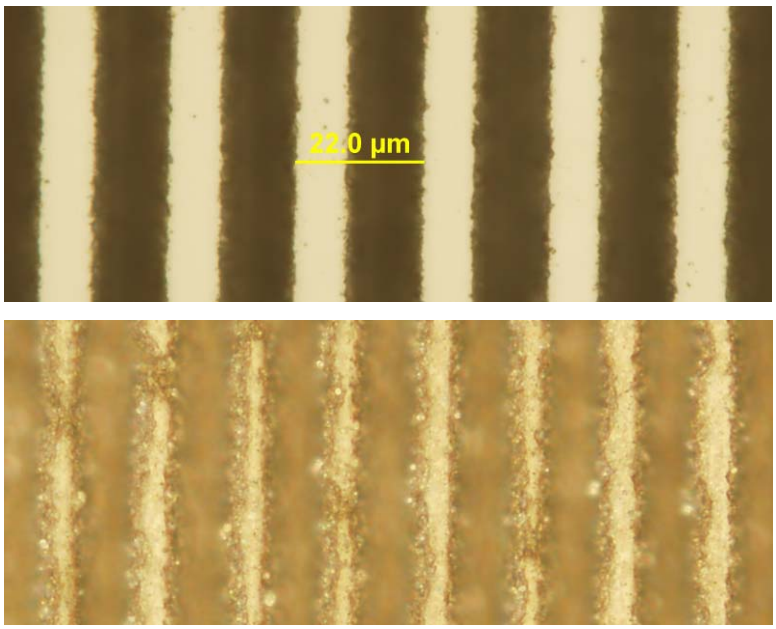

Figure 3.42 20µm period gratings machined with the 800nm ultrafast system at different incident fluences. Top: 6.5 J/cm, bottom: 12 J/cm^2

Chapter 4. Electric field poling of laser patterned lithium niobate

"The most exciting phrase to hear in science,
is not 'Eureka!' but 'That's funny...' "
- Isaac Asimov
"Research is what I'm doing
when I don't know what I'm doing."
-Wernher von Braun

4.1 Introduction

Domain engineering in ferroelectrics is an important technology in the fields of nonlinear optics and data storage. Ferroelectrics materials have various applications in electronics as miniaturised, asymmetric or reversible capacitors, the likes of which are key elements in non-volatile ferroelectric memory. As pointed out in Chapter 1, ferroelectrics crystals also have other useful properties such as good piezoelectric and electro-optic responses. There are several ferroelectric materials within the crystal families of titanates, tantalates and niobates which also have very good optical properties which can be further exploited by domain engineering the material. The domain engineering of particular interest in this dissertation is external field poling of lithium niobate crystals for quasi-phase-matching of nonlinear optical interactions. A review the development of such poling techniques for lithium niobate and lithium tantalate was made in Chapter 1. The mature and commercially viable technique for poling lithium niobate uses lithographically patterned planar conductive/insulating surface electrodes to define the regions of the design domain reversal pattern. The poling is then performed in a liquid electrolyte to ensure uniform electrical contact with the crystal surfaces and reduce the probability of dielectric breakdown and arcing due to the high poling fields. There have been many investigations into alternative domain patterning techniques for use with external field poling. These include thermal domain reversal[34], light induced domain reversal[44] chemical modification methods such as patterned proton exchange[36]. In 1998 Reich *et al*[49] demonstrated that topographical electrode geometries, such as those produced by laser machining, are a promising alternative for poling of ferroelectrics. The local reduction in the wafer thickness in the neighbourhood of laser machined features, as well as the inhomogeneous electric field introduced by the surface geometry, results

in suitable electric fields for selective domain inversion. The electric field distributions produced by topographical electrodes can be quite distinct from the planar surface electrodes. Planar electrode patterning with conductive and/or insulating materials selectively exposes or shields the crystal surface from the applied external field. The electric field distributions produced by topographical surfaces are purely a result of the geometry of the submerged surfaces in the liquid electrolyte during poling. Topographically patterning the surface with laser machining alleviates the requirement for the deposition of insulating and/or conducting layers and the lithographic patterning that accompanies this technique. As a result topographical electrodes are a promising alternative for fast prototyping or fabrication of small quantities of domain engineered crystals. The goal of this chapter is too explore the potential and limitations of topographical electrode patterning for field poling lithium niobate.

The arrangement of this chapter is as follows; section 4.2 reviews some of the basic characteristics of crystalline ferroelectrics and the conditions which give rise to stochastic and controlled ferroelectric domain reversal. Section 4.3 looks at the electrostatics of various electrode patterning techniques for electric field poling. Numerical simulations of Laplace's equation by the finite element method (FEM) have been used to gain insight into the influence that factors such as material properties and geometry have on the potential and electric field distributions in the crystal when field poling. The results presented here are complimentary to the quasi-analytical model developed by Miller[179] during his doctoral work, with the advantage of being able to analyse arbitrary geometries and layers by utilising the FEM. Section 4.4 deals with the field poling experiments carried out during this project. The domain kinetics of topographical electrodes have been investigated, along with an appraisal of the domain quality and resolution of patterning that is feasible using this poling method. A summary of the findings presented in this chapter is given in Section 4.5

4.2 Ferroelectric domain reversal

4.2.1 Ferroelectric and pyroelectric properties

Just as ferromagnetic materials exhibit spontaneous magnetic poles due to prevailing alignment of magnetic domains, ferroelectric materials exhibit spontaneous electrical polarisation due to permanent internal dipoles aligned in crystal 'domains'. These dipoles arise from a regular distribution of ions with different valences, through the material. When these dipoles are all co-

aligned, for example within crystals such lithium niobate and lithium tantalate, a permanent and directional polarisation in the crystal ferroelectric and pyroelectric orientation of the crystal. In lithium niobate and tantalate the spontaneous polarisation is parallel to the z (or c) axis. The ferroelectric phase in lithium niobate and tantalate is very stable under ordinary conditions, however the crystal structure moves towards the paraelectric phase (no net dipoles) as the crystal is heated. The Curie temperature, where the transition to the paraelectric phase is complete, is ~1150˚C in lithium niobate and ~1220˚C in lithium tantalate, but varies with stoichiometry and doping. The arrangement of lithium and niobium ions within the lithium niobate crystal matrix is illustrated in
Figure 4.1.

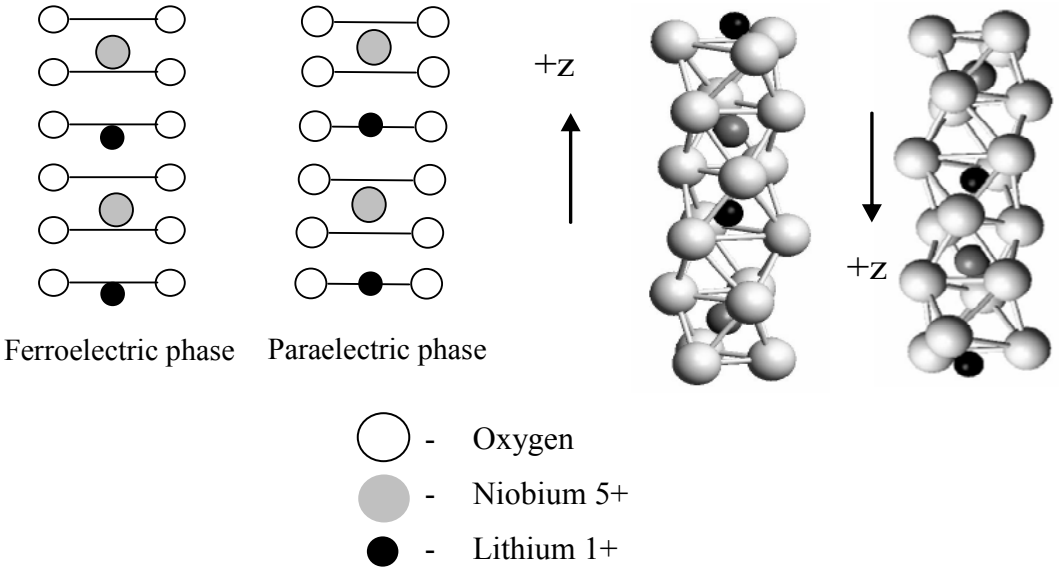

Figure 4.1 Arrangement of lithium and niobium ions which gives rise to the ferroelectric properties of lithium niobate.

As discussed in chapter 1, the move towards the paraelectric phase with heating changes the magnitude of the spontaneous polarisation in the crystal and results in charging of the crystal surfaces. This makes lithium niobate a strongly pyroelectric material. The pyroelectric effect is a convenient method for determining the orientation of the lithium niobate z-axis. Upon heating, the +z face of the crystal becomes negatively charged as it accumulates electrons in response to the relaxation of the spontaneous polarisation. The pyroelectric properties of lithium niobate can also be a problem. Charging of the crystal surface can result in defects that interfere with electric field poling. Lithium niobate is also a piezoelectric material, and the charging due to pyroelectric

effect results in straining of the crystal structure. Rapid thermal cycling can even be catastrophic and cause wafers to crack and even shatter. The spontaneous polarisation in ferroelectrics crystals is not only temperature dependent but can also be influenced by external electric fields, which is the key attribute exploited in electric field poling.

4.2.2 Electric field poling

The application of an external electric field to a ferroelectric can result in reversal of the spontaneous polarisation as it aligns with the external field. This reversal requires the applied potential to exceed the 'coercive field', E_c, of the material. This reversible behaviour of the spontaneous polarisation can be illustrated as an electric field/spontaneous polarisation hysteresis as shown in Figure 4.2.

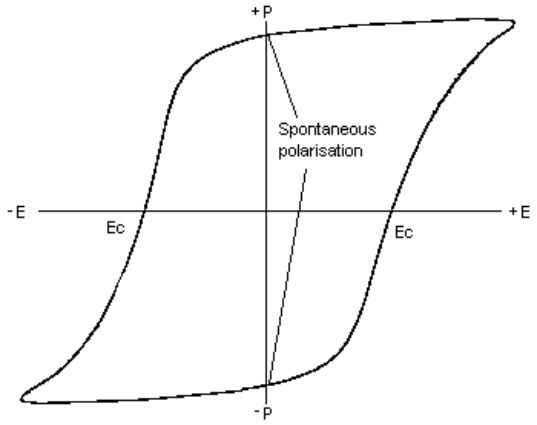

Figure 4.2 Hysteresis curve of a ferroelectric's response to an external field. The applied potential where the changing of the spontaneous polarization occurs is the coercive field, E_c.

The reversal of the spontaneous polarisation by application of an external electric field is termed *poling*. One of the challenges when poling crystalline ferroelectric materials such as lithium niobate is that the coercive fields are generally quite large (~1-25kV/mm). Electrical breakdown between closely spaced electrodes, and dielectric breakdown of the materials, are problems at these potentials. Poling with uniform contact through a liquid electrolyte, a technique pioneered by authors such as Webjorn *et al*[23] and Myers *et al*[24], has enabled reliable poling of large areas, (3' (72 mm) wafers are common), with thicknesses of up to 3 mm for some materials. In order to produce the desired domain pattern, electrode patterning of the crystal surface is required to produce the isotopic electric field for selective domain inversion. Electrode patterning techniques are discussed further in section 4.3. The poling cell is placed in a circuit with a programmable,

pulsed high voltage supply and circuit monitors. An example of electrode patterning and typical electrical circuit for field poling is reproduced from Myers *et al*[24] in Figure 4.3.

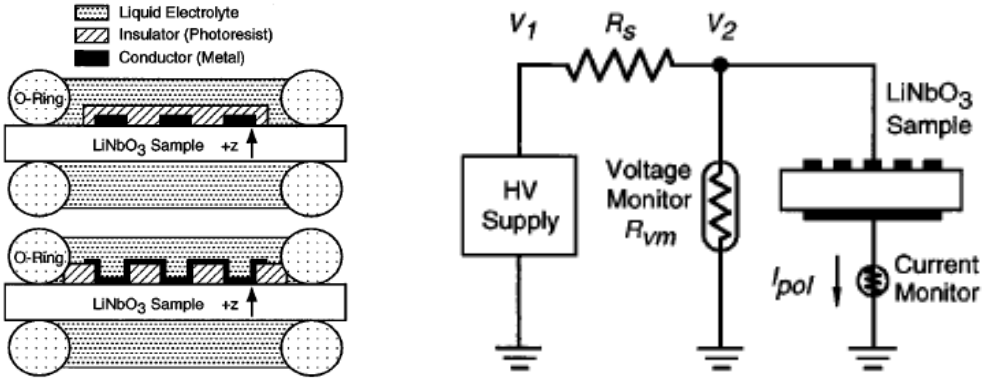

Figure 4.3 Electrode patterning (left) and typical circuit configuration (right) for electric field poling of materials such as lithium niobate. (Reproduced from Myers *et al*[24])

Poling is accompanied by a charge exchange through the ferroelectric which manifests as measurable current flow through the material. The observed poling current and charge exchange, Q, is related to the reversed area, A, and the spontaneous polarization, P_s as,

$$Q = \int_t I.dt = 2AP_s \qquad (4.1)$$

For lithium niobate the value of the spontaneous polarization is in the range 70-80μC/cm^2 range (72 μC/cm^2 is a common value given for congruent composition lithium niobate). In many poling arrangements the amount of charge exchange can be used to monitor the extent of poling. Recently authors such as Grilli *et al*[180] have also use in-situ visualisation of domain formation within the poling cell to asses poling performance.

Domain inversion in crystals such as lithium niobate and lithium tantalate will generally follow the crystallographic structure. In lithium niobate the domains form with hexagonal symmetry. The linear alignment (flat edge) of the hexagonal domain shape in lithium niobate is parallel to the y-axis of the crystal. An example of domains viewed on the –z face of lithium niobate which has been patterned on the +z face, is shown in Figure 4.4. When poling to produce QPM gratings with straight domains, alignment of the electrode pattern to the y-axis of the crystal is important. More exotic domain shapes and patterning have been demonstrated by authors such as Shur *et al*[181,182] and Kasimov *et a*l[183,184] by careful control of electrode patterning and also direct e-beam writing of domains. Lithium tantalate shows a slightly different domain

symmetry typified by a triangular shape. An example of domains viewed from the z face of lithium tantalate from the work of Meyn *et al*[185] is shown in Figure 4.5.

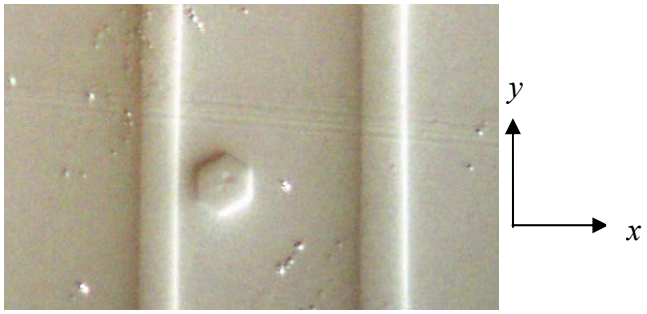

Figure 4.4 Domains in lithium niobate showing hexagonal symmetry and straight domain wall formation parallel to the y-axis of the crystal.

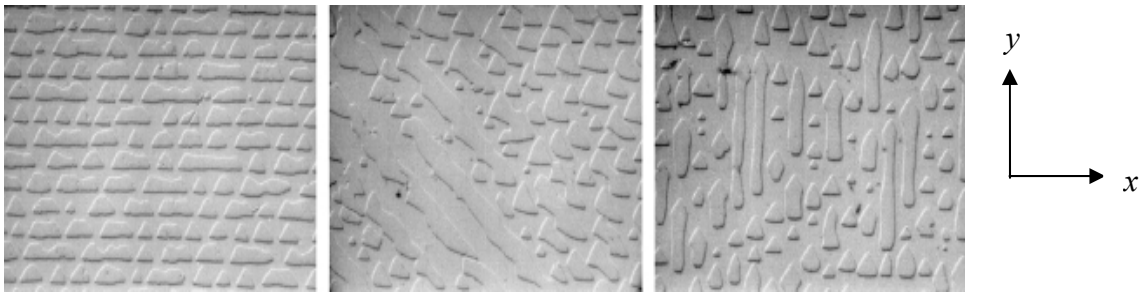

Figure 4.5 Domains in lithium tantalate showing triangular symmetry.

4.2.3 Domain kinetics

An important aspect of producing quality domain structures is understanding the evolution of the domains during the application of the poling field. This is commonly referred to as domain kinetics. Many of the concepts relevant to the domain kinetics of lithium niobate and lithium tantalate have been looked at by Vladimir Shur and colleagues at Stanford and Ural State universities (see refs [186,187,188,189,190,191,192,193,182,181]). One of the characteristic parameters of the domain inversion process is the transverse velocity of the domains walls as they propagate away from the electrode area. The results from Miller's study[179] for poling with planar patterned electrodes are shown in Figure 4.6. Domain wall velocities during switching generally show an exponential dependence on the magnitude of the poling field, though there may be more than one poling regime for different field levels. Miller's data identified two poling regimes, a slow inversion regime close to the coercive field and a faster regime for fields in excess of the coercive field.

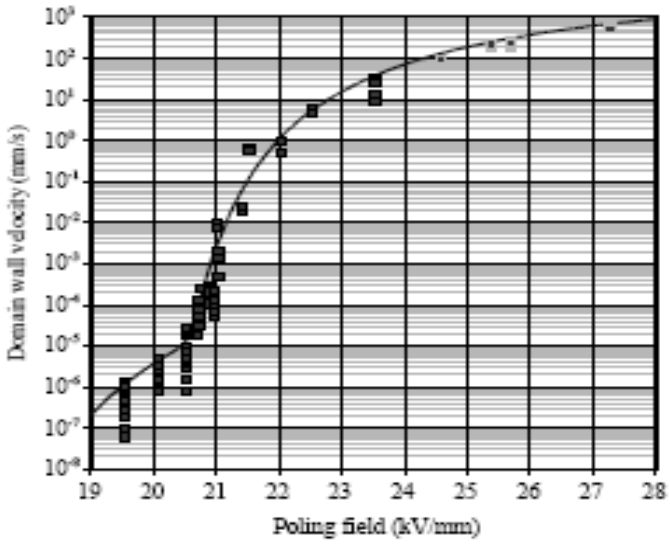

Figure 4.6 Domain wall velocity as a function of the applied poling field for planar electrodes (Miller 1998[179])

The domain wall velocity dependence on electric field can be fitted to a functional form,

$$v(E) = \Phi(E - E_1)v_1 \exp\left(-\frac{\delta_1 E_1}{E - E_1}\right) + \Phi(E - E_2)v_2 \exp\left(-\frac{\delta_2 E_2}{E - E_2}\right) \qquad (4.2)$$

where Φ is the Heaviside function which signifies the onset of the particular domain inversion regime. The fitting parameters for Eq. (4.2) for Miller's data are given below. Control of the effective poling field for planar electrode geometries is via the programmed voltage waveform of the high voltage supply. For topographical electrodes the geometry of the crystal surface provides another degree of freedom which can influence the domain kinetics. This will be explored further in the results presented in section 4.4. The follow section now concentrates on electrode patterning techniques used for electric field poling and the electrostatics which give rise to the isotropic electric fields necessary for control domain inversion.

E>20.4 kV	E<20.4 kV
E_1=19.4 kv	E_2=15.0 kV
v_1=16.3 m/sec	v_2=362 μm/sec
δ_1=1.29	δ_2=3.38

Table 4.1 Fitting parameters for Miller's data for the domain wall velocity/poling field relationship shown in Eq. (4.2)

4.3 Electrostatics associated with domain inversion

4.3.1 Electrostatics of planar surface electrodes

The most common and commercially implemented electrode geometries for poling lithium niobate are planar surface electrodes, as shown in Figure 4.7. They chiefly consist of openings in a resist layer, and are sometimes accompanied by metal layers either in the resist openings or completely over-coated by the resist layer.

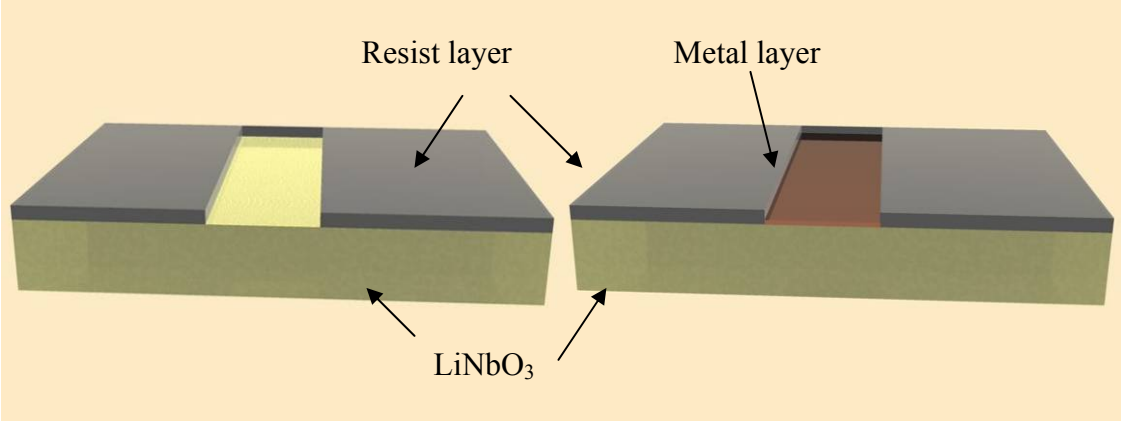

Figure 4.7 Geometry of planar surface electrodes for poling. Left: open slots in a resist layers, right: metal layer deposited onto the surface.

A semi-analytical treatment of the electrostatics and domain kinetics of poling with planar electrode structures was developed by Miller during his doctoral work[179]. The geometry for Miller's model was based on over-coated metal electrodes as reproduced in Figure 4.8.

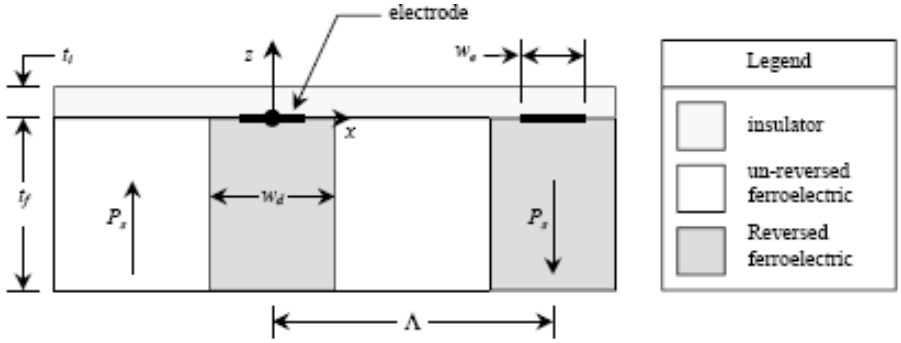

Figure 4.8 Geometry of overcoated conducting electrodes as addressed in the modelling of Miller.

One of the key points of interest is the electric field distribution, in particular the vertical component of the electric field parallel to the ferroelectric axis in z-cut crystal. It is the vertical component of the electric field which is attributed to initiating domain inversions. A plot of the distribution of the vertical component of the electric field at the ferroelectric/insulator interface

from Miller's model is reproduced in Figure 4.9. The large electric fields which occur at the electrode edges are referred to as fringing fields. The popular understanding of domain formation resulting from such an electric field distribution is illustrated in Figure 4.10. The fringing fields at the electrode edges are responsible for domain nucleation. The domains propagate through the crystal, coalesce under the electrodes and then propagate laterally. In practice the duration of the poling field and the effectiveness of the insulating layer limit the lateral propagation.

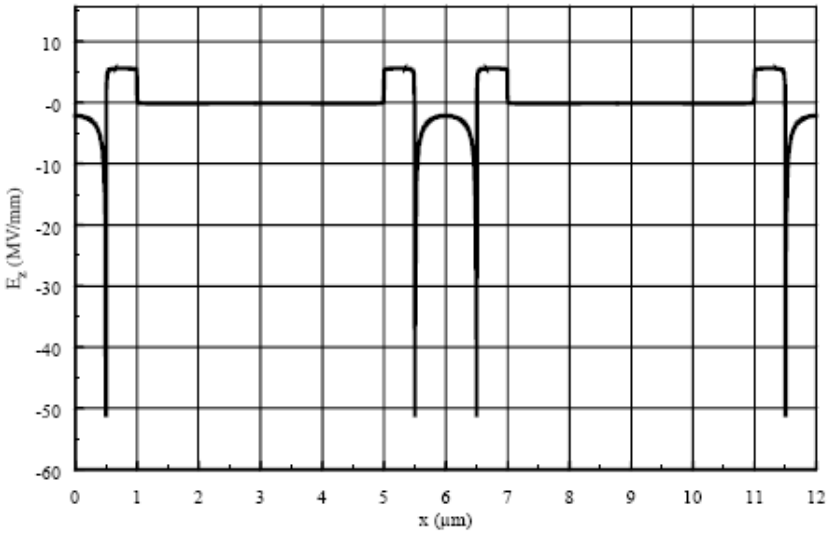

Figure 4.9 Vertical component of the electric field produced at the crystal surface from over-coated electrodes (From Miller, 1998).

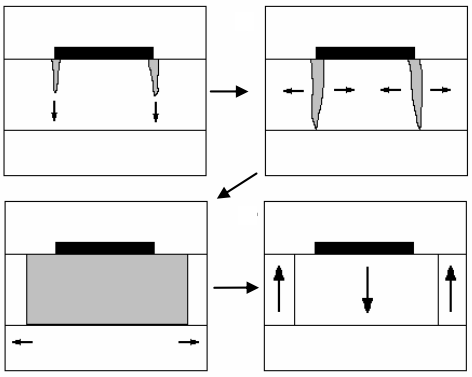

Figure 4.10 Illustration of domain formation from planar electrodes. Domains nucleate at the electrode edged due to fringing fields, propagate through the crystal, coalesce under the electrode and propagate laterally.

In the work presented here the electrostatics were dealt with numerically using the finite element method (FEM), facilitated by the Matlab PDE (partial differential equation) toolbox. Essentially

the electrostatics being investigated can be treated as a boundary value problem where the solutions for the potential distribution, V, found from elliptical equations with a general form,

$$-\nabla.(\varepsilon\nabla V) = \rho \tag{4.3}$$

where ε is the DC dielectric constant and ρ is the space charge density which may be constant or scalar functions related to the material properties. One of the benefits of using the FEM approach is that introducing regions of various material properties in arbitrary geometries is straight forward. With no free charges in the medium, as for a dielectric, Eq. (4.3) reduces to Laplace's equation,

$$-\nabla.(\vec{\varepsilon}\ \nabla V) = 0 \tag{4.4}$$

Alternatively for a good conductor we have Poisson's equation,

$$-\nabla^2 V = \frac{\rho}{\varepsilon_0} \tag{4.5}$$

The electric field is given by the gradient of the potential,

$$\vec{E} = -\nabla V \tag{4.6}$$

In order to make analogies with the work of Miller, simulations of various planar electrode arrangements were carried out. Figure 4.11 shows the geometry and boundary conditions for an idealistic case of a perfect insulator and perfect conductive electrode. The insulator perfectly shields the crystal surface and the conductor conveys the applied potential, V_0, to the crystal surface. The rear surface is grounded, and we have the Dirichlet conditions as shown. The edges of the slab are assumed to be far enough from the electrode so that the electric field is uniform, i.e. the potential drop is constant near the edges so we have the natural Neumann boundary condition, $\nabla V = 0$.

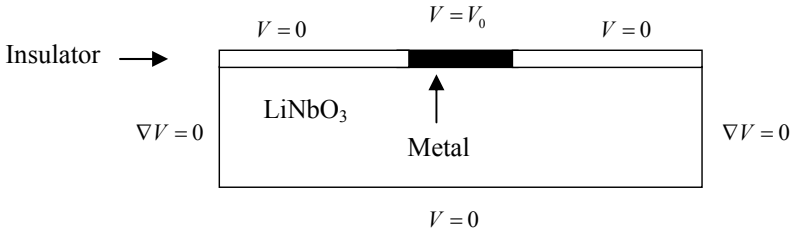

Figure 4.11 Boundary conditions for a conductive electrode with a perfect insulator.

This geometry was simulated for a thickness of 0.5 units, analogous to the 0.5 mm wafer thickness commonly used, and 3 units wide. V_0 was set to 10 kV. The solution for the potential distribution from such an electrode is shown in Figure 4.12. The corresponding electric field distribution in the crystal can be visualised as vector arrows, or as field strength colour plots.

The vector field plot near the electrode, along with the equi-potential contours, is shown in Figure 4.13. The high electric fields produced at the electrode edges are apparent, in analogy with the field distributions found in Miller's work. The electric field strength of the vertical and horizontal components of electric field are shown as more detailed colour map plots in Figure 4.14.

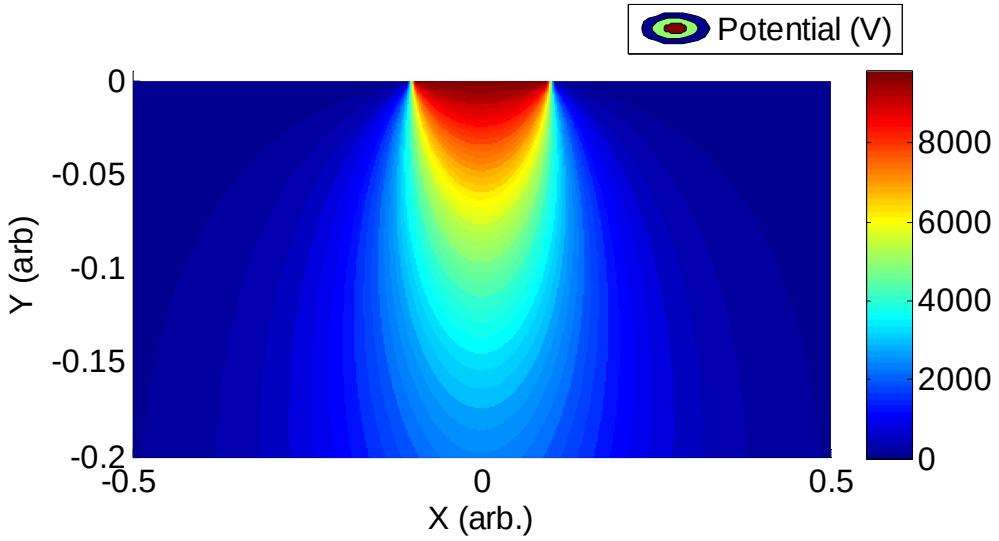

Figure 4.12 Potential distribution of an ideal planar electrode with boundary conditions as shown in Figure 4.11.

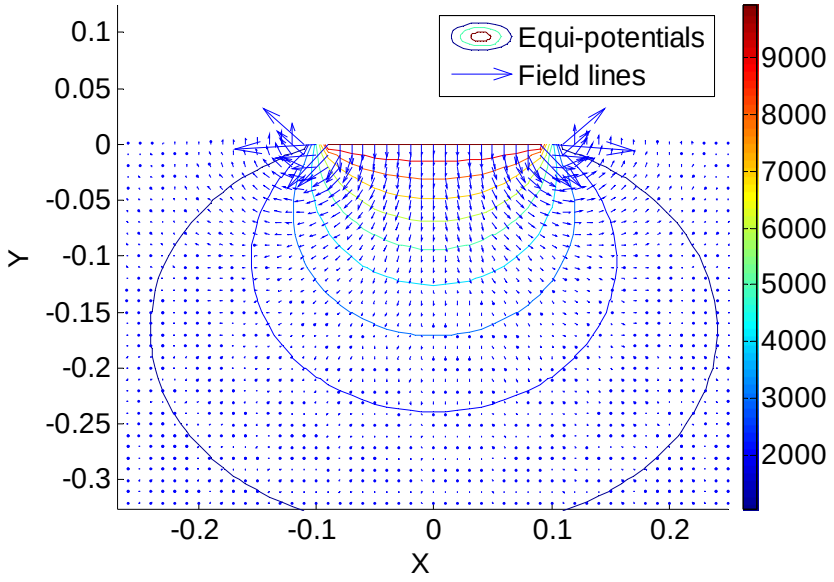

Figure 4.13 Vector plot of the electric fields produced by an ideal planar electrode.

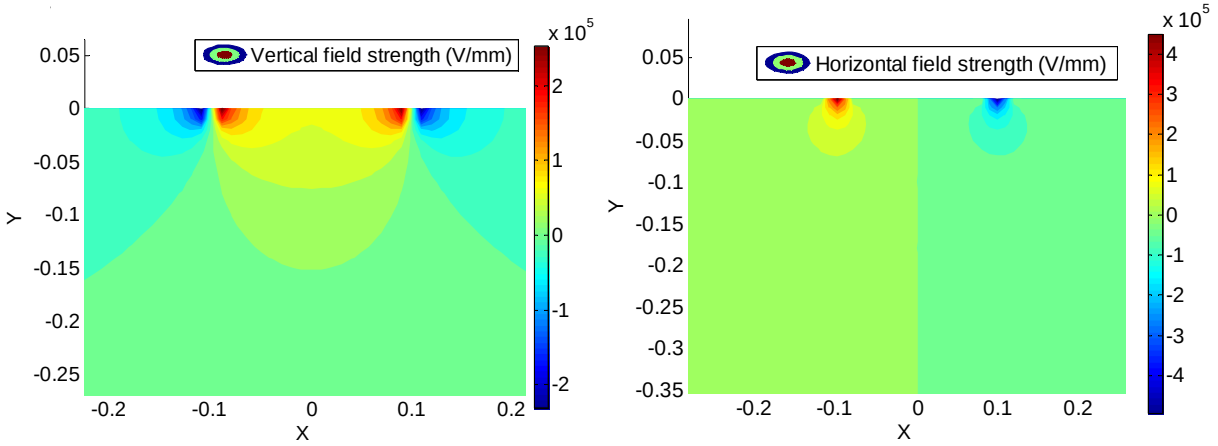

Figure 4.14 Colour plots of electric field strength for the vertical and horizontal electric field components of an ideal planar electrode.

A plot of the electric field components parallel to the crystal surface at a depth of 1µm are shown in Figure 4.15. The trend in the field distribution show obvious similarities with those of Miller's (Figure 4.9) with large fringing fields at the electrode edges.

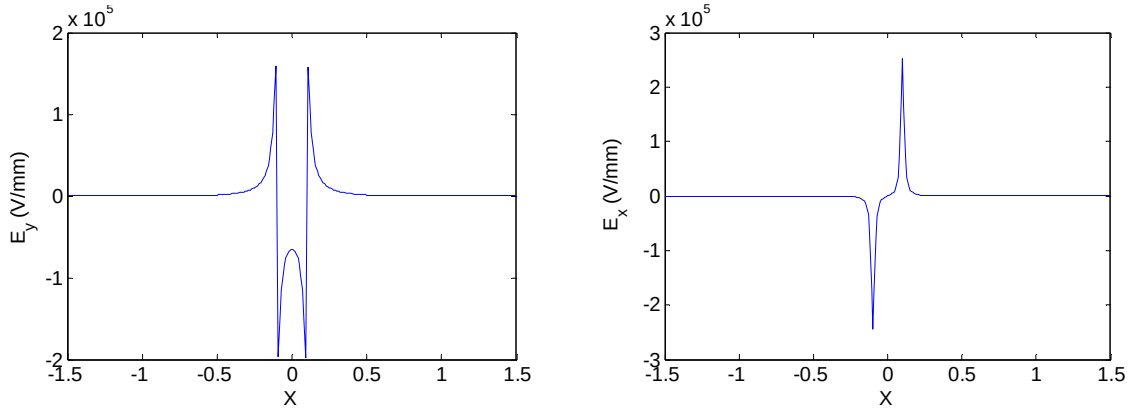

Figure 4.15 Vertical (left) and horizontal (right) electric field components 1 µm below the surface of the crystal.

When poling by submersion in a liquid electrolyte, the permittivity of the insulating layer needs to be considered. Also the dielectric strength of the resist layer also needs to be relatively high in order to withstand magnitudes of the fringing fields. These requirements dictate the choice of resist material and its preparation. The dielectric constant of a resist material may range from lower values similar to polymers (ε_r≈2-4) up to larger values depending on the solvent content and the resist processing prior to poling. The dielectric constant the slab can be considered as the dielectric constant of lithium niobate parallel to the z-axis, $\varepsilon_{r,LN} = 28$. The geometry and boundary conditions for this case is shown in Figure 4.16. Sample solutions of the potential and

electric field distributions are shown in Figure 4.17. The two major variables which affect the field distribution are thickness and dielectric constant of the resist layer. The thicker the resist layer and the lower the dielectric constant the better the lithium niobate surface is insulated. The better the insulation, the higher the electric field contrast at the resist openings. Simulations looking at the affect of the resist layer thickness and dielectric constant have been looked at by considering the maximum magnitude of the fringing field, 1 µm below the lithium niobate surface, under different conditions. The magnitude of the fringing field for a 1 µm thick resist layer is plotted in relation to the dielectric constant on the left of Figure 4.18. The plot on the right of Figure 4.18 shows the effect of the resist layer thickness for an arbitrary choice of dielectric constant, $\varepsilon_{r,resist} = 3$. These simulations demonstrate that a low dielectric constant and a thicker resist layer results in higher fringing fields at the domain edges. Higher fringing fields can be advantageous in aiding uniform domain nucleation, but can also cause problems if adhesion and dielectric strength of the resist layer is an issue.

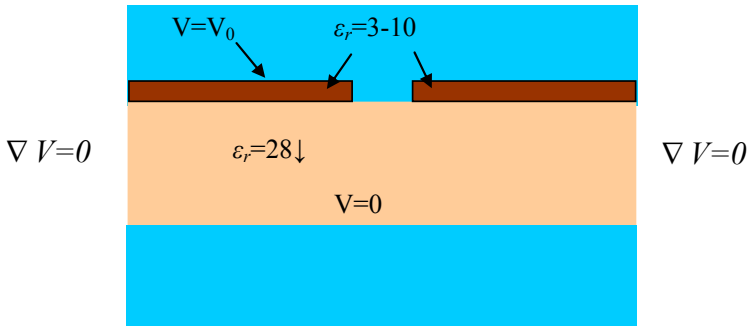

Figure 4.16 Geometry and boundary conditions for electrodes consisting of square openings in a resist layer.

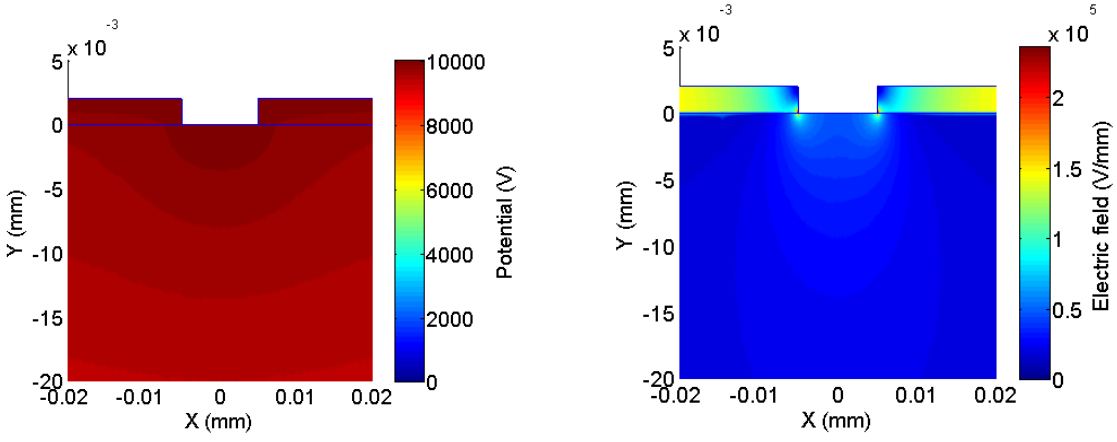

Figure 4.17 Colour map plots of the potential (left) and electrical field (right) distribution of electrodes consisting of square opening in a resist layer.

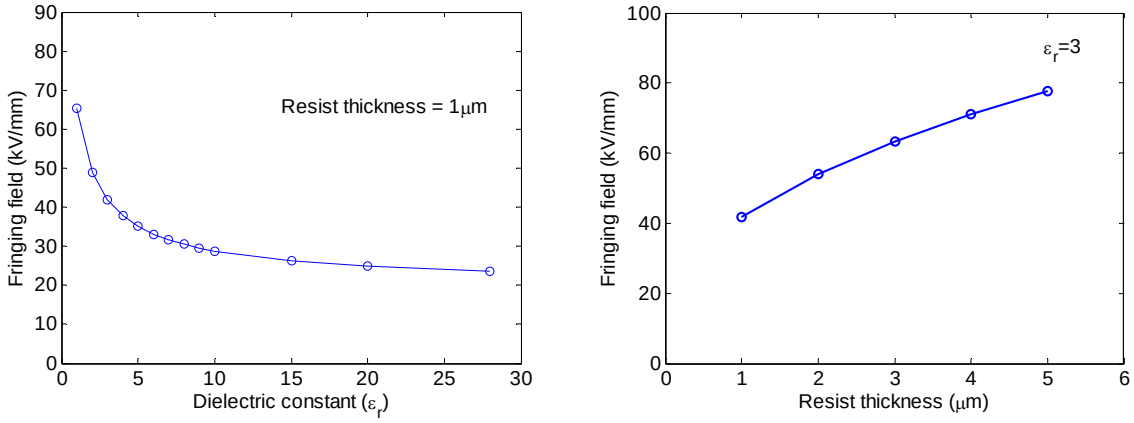

Figure 4.18 Fringing fields 1μm beneath the crystal surface contrast for the vertical electric field component compared to the resist layer thickness for a dielectric constant of ε_r=3.

Other authors have also looked at varying the geometry of the resist layer to add degrees of freedom in the domain patterning process. Ferraro and Grilli[194] have demonstrated control over the size and depth of surface domains produced during overpoling by modulating the thickness of the resist layer. Kwon *et al*[195] have also noted the effect of the resist layer thickness on the quality of periodic poling, demonstrating that a 3 μm layer performs better than a 1.7 μm layer when using AZ 4330 resist to produce poling periods of the order of 16 μm.

4.3.2 Electrostatics of topographical electrodes

For topographical electrodes it is the influence of the surface geometry on the potential and electric field distributions that is of most interest. The simplest geometry to consider is a v-groove, which is a good approximation of the geometry produced by laser machining as shown in Figure 3.33, and illustrated below in Figure 4.19. As there are no insulating layers the entire top surface is held at the applied potential, V_0, with the bottom face grounded. The boundary conditions for this are shown in Figure 4.20

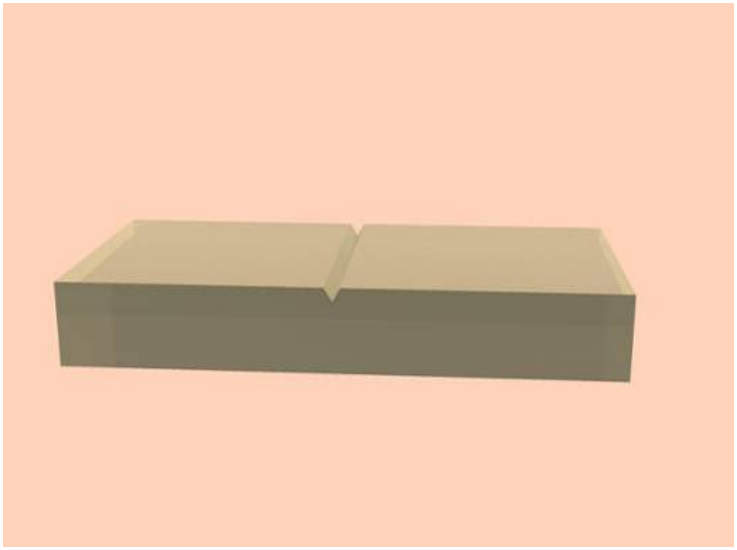

Figure 4.19 Geometry of v-groove type topographical electrodes

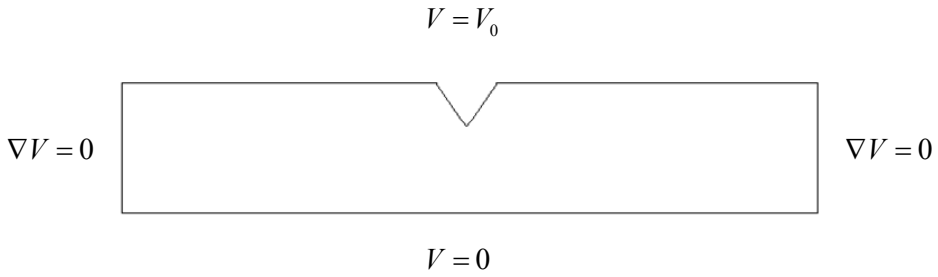

Figure 4.20 Boundary conditions for the electrostatics of a topographical surface electrode.

A typical simulated solution for the potential distribution is shown in Figure 4.21. Since the entire top surface is held at the poling potential, there would ordinarily be a steady electric field distributed through the entire slab of material. When a groove is introduced the regions of equi-potential intuitively follow the contours of the grooved surface. The local electric field near the groove is perturbed by both the local reduction in the material thickness and the geometry of the groove. A vector plot of the electric field in the vicinity a typical v-groove is shown in Figure 4.22. The electric field strength of the vertical and horizontal components are shown as colour maps in Figure 4.23 and as plots across the slab, 1μm beneath the apex of the groove, in . One of the key differences in the electric field distributions of the planar and v-groove electrodes is the single region of high electric field at the apex of the groove as compared to the twin regions cause by fringing fields for the case of the planar electrodes. This field distribution suggests that domain evolution from a single domain nucleation region will take place.

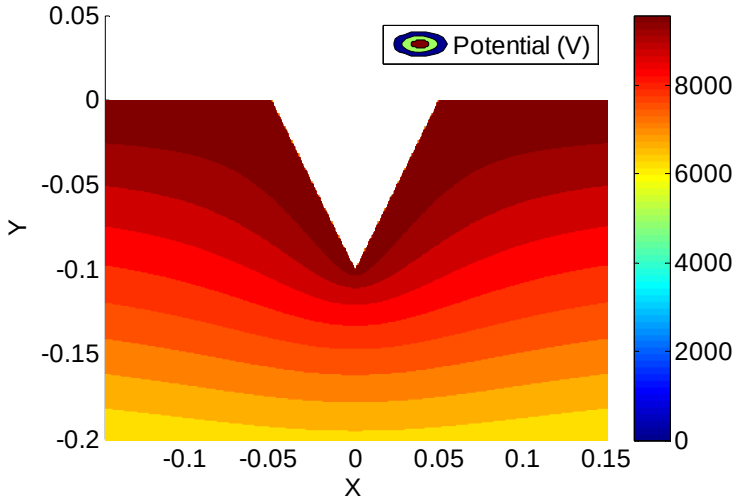

Figure 4.21 Potential distribution of a v-groove electrode with boundary conditions as shown in Figure 4.20.

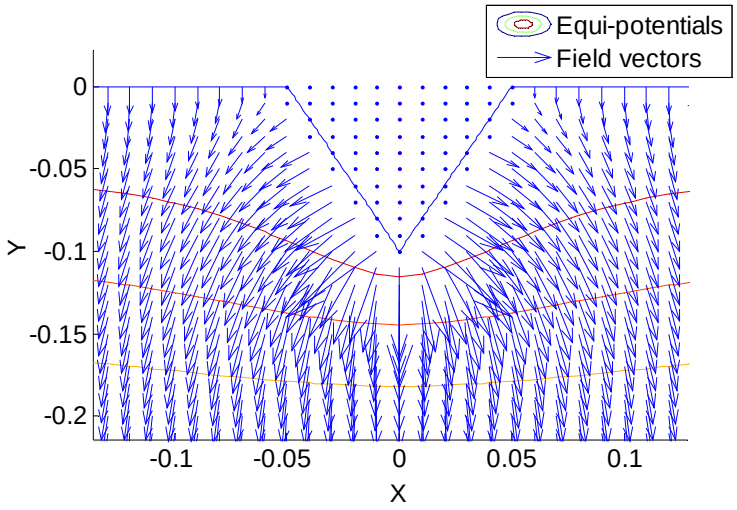

Figure 4.22 Vector plot of the electric field produced by a v-groove electrode.

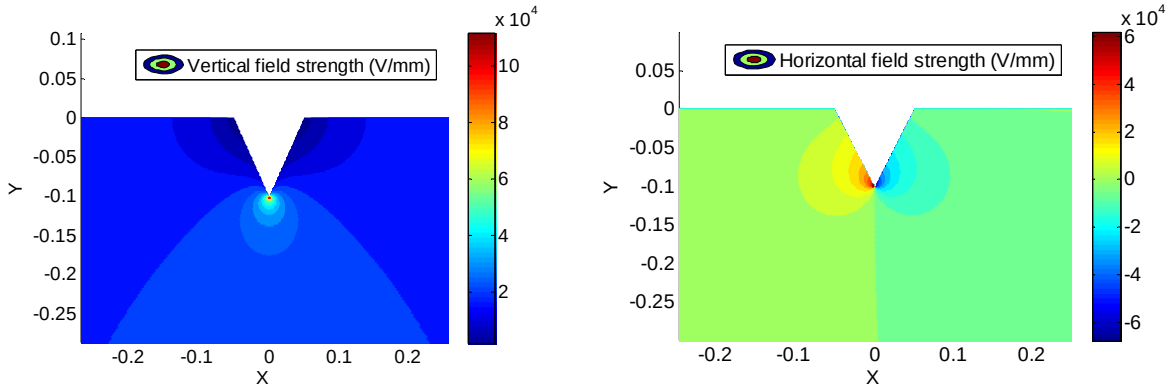

Figure 4.23 Colour plots of electric field strength for the vertical and horizontal electric field components produced by a v-groove electrode.

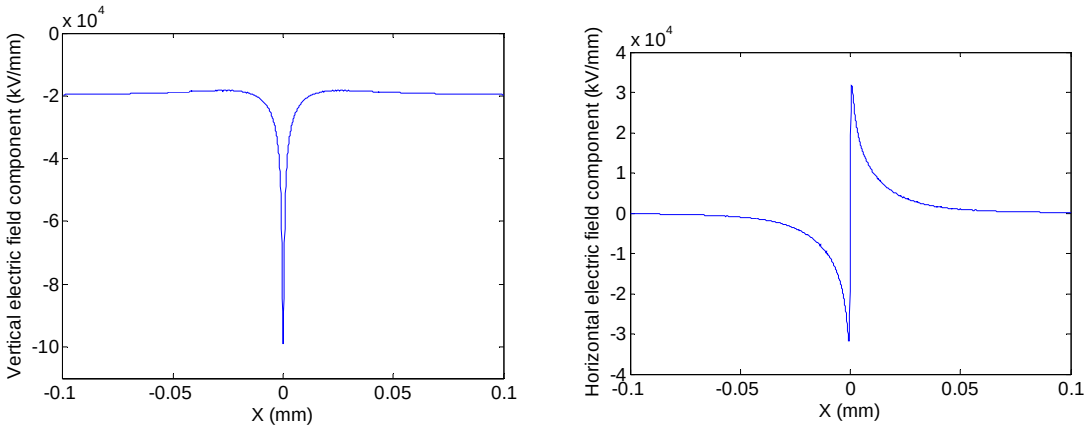

Figure 4.24 Vertical (left) and horizontal (right) electric field components 1 µm below apex of the groove.

Unlike planar electrodes, where the layer thicknesses and dielectric properties are the major variables in determining the electric field distribution, for topographical electrodes it is the physical geometry which is important. The shape, depth and aspect ratio of the topographical feature are all important factors which influence the perturbation of the electric field. For simulations which investigated the influence of the groove's shape, a geometry was chosen so to be easily constructed from primitive shapes for ease of programming and to avoid discontinuities in the geometry which may cause problems with the numerics of the FEM solver. The geometry was constructed as a straight sided groove with opening width *w*, depth *d* and with a curved apex with radius of curvature *r*. The primitives used to construct this shape along with the dimensions referred to are illustrated on the left of Figure 4.25. Typical solutions for the potential and electric field distributions for such geometry are shown in Figure 4.26.

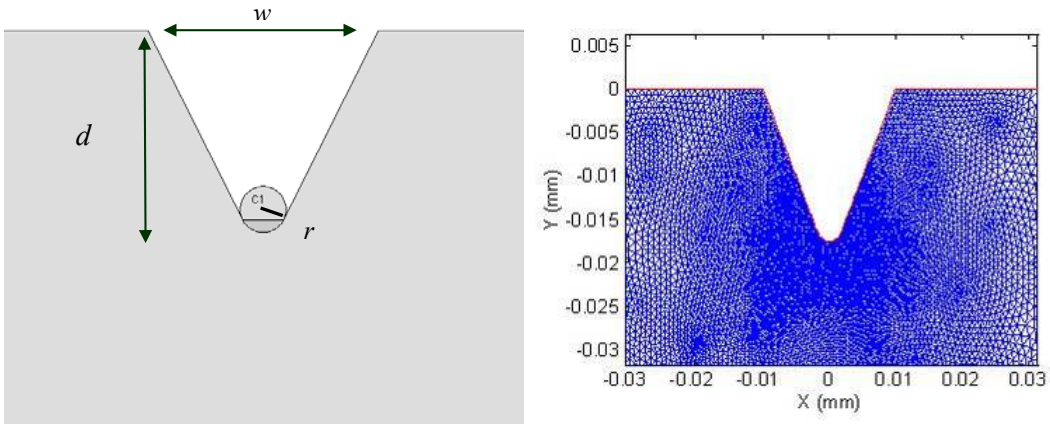

Figure 4.25 Left: primitive shapes and dimensions used to describe a groove with a curved apex for FEM simulations. Right: Typical FEM geometry and mesh.

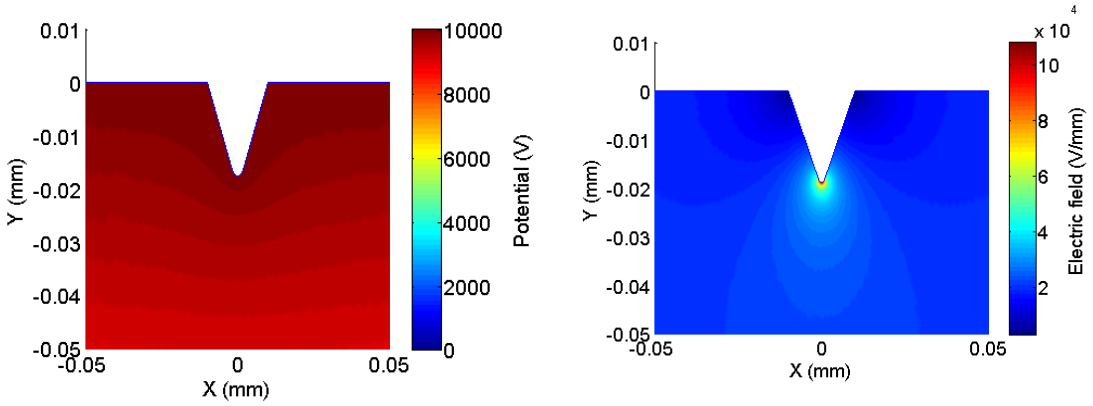

Figure 4.26 Colour map plots of the potential (left) and electrical field (right) distribution of electrodes consisting of grooves with a curved apex.

There are three major geometric variables for this type of groove geometry; the relative depth of the groove compared to the slab thickness, the aspect ratio of the groove, *h/w,* which gives an indication of the slope of the side walls, and the radius of curvature of the apex of the groove. The affect of these parameters on the electric field strength was investigated by simulations by noting the peak electric field strength at the apex of the groove as the parameters were varied. The results are shown in Figure 4.27. The top plot shows the relation between the electric field and the depth of a groove with a fixed aspect ratio and curvature at the apex. For an increasing depth of groove there is an intuitive increase in the peak electric field, as the potential drop is occurring through thinner regions of material. A more instructive comparison to make is the groove depth as a fraction of the slab thickness. The larger the fractional depth of the groove compared to the slap the larger the electric field perturbation.

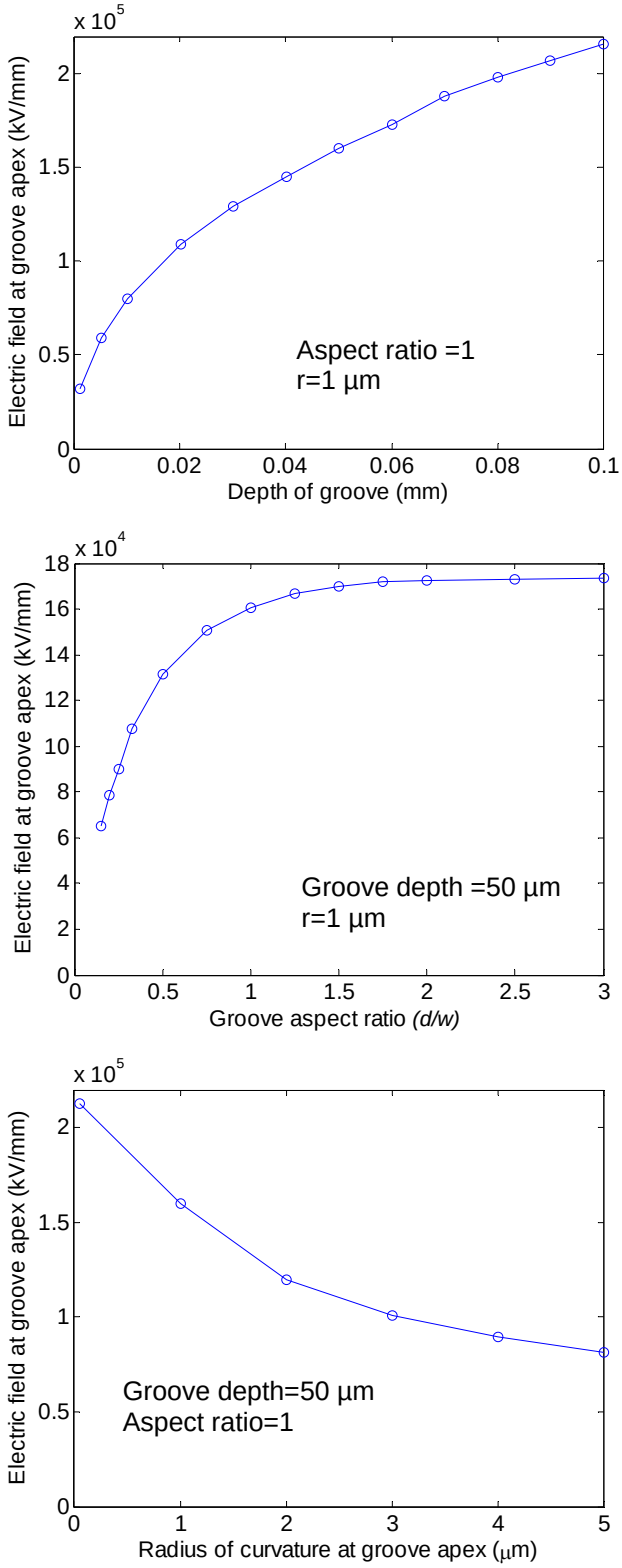

Figure 4.27 Influence that aspects of geometry of a surface groove have on the peak electric field. Top: electric field in relation the groove depth, centre: electric field in relation to the aspect ratio of the groove, bottom: electric field in relation to the curvature at the groove apex.

The centre plot in Figure 4.27 shows the relation between the peak electric field and the aspect ratio of a groove with a fixed depth and apex curvature. The perturbation of the electric field shows a clear dependence on the aspect ratio of the groove, with a significant decrease in the peak electric field for aspect ratios below h/w=1. A similar relationship between the geometry of the topographical features and electric field poling was noted previously by Reich *et al*[49]. It was noted that domain inversion was more reliable when the aspect ratio of their Gaussian shaped laser machined features was better than 0.8, as shown in the reproduced plot in Figure 4.28.

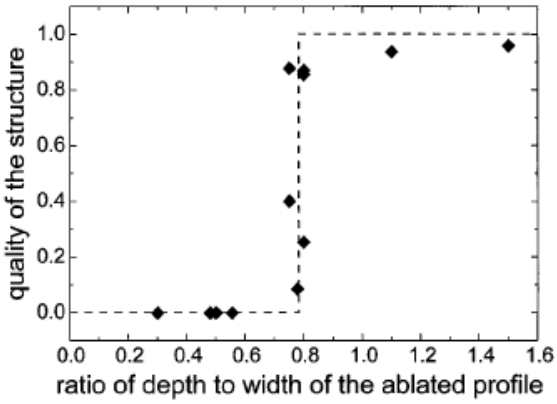

Figure 4.28 Affect of aspect ratio of Gaussian like grooves on the quality of domains produced upon poling (from Reich et al, 1998).

The bottom plot in Figure 4.27 indicates the influence that the sharpness of the groove apex can have on the peak electric field. The more 'V' like the groove is, i.e. the sharper and more singular the apex is, the steeper the potential gradient and thus higher the electric field is about the apex. As indicated in the plot, a groove whose apex that converges to a radius of curvature that is of the order of a few hundred nanometres (much less than the radius of commonly achieved laser spot sizes of~5 μm) can produce a significantly larger peak field.

In order to explore the influence of the 'shape' of the groove more extensively, comparative simulations of 'V' grooves, circular grooves, 'U' grooves and square grooves were carried out. Colourmap plots of the electric field distributions, along with a plot of the vertical electric field component across the apex of the groove, is shown in Figure 4.29 for a V-groove and a U-groove, each with a 10 μm opening and a 20μm depth. The plots of the vertical electric field across the apex for each shape are plotted on the same scale for comparison. It can be seen that the sharper apex of the V-groove results in a larger and more localised electric field at the apex.

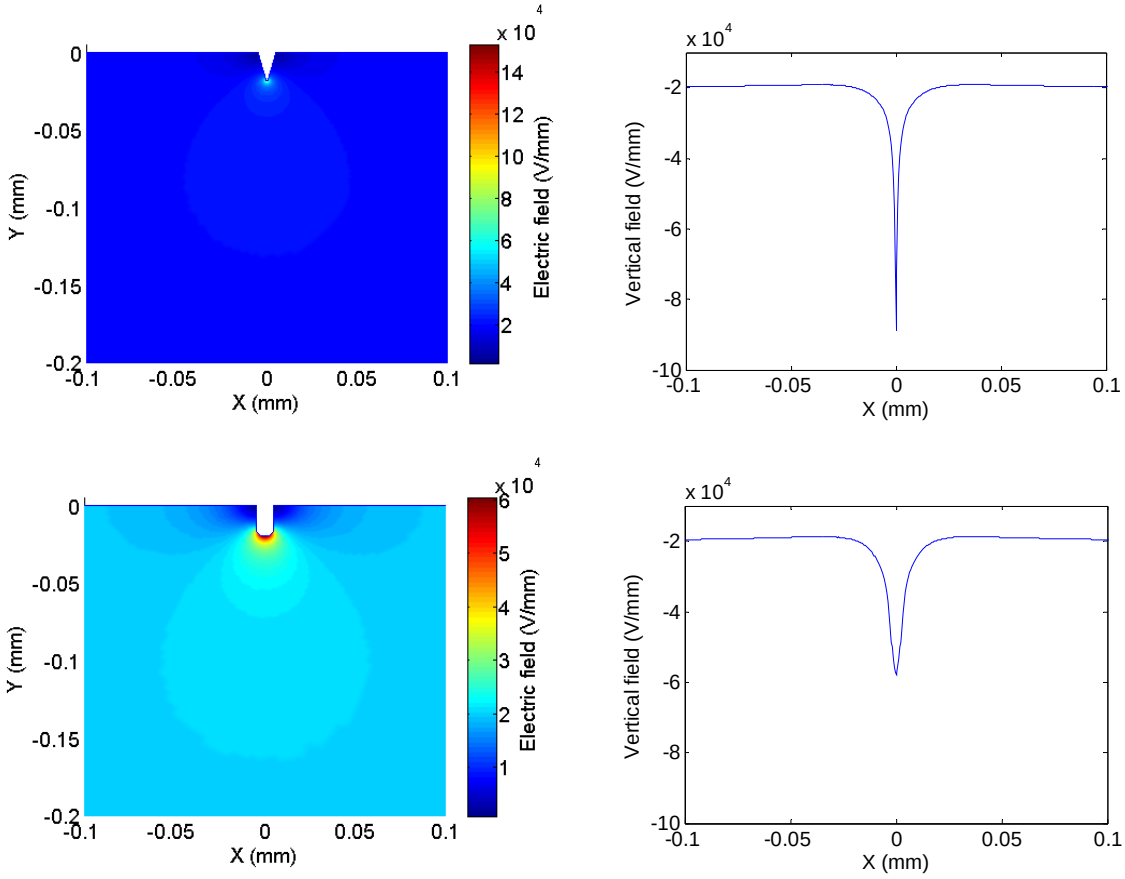

Figure 4.29 Plots of the Electric field distribution (left) and vertical electric field component across the apex (right) for different shaped grooves. Top: V-groove, bottom: U - groove.

Figure 4.30 shows the cases for a circular and a square groove. The circular groove has a radius of 20 µm in order to have the same depth as the other shapes. That the circular groove and the square groove have lower electric field magnitudes at the apex in comparison to the V-groove. The square groove also has the twin 'fringing' fields similar to planar electrodes. These different types of geometries can be produced under different fabrication conditions. For instance, V-grooves are produced when laser machining while focusing at or below the surface of the target. U or circular shapes tend to be produced when the target is behind focus and the beam is diverging. Should the grooves be produced by etching, a square geometry is to be expected. The simulations shown in Figure 4.29 and Figure 4.30 suggest that the v-groove geometry is optimal for producing a large electric field contrast at the apex.

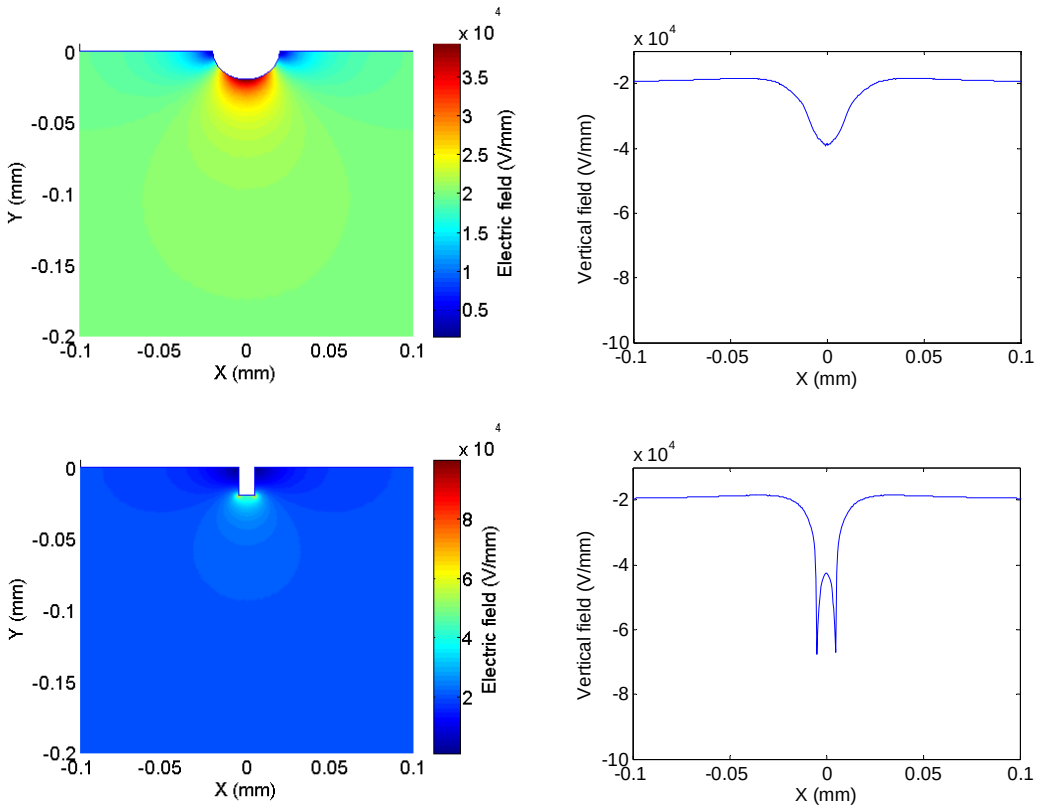

Figure 4.30 Plots of the Electric field distribution (left) and vertical electric field component across the apex (right) for different shaped grooves. Top: circular groove, bottom: square groove.

The key implications of the simulations presented here are that deep, sharp and high aspect ratio features provide the high electric field contrast necessary for controlled domain inversion with topographical electrodes. In practice, the capabilities of the laser processing system will in part dictate the feature geometries that are feasible to produce. The field dependence on the aspect ratio and depth of features presented here act as guide for the laser machining requirements for fabricating such electrode structures.

4.4 Experimental setup and procedures

4.4.1 Poling apparatus

The field poling setup used during these experiments was similar to that described by Myers *et al*[24]. For reference, a review on the development of poling technology for lithium niobate was been given by Myers at the 52nd Scottish Universities summer school in physics[196]. The majority of poling during this project was carried out in Plexiglass cells with 8 mm o-ring seals. A Trek

20/20C high voltage amplifier was used to delivered voltage pulses across the poling cell. The input voltage signal to the Trek was delivered by an M-series National Instruments PCI-DAQ card. The applied voltage waveform was monitored via the Trek output monitor and a Tektronix HV probe measured the potential across the poling cell. The poling circuit included with a 10.5 MΩ resistor in series with the poling cell and a second 100 kΩ resistor which could be used as a current monitor. The poling layout is illustrated in Figure 4.31.

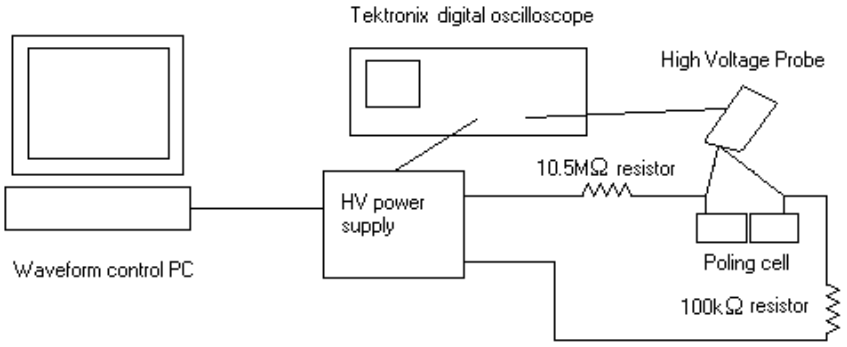

Figure 4.31 Layout of poling apparatus.

The applied voltage waveform was similar to that reported elsewhere, with a ramp up to 10kV and a hold off period to settle any current leakage. The application of the poling voltage with or without a leading edge 'nucleation' spike, was followed by a second hold off and ramp down. A typical example of recorded voltage waveforms and poling current is shown in Figure 4.32 and Figure 4.33 respectively. The voltage difference between the Trek output monitor and the poling cell indicates a poling current is flowing through the series resistors in the circuit. Due to the large series resistance, the poling voltage across the cell clamps at the value of the coercive field so that the current flow is fairly constant for a given poling voltage and can be regulated by the amount that applied poling voltage is in excess of the coercive field. For samples that poled with a consistent current, the duration of poling could be used to control the degree of domain reversal. When poling with insulating layers as the electrode pattern, the domain formation can be self terminating, or at least so a 'turn off' of the poling current, as the fields under the insulator are insufficient for domain spreading. This is not always the case for bare, topographically patterned crystals, so selecting a suitable pulse duration was important for achieving the desired level of poling. The poling electrolyte used was a saturated NaCl solution with a small amount of detergent included to aid in surface wetting to ensure good electrical contact with the crystal surface.

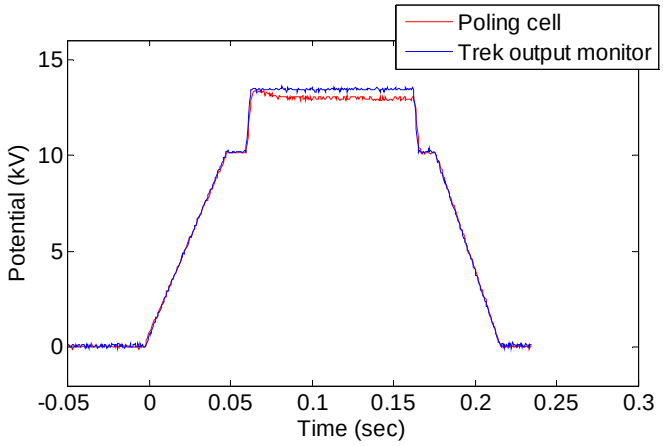

Figure 4.32 Typical captured poling voltage waveforms from the Trek and poling cell probe

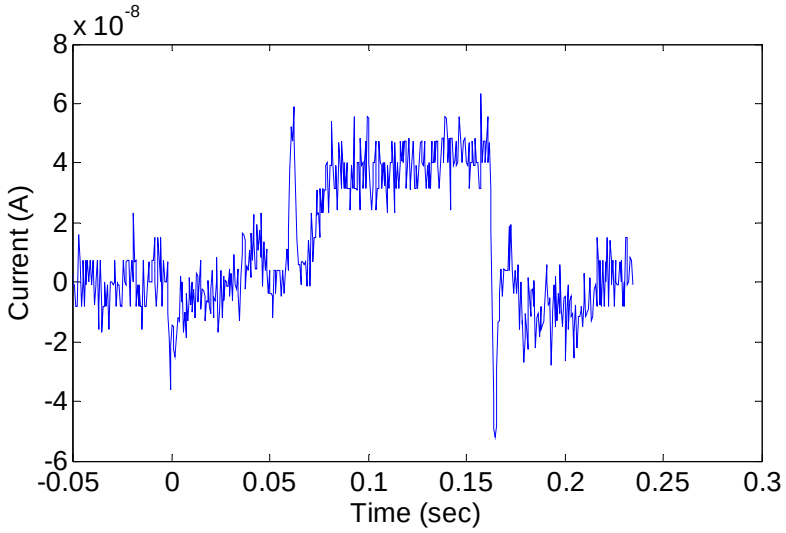

Figure 4.33 Typical poling current (corresponding to Figure 4.32) when poling congruent lithium niobate.

4.4.2 Crystal preparation

The absence of lithography in the fabrication of topographical electrodes via laser machining makes for simple and fast preparation of crystal samples prior to poling. After laser machining had been carried out the samples were clean in an ultra-sonic batch with acetone to remove any debris and solubles. After rinsing, optical cleaning polymer (a product which is applied in liquid form to optical surfaces and then sets as a soft polymer) was applied to the surface of the crystal with the laser machined features and allowed to set. The cleaning polymer was peeled from the crystal surface prior to poling and aided in removing any stubborn debris left over from the laser

processing as well as ensuring the topographical features were clean. Silicone rubber seals, along with a smear of vacuum grease, were used to form watertight seals on the crystal faces in the poling cell. After filling the poling cell with the electrolyte, the cell was gently agitated to ensure good surface wetting and remove any trapped air bubbles that may have formed at the topographical features.

4.4.3 Domain characterisation

Visualisation of crystal domains after poling is difficult in the untreated bulk crystal. While the domain boundaries have some slight stress birefringence which can be picked up when viewing under cross-polarisation, this is not always the best indication of the uniformity of domain formation. Fortunately the different domain orientations chemically etch at different rates, and the most common technique for revealing crystal domains is etching in hydrofluoric acid (HF). However HF is an extremely hazardous chemical, and while common to many semiconductor laboratories and clean room environments, avoiding HF use is always preferable. It was found during the course of this project that the different domain orientations in poled lithium niobate will also mechanically etch differently. Polishing of the ±z crystal faces on a standard lapping wheel with a common optical polishing slurry produces some slight surface relief between the ±z orientations. Although the differential etch rates are lower than for chemical etching, a surface relief of 50-100 nm between the domain orientations is easily achieved with 10-15m in polishing time. Viewing this degree of surface relief in lithium niobate is made easy by differential interference contrast (DIC) microscopy. Since the refractive of lithium niobate is of the order of $n=2$, small surface relief features show up vividly as a significant optical path differences when viewing under DIC. Figure 4.34 shows a DIC microscope image, and a 3D image from optical profilometry data, of domains of a 45 μm period sample viewed from the –z face of the crystal after polishing. The straight domain walls, parallel to the y-axis, and the triangular domain ends appear vividly under DIC. The surface relief produced by polishing was measured using optical profilometry and an example data set is shown in Figure 4.35. A 40nm etch depth between the ±z orientations is observed, with the +z face exhibiting the faster etch rate. Similar etching properties have also been found for crystal 'twinning' in YAB crystals[197].

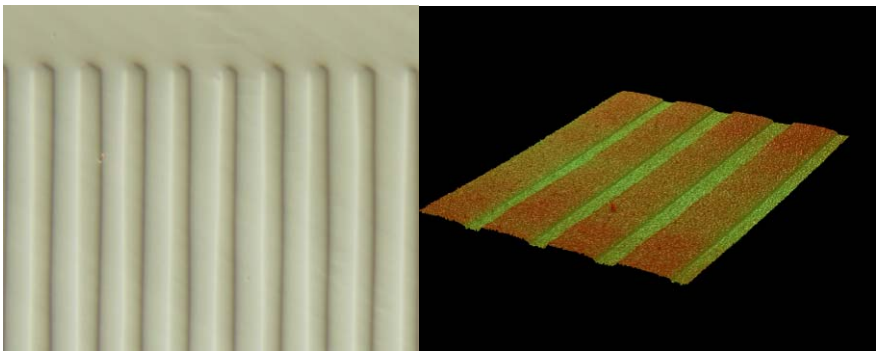

Figure 4.34 Left: domains on the -z face of lithium niobate reveal by mechanical polishing and DIC microscopy, right: 3D image from optical profilometry data.

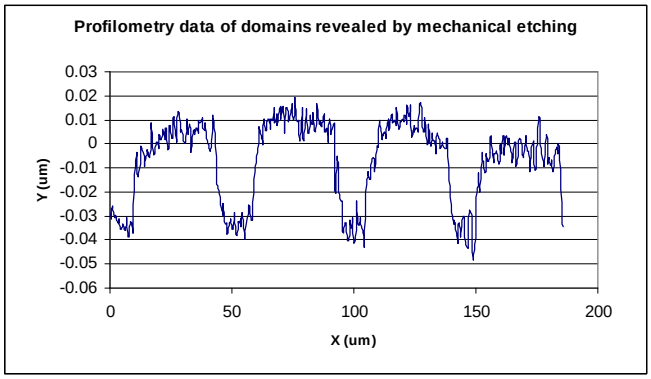

Figure 4.35 Optical profilometry data of domains reveal by mechanical polishing.

4.5 Experimental Results

4.5.1 Determining the coercive field of bare lithium niobate

In order to approximately determine the coercive field of the lithium niobate wafers in use, a poling waveform with a voltage ramp between 22-28 kV was applied to a bare crystal. The potential at which a difference in the output voltage of the Trek and the voltage measured across the cell began to be observed indicated that a poling current was flowing. For the lithium niobate wafers use for this project this voltage was determined to be 13.2 kV (according to the Trek output monitor signal) for 500 μm thick crystal, an inferred coercive field of 26.4 kV/mm. This value is of course subject to Trek's calibration, but still served as reliable reference point for the subsequent experiments.

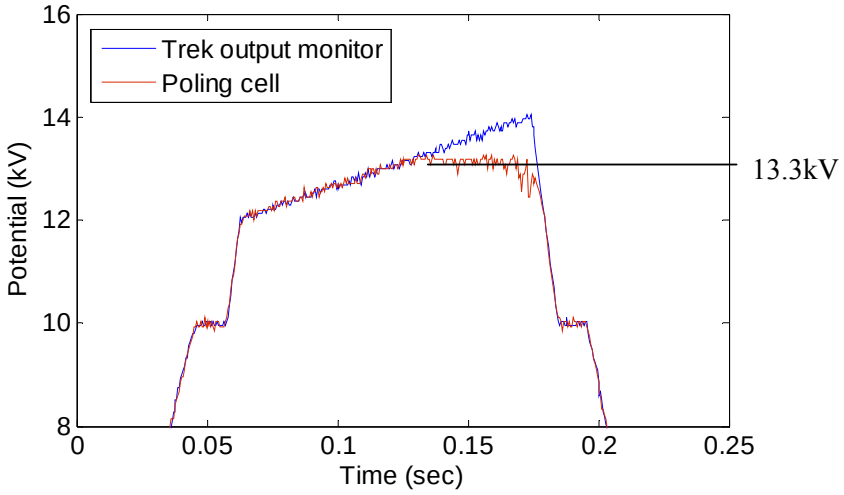

Figure 4.36 Ramped poling waveform for determining the coercive fields of bare congruent composition lithium niobate.

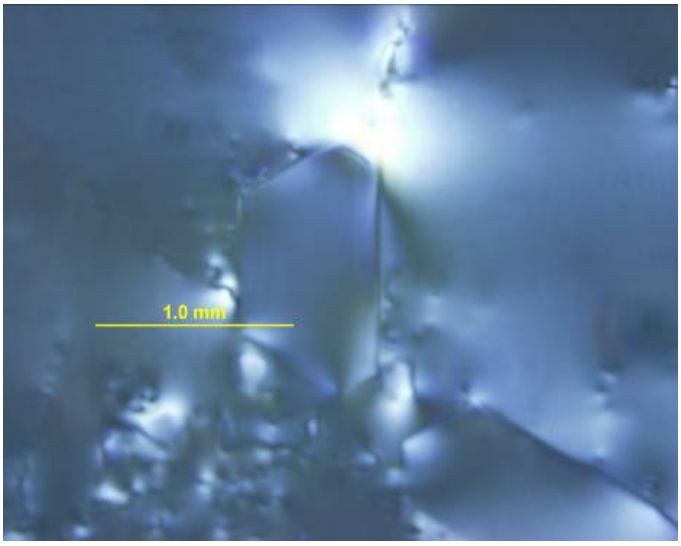

Figure 4.37 Domains produced on bare sample poled with the waveform in Figure 4.36, viewed under cross-polarization.

Samples which were patterned with laser machined features exhibited poling currents at applied voltages below the coercive field. This was due to the fact that the laser machined features reduced the local thickness of the substrate, requiring lower applied potentials for the coercive field to be exceeded. Application of poling voltages below the coercive field of the bare samples produced preferential poling at the laser machined features.

4.5.2 Poling with laser machined features

An example of domains produced in preliminary experiments of poling with laser machined electrodes are shown, viewed under cross polarisation, in Figure 4.38. Selective domain formation guided by the laser machined features is apparent. It was also confirmed that the geometry of the laser machined features influence the probability and quality of domain inversion. The results of a preliminary experiment showing this are illustrated in Figure 4.39. With low fluence laser machining (~3 J/cm^2) from the Hurricane laser system, described in chapter 3, 6 arrays of 5 grooves were machined, with the number of machining passes over each groove being increased from 1-6. This resulted in grooves which were increasing in depth and aspect ratio as the number of machining passes was increased. Upon poling this sample, a clear onset of domain inversion for grooves with 3 or more passes was observed, while the shallow grooves with only 1 or 2 machining passes did not result in domain inversion. The results of further studies on the influence of the groove geometry on domain formation and kinetics are presented in the subsequent sections.

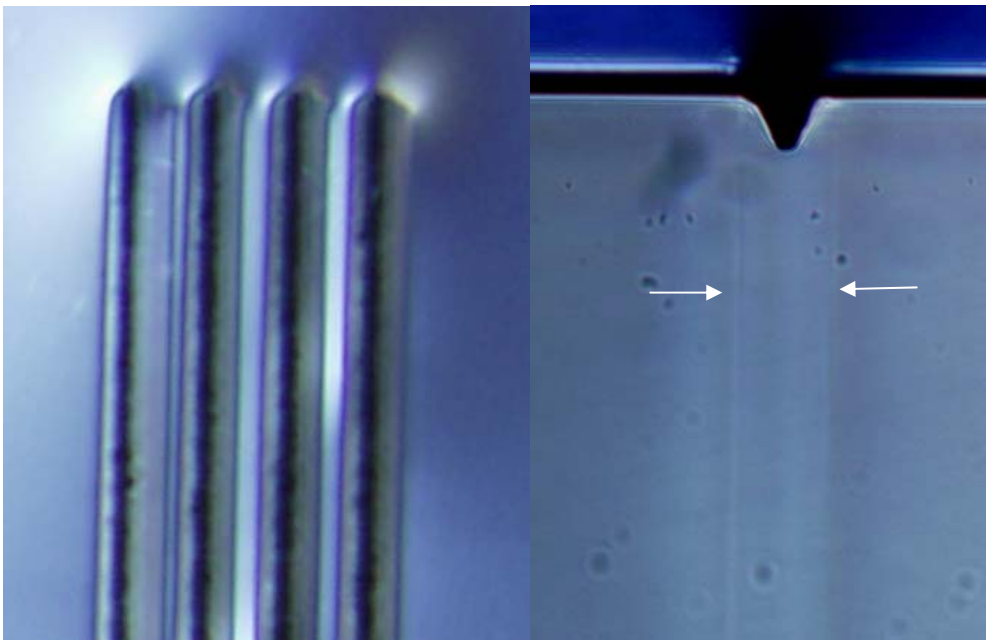

Figure 4.38 Domain formation at laser machined features in lithium niobate. Left: viewed from the +z face, right: cross-section of a domain viewed from the y-face.

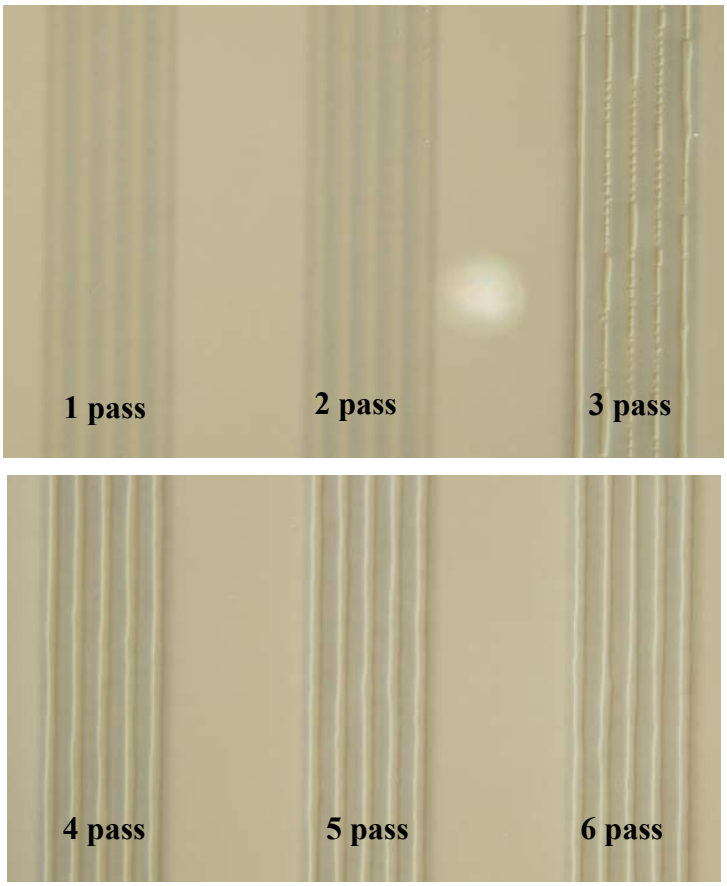

Figure 4.39 Domain inversion across a sample where the number of laser machining passes across the grooves has been varied, as indicated. Sample is view from the –z face, opposite the laser machined features.

4.5.3 Domain nucleation and shielding

Evidence of the influence of the electrostatics of groove like features on the domain formation, as simulated in section 4.3, was observed in several samples. The nucleation of domains from the apex of laser machined features was seen in some under poled samples. As expected from the electric field distribution seen in the simulations (Figure 4.23), a single region of reversed crystal could be seen in the neighbour of the groove apex after the sample was cross-sectioned and polished. For deep features with high aspect ratios which had been poled to completion, an unreversed region, adjacent to the v-groove shoulder was observed. This was also consistent with the electric field simulations, which show regions of reduced vertical electric field strength adjacent to the groove walls. This demonstrates that the v-groove geometry acts to shield regions of the crystal from the high electric fields require for domain reversal. The experimental observations are illustrated in Figure 4.40.

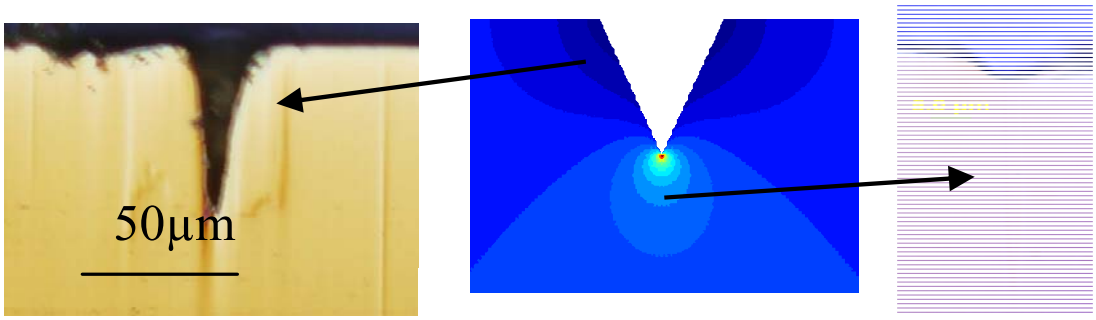

Figure 4.40 Evidence of the influence of the electrostatics of grooved surface features on the formation of domains. Left: unreversed region of material adjacent to the groove shoulders, in correlation with the suppressed electric field predicted by simulation. Right: evidence of a single region of domain nucleation from the apex of a laser machined feature.

4.5.4 Domain control and kinetics

Control over domain inversion produced from topographical electrodes was demonstrated in a number of ways. For a group of samples machined with the same laser parameters, control of the domain widths (and thus grating duty cycle) could be controlled by the poling duration. Figure 4.41 shows two sections of PPLN (period of 40 µm), machined with the same laser parameters but poled with pulse durations of 100 ms (left) and 200 ms (right).

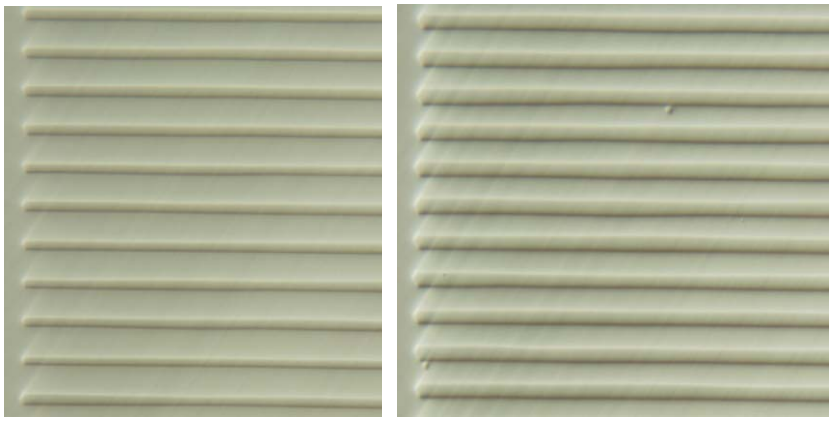

Figure 4.41 PPLN produced with laser machined electrodes with domain widths controlled by poling duration (period of 40 µm). Left: 100ms poling pulse ~20% duty cycle, right: 200ms poling pulse ~35% duty cycle.

A more interesting method for controlling the domain widths, which also provides information about the domain kinetics, is to vary the laser parameters, and thus the groove geometry across the sample. If grooves with significant variations in depth are fabricated, the domain widths produced upon poling will accordingly be of different widths. An example of this is shown in

Figure 4.42. The groove positions have been sketched in as the top edge of this particular sample edge has flaked off during polishing.

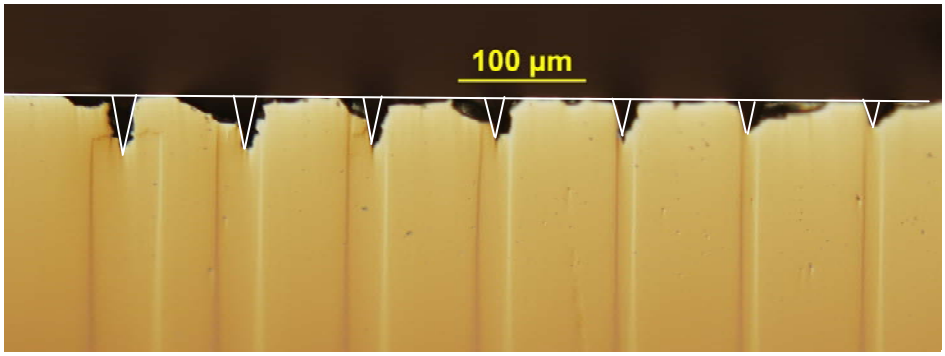

Figure 4.42 Domains with varying widths produced from laser machined grooves of varying depths.

The systematic variation of the domain width with groove depth can be attributed to the different effective poling fields for the different depth grooves. Put simply, the electric field (V/mm) would ordinarily be simply the potential drop, V_{app}, divided by the slab thickness, t, but is perturbed by the reduced thickness at a groove of depth d.

$$E_{eff} = \frac{V_{app}}{t - d} \tag{4.7}$$

This enhanced field results in different domain wall velocities as discussed above in section 4.2.3. The domain wall velocity can be estimated by the measured domain width w for a poling pulse duration t_{pol} is simply,

$$v = \frac{w}{2t_{pol}} \tag{4.8}$$

where the factor of two accounts for the fact that the domain walls spread in both directions from the apex of the groove. The plot of the experimental results from a selection of samples similar to that shown in Figure 4.42 is shown in Figure 4.43. The experimental domain wall velocities can be roughly fitted to an exponential function of the poling field, as suggest in Eq. (4.2). For the results found in these experiments a single exponential relationship between the domain wall velocity and the inferred effective poling field was observed. Following the function form of Eq (4.2) the values of the fitting for the domain walls velocity $v(E)$ are,

$$v(E) = \Phi(E - E_1) v_1 \exp\left(-\frac{\delta_1 E_1}{E - E_1} \right)$$

E_1	24
v_1	6500
δ_1	1.15

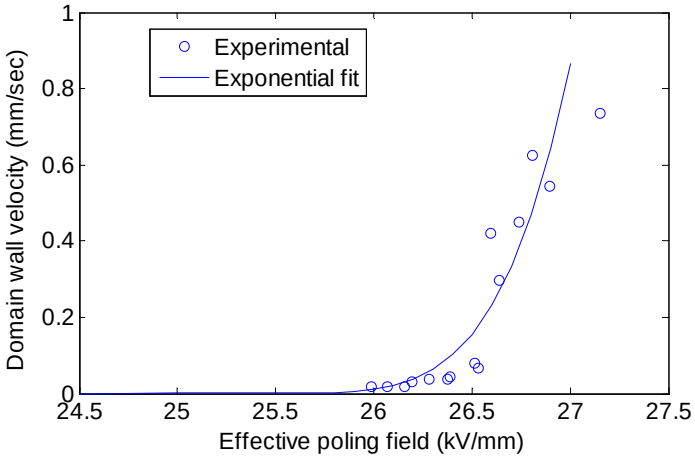

Figure 4.43 Domain wall velocity in relation to the effective poling field that is produced by grooves of varying depths.

Despite the control over domains demonstrated via the poling duration and fabricated groove depth, there was a further practical limitation on the poling periods achievable using this technique. The topographical electrodes described here have been implemented without any insulating layers and so close packing of the grooves tended to reduce the electric field contrast and uniformity. This was observed as a significant difference in the quality of domain patterns when periods <20 µm were attempted. This is shown in Figure 4.44, where two domain patterned regions have been laser machined with the same laser parameters but with periods of 50 µm on the left of the sample and 20 µm period on the right of the sample. It is apparent in the region patterned with a 20 µm period that domain formation in the central area of the grating is not uniform.

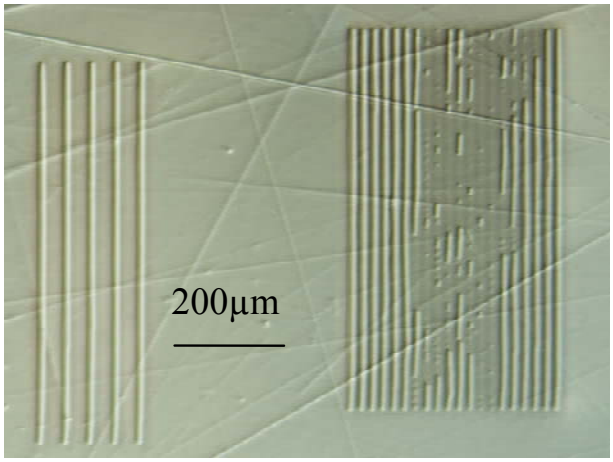

Figure 4.44 Domain patterning for the same laser machining parameters but with different periods. Left: 50 µm, right: 20 µm.

The basis for this reduction in poling quality when using close packed topographical electrodes has been explored with simulations of the electrostatics. Starting with a typical groove geometry, aspect ratio of 2 with depth d=20 µm and opening width w= 10 µm, simulations of the electrostatics for an array of 10 grooves with various periods were looked at. Typical potential and electric field distributions for these simulations are shown as colour map plots in Figure 4.45. The magnitude of the vertical component of electric field at a depth of 21 µm (1µm below the apex of groove) was plotted to indicate field uniformity across the array. The electric field distribution when the grooves are placed 100 µm apart (10x the groove opening width) is shown in Figure 4.46. At this relatively wide spacing the electric field in the proximity of each groove apex is the same with a simulated electric field of ~67 kV/mm in contrast to the uniform field of 20 kV/mm. As the spacing of the grooves is decreased the field uniformity and the electric field contrast begins to become poorer. The results of simulations of 50,40,30 and 20µm groove spacings are shown in Figure 4.47. Two major influences on the electric field can been as the grooves are moved to closer proximities. Firstly, there is a reduction in contrast in the electric field at the apex compared to the uniform field away from the grooves. Secondly the arrays with closely packed grooves show a collective perturbation of the electric field with larger 'fringing' fields at the edges of the array and reduced fields in the central region. This is in good correlation with the distributions of the domain patterning quality observed in samples such as that shown in Figure 4.44. The domain formation at the outer edges of the 20 µm period region, where a large field contrast is predicted, is complete while the domain formation is sparse in the central area where there is predicted reduction of the electric field contrast.

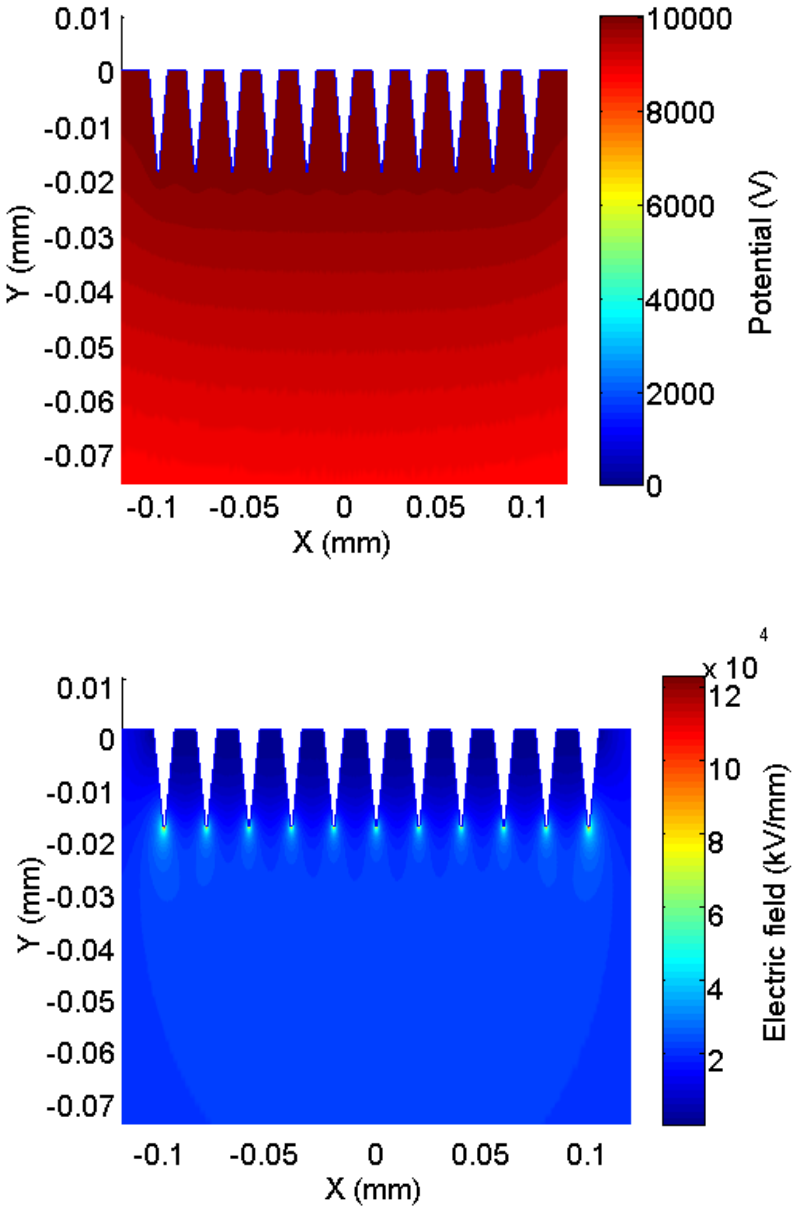

Figure 4.45 Typical potential (top) and electric field distributions (bottom) simulated for an array of grooves.

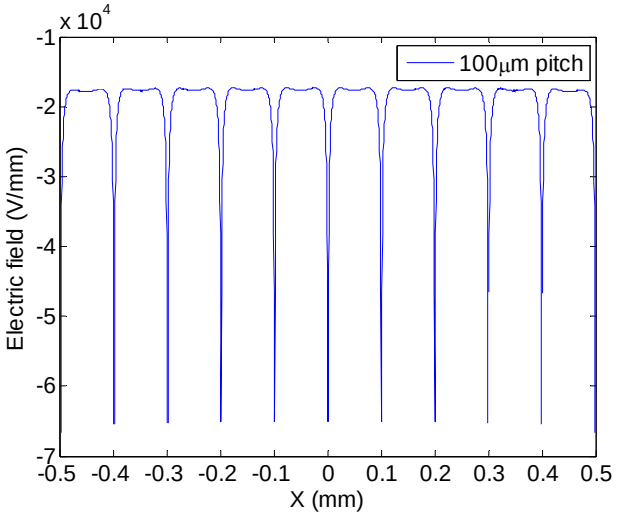

Figure 4.46 Electric field distribution in proximity of the groove apexes for a groove spacing of 100μm.

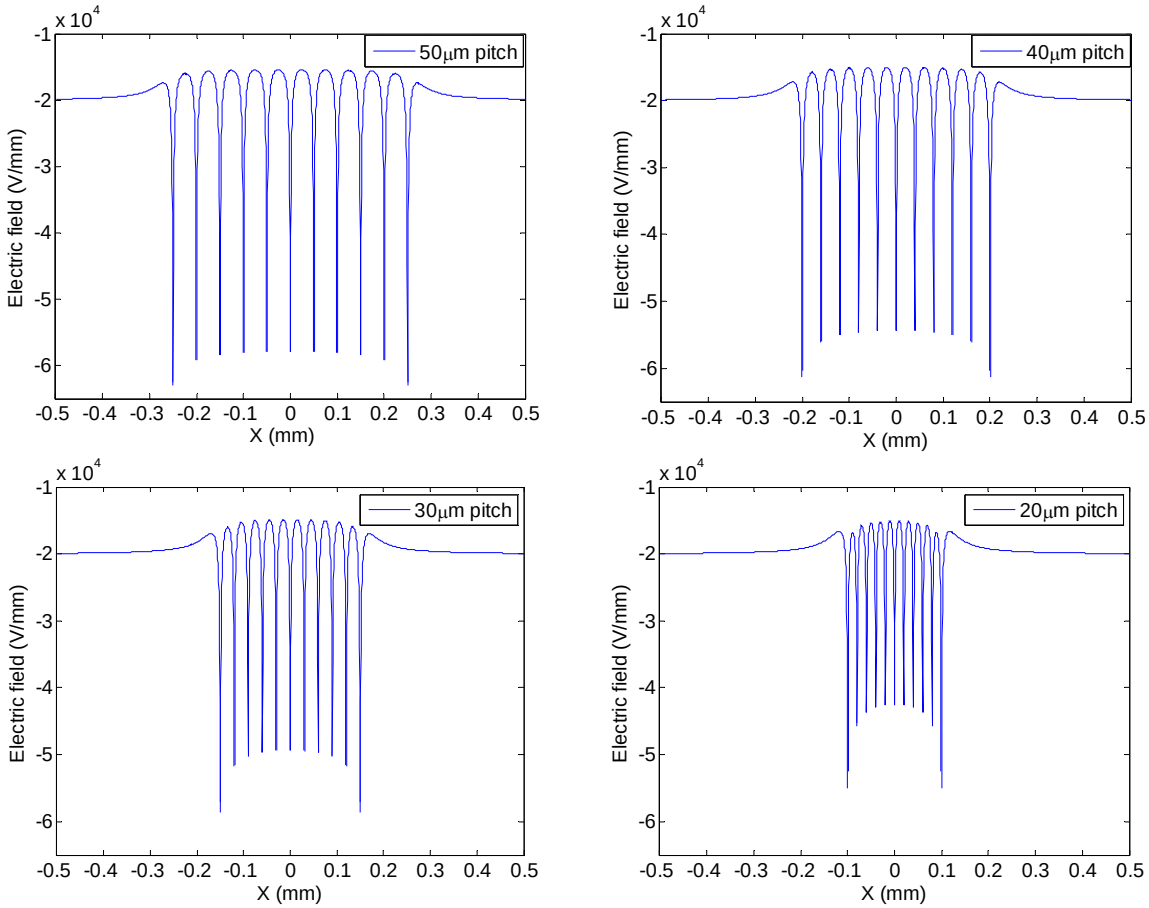

Figure 4.47 Distributions of the vertical electric field component across arrays of otherwise uniform grooves but with different spacings.

4.6 Summary of findings

This chapter has presented numerical and experimental investigations into electric field poling of lithium niobate patterned with laser machined topographical electrodes. Strong correlations between the simulated electrostatics of these surface structures and the characteristics of domain inversion resulting from electric field poling have been identified. Groove geometry, poling duration and packing density of grooves have been shown to be important factors in the control and quality of domain patterns produced with this technique. Most notably it has been shown that the groove's depth and aspect ratio play an important role in providing the electric field contrast suitable for poling. Grooves which have a significant depth, relative to the thickness of the substrate, introduce a substantial perturbation in the electric field which give rise to controlled domain inversion. Grooves whose depths that were at least 5% the thickness of substrate - a 20 μm depth in the 500 μm thicknesses looked at here – ensured reliable domain inversion. The aspect ratio of the grooves also plays an important role as noted in the previous investigations by Reich *et al* [49]. The simulations of the electrostatics of laser machined grooves has shown that there is a significant reduction in the electric field contrast for groove aspect ratios below $h{:}w \rightarrow$ 1:1. It has also been shown that the packing density of grooves may ultimately limit the periods achievable using this technique without any insulating layers. Discussions off future investigations which may improve the resolution of domain patterning with this technique and enable smaller periods to be reliably fabricated will be present in chapter 6.

Chapter 5. Frequency conversion and cascaded processes in laser fabricated PPLN crystals.

"The true delight is in the finding out
rather than in the knowing."
-Isaac Asimov
"In theory, there is no difference
between theory and practice.
But, in practice, there is"
- Manfred Eigen

5.1 Introduction

5.1.1 Chapter overview

This chapter looks at experimental demonstrations of optical frequency conversion with PPLN fabricated using laser machined electrodes and brings together the researh themes presented in previus chapters. For example the fabrication of the PPLN samples used in these experiments capitalises on the rapid prototyping attributes of the laser machined electrode patterning technique. With this technique, samples of poled crystal were taken from concept to finished product over the course of a day or less.

There will be three major themes developed in the subsequent sections of this chapter as follows;

- Section 5.2 deals with basic second harmonic generation (SHG), including the influence of chirped and phase reversed QPM gratings.
- Section 5.3 introduces the concept of simultaneous phase-matching of two distinct but wavelength equivalent SHG interactions via fabrication of the appropriate QPM grating. Both calculations and experimental demonstrations of the coherent interactions of simultaneously phase-matched processes are presented.
- Section 5.4 goes a step further with simultaneous interactions, and looks at the cascading that can take place between two phase-matched processes. A review of cascading in second order nonlinear optics is included, along with experimental results demonstrating

energy transfer between orthogonally polarised fundamentals can result from the scheme under study.

The following subsection presents an overview of the fabrication capabilities when using laser machined electrodes.

5.1.2 Poling quality and viable periods

In order to demonstrate both the flexibility and limitations of laser patterned electrodes for poling, and to reiterate the findings presented in Chapter 4, a section of crystal with 50 µm, 40 µm, 30 µm and 20 µm period gratings, each ~2.5 mm long, was fabricated using the same laser parameters for each grating (Figure 5.1). The sample was then poled with a 200 ms poling waveform.

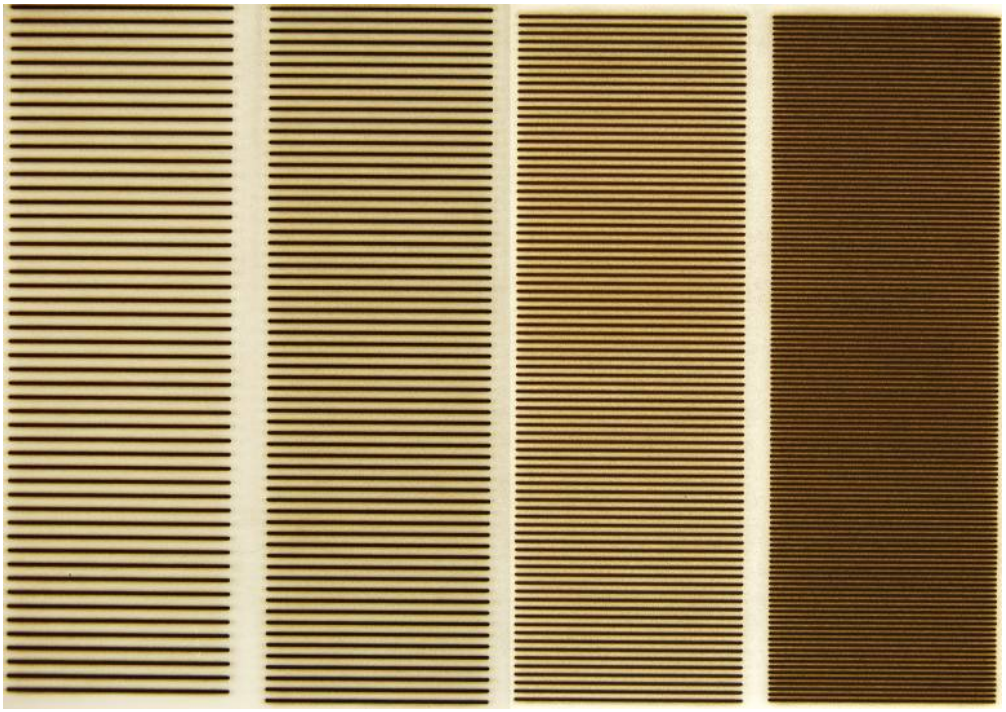

Figure 5.1 Laser machined gratings in lithium niobate. 2.5mm long sections with 50µm, 40µm, 30µm and 20µm periods.

The resulting domain patterns are shown below in Figure 5.2. The domain widths for all the gratings are very similar, an average width of ~8µm, which reflects the consistency of the laser machining. The 50 µm, 40 µm, and 30 µm gratings demonstrated regular domain formation with no missing inversions and very little duty cycle fluctuation. The 20µm period grating was of a poorer quality due to the collaborative field effect suggested in Chapter 4. Suffice to say that periods of 20 µm are the lower limit for reasonable quality PPLN fabricated with laser machined

electrodes in 500 µm thick crystal. The 2.5 mm lengths of 30 µm and 20 µm period are shown below in Figure 5.3 for comparison. With the fabrication capability demonstrated here there is still scope for some interesting experiments in QPM nonlinear optics, especially with type-I SHG in PPLN.

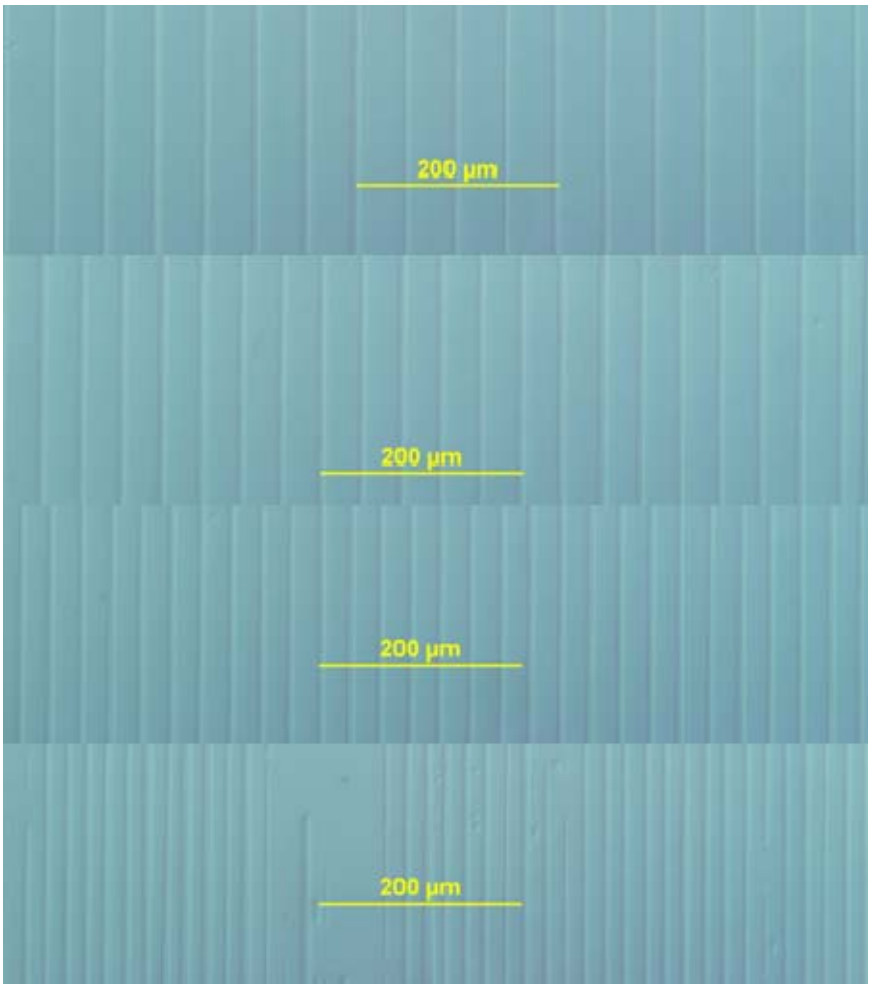

Figure 5.2 Domain patterns resulting from poling the sample in Figure 5.1.

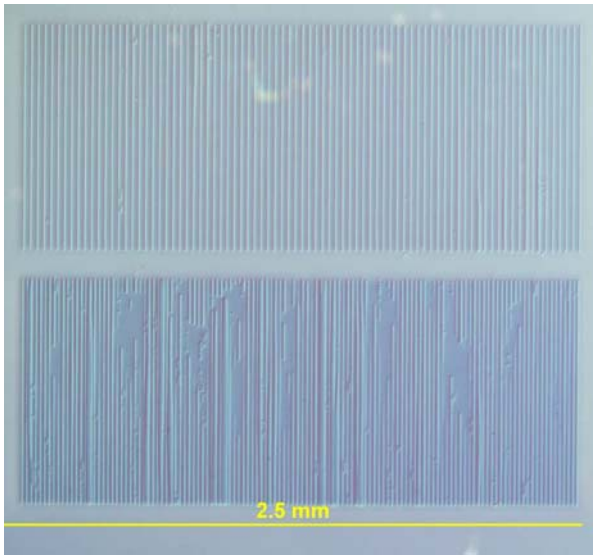

Figure 5.3 View of the 30µm (top) and 20µm (bottom) domain patterns fabricated under the same conditions.

Two dimensional and random domain patterning was also demonstrated using laser direct write fabrication. Ablation craters produced with 50-100 pulses arranged in arbitrary 2D arrays proved to be suitable for producing 2D domain patterns. Examples of a hexagonal and random distribution of domains fabricated using this technique are shown in Figure 5.4.

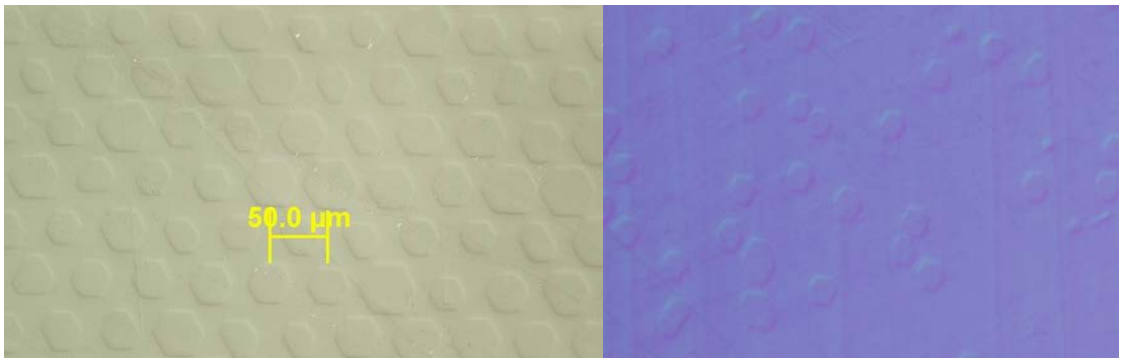

Figure 5.4 2D domain patterns fabricated by laser direct write machining. Left: Hexagonally arranged domains, right: random distribution of domains.

5.2 Temperature acceptance curves of SHG at 1064nm

5.2.1 Experimental setup

The nonlinear optics experiments in this project centred around a lab built Q-switched Nd:Gd:VO_4 (vanadate) laser. This laser produced 1 kW peak power pulses with a pulse repetition rate of 10kHz and pulse duration of 15 ns, operating on a single transverse mode with ~2 mm beam diameter. The laser was brought to focus with a 50 mm focal length lens coated for

IR transmission. Temperature control of the PPLN crystal was managed using a resistive cartridge heater controlled by a Eurotherm temperature control unit. This allowed either a steady temperature to be held or a temporal temperature profile to be applied to the heating element. The cartridge heater was slotted into a brass block, which had a flat ground top for the PPLN crystal. The beam was re-collimated using a second lens coated for visible imaging. Wave-plates were used to control the input polarization of the laser to the crystal, and a Glan prism was used to resolve the vertical and horizontal polarization components after passing through the PPLN. The setup is shown schematically in Figure 5.5.

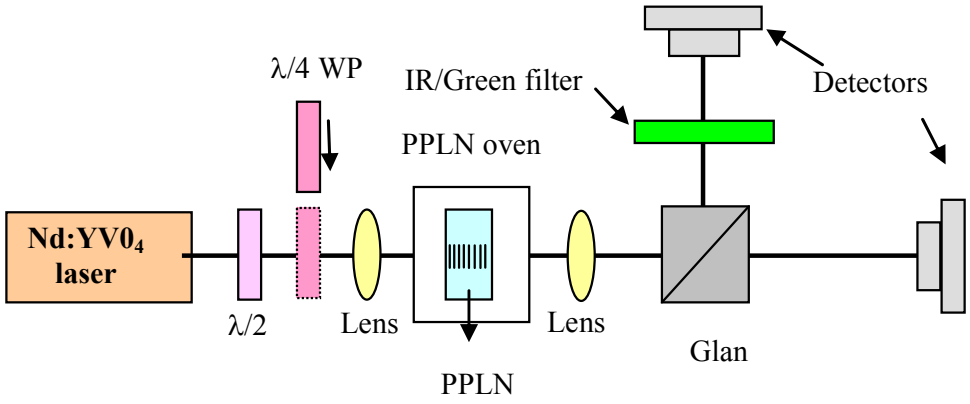

Figure 5.5 Schematic of experimental layout for frequency conversion experiments.

Data collection from a monitor thermocouple was carried out using a National Instruments E-series DAQ card and LabView 7 software. The fundamental or SHG power vs. crystal temperature relationship could thus be recorded in an automated fashion at 4 Hz sample rate.

5.2.2 Temperature detuning curves for SHG in PPLN

Preliminary measurements of second harmonic temperature acceptance curves were carried out with the crystal shown in Figure 5.2. The target QPM interactions with these gratings are 3rd order type-0 (*eee*) SHG at 107°C with the 20 μm period sample, and 1st order type-I SHG at temperatures between 160°C and 260°C with the 50, 40 and 30 μm periods. The experimentally measured type-0 temperature detuning curve is shown in Figure 5.6 with the calculated detuning curve based on Sellmeier equations from ref.[5]. The beam propagation for the data in Figure 5.6 was through the lower section of the 20 μm grating shown in Figure 5.3, where all of the domain inversions are present and merging of some inverted sections is the major defect. As a result the shape of the detuning curve was similar to a $sinc^2$ form as expected. The experimental temperature acceptance width is in good agreement with the calculated curve for the 2.5 mm

length of crystal. The apparent temperature offset of ~2°C may be due to either a discrepancy between the Sellmeier equations and the actual refractive indices, or an offset in the experimental temperature measurements due to the cold junction compensation setting on the probe thermal data.

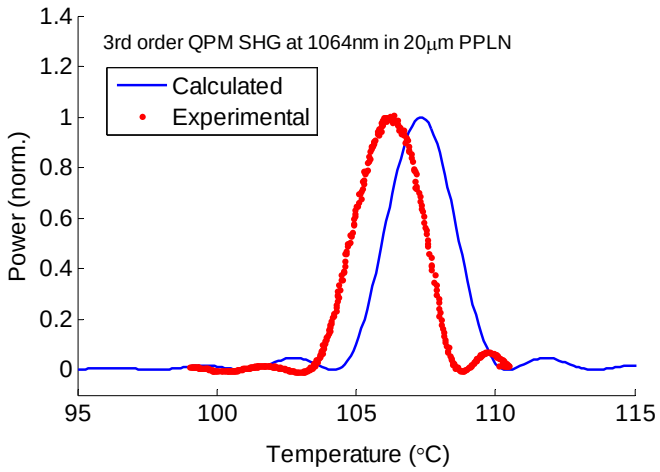

Figure 5.6 Experimental and calculated temperature detuning curves for 3rd order, type-0 SHG in 20 μm PPLN.

The measured type-I detuning curves for the 50, 40 and 30 μm period gratings are shown along side the plot of calculated curves in Figure 5.7. As shown in Figure 5.2, the gratings share the same domain size for all three periods. This results in a different duty cycle for each grating period, which based on an approximate domain size of 8 μm corresponds to duty cycles of 16%, 20% and 27% for the 50, 40 and 30μm periods respectively. The conversion efficiency from these different duty cycles is expected to scale as $\sin^2(\pi D)$, and the calculated plots have been scaled to reflect this. The experimental results show fair correlation with the expected relative efficiencies as the SHG increases across the three duty cycles, though the efficiency of the SHG from the 30 μm grating is not as high as expected. The measured temperature for phase-matching in the 30 μm grating is also lower than predicted, due to either discrepancies between Sellmeier equations and actual refractive indices or appreciable thermal expansion of the crystal at the higher temperatures, resulting in a longer than intended period. To demonstrate the scalability of the fabrication technique and the efficiency of type-I phase-matching a 10 mm section of crystal with a 40μm period was fabricated. An image of the domains across the sample from stitched microscope photos is shown in Figure 5.8.

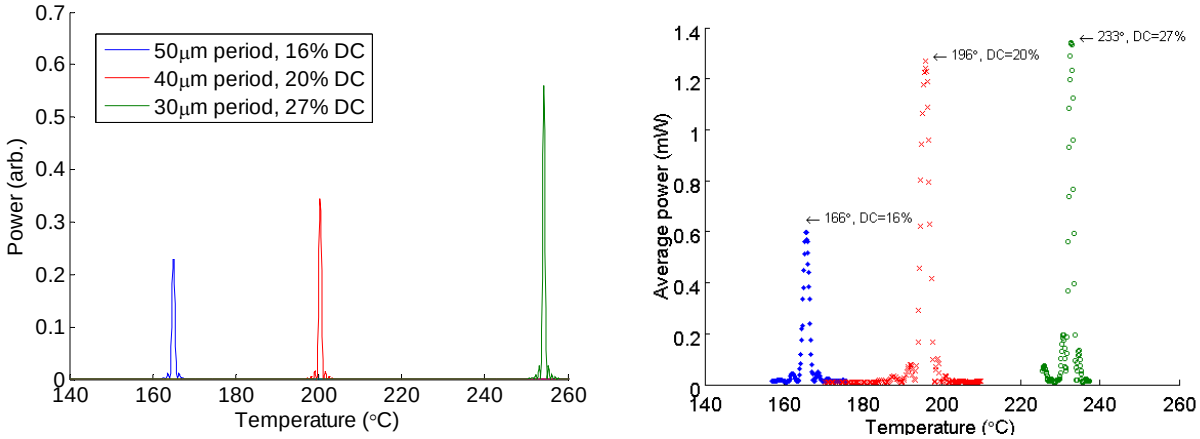

Figure 5.7 Temperature detuning curves for type-I SHG with 50, 40 and 30 µm period gratings in a 2.5 mm length of PPLN. Left: Calculated detuning curves for the period and duty cycles indicated. Right: measured detuning curves for the crystal sample shown in Figure 5.2.

Figure 5.8 Domains across a 10 mm section of laser direct write fabricated PPLN with a 40 µm period.

The temperature detuning curves for SHG in the 10 mm sample are in Figure 5.9. The overall efficiency of the SHG conversion is ~20% with was consistent with the efficiency expected for QPM with the d_{31} nonlinear coefficient. The shape of the detuning curves are asymmetric, compared to expected $sinc^2$ form. As discussed near the end of section 2.4, this type of asymmetric distortion of the tuning curve points to a distributed phase-mismatched across the sample, as shown in the lower plots of Figure 5.9. The most likely cause of this in these experiments was thermal inhomogeneities within our lab-built crystal oven, as the facets of the 10 mm crystal were close to the openings in the oven. This issue did not obviously affect shorter lengths of crystal, such as the 4.5 mm lengths used for the experiments reported later in this chapter.

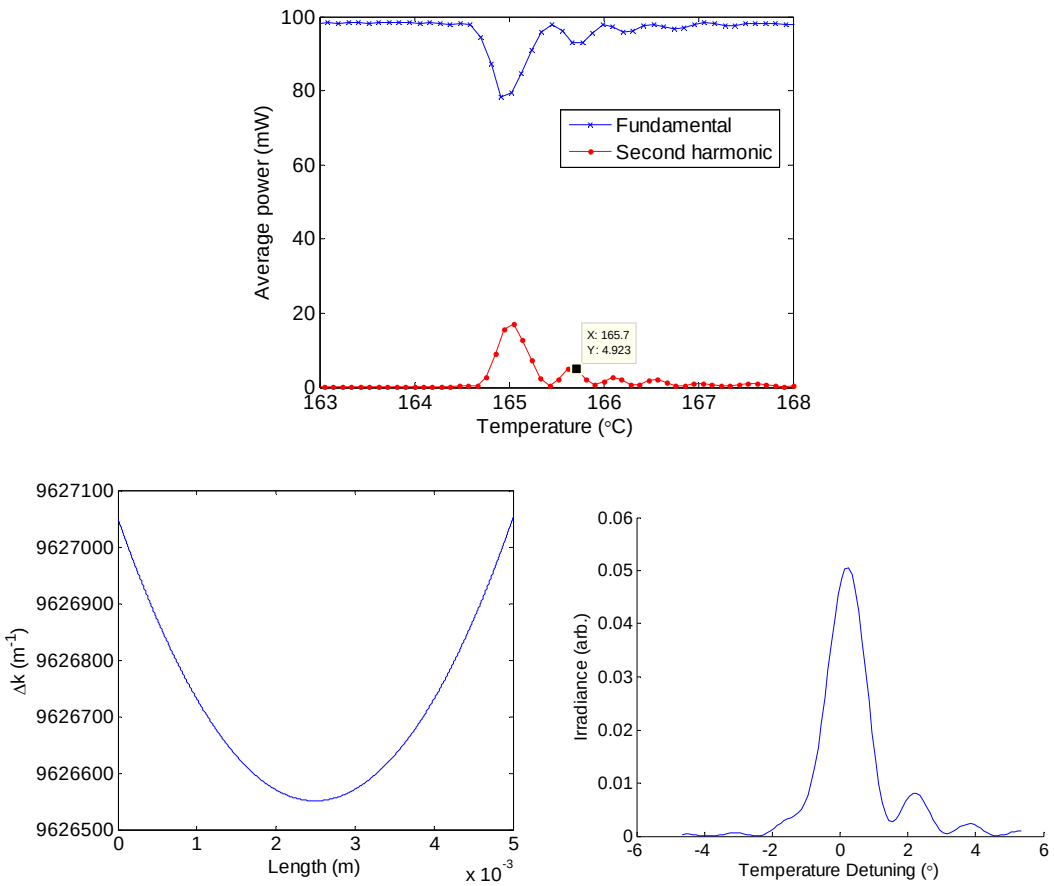

Figure 5.9 Top: temperature detuning curves for type-I SHG in a 10 mm long 40 µm period PPLN sample. Bottom: simulated quadratic phase-mismatch distribution through a length of crystal and the corresponding detuning curve.

One of the advantages of the direct write method is the ability to quickly make prototypes of different domain patterns simply by programming the motion control system. As examples of this capability, poled samples with chirped and phase-reversed domain patterns were fabricated. The chirped sample consisted of two gratings, each of 100 periods, one of which was programmed to have a fixed period at 45 µm, the other had its period programmed to increase by 25 nm each period, resulting in a grating which had a linearly chirped period from 45 µm to 47.5 µm. The calculated Fourier spectra for these two gratings are shown in on the left of Figure 5.10. The measured temperature detuning curves for Type-I SHG showed very good qualitative agreement with shape and relative strength of the chirped and fixed period grating.

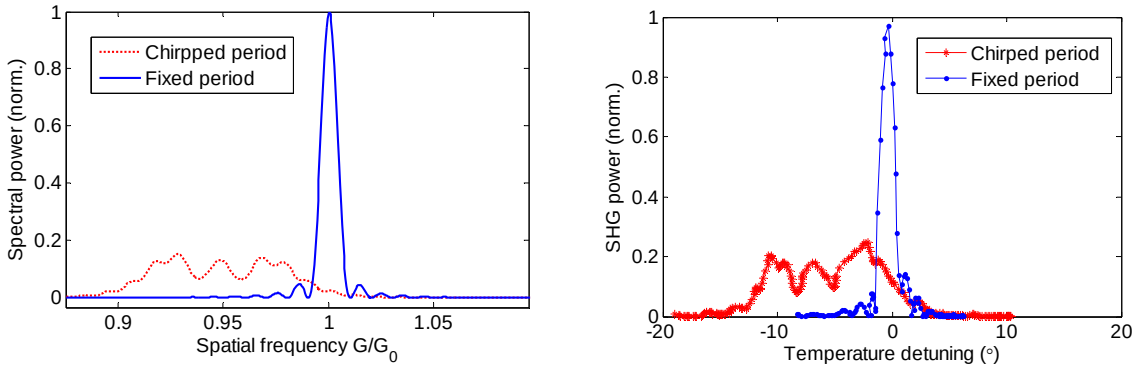

Figure 5.10 Left: Calculated Fourier spectra gratings with 100 periods containing chirped (45 - 47.5 µm) and fixed (45um) periods. Right: Experimentally measured temperature detuning curves for these gratings for Type-I SHG at 1064 nm.

The design for the example phase-reversed grating was selected so that the domains which were reversed during poling were all of the same width. This design stipulation is achieved by setting the period of the phase reversal to be an integer multiple of the primary period, and to set the duty cycle of the phase reversal envelope to be 25%. A section of the domains in the fabricated sample is shown in Figure 5.12.

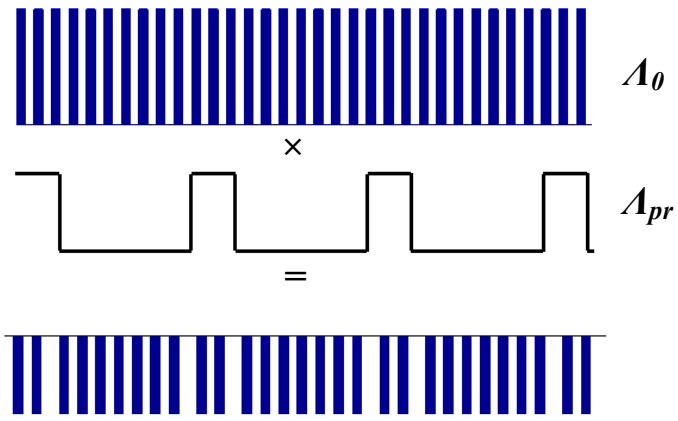

Figure 5.11 Phase-reversed grating with 25% duty cycle phase-reversal modulation.

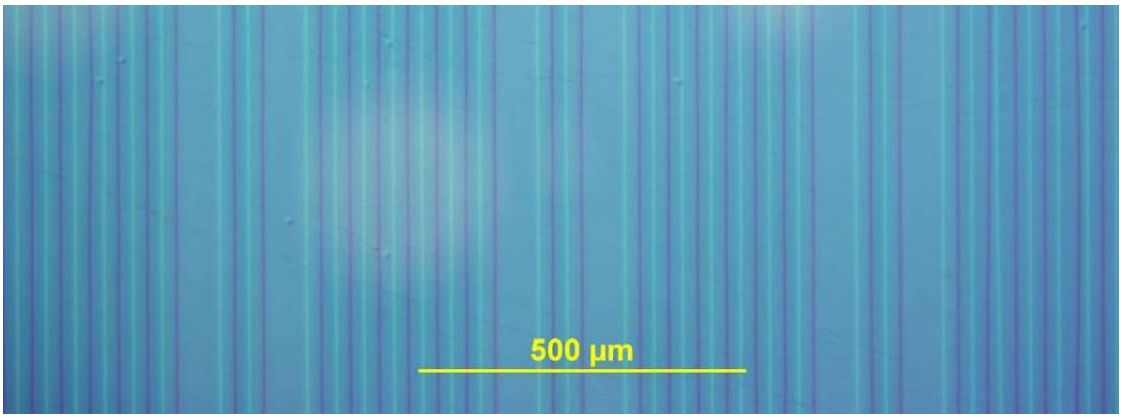

Figure 5.12 Sample fabricated with the phase-reversed domain structure shown above in Figure 5.11.

The temperature detuning curves for the phase-reversed sample was measured across a temperature range of 120-220°C. The experimental data is shown Figure 5.13. Periodicity errors in this particular grating meant that the performance of the sample was not optimal. Phase-matching at 'sideband' temperatures around the primary peak were clearly observed, demonstrating the spatial content of the domain pattern had been diversified by fabrication of the phase-reversed grating.

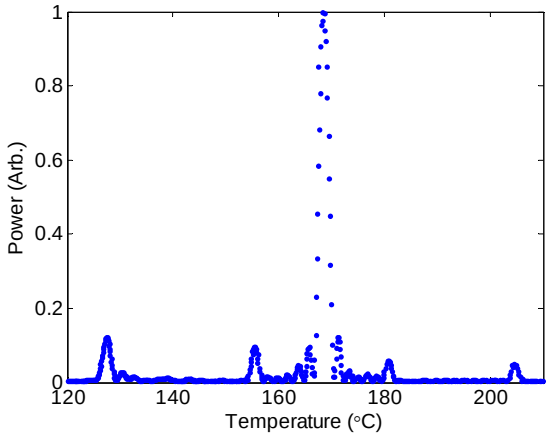

Figure 5.13 Temperature detuning curve for SHG in the phase-reversed crystal shown in Figure 5.12.

5.3 Simultaneous phase-matching of two SHG types

5.3.1 Background and calculations

As pointed out previously in section 2.2, there are several components of lithium niobate's second order optical nonlinearity which can be accessed by quasi-phase-matching. In particular,

the second order polarisation of lithium niobate is given by

$$\begin{pmatrix} p_x \\ p_y \\ p_z \end{pmatrix}^{(2)} = \sum_{j,k} \chi_{ijk}^{(2)} E_j^{\omega_1} E_k^{\omega_2} = 2\varepsilon_o \begin{pmatrix} 0 & 0 & 0 & 0 & d_{31} & -d_{22} \\ -d_{22} & d_{22} & 0 & d_{31} & 0 & 0 \\ d_{31} & d_{31} & d_{33} & 0 & 0 & 0 \end{pmatrix} \begin{pmatrix} E_x^2 \\ E_y^2 \\ E_z^2 \\ 2E_yE_z \\ 2E_xE_z \\ 2E_xE_y \end{pmatrix}^{(\omega_x,\omega_y,\omega_z)} \quad (5.1)$$

For d_{33} and d_{31} terms, which induce polarisation components along the ferroelectric z-axis of the crystal, the inversion of the nonlinear susceptibility with domain reversal is intuitive. The d_{22} terms, however, are not obviously linked to the ferroelectric axes of the crystal. Recent investigations by Ganany *et al*[198] have shown that full inversion of the χ^2 susceptibility takes place and that QPM with the d_{22} nonlinear coefficient is also attainable. The inversion of the d_{22} coefficient is not surprising, as it is required for the crystal symmetry to be preserved, i.e. for the axes to remain a 'right handed' set for example. Practically and historically, QPM on the d_{33} nonlinear, coefficients in LN, LT and KTP has been of most interest as they are some of the largest second-order nonlinearities available in inorganic crystals. Interactions using this nonlinear coefficient require all fields to be co-polarized, so it is not accessible via birefringent phase-matching, hence the use of periodic poling. There are also some interesting processes which can be investigated by considering the other nonlinear coefficients accessible by QPM. In particular, by fabricating the appropriate QPM grating simultaneous phase-matching on more than one nonlinear coefficient can be achieved.

For clarity, in this chapter the definition of phase-matching 'type' will be as follows;

- Type-0, all participating fields are co-polarized in the crystal
- Type-I, the two longer wavelengths are co-polarized, with the shortest wavelength polarized orthogonally to those.
- Type-II, the two longer wavelengths are orthogonally polarized to each other, with the shorter wavelength being co-polarized with one or other of the longer wavelength fields.

Utilizing the d_{33} and the d_{24} nonlinear coefficients simultaneously in PPKTP has been demonstrated by Pasiskevicius *et al*[199] for SHG of a tuneable Ti:Sapphire laser (blue SHG). As Pasiskevicius *et al* points out, the benefits of using type-I phase-matching in KTP and lithium niobate include broader wavelength acceptance and polarisation separable fundamental and second-harmonic. One of the recent application areas of type-II phase-matching is parametric

down conversion as it allows generation of frequency degenerate orthogonally polarized photon pairs[200] for quantum information applications. In z-cut lithium niobate, the focus of this dissertation, the nonlinear interactions of interest are those with fields propagating perpendicular to the z-axis of the crystal. For SHG these include type-0 QPM on the d_{33} (eee) or d_{22} (ooo) coefficients, type-I QPM on the $d_{31}=d_{32}$ (ooe) coefficients, and type-II (oeo) QPM on the d_{24}, $d_{15}=d_{32}$ coefficients. These interactions are summarized in Table 5.1.

QPM type	**Refractive indices**	**Crystal axes**	**Nonlinear coefficient**
Type-0	ee-e	zz-z	d_{33}
Type-0	oo-o	xx-x or yy-y	d_{22}
Type-I	oo-e	yy-z or xx-z	$d_{32}=d_{31}$
Type-II	oe-o	yz-y or xz-z	$d_{14}=d_{24}=d_{31}$

Table 5.1 Options for QPM in z-cut PPLN

Another degree of freedom when using periodically poled materials is the choice of the QPM order. This allows longer periods to be used, albeit with sacrifices of the effective nonlinearity. Chen *et al*[201] have demonstrated type-0 and type-I QPM using the same period grating in the for blue light generation. This is achieved by utilising a higher order QPM for the type-0 process and finding a crystal temperature and grating period where simultaneous phase-matching with the type-I interaction can be achieved. Plots of the required poling period for SHG common laser wavelengths of 976 nm, 1064 nm, 1342 nm and 1550 nm are shown in relation to temperature in Figure 5.14. The type-0, type-I and type-II processes have all been considered along with some of the higher QPM orders. It is also interesting to look at some of the phase-matching periods which coincide across the wavelengths being considered. A selection of these for the type-0 (*eee*) and type-I (*ooe*) interactions are shown in Figure 5.15.

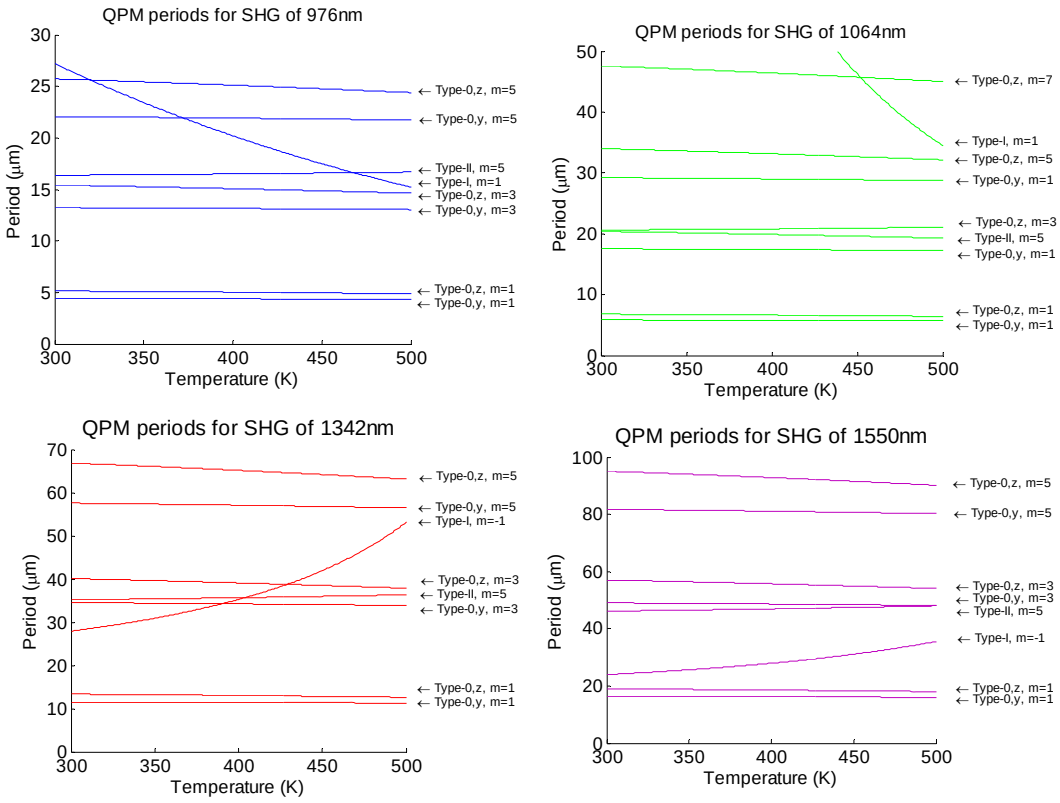

Figure 5.14 QPM periods for SHG at some common laser wavelengths.

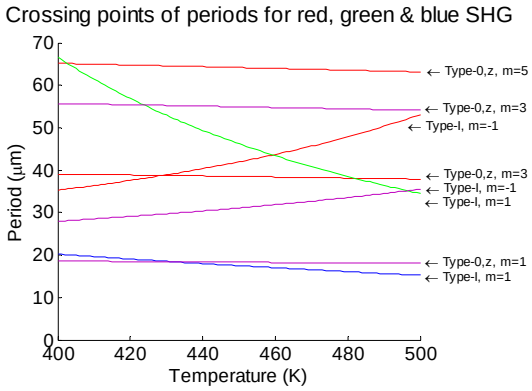

Figure 5.15 Crossing points of QPM periods for red, green and blue SHG. Red plots indicate 1342nm fundamental, green 1064nm, blue 976nm and mauve 1550nm.

Of interest in Figure 5.14 are the crossing points for the different phase-matching types. These are brought about because the type-I interaction in lithium niobate has a much faster change in period with temperature ($d\Lambda/dt$) than the other process. This is due to the fundamental and second-harmonic propagating on the *o* and *e* refractive indices, respectively, which have significantly different thermo-optic responses (dn/dt). On the other hand the Type-I processes utilize the same refractive indices for both wavelengths and the dn/dt at the fundamental and

second-harmonic wavelengths is only slightly different. This results in type-0 QPM periods which change only 100's of nanometers over 100's of degrees, whereas the type-I QPM periods can change over 10's of micrometers for the same change in temperature. The sign of the phase-mismatch, Δk, can also change from being positive to negative about the non-critical phase-matching point (where the nonlinear coherence length and thus required poling period become very large). In congruent lithium niobate above 300 K this is in the 1080-1200 nm range as shown below in Figure 5.16.

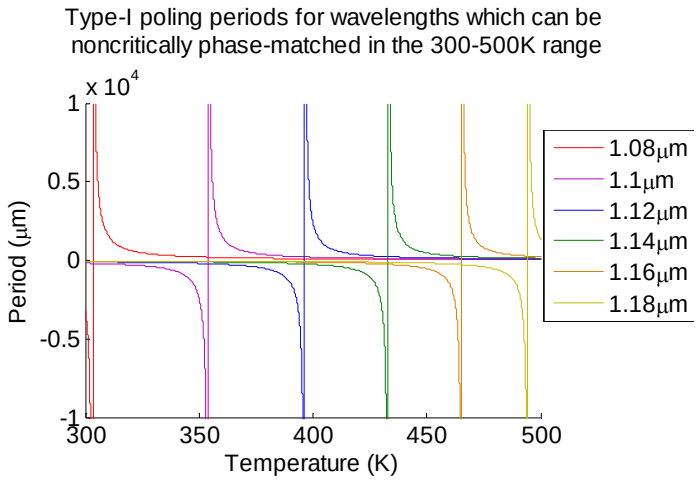

Figure 5.16 QPM periods for wavelengths near non-critical type-I phase-matching in congruent composition lithium niobate.

For conditions where Δk, and thus the implied required period becomes negative, the negative QPM orders come into play, with no real practical difference to the SHG process. These large changes in Δk for the type-0 processes, over the temperature range 300-500K, results in several periods and temperatures at which simultaneous phase-matching with other phase-matching types occurs. A summary of these points for the 976nm, 1064nm and 1342nm wavelengths, as shown above in Figure 5.14, is given in Table 5.2.

Wavelength	Phase-matching types	Period	Temperature
976nm	Type-I, Type-0,z (m=5)	25.616μm	320.15K
976nm	Type-I, Type-0,y (m=5)	21.967μm	371.63K
976nm	Type-I, Type-II (m=5)	16.624μm	468.04K
976nm	Type-I, Type-0,z (m=3)	14.561μm	516.35K
1064nm	Type-I, Type-0,z (m=5)	31.994μm	514.46K
1064nm	Type-I, Type-0,z (m=7)	45.712μm	451.76K
1342nm	Type-I, Type-0,z (m=5)	62.561μm	526.23K
1342nm	Type-I, Type-0,y (m=5)	56.393μm	510.23K
1342nm	Type-I, Type-0,z (m=3)	38.763μm	428.91K
1342nm	Type-I, Type-II (m=5)	35.705μm	403.85K
1342nm	Type-I, Type-0,y, (m=3)	34.283μm	390.09K

Table 5.2 Conditions for simultaneous type-I with another phase-matching type for some common laser wavelengths.

Returning attention to Figure 5.15, it can be seen that there are some particular periods where multiple SHG wavelengths cans be simultaneously phase-matched. Of particular interest are the crossing points where simultaneous phase-matching of 1064nm and 1342nm (both type-I processes) occur. Type-I SHG for these wavelengths at a temperature of 460K has the same size, but differently signed, phase-mismatch. This means that a single PPLN crystal with a period of 43.56μm at 460 K can be used to phase-match SHG from both these both Nd laser lines without requiring a complex grating pattern. There are several other wavelengths pairs, one on either side of the non-critical phase-matching wavelengths which can be simultaneously type-I phase-matched by a single period crystal. This is a potentially interesting prospect for dual wavelength visible Nd or Raman lasers which can utilise a single nonlinear crystal which does not require tuning when changing between colours, and can generate both colours simultaneously if both fundamentals are present.

The scope of the experimental work in this dissertation is based around the 1064 nm Nd laser line. The 5th order and 7th order type-0 SHG processes can be simultaneously phase-matched with the type-I process at particular periods and temperatures, as reiterated below in Figure 5.17. While using the higher orders for the type-0 process does sacrifice the high nonlinearity commonly sought from the d_{33} nonlinear coefficient, use of the 5th and 7th orders

turns out to be somewhat favourable as the effective nonlinearities of the type-0 and type-I phase-matchings can be made very similar. For instance, the 5th and 7th type-0 SHG have effective nonlinearities of,

$$\frac{2d_{33}}{5\pi} \approx 3.8 pm/V \tag{5.2}$$

$$\frac{2d_{33}}{7\pi} \approx 2.7 pm/V \tag{5.3}$$

which are very similar to the effective nonlinearity for the type-0 process,

$$\frac{2d_{31}}{\pi} \approx 3 pm/V \tag{5.4}$$

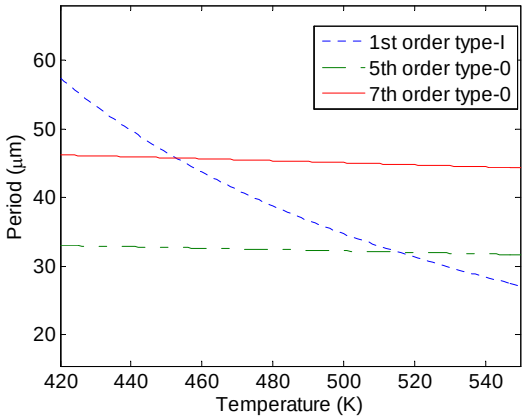

Figure 5.17 QPM periods for 5th and 7th order type-0 and 1st order type-I SHG at 1064nm.

The coupled field equations which describe simultaneous phase-matching are a superposition of the two individual processes, bearing in mind that the second harmonic field for the type-0 and type-I SHG is co-polarized and can be treated as a common component. The field equations can thus be written as,

$$\frac{dE_z^{\omega}}{dx} = -i\sigma_1 \vec{E}_z^{2\omega} \vec{E}_z^{\omega *} e^{-i\Delta k_0 x} \tag{5.5}$$

$$\frac{dE_y^{\omega}}{dx} = -i\sigma_2 \vec{E}_z^{2\omega} \vec{E}_y^{\omega *} \mathrm{e}^{-i\Delta k_I x} \tag{5.6}$$

$$\frac{dE_z^{2\omega}}{dx} = -i\sigma_1 (\vec{E}_z^{\omega})^2 \mathrm{e}^{i\Delta k_0 x} - i\sigma_2 (\vec{E}_y^{\omega})^2 \mathrm{e}^{i\Delta k_I x} \tag{5.7}$$

where the nonlinear and propagation constants have been collected into the σ terms and Δk_0 and Δk_I are the phase mismatch terms for type-0 and type-I respectively. The subscripts denote the fields' polarization and the superscripts denote the frequency. The relative phase between the two contributing fundamental fields plays an important role in the simultaneous phase-matching

scenario. In general the plane-wave electric field with an amplitude A can be written with an arbitrary phase, ϕ,

$$\vec{E}^{\omega} = \tfrac{1}{2} A e^{i(\omega t - kx + \phi)} + cc \tag{5.8}$$

This generalization is usually ignored in the equations describing SHG with a single fundamental field as the generated second-harmonic is phase-locked to it the fundamental with a $\pi/2$ phase shift. The phase of fundamental is thus the point of reference and is set to zero. For the case of two fundamentals which are simultaneously phase-matched, a phase term to account for the phase difference between the contributing fundamentals needs to be included. The time invariant form of the second harmonic term, Eq (5.7), in the coupled field equations is then written as,

$$\frac{dE_z^{2\omega}}{dx} = -\sigma_3 \left(A_y\right)^2 e^{i\Delta k_I x} - \sigma_4 \left(A_z e^{i\phi}\right)^2 e^{i\Delta k_0 x} \tag{5.9}$$

where the type-I fundamental has been taken as the reference field and the type-0 fundamental has an arbitrary phase-shift ϕ with respect to it. In the negligible depletion regime Eq. (5.9) can be integrated in a similar fashion as for the single process,

$$E_z^{2\omega} = \int_0^L \frac{dE_z^{2\omega}}{dx} dx = -\sigma_3 \left(A_y^{\omega}\right)^2 L e^{i\Delta k_1 L/2} \, \mathrm{s}inc(\Delta k_1 L/2) - \sigma_4 \left(A_z^{\omega} e^{i\phi}\right)^2 L \, \mathrm{e}^{i\Delta k_0 L/2} \, \mathrm{s}inc(\Delta k_0 L/2) \tag{5.10}$$

For ideal phase-matching of both processes, $\Delta k_I = \Delta k_0 = 0$, so that (5.10) reduces to,

$$E_z^{2\omega} = -\sigma_3 A_y^2 L - \sigma_4 A_z^2 e^{2i\phi} L \tag{5.11}$$

The irradiance of the second-harmonic ($I = \dfrac{E^* E}{2Z}$) is then,

$$\begin{aligned} I^{2\omega} 2Z^{2\omega} &= \left(-\sigma_3 \left(A_y^{\omega}\right)^2 L - \sigma_4 \left(A_z^{\omega}\right)^2 e^{2i\phi} L\right).\left(-\sigma_3 \left(A_y^{\omega}\right)^2 L - \sigma_4 \left(A_z^{\omega}\right)^2 e^{-2i\phi} L\right) \\ &= {\sigma_3}^2 \left(A_y^{\omega}\right)^4 L^2 + {\sigma_4}^2 \left(A_z^{\omega}\right)^4 L^2 + \sigma_4 \sigma_3 L \left(A_z^{\omega}\right)^2 \left(A_y^{\omega}\right)^2 e^{2i\phi} + \sigma_4 \sigma_3 L \left(A_y^{\omega}\right)^2 \left(A_z^{\omega}\right)^2 e^{-2i\phi} \\ &= {\sigma_3}^2 4 Z_y^2 I_y^{\omega 2} L^2 + {\sigma_4}^2 4 Z_z^2 I_z^{\omega 2} L^2 + \sigma_4 \sigma_3 L^2 2 Z_z I_z^{\omega} 2 Z_y I_y^{\omega} \left[2 \cos 2\phi\right] \end{aligned} \tag{5.12}$$

Note the cross term which has been introduced into in the expression for the second harmonic irradiance. This means the second harmonic will have a strong dependence on the phase between the two fundamentals. Most notably if the nonlinearities and impedances for the two processes are similar so that,

$$\frac{\sigma_1 Z_y^{\omega}}{Z_z^{2\omega}} \approx \frac{\sigma_2 Z_z^{\omega}}{Z_z^{2\omega}} = \alpha \tag{5.13}$$

We can reduce the expression to,

$$I^{2\omega} = \underbrace{2\alpha^2 I_y^{\omega 2} L^2}_{\text{Y-polarised fundamental}} + \underbrace{2\alpha^2 I_z^{\omega 2} L^2}_{\text{Z-polarised fundamental}} + \underbrace{4\alpha^2 L^2 I_z^{\omega} I_y^{\omega} \left[\cos 2\phi\right]}_{\text{Cross term}} \tag{5.14}$$

Looking in detail at Eq. (5.14), when equal irradiance fundamentals with a $\phi = \pi/2$ (¼ wave) phase-shift are incident on the crystal the second harmonic output can actually be suppressed by the two competing nonlinear processes. The amount of second-harmonic produced by simultaneously phase-matched fundamentals is therefore not only dependant on the amplitudes of the fundamentals, but also their relative phase. Slight departures from the phase-mismatching conditions complicate things further, with the complete expression for the small signal second-harmonic found as:

$$\begin{aligned} I^{2\omega} &= 2\alpha^2 I_y^2 L^2 \,\mathrm{s}inc^2(\Delta k_1 L/2) + 2\alpha^2 I_z^2 L^2 \,\mathrm{s}inc^2(\Delta k_0 L/2) \\ &+4\alpha^2 I_z I_y L^2 \,\mathrm{s}inc(\Delta k_1 L/2)\,\mathrm{s}inc(\Delta k_0 L/2)\cos\left[2\phi + \Delta k_0 L/2 - \Delta k_1 L/2\right] \end{aligned} \tag{5.15}$$

It can be seen that any slight phase-mismatch will also play a significant role in determining the amount of second-harmonic output seen in the term, $\cos\left[2\phi + \Delta k_0 L/2 - \Delta k_1 L/2\right]$, especially since Δk_0 and Δk_1 can be of different signs and magnitudes for a given temperature, wavelength or grating period detuning. It is interesting to note that for the phase-matched case with no phase-shift, $\phi = 0$, any linear input polarisation for a given irradiance will produce the same amount of second-harmonic. For a linearly polarised input with irradiance, I_0, polarized at an angle θ from the z-axis, the linear polarisation components can be expressed as,

$$\begin{aligned} E_z &= E_0 \sin\theta \\ E_y &= E_0 \cos\theta \\ &\therefore \\ I_z &= I_0 \sin^2\theta \\ I_y &= I_0 \cos^2\theta \end{aligned} \tag{5.16}$$

Referring back to Eq (3.1),

$$\begin{aligned} I^{2\omega} &= 2\alpha^2 (I_0 \cos^2\theta)^2 L^2 + 2\alpha^2 (I_0 \sin^2\theta)^2 L^2 + 4\alpha^2 L^2 I_0^2 \sin^2\theta\cos^2\theta[\cos 2\phi = 1] \\ I^{2\omega} &= 2\alpha^2 I_0^2 \left[\cos^2\theta + \sin^2\theta\right]^2 L^2 \\ I^{2\omega} &= 2\alpha^2 I_0^2 L^2 \end{aligned} \tag{5.17}$$

So with perfect simultaneous phase-matching with similar nonlinearities and a linear input polarization state, the direction of the polarization does not affect the second-harmonic output. It may also be expected that a randomly polarized fundamental, such as from a free running fibre laser, may see improved generation of a polarized second-harmonic by utilizing such a phase-matching scheme.

5.3.2 Experimental results and simulations

As mentioned, the simultaneous phase-matching experiments looked at during this project targeted the coincident period for 1st order type-I and 7th order type-0 SHG with a fundamental wavelength at 1064 nm. The calculated period for this from Sellmeier equations is 45.712 µm, however Sellmeier equations from reference may not be exact for our particular crystal, and thermal expansion of the crystal may result in a grating period slightly different to that intended from fabrication. In order to empirically find the correct period for simultaneous phase-matching, a section of PPLN containing two gratings with 45 µm and 46 µm periods, above and below the predicted period, was fabricated. The temperatures (un-calibrated) where the optimal phase-matching for the type-0 and type-I processes were recorded and plotted on the same graph, shown in Figure 5.18.

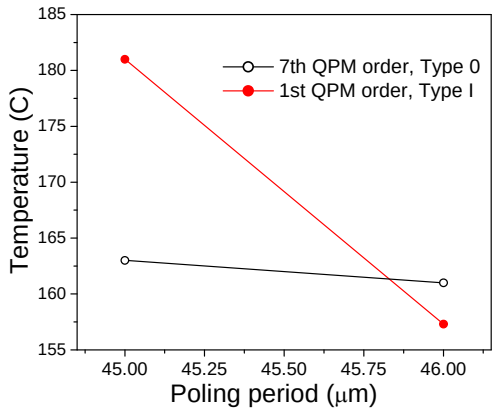

Figure 5.18 Phase-matching temperatures observed for type-0 and type-I QPM in 45µm and 46µm period PPLN

From the linear intersection between the phase-matching temperatures for the 45 µm and 46 µm gratings, an indication of the period required for simultaneous phase-matching was made. As seen in Figure 5.18, this period lies between 45.75µm and 45.8µm, slightly longer than the period predicted from Sellmeier equations. Angle tuning of gratings with slightly shorter periods than

required is an easy technique for fine tuning the effective period of the grating so fabrication of the exact period is not entirely necessary. A section of PPLN containing with programmed periods of 45.75 μm and 45.8 μm was fabricated. A section of one of these gratings is shown in Figure 5.19. The crystal was ~3mm in length containing 67 QPM periods. Upon visual inspection this crystal showed good domain quality but was slightly under-poled with an average duty cycle of 26%. Such a duty cycle is far from optimal for the 7th order process, as shown in the plot of relative efficiency vs. duty cycle in Figure 5.20. This crystal did show overlapping of the two phase-matching curves in both gratings as shown in Figure 5.21, however the 7th order type-0 curves were strongly distorted from the expected $sinc^2$ form. This was perhaps not surprising as 7th order QPM is much more sensitive to short range fluctuations in the domain duty cycle and periodicity (especially with 26% duty cycle), as was discussed in detail in section 2.4. The grating with the 45.8 μm period showed the best overlap between the maxima of the type-0 and type-I curves, while the best conversion efficiency was observed in the 45.75μm period grating, with ~40% of the conversion efficiency of the type-I process.

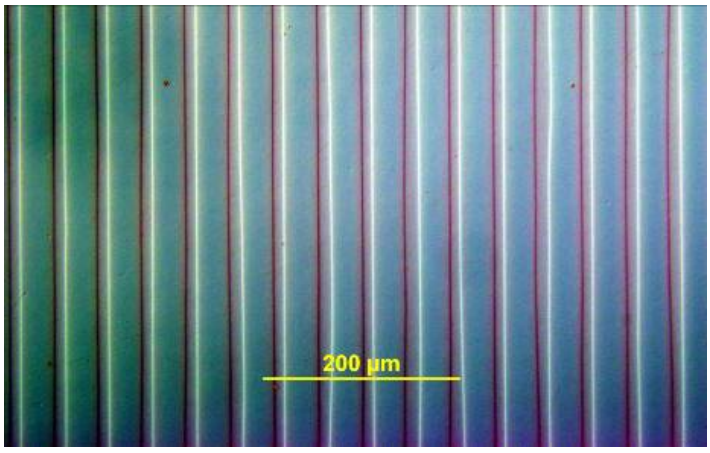

Figure 5.19 Section of a PPLN crystal containing 45.75μm and 45.8μm period gratings.

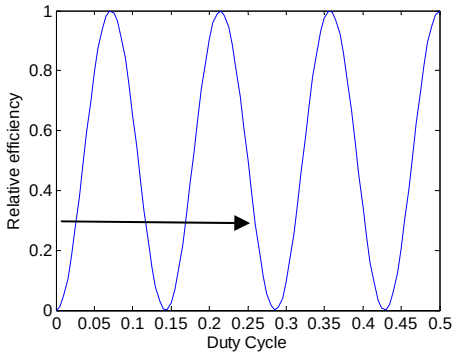

Figure 5.20 Relative SHG efficiency in relation to domain duty cycle for a 7th order process. Arrow indicated the predicted relative efficiency for of a 7th order QPM grating with a duty cycle of 26%.

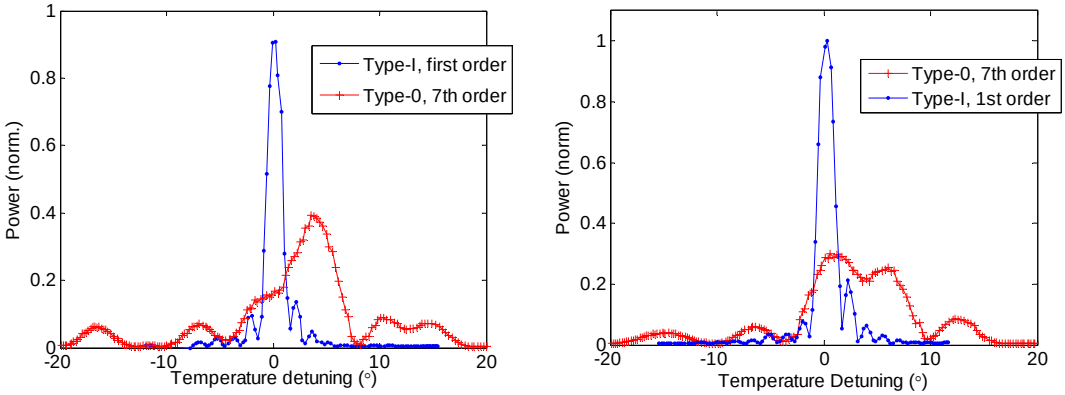

Figure 5.21 Experimental temperature detuning curves of 7th order type-0 and 1st order type-I SHG. Left: 45.75µm period grating, right: 45.8µm period grating.

Experiments investigating the effects of the input fundamental's polarisation state were carried out with these gratings using the experimental setup shown in Figure 5.5. The temperature was set to phase-match the type-I process, and wave-plates were used to prepare the fundamental's polarisation state. Rotation of the half-wave-plate (HWP) changed the relative irradiances of the vertical and horizontal components while the quarter-wave-plate (QWP) was fixed with is fast and slow axes aligned to the lithium niobate axes so that a quarter-wave retardance between the vertical and horizontal polarization components was maintained. The second-harmonic output was then plotted as a function of the input polarization state, either for linear states without the QWP or elliptical polarization states with the QWP. The progression of the polarization state as the HWP is rotated is illustrated in Figure 5.22.

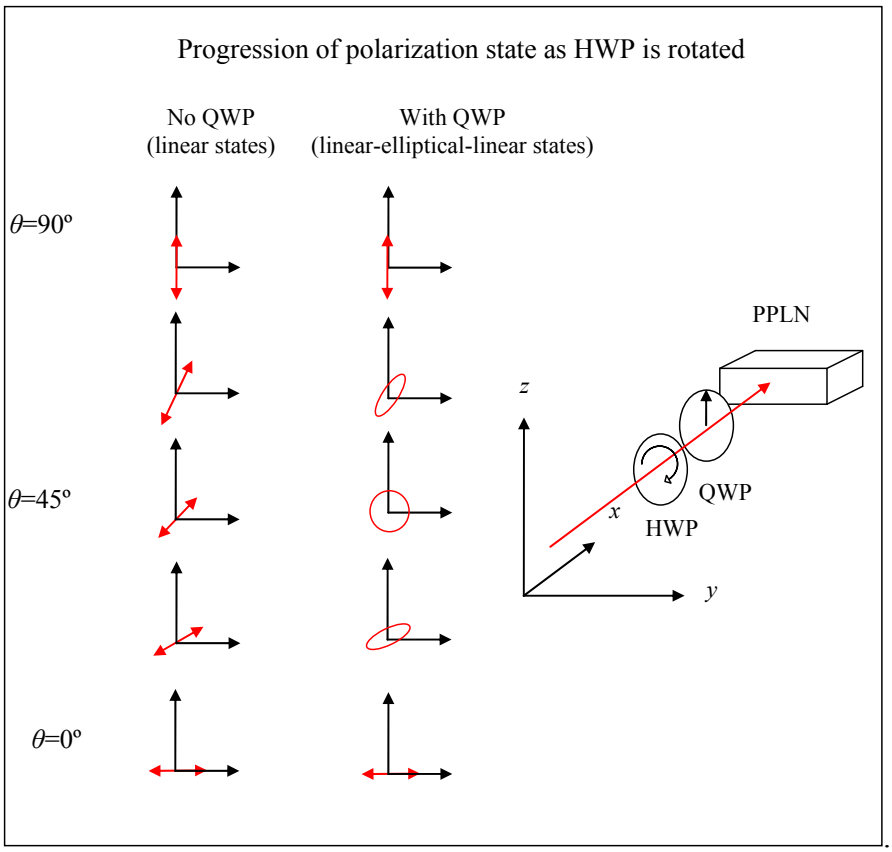

Figure 5.22. Preparation of the input polarisation state to the PPLN crystal as a half-wave-plate is rotated. The axes on the left show the linear polarisation states prepared with only the HWP, while the axes on the right indicate the polarisation states with a QWP in tandem, with its axes aligned on the crystal axes.

The ¼ wave shift between the vertical and horizontal polarization components produced by the QWP results in elliptical polarization states, with circular polarization being produced for equal vertical and horizontal components. Intuitively, such a polarization state drives the nonlinear susceptibilities along the z and x axes of the crystals out of phase with each other so that the second-harmonic wavelets generated from the two processes interfere destructively. This type of behaviour can be simulated using Eq (5.17) by plotting the second harmonic as a function of the polarization (HWP) orientation, θ, and for the two phase differences of $\phi = 0$ for linear polarizations and $\phi = \pi/2$ for elliptical polarizations. The **normalized** equation for simulations phase-matching is simply,

$$I^{2\omega} = \alpha_y^2(\cos^2\theta)^2 + \alpha_z^2(\sin^2\theta)^2 + 2\alpha_y\alpha_z \sin^2\theta\cos^2\theta[\cos 2\phi] \qquad (5.18)$$

where α_y and α_z (≤ 1) account for the different nonlinear efficiencies of the type-0 and type-I processes (the notation for *x* and *y* coming from the crystal axis that the fundamental for each particular process is polarised along as suggested in Figure 5.22). The ratio of the individually measured irradiances of the two processes goes as the square of this, $\left(\alpha_y : \alpha_z\right)^2$. If we consider the 'best-case' scenario for the nonlinear coefficients being utilised in lithium niobate, as indicated by Eqs (5.3) and (5.4), the ratio of the nonlinearities, $\alpha_y : \alpha_z$, is ~1:0.9. The simulation of the SHG output in relation to the input polarisation state for this ratio of nonlinearities is shown in Figure 5.23. The points where the input polarization state is linear-vertical and linear-horizontal as well as circularly polarized have been indicated. The SHG output is suppressed near, but not at the exactly, at the circular polarization state. The offset from SHG suppression being produced at circular polarization is due to the difference in the nonlinearities. In practice such measurements can be used to accurately measure the ratio of the nonlinearities of the simultaneous processes. A series of plots with nonlinear ratios of $\alpha_y : \alpha_z = 1, 0.75, 0.5, 0.25$ are shown in Figure 5.24. The difference in the SHG output for the vertical and horizontal components becoming larger as the difference in nonlinearities is increased. The orientation of the elliptical polarization state where complete suppression is reached also changes for different ratios of the nonlinearities. We can see this from Eq (5.18) by setting the left hand side to zero and the phase to relative phase of the vertical and horizontal components to $\phi = \pi/2$. Note again that θ is the angle which indicates the polarisation of the fundamental field, controlled by a half-wave plate, and ϕ is the phase difference between the vertical and horizontal components, controlled by a quarter-wave or variable retardance wave plate.

$$\alpha_y^2(\cos^2\theta)^2 + \alpha_z^2(\sin^2\theta)^2 - 2\alpha_y\alpha_z \sin^2\theta\cos^2\theta = 0 \qquad (5.19)$$

Dividing through by $(\cos^2\theta)^2$ and factorizing,

$$\alpha_y + \alpha_z^2(\tan^2\theta)^2 - 2\alpha_y\alpha_z \tan^2\theta = 0$$
$$(\alpha_y - \alpha_z(\tan^2\theta)^2 = 0$$

We arrive at the expression for the polarization orientation, with $\phi = \pi/2$, at which the SHG is completely suppressed by the competing processes.

$$\sqrt{\frac{\alpha_y}{\alpha_z}} = \tan\theta \qquad (5.20)$$

A plot of Eq. (5.20) is shown in Figure 5.25. As indicated in Figure 5.24, the suppression orientation is at 45º (circular polarization) for equal nonlinearities and moves closer to 90º for reduced ratios.

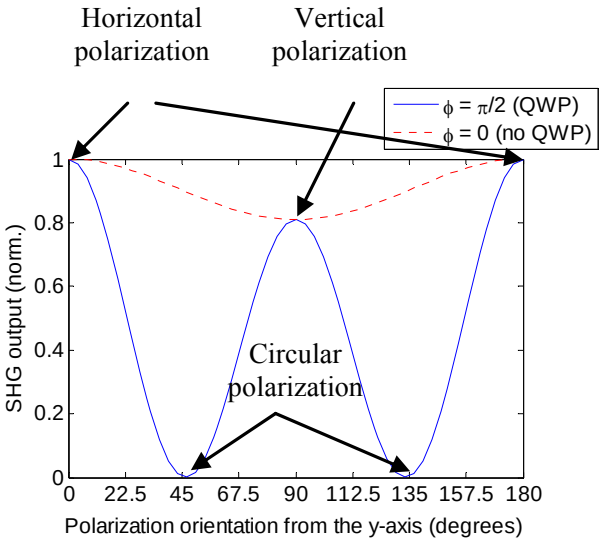

Figure 5.23 SHG output in relation to the polarization state of the fundamental. The blue (solid) plot indicates the case for a quarter-wave phase shift between the vertical and horizontal components, while the red (dashed) line indicates linear polarization.

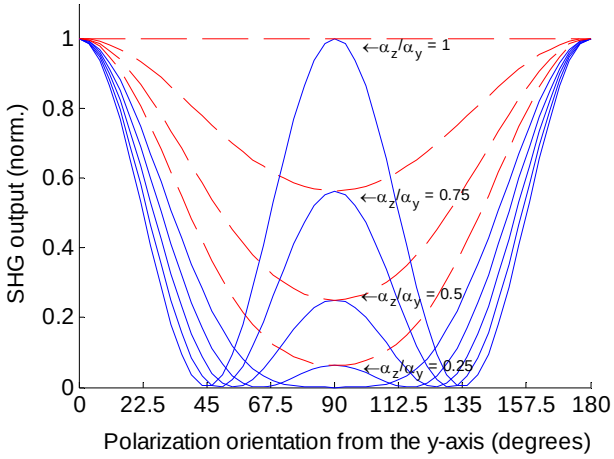

Figure 5.24 Polarization plots for simultaneous SHG from two processes (type-I and type-0) with nonlinearity ratios of 1, 0.75, 0.5, and 0.25.

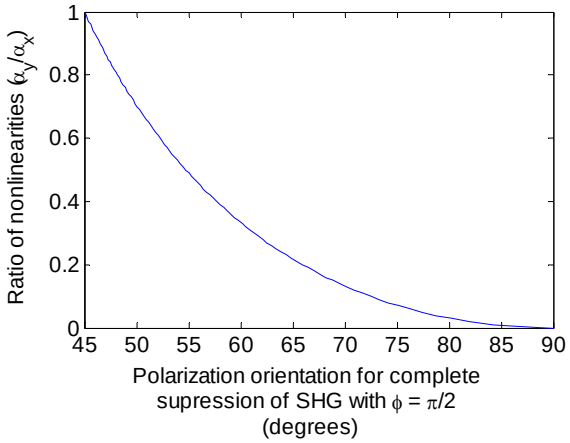

Figure 5.25 Ratio of the nonlinearities of simultaneously phase-matched type-I and type-0 processes in relation to the polarization orientation with $\phi = \pi / 2$, which results in suppression of the SHG.

The experimental temperature detuning curves for the 45.8 µm grating shown on the right of Figure 5.21, indicate good overlap between the type-I and type-0 detuning curves and that the ratio of the measured irradiances is ~1:0.25. This corresponds to a ratio of 1:0.5 for the nonlinearities. The experimental data for the SHG dependence on polarization states corresponding to the simulations in Figure 5.23 and Figure 5.24 are shown in Figure 5.26. The experimental results showed good agreement with the calculated curves and demonstrated that coherent internal interference of two distinct but simultaneously phase-matched SHG processes occurs, and that the equations developed here provide a good physical model of this interaction.

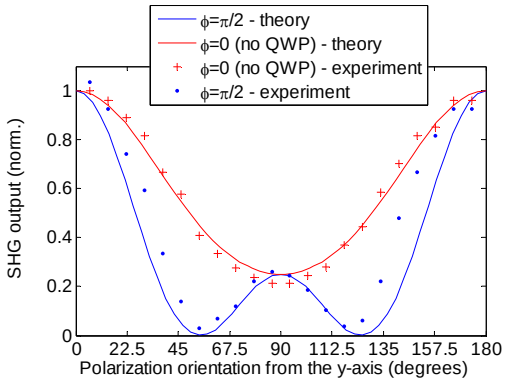

Figure 5.26 Experimentally measured SHG output in relation to the input polarization state for simultaneously phase-matched type-I and type-0 SHG in a 45.8µm period grating. The SHG temperature detuning curves for the individual processes are shown on the right of Figure 5.21.

The polarization measurements for the 45.75 μm period grating at normal incidence were affected by slight phase-matching offset between the two processes, as the phase-matching curves did not exactly overlap at the same temperature, as shown on the right of Figure 5.21. With the temperature set for phase-matching of the type-I process there was a finite Δk_0 which contributes to the internal interference between the two SHG processes. It should also be noted that the ratio of efficiencies of the two processes was also less in this case, 1:0.2 as opposed to 1:0.25 for the 45.8 μm grating. The phase-mismatch that was present, Δk_0, came from an incorrect period for the type-0 phase-matching when the type-I is phase-matched. The period was incorrect by ~50nm so that the mismatch could be found as $\Delta k_{res} = \Delta k - \frac{2\pi m}{\Lambda} = \Delta k - \frac{14\pi}{\Lambda_0 - 50nm}$ or alternatively, the residual mismatch scales with the period error, i.e.

$$\frac{\Delta k_{res}}{\Delta k} = \frac{\Delta\Lambda}{\Lambda_{ideal}} \tag{5.21}$$

This phase-mismatch shows up as a phase-offset in the way the two processes interact in the crystal, i.e. in Eq (5.15) the cross (phase) term between the two interacting fields contains contributions from both the fundamental fields' phases and the residual phase-matches, $\cos\left[2\phi + \Delta k_0 L/2 - \Delta k_1 L/2\right]$. The phase-mismatch for 1064 nm, type-0 SHG in lithium niobate is approximately 0.96102 μm^{-1} at the temperature at which simultaneous phase-matching is predicted (~452 K). An offset in the period of 50nm, departing from an ideal period of 45.75 μm, therefore results in a residual phase-mismatch of approximately $\Delta k_0 = \Delta k \frac{\Delta\Lambda}{\Lambda_{ideal}} = 0.91062 \frac{-0.05}{45.75} = -0.00105 \mu m^{-1}$. The contribution of the mismatch to the phase-term for a 3mm crystal length is thus, $\Delta k_0 L/2 = -1.575 rads \approx -\pi/2$. The experimentally measured data and the calculated curves from Eq (5.18) for simultaneous SHG with nonlinear ratios of 1:0.447 (corresponding to the observed ratio in irradiances of 1:0.2), with the phase offset of $-\pi/2$ included is shown in Figure 5.27.

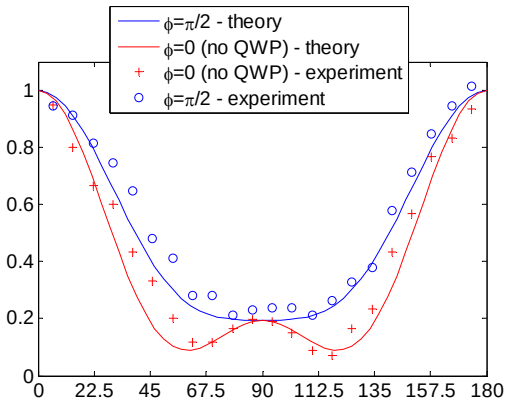

Figure 5.27 Experimentally measured SHG output in relation to the input polarization state for simultaneously phase-matched type-I and type-0 SHG with a 45.75μm period grating. A slight phase-mismatch is apparent for the type-0 process. The SHG temperature detuning curves for the individual processes are shown on the left of Figure 5.21.

As seen in Figure 5.27 the minimum level of SHG output was actually observed for a linear polarization state, which is in good agreement with the calculated effect of a phase-mismatch cause by an incorrect period of 50 nm from an ideal period of 45.8 μm. The results presented in Figure 5.26 and Figure 5.27 demonstrate that the internal interference between two simultaneously, or almost simultaneously, phase-matched processes can be well understood by working from the coupled field equations developed here.

Fabrication of a better quality crystal with a period of 45.75 μm and 100 periods long (~4.6mm) was carried out next, paying special attention to optimizing the laser machining and poling parameters. This crystal performed markedly better with close adherence to the ideal $sinc^2$ form for both the temperature tuning curves. The duty cycle was 36% which is almost an optimal duty cycle for the 7th order process (Figure 5.20). A section of this particular crystal is shown in Figure 5.28. The two temperature detuning curves at normal incidence are shown in the left of Figure 5.29. The curves are offset in a similar fashion to those of the previous 45.75μm grating shown on the left of Figure 5.21. Slight angular tuning of the crystal allowed the two temperature detuning curves to be overlapped almost perfectly as shown on the right of Figure 5.29. The efficiency of the type-0 and type-I processes in this crystal were almost identical, which is in good agreement with the nonlinearities suggested in (5.3) and (5.4), given that the nonlinear coefficient of the 7th order process on d_{33} is almost optimum, $d_{Q7th} = \frac{2d_{33}}{7\pi} = 2.7\,pm/V$,

and the 36% duty cycle reduces the nonlinear coefficient of the 1st order process on d_{31} to $d_{Q1st} = \frac{2d_{31}\sin(0.36\pi)}{\pi} = 2.71 pm/V$.

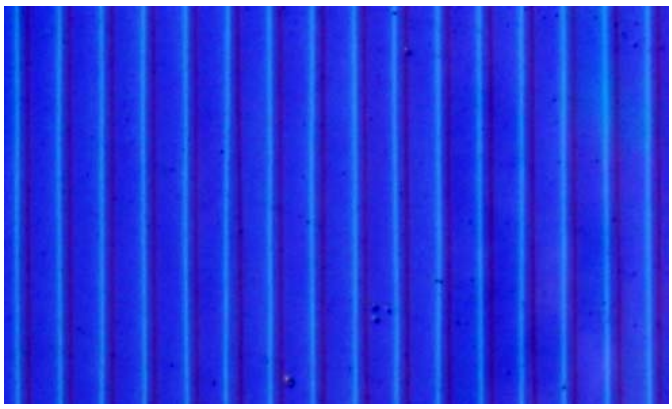

Figure 5.28 Section of a high quality 45.75µm period PPLN crystal.

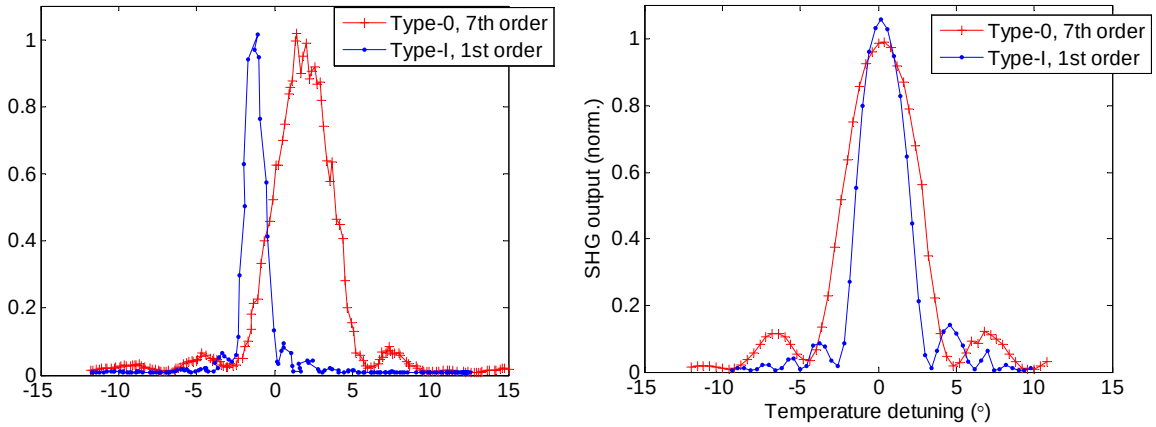

Figure 5.29 Experimental temperature detuning curves for a good quality 45.75µm period PPLN crystal. Left: type-I and type-0 curves measured at normal incidence, right: measured with slight angular tuning of the crystal to achieve good overlap of the two processes.

The SHG output in relation for the input polarization state was also measured for this crystal, the results and calculated plots are shown in Figure 5.30. A slight phase-mismatch was included in the calculated curves to aid in fitting to the data, indicating that the angle tuning or the temperature were not quite set for perfect simultaneous phase-matching. This is reflected somewhat by the slight offset of the temperature curve observed on the right of Figure 5.29. Beam pointing of the laser, slight deflections by moving optics and temperature fluctuations

during measurements all contribute to these slight offsets; however the data recorded is readily interpreted from the equations developed above.

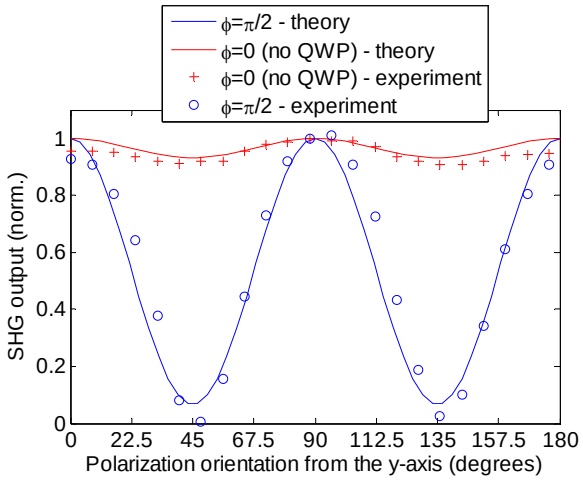

Figure 5.30 Experimentally measured SHG output in relation to the input polarization state for simultaneously phase-matched type-I and type-0 SHG with a good quality 45.75 μm period grating. The SHG temperature detuning curves for the individual processes are shown in Figure 5.29.

The higher quality crystal showed SHG output which was almost independent of the polarization orientation for the linear polarization states, as suggested by (5.17) for a crystal with equal nonlinearities. For the polarization states with the $\phi = \pi/2$ phase-shift, almost complete modulation of the SHG from maximum values near the linear polarizations to complete suppression near circular polarization can be seen. A secondary experiment looking at the SHG output when varying the phase-shift, ϕ, was also carried out with this crystal. The initial polarization state was set to 45º for equal horizontal and vertical components. The phase-shift between the two components was then varied continuously using a Berek polarization compensator from Newfocus. The Berek utilizes an orientation plate in tandem with a variably tilted birefringent plate to perform an arbitrary polarization transformation. In this experiment the tilt setting on the birefringent plate was changed in order to vary the retardance/phase-difference between the vertical and horizontal components and observe the SHG output. The results are shown in Figure 5.31. The observed level of SHG as the retardance is varied from 0 to ½ wave is in good agreement with the calculations with the phase ϕ is varied from $0 \rightarrow \pi$. This demonstrated that the SHG output could be controlled by the phase difference between the two fundamentals.

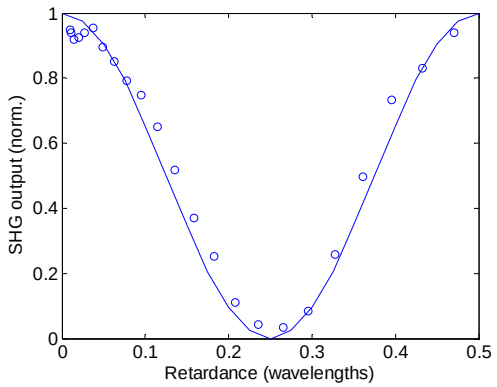

Figure 5.31 SHG output in relation to the retardence between equal vertical and horizontal fundamental components. The SHG is suppressed for ¼ wave retardence corresponding to a π/2 phase-shift between the fundamentals.

The internal interference between the two fundamental components can also be observed across the entire SHG temperature detuning range. This experiment was carried out by setting the input polarization to 45º so that both fundamentals were contributing to the SHG and then measuring the temperature detuning curves with and without the QWP in place. The in-phase (linear input polarization) and out-of-phase super-positions (circular polarization) of the temperature detuning of the two processes was observed. The experimental results for the two 45.75μm crystals are shown below in Figure 5.32 and Figure 5.33. These curves can be modelled from Eq (5.15), keeping in mind that the two phase-match parameters, Δk_0 and Δk_1 vary differently with temperature, as evidenced by the different temperature acceptance bandwidths of the type-0 and type-I processes. The calculated interference temperature detuning curves for equal processes in an ideal grating are shown in Figure 5.34. The experimental results for the high quality grating show excellent agreement with the calculated curves, confirming the validity of Eq (5.15) and the accuracy of Sellmeier equations in predicting the behaviour of simultaneously phase-matched SHG.

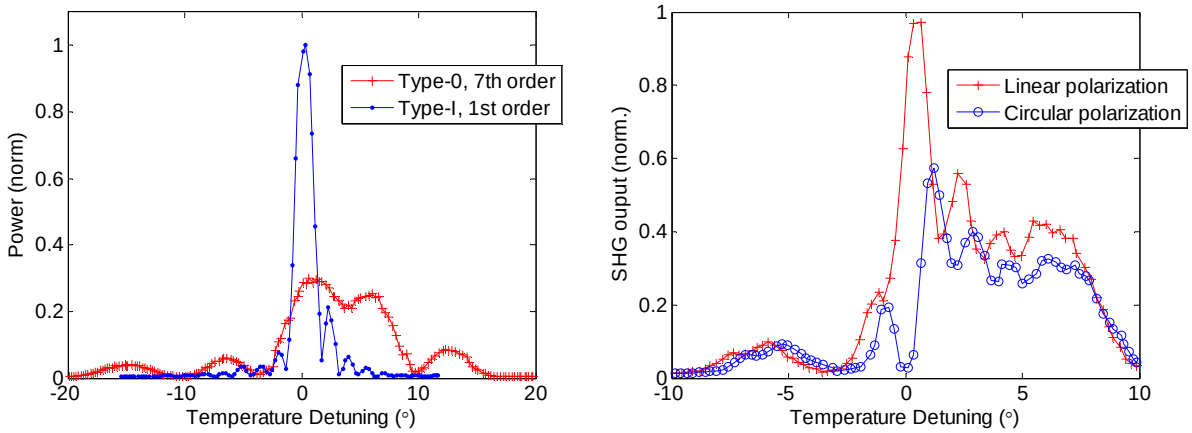

Figure 5.32 Temperature detuning curves for a 45.75µm period PPLN crystal with distorted type-0 curve. Left: individual phase-matching curves, right: SHG internal interference curves for equal fundamental components with linear input polarization (in-phase components) and circular (out-of-phase components).

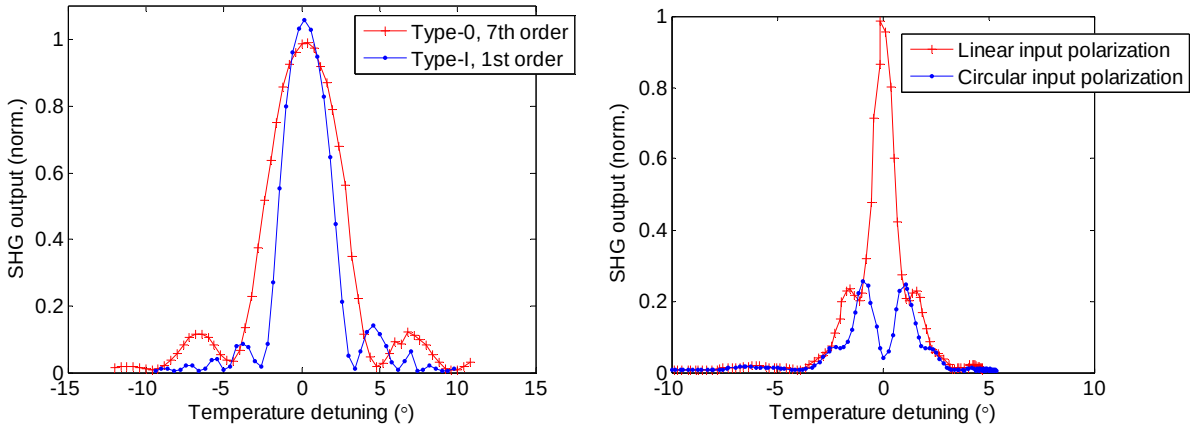

Figure 5.33 Overlapping temperature detuning curves for a good quality 45.75µm period PPLN crystal. Left: individual phase-matching curves, right: SHG internal interference curves for equal fundamental components with linear input polarization (in-phase components) and circular (out-of-phase components).

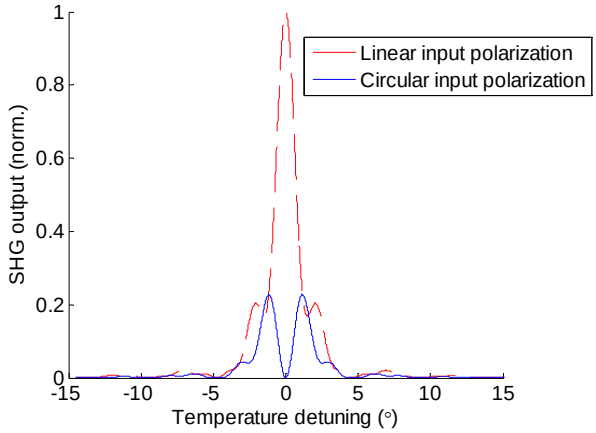

Figure 5.34 Calculated temperature detuning curves for simultaneous SHG.

5.3.3 Further simulations and discussion

The response of the SHG to the phase of the two simultaneously phase-matched fundamental components may have some useful applications. One proposal is to use this scheme to stabilize or modulate the SH output using electro-optic (Pockels cell) polarisation control. A schematic is shown in Figure 5.35.

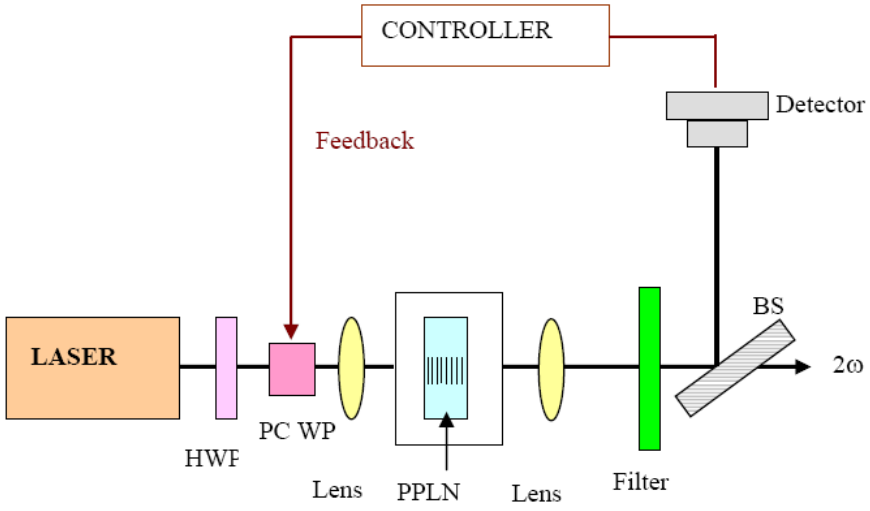

Figure 5.35 Schematic of proposed setup for controlling SHG output, utilizing phase-control between simultaneously phase-matched type-I and type-0 processes.

This scheme relies on using the Pockels cell as an electronically controlled variable retardence element, to either stabilize the SHG output in lieu of amplitude variations in the source laser, or to modulate the SH output for signalling or display applications. Alternatively the SHG maybe utilized as a diagnostic of the input light. It has previously been proposed that SHG can be used

to aid in the monitoring of certain polarisation mode dispersion compensation[202] (PMD) schemes. PMD is the temporal broadening and breaking up of optical pulses during transmission due to residual birefringence in optical fibres, fibre components or waveguides, and is a major performance issue concern for high bit-rate optical transmission. In transmission systems where the optical signal is easily understood in terms of its principal states of polarization, SHG may be used to monitor the temporal dispersing of the pulses. For a transmission system with a simple and consistent birefringence the temporal dispersion can be easily understood as transmission on a fast and a slow axis within the system. The temporal dispersion of a pulse as it travels with components polarized on the fast and slow axes\are illustrated in Figure 5.5.

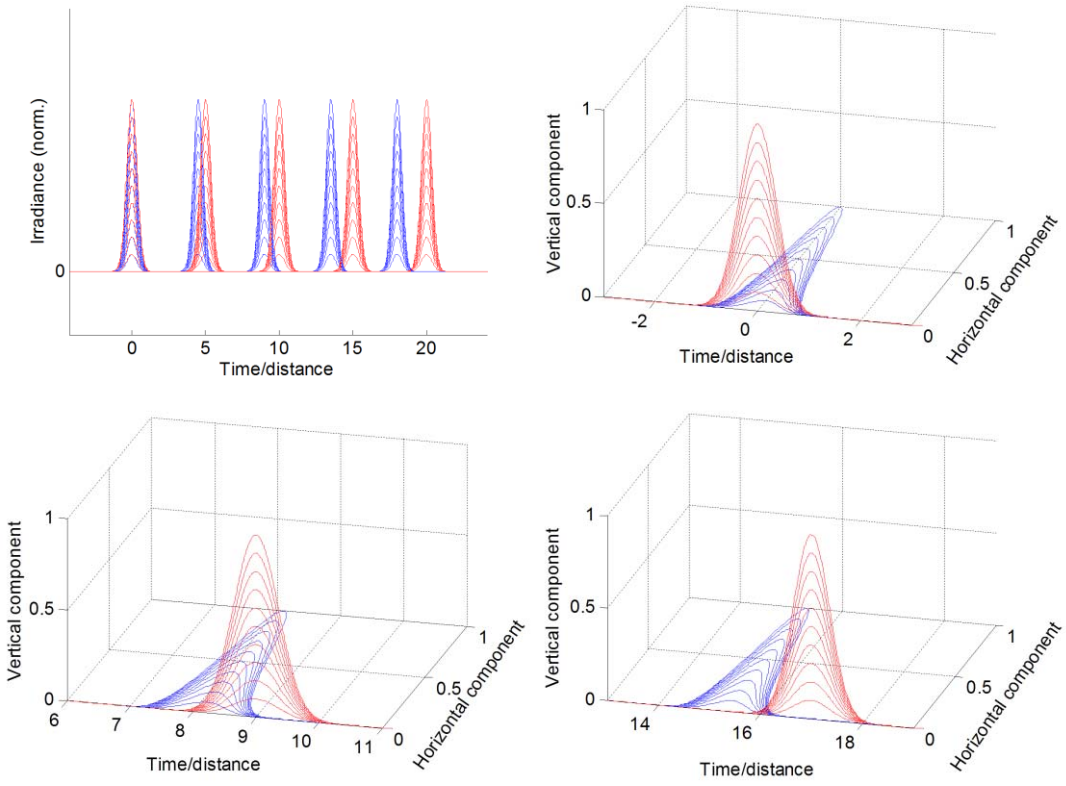

Figure 5.36 Temporal dispersion between different pulse polarizations in a birefringent optical transmission line. Red plots indicate the vertical polarization (fast axis in these plots), blue plots the horizontal polarization (slow axis) Top left: dispersion off fast and slow components during an arbitrary propagation distance or flight time. Top right through lower plots: separation of polarizations at different times/displacements along the transmission line.

The previous PMD monitoring proposal[202] was based on type-0 SHG with the fast and slow components of the optical signal incident at 45º from the z-axis of the crystal. In this way the two components have projections onto the z-axis of the crystal. The SHG output will thus

depend on the overlap integral of the fast and slow components of the incident signal. As the PMD compensation is tuned to recover the pulses, this overlap integral becomes more isolated in time, raising the peak power of the pulse and increasing the SHG output. A drop in the SHG level signifies a change in the PMD on the transmission line and that retuning of the PMD compensation device is needed. The simultaneous phase-matching scheme presented here may be used in a similar fashion, with the additional information of the relative phase of the fast and slow components being included within the overlap integral. The SHG output acts as a type of nonlinear interferometer for the fundamental components. If the small amount of dispersion in the short length of nonlinear crystal is ignored, we can consider the SHG of the vertically and horizontally polarized components of a pulse, dispersed temporally by a duration Δt so that the relative phase between the fields of two pulses is given by $\phi = \omega\Delta t$ in time or equivalently $\phi = k\Delta x$ in space. For simplicity plain-wave pulses with a Gaussian temporal envelope are assumed,

$$I_z(t) = I_z e^{(-(t)^2/2t_p^2)}$$
$$I_y(t) = I_y e^{(-(t-\Delta t)^2/2t_p^2)} \qquad (5.22)$$

The temporal irradiance profiles described by (5.22) and a phase depending on the time delay, $\phi = \omega\Delta t$, can be directly used in Eq (5.14) to calculate $I^{2\omega}(t)$, allowing approximate calculation of the SHG output pulses for various delay times between the fundamental polarization components. The average power of the second-harmonic in the time interval under consideration, $t = -\delta t \rightarrow +\delta t$ can calculated numerically as,

$$I_{avg}^{2\omega} = \frac{1}{2\delta t}\sum_{t=-\delta t}^{\delta t} I^{2\omega}(t) \qquad (5.23)$$

This time interval is chosen to be sufficient to include the majority of the power from both the pulses and with a small enough step size to be able to resolve the interference between optical cycles from the constituent pulses (<2/ω). As an example the average simultaneously phase-matched SHG power output, calculated for a wavelength of 1064 nm, a Gaussian pulse width of t_p=1ps and a temporal from delay varied between -4-4 ps is shown below in Figure 5.37. The left hand plot shows the envelope of the SHG signal as the time delay between the vertical and horizontally polarised pulses is varied, while the right hand plot shows a 20 fs interval at the centre of the envelope where the SHG interference between optical cycles of the pulses can be

seen as the time delay is varied. In essence the SHG signal provides interferometric information about the overlap and phase of the two pulse components.

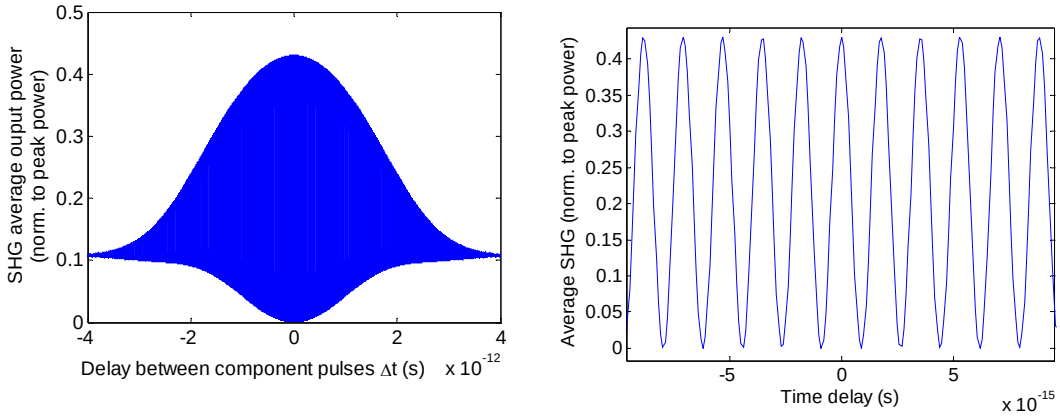

Figure 5.37 SHG output, time averaged over an 8ps interval, for simultaneously phase-matched 1ps pulses with various time offsets. Left: full 8ps interval, showing maximum SHG signal when there is zero time delay between pulses, and minimum level when pulses separated by 4ps. Right: SHG signal in the ±10fs interval, showing interference between the optical cycles of the pulses as the time delay between them is varied.

5.4 Two colour cascading.

5.4.1 Review of 'two colour cascading' in nonlinear optics

Cascading of second order nonlinear processes has diversified the application areas of second order materials such as PPLN. Many authors have explored cascading in second order materials as a means of producing higher order harmonics, such as 3rd and 4th harmonic generation, multi-step wavelength conversion processes for optical processing in WDM networks or spectroscopy, and also for producing nonlinear phase-shifts. Nonlinear phase-shifts in second order materials has attracted attention as there are potential avenues for realising some all-optical processing devices which would otherwise require 3rd order nonlinearties. The simplest scheme for producing a nonlinear-phase shift (NPS) is with a single and efficient type-I or type-0 SHG interaction. The origin of this phase-shift is the cascading of energy from the fundamental to second harmonic and then back again, a process that occurs when the SHG is not perfectly phase-matched. Second-harmonic wavelets are generated out of phase with the fundamental, while the back conversion process produces fundamental wavelets in-phase with the second-harmonic.

This phase-shifting of fundamental wavelets via the second-harmonic accumulates an average phase-shift in the fundamental field as it propagates through the nonlinear medium. This phenomenon has received much attention in the literature since it was experimentally brought to light by DeSalvo *et al* [203] in 1992. In bulk crystals the nonlinear phase-shift manifests as a nonlinear refractive index, generally thought of as a $\chi^{(3)}$ phenomenon. Experimental verification of this is often carried out using the z-scan technique as implemented by Sheik-Bahae *et al*[204]. The NPS and corresponding nonlinear refractive index produced by a $\chi^{(3)}$ interaction has either a positive or negative sign depending on the material, for example self-focusing in positive Kerr media. The sign of the NPS resulting from cascaded $\chi^{(2)}$ interactions can be controlled as either positive or negative depending on the phase-matching conditions. In DeSalvo's experiments Z-scan measurements of the nonlinear lensing of the fundamental field demonstrated that a focusing and defocusing effect, much larger than the Kerr effect, was taking place in KTP when tuning across the phase-matching bandwidth of a SHG process. Approximate analytical approaches for describing the NPS have been developed by DeSalvo *et al* and other authors such as Saltiel[205] since. The phenomenon quickly becomes apparent when the coupled field equations for both the second-harmonic and the fundamental are considered numerically. For a single SHG process the field equations can be simplified to,

$$\begin{aligned} \frac{dE_{\omega}}{dx} &= -i\sigma E_{2\omega} E_{\omega}^{*} e^{-i\Delta kx} \\ \frac{dE_{2\omega}}{dx} &= -i\sigma E_{\omega} E_{\omega} e^{i\Delta kx} \end{aligned} \tag{5.24}$$

Where $\sigma = \frac{\omega d_{eff}}{4nc}$ encapsulates the appropriate nonlinear coefficient and propagation constants associated with the fields. The nonlinear phase-shift which the fundamental field accumulates can be found by numerically interrogating the argument (angle/phasor in the complex plane) of the fundamental field as these equations are integrated (propagated). The amount of phase-shift observed depends on the input amplitude of the fundamental field, the nonlinearity of the material and the phase-mismatch (detuning) present. When considering the nonlinear phase-shift in relation to the phase-mismatch, the unitless quantity of $\Delta kL/\pi$ (or sometimes ΔkL, $\Delta kL/2$) is adopted to describe the phase-mismatch, as this is the indicative parameter which determines the SHG output at a particular detuning. The usual detuning curves for SHG, found by integrating

(5.24) and plotting the irradiances as a function of $\Delta kL/\pi$ are shown for a 50% efficient process in Figure 5.38.

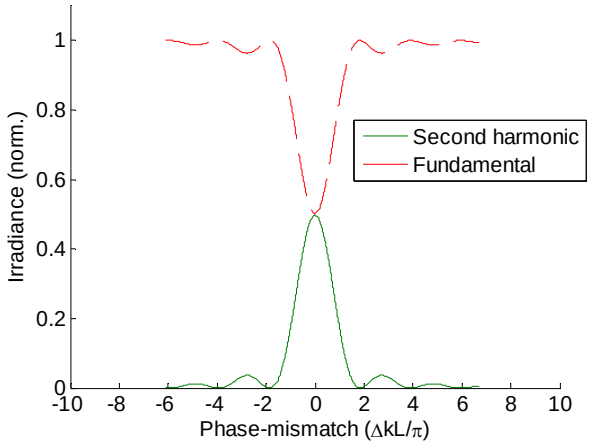

Figure 5.38 Fundamental and SHG irradiance plotted in relation to the phase-mismatch parameter $\Delta kL/\pi$ for a 50% efficient process.

As outlined in chapter 2, a phase-mismatch results in an oscillatory growing and decaying of the second-harmonic field with a characteristic coherence length. For efficient processes this also has a significant affect on the fundamental field, depleting and then regenerating it, resulting in the accumulated nonlinear phase-shift described above. The rate of the conversion also plays a role in determining the magnitude of the resulting phase-shift, with the parameter of interest being σL, i.e. the product of the nonlinearity of the material and its length. Plots showing the evolution of the irradiances of the fundamental and second-harmonic, along with the nonlinear phase shift, for different values of phase-mismatch and a nonlinearity of σL=1 are shown in Figure 5.39. The accumulated nonlinear phase-shift as a function of phase-mismatch, along with the SHG detuning for reference, is shown in Figure 5.40. The magnitude of the maximum nonlinear phase-shift and the value of $\Delta kL/\pi$ at which it occurs depends on the overall efficiency of the process. As noted in chapter 2, highly efficient SHG processes have a narrower acceptance bandwidth, and the detuning at which the maximum NPS is achieved shifts accordingly towards lower detuning values. The larger amount of intermediate second-harmonic present in an efficient process also results in a larger amount of cascaded energy and correspondingly larger NPS. This is illustrated for SHG with 20% and 90% efficiencies in Figure 5.41. In reality the value of σL is not very large and SHG efficiencies rarely exceed 80%. For example a 20 mm length of PPLN with d_{eff}=15pm/V has $\sigma L \approx 2.33\times10^{-7}$. If such a sample is pumped sufficiently for 80% conversion efficiency with a single pass, the maximum phase-shift

possible according to numerical calculation, is 0.6 radians. To produce full modulation of the optical field, as in a Mach-Zehnder arrangement, a nonlinear phase-shift nearing π/2 is required. In general the phase-shift produced from a practical type-I or type-0 process is insufficient for practical applications. While phase-matching schemes in highly nonlinear materials, such as organics and semiconductors, have been suggested, there are other avenues to achieving a larger and more functional NPS as will be reviewed below.

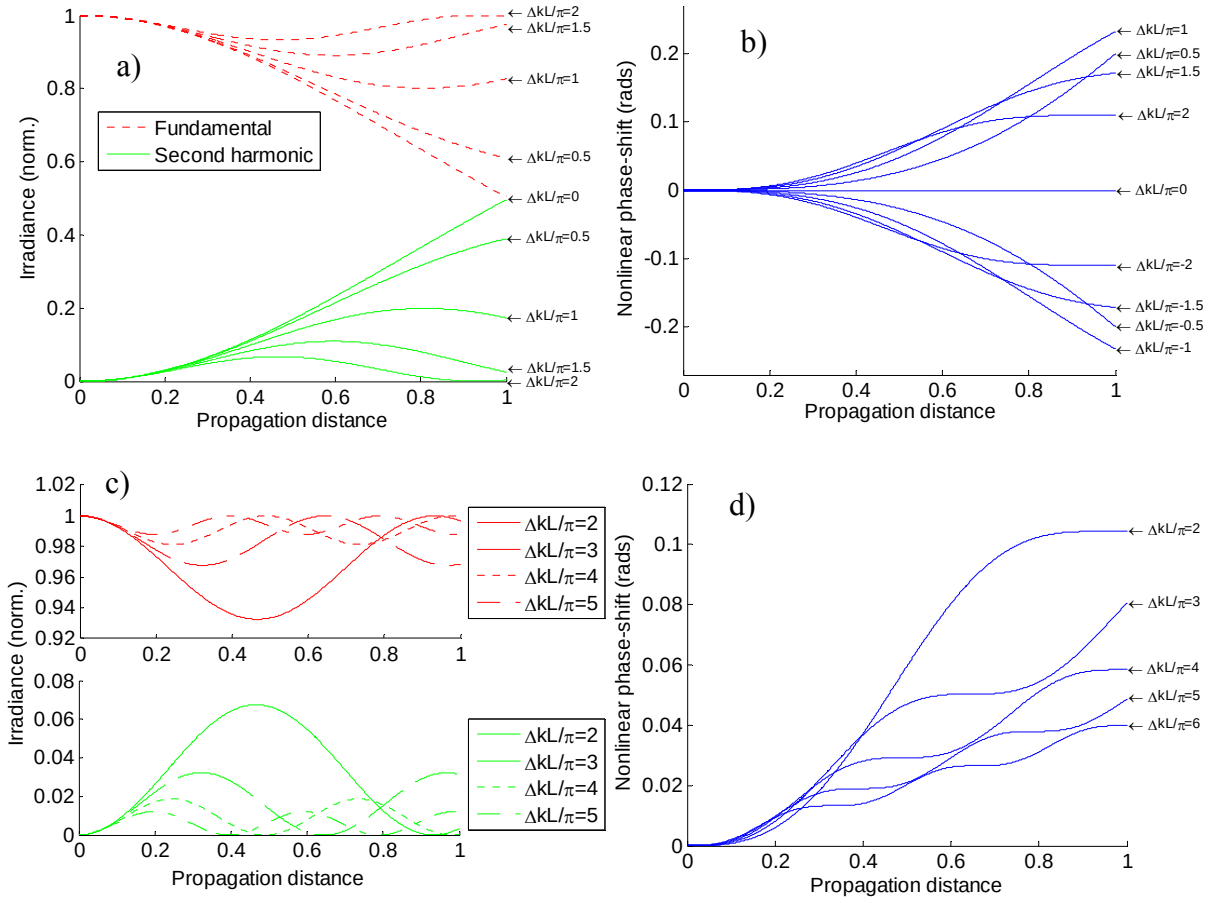

Figure 5.39 Evolution of the irradiances of the fundamental and the second-harmonic and the nonlinear phase-shift, for a 50% efficient process with various phase-mismatches. Low values of phase-mismatch are shown in plots a) and b), large phase-mismatches are shown in plots c) and d).

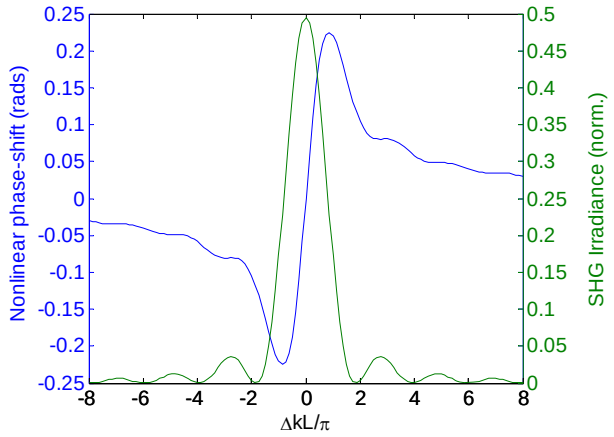

Figure 5.40 Accumulated nonlinear phase-shift in relation to phase-mismatched for a 50% efficient process.

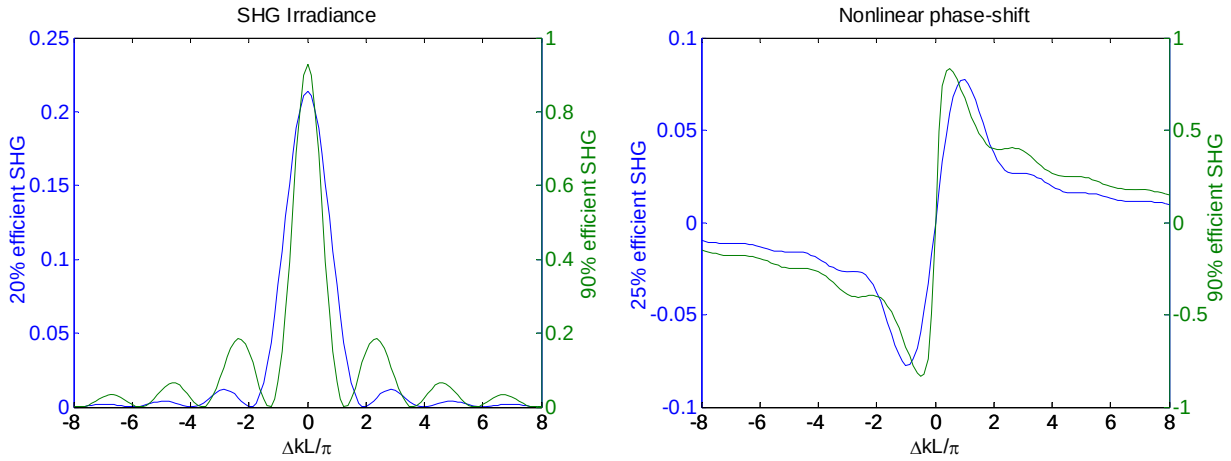

Figure 5.41 SHG detuning and nonlinear-phase shifts for a single process with efficiencies of 20% (blue plots) and 90% (green plots). The detuning curves and NPS curves tend to narrow for higher efficiencies, changing the detuning required for maximum NPS.

Cascading in a type-II SHG process is more subtle process and potentially very useful. The 'transistor' like functionality of type-II cascading was suggested by Assanto[206] in 1995. For a type-II process there are two distinct fundamental fields who contribute to the SHG and the relative amplitude of these fields play an important role in determining the nature of the nonlinear phase shift. The field equations describing the type-II process for an *oe-e* SHG process (second harmonic polarized in the direction which utilises the extraordinary refractive index) are given as,

$$\begin{aligned}\frac{dE_i^{\omega}}{dx} &= -i\sigma E_i^{2\omega} E_j^{\omega *} e^{-i\Delta kx} \\ \frac{dE_j^{\omega}}{dx} &= -i\sigma E_i^{2\omega} E_i^{\omega *} e^{-i\Delta kx} \\ \frac{dE_i^{2\omega}}{dx} &= -i2\sigma E_j^{\omega} E_i^{\omega} e^{i\Delta kx}\end{aligned} \tag{5.25}$$

where *i* and *j* denote orthogonal polarizations. One of the features of the type-II interaction is that the regenerated fundamental wavelets which result from cascading depend on the orthogonal fundamental field. As the ratio of the power in the two fundamental fields is changed, the amount of phase-shift produced in either field changes, with the weaker component collecting a larger accumulated phase-shift. Figure 5.42 shows the NPS of the two fundamental components for a steady total input power shared in various ratios between the two fundamentals with for $\sigma L=1$ and a phase-matched SHG efficiency of 50%.

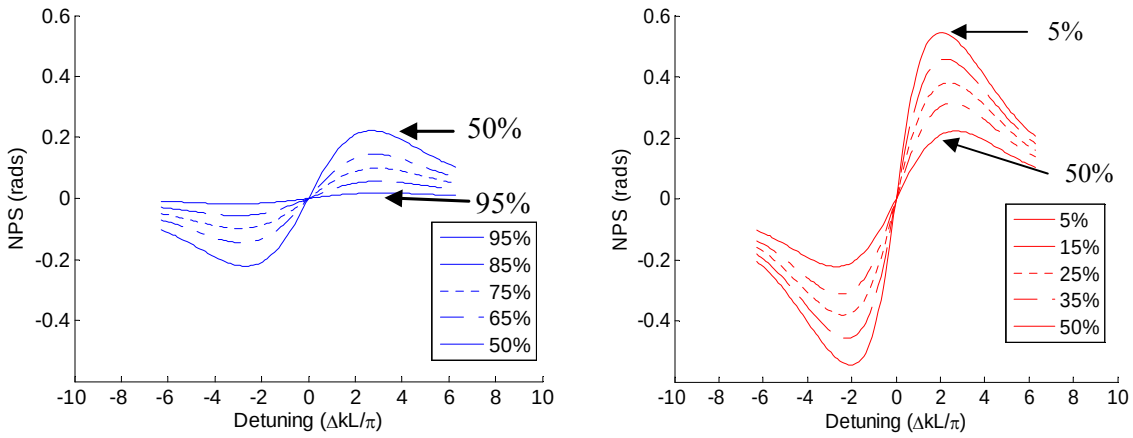

Figure 5.42 NPS as a function of detuning for type-II SHG (50% efficient when optimised) with various ratios of the *o:e* fundamentals. Percentages indicate the share of the fundamental power that is present in that particular field. Left: NPS for the stronger fundamental, which decreases as its share of the input power is increase. Right: NPS for the weaker fundamental which increases as its share of the input power is decreased.

As indicated in Figure 5.42, the weaker fundamental component accumulates quite a large nonlinear phase-shift compared to that produced in a type-I interaction with same efficiency. The lower signal intensities and larger NPS experienced by the weaker component of the type-II interaction make it a better candidate for a functional device. The throughput of the fundamental fields in efficient type-II interactions under different conditions is also of interest for optical processing, which has also been suggested by Assanto[206]. The transmission of a *pump*

fundamental can be strongly modulated by small changes in the orthogonal *gate* fundamental at zero or slight phase-mismatch. For a fixed *pump* power, the transmission as a function of the ratio of the *gate* : *pump* powers is shown in Figure 5.43. The point of interest is the rapid and strong modulation of the *pump* transmission when the *gate* fundamental is biased and modulated around 84% of the pump input, as indicated by the dashed lines in Figure 5.43. Assanto has suggested this as a potential scheme for realising an all-optical transistor, but the nonlinear efficiency required for implementation is also beyond what is still readily practically achieved

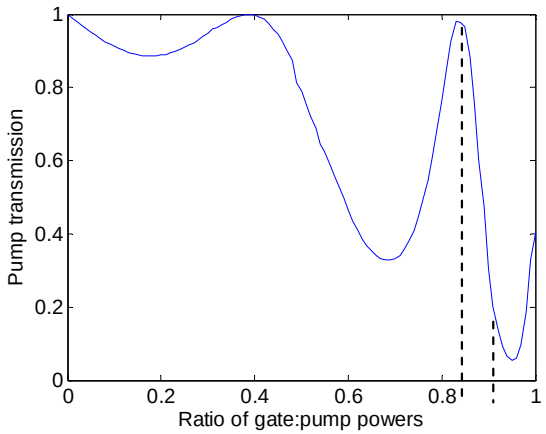

Figure 5.43 Transmission of a 'pump' fundamental polarization in relation to its ratio with the orthogonal 'gate' fundamental in an efficient (99% SHG) type-II interaction.

There have been some promising suggestions of methods for improving the efficacy of cascading, including tailoring of QPM gratings to produce optimal phase-shift for the interaction length, as suggested by Cha[207]. Moving to processes in which more than one interaction is involved can also be beneficial, and other phenomena such as cross-polarized wave generation can arise. The interaction suggested by Assanto *et al* in ref [208] involves two fundamental fields which both contribute photon pairs to a common second harmonic via two individual type-I process acting simultaneously. An alternate scheme proposed by Saltiel *et al*[209] involves simultaneous action of type-I and type-II processes which also share a common second harmonic. Other variations in multistep cascading between two discrete processes have also been suggested and a summary of these two colour multistep processes, similar to the classifications of Saltiel *et al*[210], is reproduced in Table 5.3.

Cascading scheme	SHG processes	Refs.
$\omega+\omega \leftrightarrow 2\omega_\perp : \omega_\perp+\omega \leftrightarrow 2\omega_\perp$	Type-I:Type-II	209,211,212
$\omega+\omega \leftrightarrow 2\omega_\perp : \omega_\perp+\omega \leftrightarrow 2\omega$	Type-I:Type-II	213,199
$\omega+\omega \leftrightarrow 2\omega_\perp : \omega_\perp+\omega_\perp \leftrightarrow 2\omega_\perp$	Type-I:Type-0	208,214,215,216
$\omega+\omega \leftrightarrow 2\omega_\perp : \omega_\perp+\omega_\perp \leftrightarrow 2\omega$	Type-I:Type-I	214,217
$\omega+\omega_\perp \leftrightarrow 2\omega_\perp : \omega_\perp+\omega \leftrightarrow 2\omega$	Type-II:Type-II	

Table 5.3 Two colour multistep processes

5.4.2 Cascading between type-0 and type-I QPM interactions

The scenario of particular interest in this dissertation is the third entry in Table 5.3, two simultaneously phase-matched processes using type-I and type-0 interactions. As demonstrated previously, the coupled field equations for simultaneous type-0 and type-I phase-matching with respect to the crystal axes in lithium niobate can be given as,

$$\begin{aligned}
\frac{dE_z^{\omega}}{dx} &= -i\sigma_1 \vec{E}_z^{2\omega} \vec{E}_z^{\omega *} e^{-i\Delta k_0 x} \\
\frac{dE_y^{\omega}}{dx} &= -i\sigma_2 \vec{E}_z^{2\omega} \vec{E}_y^{\omega *} e^{-i\Delta k_I x} \\
\frac{dE_z^{2\omega}}{dx} &= -i\sigma_1 (\vec{E}_z^{\omega})^2 e^{i\Delta k_0 x} - i\sigma_2 (\vec{E}_y^{\omega})^2 e^{i\Delta k_I x}
\end{aligned} \qquad (5.26)$$

This type of interaction has also been previously identified by Assanto *et al*[208] and practically considered in various crystals by Grechin and Dmitriev[214]. Potential applications in all optical modulation and polarization switching have been suggested along with control of the second harmonic output via phase and amplitude controlled fundamentals as demonstrated in the previous section. One of the features of utilising two distinct processes is that the phase-mismatch will be different for the two processes for a particular temperature or wavelength detuning. The offset from ideal simultaneity between the phase-matchings can also be controlled by tuning the period of the grating (or equivalently the angle of incidence). The detuning curves and the nonlinear phase-shifts for perfect simultaneous phase-matching of type-0 and type-I SHG from equal fundamental components in a 4.6 mm length of PPLN are shown in Figure 5.44. Each process has been simulated with a 30% efficiency and the cases of in-phase and π/2 phase-shifted fundamentals are shown in the left and right hand of the figure respectively.. The QPM

grating required to achieve this at 1064 nm was shown in the previous section (see Figure 5.17, Figure 5.28, and Figure 5.29). Of particular interest in this system is the energy flow from one fundamental polarization to the other. This phenomenon is the result of cascading between SHG and degenerate difference frequency mixing and gives rise to 'polarisation switching'. A similar type of interaction between type-I and type-II processes has been looked at previously by Saltiel and Deyanova[211]. Such a process can be considered as an equivalent 3rd order process, but with the intrinsic benefits of an instantaneous second order process. That is, the two second order processes involved, $\omega+\omega \leftrightarrow 2\omega_\perp : \omega_\perp+\omega_\perp \leftrightarrow 2\omega_\perp$, can emulate an equivalent cubic effect, $\omega+\omega-\omega_\perp \leftrightarrow \omega_\perp$ or $\omega_\perp+\omega_\perp-\omega \leftrightarrow \omega$.

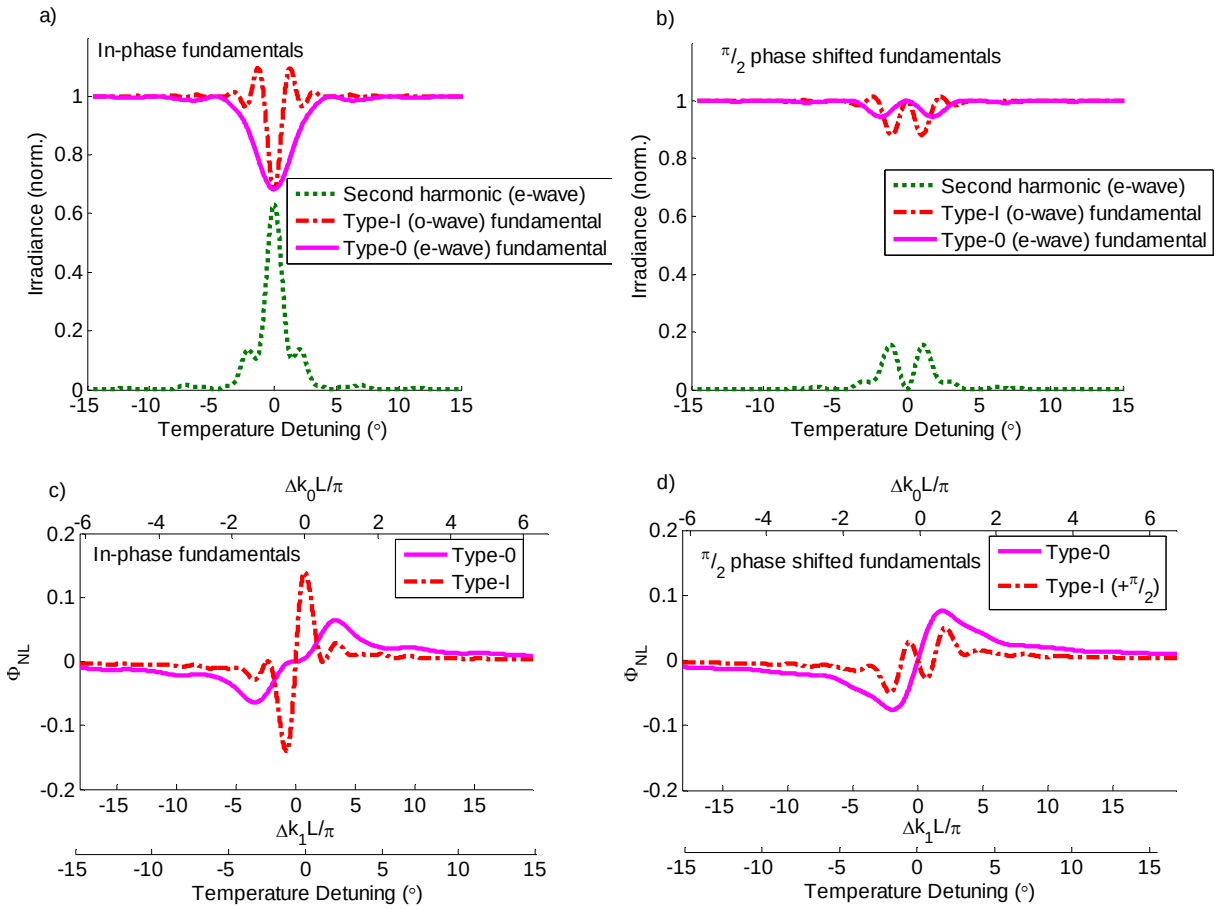

Figure 5.44 Detuning curves and nonlinear phase-shift for simultaneously phase-matched type-0 and type-I SHG in a 4.6mm length of PPLN. Plots a) and b) show the detuning curves for in-phase and π/2 phase-shifted fundamentals respectively. Plots c) and d) show corresponding nonlinear phase-shifts of the type-0 and type-I fundamentals.

The evidence for this 'cubic' interaction in Figure 5.44 is brought about by the different temperature acceptances of the type-0 and type-I processes in PPLN. This results in the cascading of energy between the two fundamentals at slight detuning, as demonstrated in plot a) of Figure 5.44. The broader temperature acceptance of the type-0 interaction provides the second harmonic irradiance necessary to observe cascading to the narrower type-I interaction at slight detuning. This cascading to the type-I process is also accompanied by an enhancement of its NPS, as shown in plot c) of Figure 5.44. The detuning curves and the NPS for fundamentals with equivalent magnitudes but with a $\pi/2$ phase shift are not as interesting as the two interactions behave as competing nonlinear processes and the majority of the energy flow is suppressed. The energy flow between the orthogonal fundamental fields is most prevalent when **unequal** fundamental components are launched with perfect phase-matching with a $\pi/2$ phase difference between the fields. Numerical plots of the irradiances of the second harmonic and the two fundamental components as they propagate through the crystal are shown for an efficient process in Figure 5.45. The fundamental components are shown polarised along orthogonal *o* and *e* directions in the crystal, and with various ratios of initial irradiance incident on the crystal. A large degree of energy transfer between the fundamental components can be seen for significant differences in the initial irradiances. The rapid growth of the second harmonic due to a large 'pump' fundamental then becomes available for difference frequency mixing with the weaker 'signal' fundamental component, effectively rotating the polarisation of the incident beam.

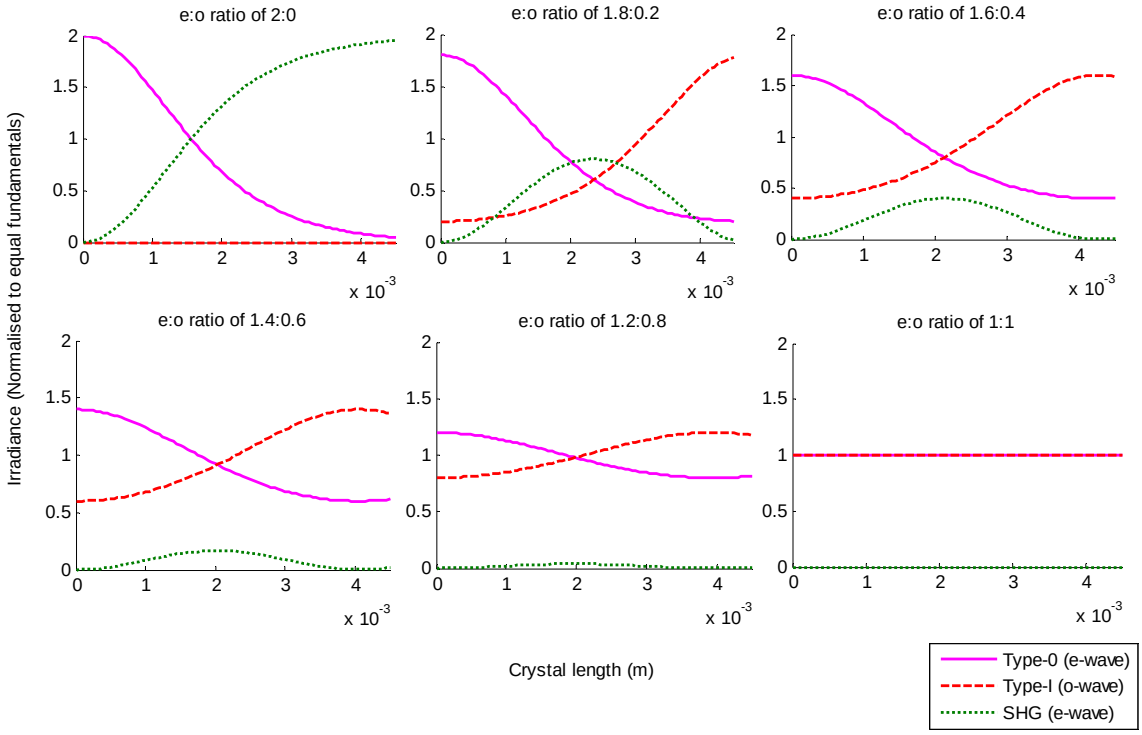

Figure 5.45 Propagation of the fundamentals and second harmonic irradiances for simultaneously phase-matched type-0 and type-I interactions with a π/2 phase shift between ordinary and extraordinary polarisations. A normalised power of $I_0=2$ is shared in various ratios between the two fundamental components.

5.4.3 Experimental observation of two colour cascading

Experimental measurements of the detuning curves for the two fundamental components and the second-harmonic were made with the same 45.75μm period crystal described above (Figure 5.28, Figure 5.29). The fundamental depletion (measured as the average power) at phase-matching in this crystal was ~12%. The experimental data has been normalized to the average input power of the fundamental, so that when equal horizontal and vertical components were incident on the crystal (45º linear polarization) 6% depletion from either polarization of the fundamental was observed at phase-matching. The fundamental and second-harmonic detuning curves are shown in Figure 5.46. Even with 6% SHG efficiency the energy exchange to the narrow band type-I fundamental at slight detuning is clearly observed in the experimental data. A 2% increase in the average power of the type-I fundamental was measured, which is in excellent agreement with numerical simulations for a 6% efficient process. The depletion for the phase-shifted fundamentals only reaches ~2% at slight detuning and returns to zero depletion at the phase-

matching temperature, as expected for coherent and equivalent processes which are out of phase. The measured detuning curves for the second harmonic are also in very good agreement with the calculated curves, showing complete suppression of the second harmonic at zero detuning for fundamentals with a $\pi/2$ phase shift. Experiments to measure the cascading between fundamentals launched with a $\pi/2$ phase shift different initial irradiances were also carried out by measuring the temperature detuning curves. If cascading between fundamentals is taking place, parametric gain should be observed at the zero detuning point. The simulation for a parent SHG process which is 30% efficient with fundamentals launched in a 1.4:0.6 ratio is shown in Figure 5.47. The detuning curve for the weaker fundamental can be seen to offer some depletion to the second harmonic at slight detunings, but experiences appreciable parametric gain at zero detuning due to cascading. The amount of parametric gain experienced at zero detuning depends on the overall efficiency of the parent process and the ratio of powers in the fundamental components. Simulated values of parametric gain in relation to the ratios of fundamental components for various efficiencies of the parent process is shown in Figure 5.48. The 'efficiency' referred to here is in reference to the depletion that the fundamentals would undergo when launched in phase with equal powers, as is the case for Figure 5.44 a) where each fundamental component is depleted by 30%.

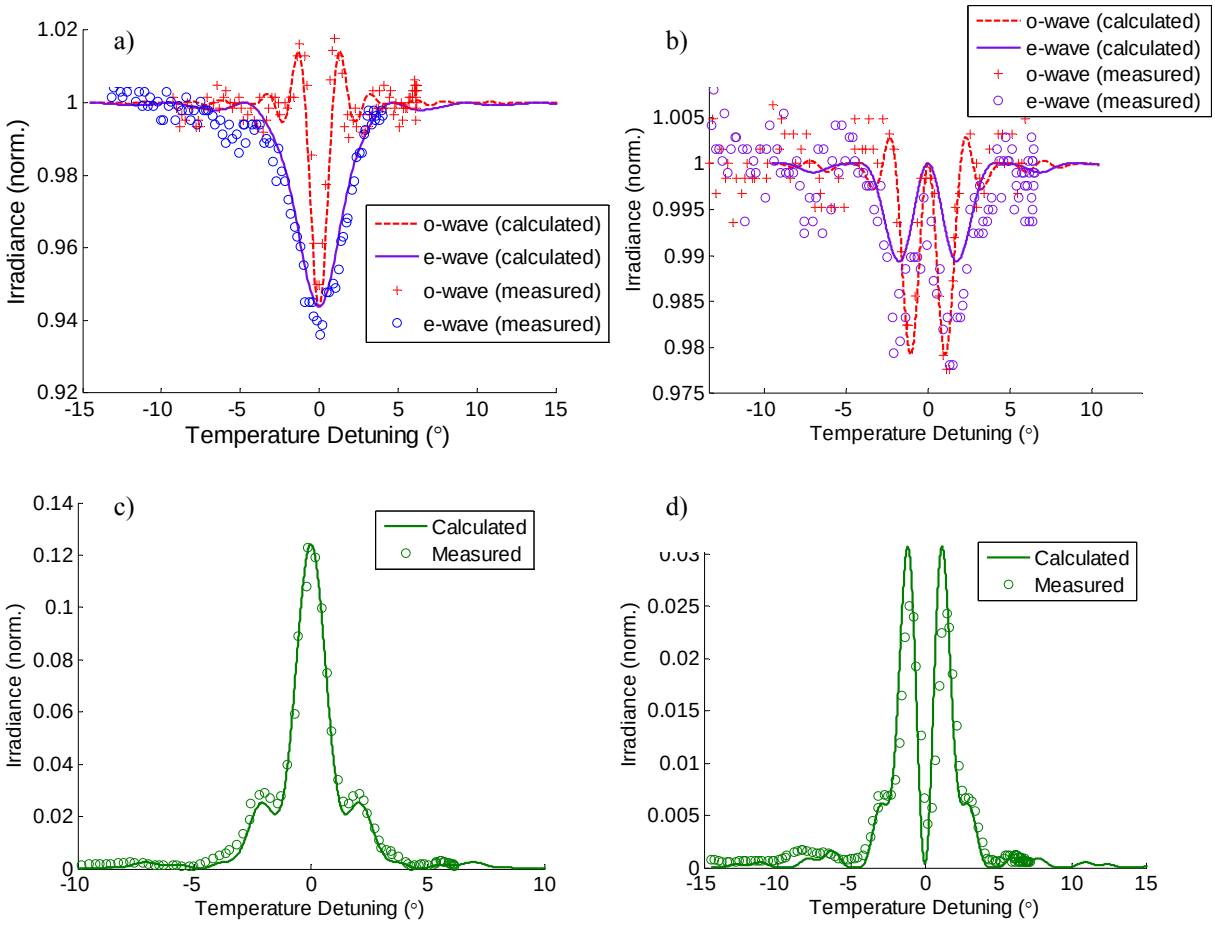

Figure 5.46 Experimentally measured fundamental and second-harmonic detuning curves for simultaneous phase-matching of equal type-0 and type-I fundamental components. Plots a) and b) show the fundamental depletion for in-phase fundamentals and π/2 phase-shifted fundamentals respectively, plots c) and d) show the corresponding second-harmonics.

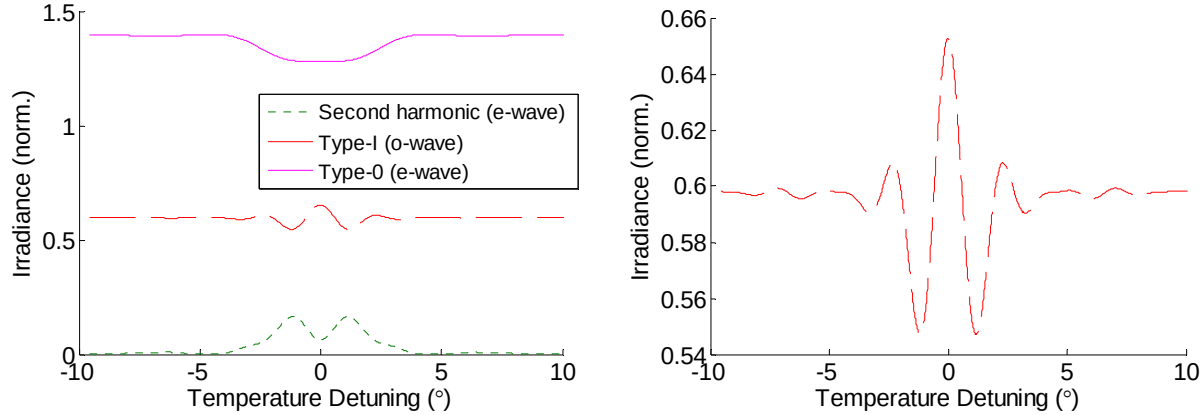

Figure 5.47 Simulated temperature detuning curves for simultaneously phase-matched fundamentals launched with irradiances in a 1.4:0.6 (70%:30%) ratio. Left: All components shown on the same scale, right: expanded scale showing the weaker fundamental, in this case the type-I component. Parametric gain due to cascading is seen at zero detuning.

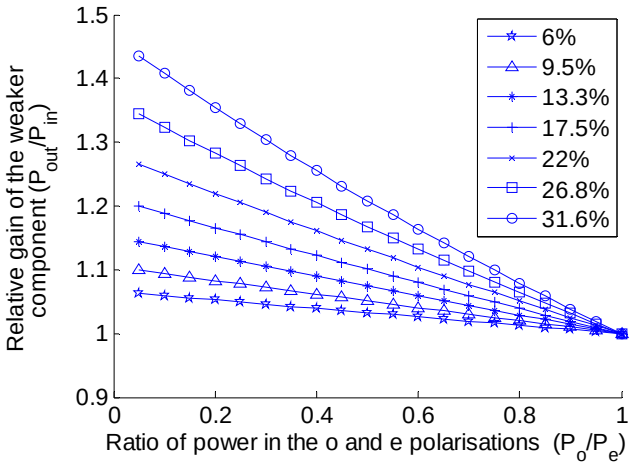

Figure 5.48 Parametric gain experienced by the weaker fundamental component in relation to the ratio between the launched fundamental powers. The parametric gains for various efficiencies of the parent process have been plotted, with the 'efficiency' referring to the depletion that the fundamentals would undergo when launched in phase with equal powers, as in Figure 5.44 a).

For this set experiments the ratio of the two fundamental components was varied using the half-wave plate shown in the setup in Figure 5.5, with the quarter-wave plate fixed on the crystal axes to produce the π/2 phase shift between the vertical (*e*-wave) and horizontal (*o*-wave) components. The temperature detuning curves were measured for a range of fundamental ratios, with detection of the weaker fundamental the point of interest. The measured detuning curve for the weaker fundamental when launched in a 1.4 : 0.6 (70% : 30%) ratio is shown in Figure 5.49. The simulations shown in Figure 5.47 were reproduced to take into account the experimental efficiency of %6, and the calculated detuning curve for the case of 1.4 : 0.6 (70% : 30%) is plotted alongside the data in Figure 5.49. The agreement between the calculated and measured detuning curves is in very good agreement with a parametric gain of ~1% measured at zero detuning. As the difference in the launched fundamental powers was increased from a ratio of 1 : 1 (50% : 50%) to a ratio of 1.9 : 0.1 (95% : 5%) the parametric gain seen from the weaker component also increased. The measured parametric gain at zero detuning across this range is shown in Figure 5.50. A gain of 6% was observed for the input ratio of (95% : 5), in good agreement with the gain expected from calculations.

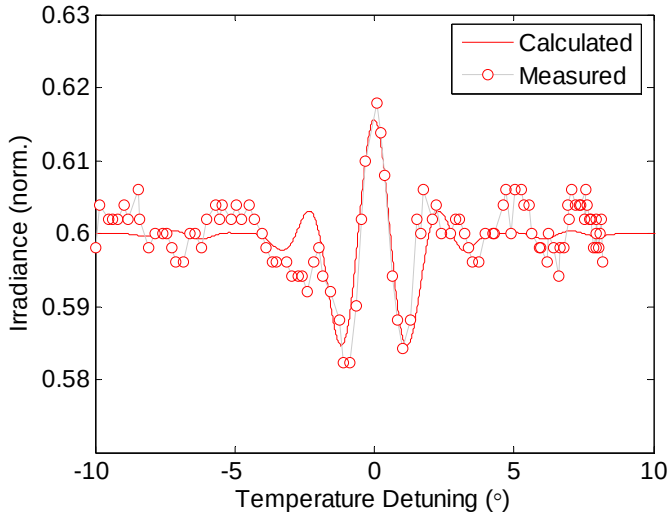

Figure 5.49 Temperature detuning curve for the weaker fundamental when launched in a 1.4 : 0.6 (70% : 30%) ratio with the stronger fundamental component. Parametric gain is seen at zero detuning as a result of cascading.

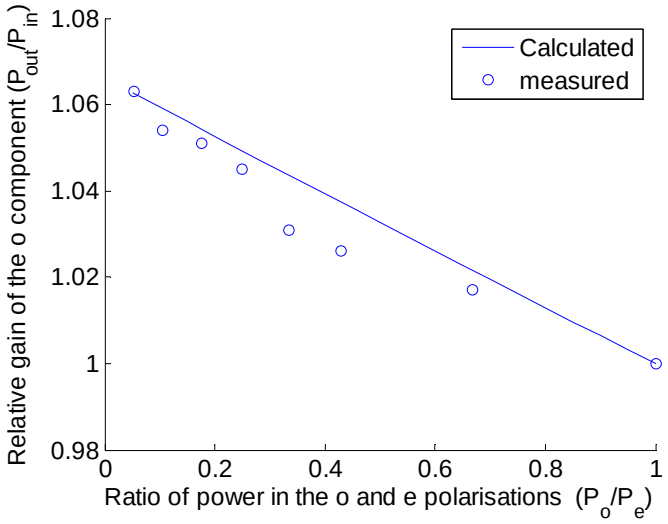

Figure 5.50 Measured gain of the weaker fundamental component, for various ratios of the fundamental input powers, due to cascading between simultaneously phase-matched SHG interactions. The parent SHG process, shown in Figure 5.46, had an efficiency of 6%.

Another point of interest in the cascaded interaction being looked at here is the power dependant 'transfer function' that an incident beam experiences. That is, for polarisation separable fundamentals, one polarisation can be set as the 'pump' input and held at a fixed input power, while the other polarisation can is treated as a 'signal' and modulated. The transmission of the signal beam will be determined in part by the nonlinear interaction taking place in the crystal.

Figure 5.51 shows simulations of the throughput of a signal beam in relation to its relative power compared to the pump. The shape of the transfer function shows a strong dependence on the efficiency of the parent SHG process. Perhaps the most interesting transfer functions are for efficiencies of 50-60% where the signal sees parametric gain at low to moderate input powers and then experiences depletion to the second-harmonic once its input power has exceed that on the pump, in essence making the interaction an amplitude limiting filter while improving the signal to noise ratio at powers less than the pump input via intensity dependant parametric gain.

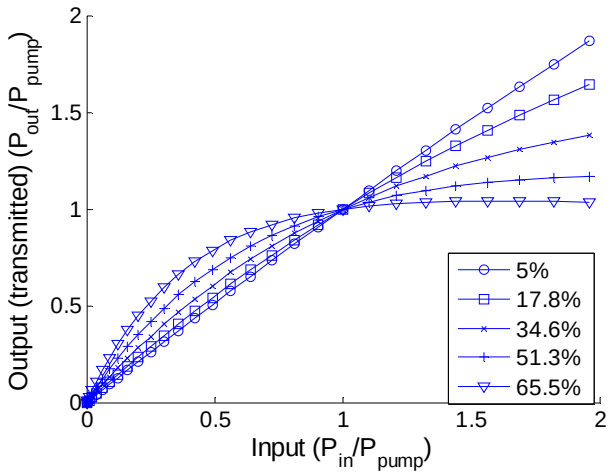

Figure 5.51 Transfer function for a 'signal' beam incident on a engineered for simultaneous phase-matching.

5.5 Summary

In this chapter the experimental results of second-harmonic generation and cascaded interactions in periodically poled lithium niobate crystals, fabricated with laser machined electrodes, have been reported. The results demonstrate that the laser fabrication technique is suitable for producing PPLN with periods >20 µm, and that advanced structures such as chirped and aperiodic domain patterns are easily prototyped using this technique.

Simultaneous phase-matching of type-0 and type-I SHG interactions at 1064 nm in PPLN with a 45.75 µm period has been demonstrated. This interaction utilises orthogonally polarised fundamentals, which act coherently in generating a common second harmonic field. For a linear input polarisation the generation of a second harmonic field can be independent of the input polarisation direction. Generation of a polarised second harmonic output from a randomly polarised incident laser beam can also be realised. Control of the relative magnitudes and phases of the fundamental components can result in modulation of the second harmonic. Alternatively it

has been suggested that the SHG from this simultaneously phase-matched interaction can be used to analyse the amplitude and phase-relation between the fundamental's orthogonal components.

The energy cascading between orthogonal fundamental components which takes place in an efficient simultaneously phase-matched interaction has been simulated from the coupled field equations and verified experimentally. These experiments demonstrated that cascading between two simultaneously phase-matched and wavelength degenerate SHG interactions does occur. This cascaded interaction results in an exchange of energy between orthogonally polarised laser beams. The following chapter will summarise the findings presented in this dissertation and suggest future directions of inquiry in the fields of laser fabricated PPLN and cascaded nonlinear optics.

Chapter 6. Conclusion

"Take young researchers; put them together in virtual seclusion,
give them an unprecedented degree of freedom
and turn up the pressure by fostering competitiveness."
James D. Watson
"The future has already arrived.
It's just not evenly distributed yet."
William Gibson

6.1 Concluding remarks on topographical electrodes for poling

The major research themes of this dissertation have been to further investigate the potential of laser micromachined topographical electrodes as a processing step in the fabrication of PPLN, and frequency conversion and cascaded processes with laser fabricated PPLN. During the development of the fabrication techniques there have been fundamental investigations including ablation studies and modelling of the electrostatic behaviour of topographical electrodes.

The ablation studies have appraised laser processing characteristics such as the ablation threshold and ablation rate scaling of lithium niobate, along with a parallel comparative study of silicon. In the ultrafast pulsed laser investigations a key result was identifying a double logarithmic trend in the fluence dependent ablation rate of silicon which was not present in lithium niobate or lithium tantalate over the same range of fluences. This observation points to a clear difference between the ultrafast laser ablation mechanisms at different fluences for semi-conductor materials and dielectrics. Different superficial ablation regimes were also identified for lithium niobate itself. There was a well defined transition from 'clean' ablation at low to moderate fluences, to ablation which produced a significant amount of particulate debris around the ablation craters. This transition in the ablation behaviour was in the vicinity of an incident fluence of 10 J/cm^2. The influence of machining parameters such as feed-rate and number of passes has also been examined, and the control over the geometry of laser machined features has been evaluated. The influence of the electrode geometry on the electric fields that result in poling has been investigated via finite element modelling. The shape, aspect ratio and depth of surface features have been identified as key parameters that influence the electric field distribution. High aspect ratio V-shaped grooves have been shown to be the optimal feature for providing high

electric field contrast. The process for PPLN fabrication with laser machined electrodes is summarised in the flow chart shown in Figure 6.1.

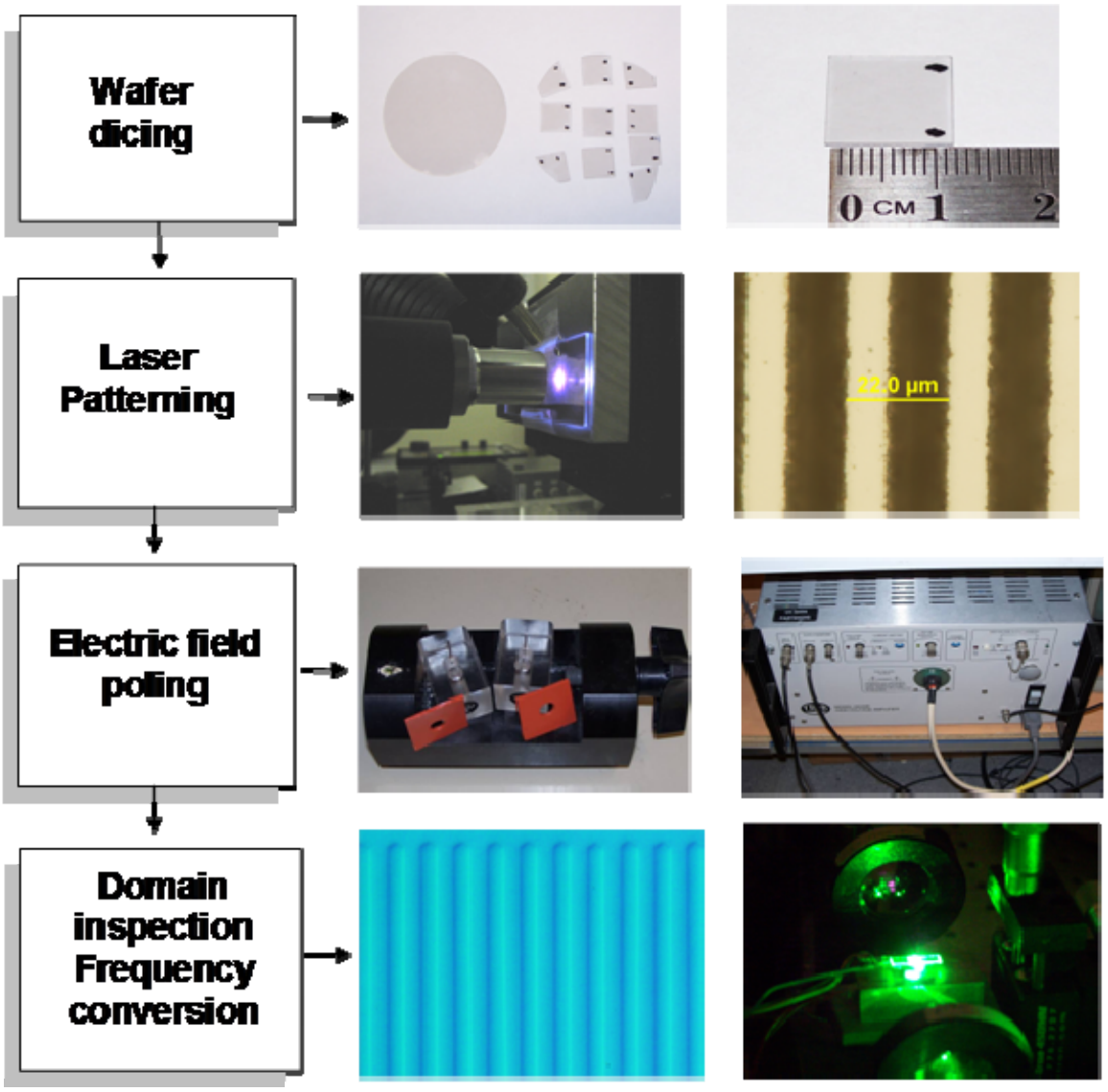

Figure 6.1 Summary of processing steps involved in the fabrication of PPLN with laser machined topographical electrodes.

While this fabrication technique may not be immediately applicable to the shorter periods required for efficient generation of visible wavelengths, there is a growing interest in larger scale domain engineering for applications in the mid-infrared and terahertz spectral regions. The nonlinear processes of interest for producing these wavelengths include optical parametric generation and amplification, difference frequency mixing and optical rectification. For example, typical poling periods of crystals designed for optical parametric generators and amplifiers pumped with 1064 nm laser sources are in the 25-32 µm range, which are immediately viable

periods for this fabrication technique. Terahertz frequency generation in the form of surface emitted radiation from optical self-rectification and difference frequency generation of closely spaced laser lines has also been demonstrated with large scale domain engineering. Weiss *et al*[218] have demonstrated terahertz generation by optical rectification in PPLN with periods as long as 127 μm. This scheme is illustrated in Figure 6.2. Sasaki *et al*[219,220] have demonstrated terahertz generation by difference frequency generation. The novel PPLN designs used in Sasaki *et al's* experiments are compatible with the laser machining technique presented in this dissertation. They include phase-reversed PPLN with a primary period of 29 μm and a phase-reverse period of 11.6 mm for dual wavelength optical parametric generation and parametric amplification, as well as difference frequency mixing in slanted and 2D domain patterns with domain widths on the order of 35 μm. The optical layout and an illustration of the difference frequency mixing employed by Sasaki *et al* are shown in Figure 6.3 and Figure 6.4 respectively.

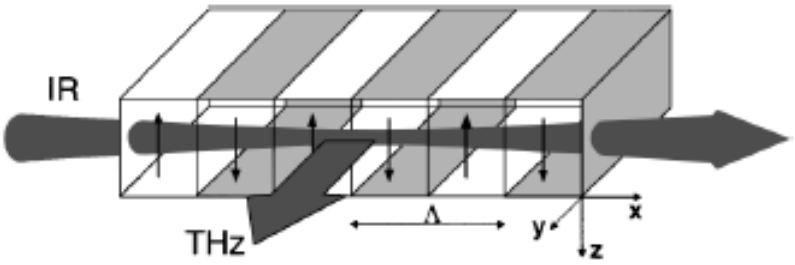

Figure 6.2 Schematic of terahertz generation by optical rectification in PPLN from Weiss *et al*[218] . Poling periods required for this implentation are long, on the order of 100μm

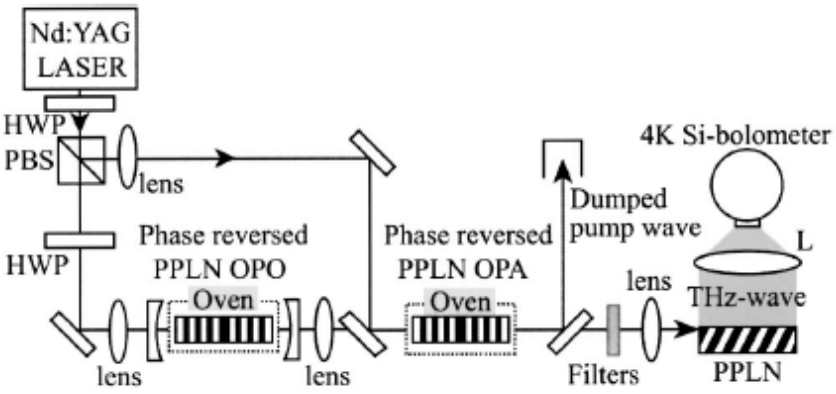

Figure 6.3 Terahertz generation in PPLN by diffference frequency generation between the lines of a dual wavelength optical parametric generator, from the work of Saski *et al*[221,220].

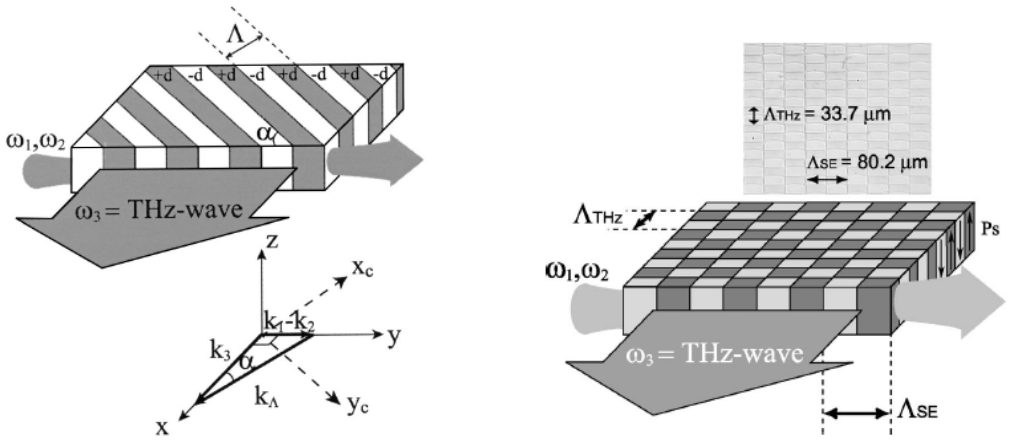

Figure 6.4 Schemes for difference frequency generation based on slanted (left) and 2D (right) domain patterns in poled lithium niobate, from Saski *et al*[221,220].

There are also other opportunities for utilising this fabrication technique for producing PPLN suitable for type-I phase-matching, as has been discussed in chapter 5. Periods suitable for generation of red, green and blue wavelengths using the d_{31} nonlinear coefficient are all within the capability of this technique. The proposal of producing PPLN suitable for simultaneous type-I generation of red and green wavelengths is also is also a point of interest to be pursued in the future. The outcomes of this dissertation demonstrate that fabrication of PPLN for applications which require domain widths in excess of 20 μm is viable using laser machined electrodes in place of lithographic patterning.

6.2 Concluding remarks on simultaneous phase-matching and cascading with QPM materials

In this dissertation a novel nonlinear phase-matching scheme has been presented. It involves simultaneously phase-matching 1st order type-I SHG with a wavelength equivalent type-0 interaction with a high QPM order. Experimentally this has been demonstrated for the type-I and 7th order type-0 SHG interactions for a 1064 nm pump wavelength. The poling period required for this interaction is 45.8 μm, easily fabricated by the laser machined electrode technique that has been presented. It has been demonstrated that second harmonic generation via simultaneous phase-matching is a coherent process which is responsive to the relative phases and amplitudes of the incident fundamental fields, as well as showing dependence on the intrinsic nonlinearities that are accessed in the crystal. For simultaneous phase matching of equivalent nonlinearites, second harmonic generation which is independent of input polariation direction can

be achieved. In the same way, equivalent nonlinearities result in the second-harmonic being completely modulated as the phase between equivalent vertical and horizontal fundamental polarisation components is changed from $0 \rightarrow \pi/4$ (from linear to circular polarisation). Going one step further, it has been demonstrated that such a phase-matching regime results in cascading between the two processes. The cascaded process facilitates the flow of energy between orthogonally polarised fundamental fields. It has been shown that this cascading of two χ^2 interactions gives rise to a coupling of energy which would otherwise be associated with a cubic interation. Similar interactions in quadratic materials have been noted for their potential applications in optical processing and for other exotic optical phenomena such as soliton formation and pulse compression. There is scope for further investigations looking at the potential of the particular process presented here in the afore mentioned applications and interactions.

6.3 Future investigations

An immediate future direction for this work is to extend the laser machined electrode technique for poling to other compositions such as MgO doped and stoichiometric lithium niobate, and to other ferroelectric crystals such as lithium tantalate and KTP. It is suspected that the lower coercive fields in these materials may prove even more amenable to this fabrication technique. It has also been suggested in Chapter 4 that the relative depth of the topographical features compared to the substrate may help improve the electric field contrast, and thus allow smaller periods to be produced. Laser machining of small features with high magnification objectives is somewhat limited in the depth of features that can be easily produced. As such a more practical approach is to move to thinner substrates where small laser machined features have a bigger impact on the electric field distribution. This may be a future avenue to improving the viable periods and resolutions of periodic poling with laser machined electrode patterning. Another approach may be to use a hybrid electrode patterning technique where laser machining is performed through an insulating layer such as photoresist or spin-on-glass. While this approach requires a spin coat and baking step, it is still direct-write in nature and alleviates the requirement for lithography mask design and fabrication. By including the insulating layer the electric field distributions in the crystal may be more suitable for producing shorter periods than has proven possible by laser machining of otherwise bare substrates.

An improved implementation of the cascaded interaction presented in this dissertation would involve the inclusion of waveguides and increasing the interaction length. Ideally the design wavelength would also be changed to target wavelengths suited to optical communications. In closing, the laser direct write technique for topographical electrode patterning of ferroelectric optical crystals has been shown to be a viable technique, suitable for use in the fabrication of domain engineered crystals for a variety of applications.

Bibliography

1 *Properties of Lithium Niobate*, Edited by K. K. Wong, IEE Datareview series. (IET, 2002).

2 *Physics and Chemistry of Crystalline Lithium Niobate*, A. M. Prokhorov, Inst of Physics Pub Inc, 1990).

3 *Lithium Niobate Crystals*, I. U. S. Kuz'minov, Cambridge International Science Publishing, 1999).

4 R. S. Weis and T. K. Gaylord, "*Lithium niobate: Summary of physical properties and crystal structure,*" Applied Physics A: Materials Science & Processing **37** (4), 191-203 (1985).

5 *Handbook of Nonlinear Optical Crystals, 3rd Ed.*, G. G. Gurzadian, V. G. Dmitriev, and D. N. Nikogosian, Springer Series in Optical Sciences. (Springer-Verlag, New York, 1999).

6 H. Ogi, Y. Kawasaki, M. Hirao, and H. Ledbetter, "*Acoustic spectroscopy of lithium niobate: Elastic and piezoelectric coefficients,*" Journal of Applied Physics **92**, 2451 (2002).

7 H. Ogi, N. Nakamura, M. Hirao, and H. Ledbetter, "*Determination of elastic, anelastic, and piezoelectric coefficients of piezoelectric materials from a single specimen by acoustic resonance spectroscopy,*" Ultrasonics **42** (1-9), 183-187 (2004).

8 E. L. Wooten, K. M. Kissa, A. Yi-Yan, E. J. Murphy, D. A. Lafaw, P. F. Hallemeier, D. Maack, D. V. Attanasio, D. J. Fritz, and G. J. McBrien, "*A review of lithium niobate modulators for fiber-opticcommunications systems,*" Selected Topics in Quantum Electronics, IEEE Journal of **6** (1), 69-82 (2000).

9 J. A. Armstrong, N. Bloembergen, J. Ducuing, and P. S. Pershan, "*Interactions between light waves in a nonlinear dielectric,*" Phys. Rev. **127**, 1918 (1962).

10 S. Miyazawa, "*Ferroelectric domain inversion in Ti-diffused $LiNbO_3$ optical waveguide,*" Journal of Applied Physics **50**, 4599 (1979).

11 D. Feng, N. B. Ming, J. F. Hong, Y. S. Yang, J. S. Zhu, Z. Yang, and Y. N. Wang, "*Enhancement of second-harmonic generation in $LiNbO_3$ crystals with periodic laminar ferroelectric domains,*" Appl. Phys. Lett. **37**, 607 (1980).

12 M. Okada, K. Takizawa, and S. Ieiri, "*Second harmonic generation by periodic laminar structure of nonlinear optical crystal,*" Optics Communications **18** (3), 331-334 (1976).

13 D. E. Thompson, J. D. McMullen, and D. B. Anderson, "*Second-harmonic generation in GaAs''stack of plates''using high-power CO laser radiation,*" Appl. Phys. Lett. **29**, 113 (1976).

14 A. Feisst and P. Koidl, "*Current induced periodic ferroelectric domain structures in $LiNbO_3$ applied for efficient nonlinear optical frequency mixing,*" Appl Phys Lett **47**, 1125 (1985).

15 G. A. Magel, M. M. Fejer, and R. L. Byer, "*Quasi-phase-matched second harmonic generation of blue light in periodically poled $LiNbO_3$,*" Appl. Phys. Lett. **56** (2), 108-110 (1990).

16 D. H. Jundt, G. A. Magel, M. M. Fejer, and R. L. Byer, "*Periodically poled $LiNbO_3$ for high-efficiency second-harmonic generation,*" Appl. Phys. Lett. **59** (21), 2657-2659 (1991).

[17] E. J. Lim, M. M. Fejer, and R. L. Byer, "*Second-harmonic generation of green light in periodically poled planar lithium niobate waveguide,*" Electronics Letters **25** (3), 174-175 (1989).

[18] E. J. Lim, M. M. Fejer, R. L. Byer, and W. J. Kozlovsky, "*Blue light generation by frequency doubling in periodically poled lithium niobate channel waveguide,*" Electronics Letters **25** (11), 731-732 (1989).

[19] E. J. Lim, H. M. Hertz, M. L. Bortz, and M. M. Fejer, "*Infrared radiation generated by quasi-phase-matched difference-frequency mixing in a periodically poled lithium niobate waveguide,*" Appl. Phys. Lett. **59** (18), 2207-2209 (1991).

[20] S. Matsumoto, E. J. Lim, H. M. Hertz, and M. M. Fejer, "*Quasiphase-matched second harmonic generation of blue light in electrically periodically-poled lithium tantalate waveguides,*" Electronics Letters **27** (22), 2040-2042 (1991).

[21] M. Yamada, N. Nada, M. Saitoh, and K. Watanabe, "*First-order quasi-phased matched $LiNbO_3$ waveguide periodically poled by applying an external field for efficient blue second-harmonic generation,*" Appl. Phys. Lett. **62** (5), 435-436 (1993).

[22] W. K. Burns, W. McElhanon, and L. Goldberg, "*Second harmonic generation in field poled, quasi-phase-matched, bulk $LiNbO_3$,*" IEEE Photonics Technology Letters **6** (2), 252-254 (1994).

[23] J. Webjorn, V. Pruneri, P. S. J. Russell, J. R. M. Barr, and D. C. Hanna, "*Quasi-phase-matched blue light generation in bulk lithium niobate, electrically poled via periodic liquid electrodes,*" Electronics Letters **30** (11), 894-895 (1994).

[24] L. E. Myers, R. C. Eckardt, M. M. Fejer, R. L. Byer, W. R. Bosenberg, and J. W. Pierce, "*Quasi-phase-matched optical parametric oscillators in bulk periodically poled $LiNbO_3$,*" Journal of the Optical Society of America B-Optical Physics **12** (11), 2102-2116 (1995).

[25] L. E. Myers, G. D. Miller, R. C. Eckardt, M. M. Fejer, R. L. Byer, and W. R. Bosenberg, "*Quasi-phase-matched 1.064- mu m-pumped optical parametric oscillator in bulk periodically poled $LiNbO_3$,*" Opt. Lett. **20** (1), 52-54 (1995).

[26] G. D. Miller, *"Periodically poled lithium niobate: modeling, fabrication, and non-linear performance"* PhD, Stanford University, 1998.

[27] G. D. Miller, R. G. Batchko, W. M. Tulloch, D. R. Weise, M. M. Fejer, and R. L. Byer, "*42%-efficient single-pass cw second-harmonic generation in periodically poled lithium niobate,*" Opt. Lett. **22** (24), 1834-1836 (1997).

[28] R. G. Batchko, V. Y. Shur, M. M. Fejer, and R. L. Byer, "*Backswitch poling in lithium niobate for high-fidelity domain patterning and efficient blue light generation,*" Appl. Phys. Lett. **75**, 1673 (1999).

[29] M. J. Missey, V. Dominic, L. E. Myers, and R. C. Eckardt, "*Diffusion-bonded stacks of periodically poled lithium niobate,*" Opt. Lett. **23** (9), 664-666 (1998).

[30] A. Grisard, E. Lallier, K. Polgar, and A. Peter, "*3 mm-thick periodically poled lithium niobate,*" Lasers and Electro-Optics, 2001. CLEO'01. Technical Digest. Summaries of papers presented at the Conference on (2001).

[31] H. Ishizuki, T. Taira, S. Kurimura, J. H. Ro, and M. Cha, "*Periodic poling in 3-mm-thick MgO: $LiNbO_3$ Crystals,*" Japanese J. of Appl. Phys **42**, 108–110 (2003).

[32] H. Ishizuki and T. Taira, "*Fabrication and characterization of 5-mm-thick periodically poled MgO: $LiNbO_3$ device,*" Lasers and Electro-Optics, 2005.(CLEO). Conference on **3** (2005).

[33] H. Ito, C. Takyu, and H. Inaba, "*Fabrication of periodic domain grating in $LiNbO_3$ byelectron beam writing for application of nonlinear opticalprocesses,*" Electronics Letters **27** (14), 1221-1222 (1991).

[34] M. Houé and P. D. Townsend, "*Thermal polarization reversal of lithium niobate,*" Appl. Phys. Lett. **66**, 2667 (1995).

[35] A. Harada and Y. Nihei, "*Bulk periodically poled MgO-$LiNbO_3$ by corona discharge method,*" Appl. Phys. Lett. **69**, 2629 (1996).

[36] S. Grilli, C. Canalias, F. Laurell, P. Ferraro, and P. De Natale, "*Control of lateral domain spreading in congruent lithium niobate by selective proton exchange,*" Appl. Phys. Lett. **89**, 032902 (2006).

[37] S. Chao, W. Davis, D. D. Tuschel, R. Nichols, M. Gupta, and H. C. Cheng, "*Time dependence of ferroelectric coercive field after domain inversion for lithium-tantalate crystal,*" Appl. Phys. Lett. **67**, 1066 (1995).

[38] S. Chao and C. C. Hung, "*Large photoinduced ferroelectric coercive field increase and photodefined domain pattern in lithium-tantalate crystal,*" Appl. Phys. Lett. **69**, 3803 (1996).

[39] P. T. Brown, S. Mailis, I. Zergioti, and R. W. Eason, "*Microstructuring of lithium niobate single crystals using pulsed UV laser modification of etching characteristics,*" Optical Materials **20** (2), 125-134 (2002).

[40] M. Fujimura, T. Sohmura, and T. Suhara, "*Fabrication of domain-inverted gratings in MgO: $LiNbO_3$ by applying voltage under ultraviolet irradiation through photomask at room temperature,*" Electronics Letters **39** (9), 719-721 (2003).

[41] M. Müller, E. Soergel, and K. Buse, "*Influence of ultraviolet illumination on the poling characteristics of lithium niobate crystals,*" Appl. Phys. Lett. **83**, 1824 (2003).

[42] M. C. Wengler, B. Fassbender, E. Soergel, and K. Buse, "*Impact of ultraviolet light on coercive field, poling dynamics and poling quality of various lithium niobate crystals from different sources,*" Journal of Applied Physics **96**, 2816 (2004).

[43] Wang Wenfeng, Wang Youfa, K. Allaart, and D. Lenstra, "*Ultrashort rectangular optical pulse generation by nonlinear directional couplers,*" Optics Communications **253** (1-3), 164-171 (2005).

[44] C. L. Sones, M. C. Wengler, C. E. Valdivia, S. Mailis, R. W. Eason, and K. Buse, "*Light-induced order-of-magnitude decrease in the electric field for domain nucleation in MgO-doped lithium niobate crystals,*" Appl. Phys. Lett. **86**, 212901 (2005).

[45] C. L. Sones, C. E. Valdivia, J. G. Scott, S. Mailis, R. W. Eason, D. A. Scrymgeour, V. Gopalan, T. Jungk, and E. Soergel, "*Ultraviolet laser-induced sub-micron periodic domain formation in congruent undoped lithium niobate crystals,*" Applied Physics B: Lasers and Optics **80** (3), 341-344 (2005).

[46] C. L. Sones, A. C. Muir, Y. J. Ying, S. Mailis, R. W. Eason, T. Jungk, Á Hoffmann, and E. Soergel, "*Precision nanoscale domain engineering of lithium niobate via UV laser induced inhibition of poling,*" Appl. Phys. Lett. **92**, 072905 (2008).

[47] V. Dierolf and C. Sandmann, "*Direct-write method for domain inversion patterns in $LiNbO_3$,*" Appl. Phys. Lett. **84**, 3987 (2004).

[48] M. Mohageg, D. Strekalov, A. Savchenkov, A. Matsko, V. Ilchenko, and L. Maleki, "*Calligraphic poling of Lithium Niobate,*" Opt. Express **13** (9), 3408-3419 (2005).

[49] M. Reich, F. Korte, C. Fallnich, H. Welling, and A. Tunnermann, "*Electrode geometries for periodic poling of ferroelectric materials,*" Optics Letters **23** (23), 1817-1819 (1998).

[50] M. H. Chou, I. Brener, M. M. Fejer, E. E. Chaban, and S. B. Christman, "*1.5- mu m-band wavelength conversion based on cascaded second-order nonlinearity in $LiNbO_3$ waveguides,*" IEEE Photonics Technology Letters **11** (6), 653-655 (1999).

[51] I. Brener, M. H. Chou, E. Chaban, K. R. Parameswaran, M. M. Fejer, and S. Kosinski, presented at the Optical Fiber Communication Conference. Technical Digest Postconference Edition. Trends in Optics and Photonics Vol.37, Baltimore, MD, 2000

[52] I. Brener, B. Mikkelsen, G. Raybon, R. Harel, K. Parameswaran, J. R. Kurz, and M. M. Fejer, "*160Gbit/s wavelength shifting and phase conjugation using periodically poled $LiNbO_3$ waveguide parametric converter,*" Electronics Letters **36** (21), 1788-1790 (2000).

[53] Sun Junqiang, Liu Wei, Tian Jing, J. R. Kurz, and M. M. Fejer, "*Multichannel wavelength conversion exploiting cascaded second-order nonlinearity in $LiNbO_3$ waveguides,*" IEEE Photonics Technology Letters **15** (12), 1743-1745 (2003).

[54] D. Gurkan, S. Kumar, A. E. Willner, K. R. Parameswaran, and M. M. Fejer, "*Simultaneous label swapping and wavelength conversion of multiple independent WDM channels in an all-optical MPLS network using PPLN waveguides as wavelength converters,*" Journal of Lightwave Technology **21** (11), 2739-2745 (2003).

[55] T. Ohara, H. Takara, I. Shake, K. Mori, S. Kawanishi, S. Mino, T. Yamada, M. Ishii, T. Kitoh, T. Kitagawa, K. R. Parameswaran, and M. M. Fejer, "*160-Gb/s optical-time-division multiplexing with PPLN hybrid integrated planar lightwave circuit,*" Ieee Photonics Technology Letters **15** (2), 302-304 (2003).

[56] T. Ohara, H. Takara, I. Shake, K. Mori, K. Sato, S. Kawanishi, S. Mino, T. Yamada, M. Ishii, I. Ogawa, T. Kitoh, K. Magari, M. Okamoto, R. V. Roussev, J. R. Kurz, K. R. Parameswaran, and M. M. Fejer, "*160-Gb/s OTDM transmission using integrated all-optical MUX/DEMUX with all-channel modulation and demultiplexing,*" IEEE Photonics Technology Letters **16** (2), 650-652 (2004).

[57] Z. Jiang, D. S. Seo, S. D. Yang, D. E. Leaird, R. V. Roussev, C. Langrock, M. M. Fejer, and A. M. Weiner, "*Low-power high-contrast coded waveform discrimination at 10 GHz via nonlinear processing,*" IEEE Photonics Technology Letters **16** (7), 1778-1780 (2004).

[58] Z. Jiang, D. S. Seo, S. D. Yang, D. E. Leaird, R. V. Roussev, C. Langrock, M. M. Fejer, and A. M. Weiner, "*Four-user, 2.5-Gb/s, spectrally coded OCDMA system demonstration using low-power nonlinear processing,*" Journal of Lightwave Technology **23** (1), 143-158 (2005).

[59] Wang Jian, Sun Junqiang, Sun Qizhen, Wang Dalin, and Huang Dexiu, "*Proposal and simulation of all-optical NRZ-to-RZ format conversion using cascaded sum- and difference-frequency generation,*" Opt. Express **15** (2) (2007).

[60] A. Kwok, L. Jusinski, M. A. Krumbiigel, J. N. Sweetser, D. N. Fittinghoff, and R. Trebino, "*Frequency-resolved optical gating using cascaded second-order nonlinearities,*" IEEE Journal of Selected Topics in Quantum Electronics **4** (2), 271-277 (1998).

[61] S. Nogiwa, H. Ohta, and Y. Kawaguchi, "*Optical sampling system using a periodically poled lithium niobate crystal,*" Ieice Transactions on Electronics **E85C** (1), 156-164 (2002).

[62] K. Gallo, J. Prawiharjo, F. Parmigiani, P. Almeida, P. Petropoulos, and D. J. Richardson, presented at the Proceedings of 2006 8th International Conference on Transparent Optical Networks, Nottingham, UK, 2006.

[63] V. Pruneri, J. Webjorn, P. S. Russell, and D. C. Hanna, "*532 Nm Pumped Optical Parametric Oscillator in Bulk Periodically Poled Lithium-Niobate,*" Appl. Phys. Lett. **67** (15), 2126-2128 (1995).

[64] W. R. Bosenberg, A. Drobshoff, J. I. Alexander, L. E. Myers, and R. L. Byer, "*93% pump depletion, 3.5-W continuous-wave, singly resonant optical parametric oscillator,*" Opt. Lett. **21** (17), 1336-1338 (1996).

[65] G. W. Baxter, Y. He, and B. J. Orr, "*A pulsed optical parametric oscillator, based on periodically poled lithium niobate (PPLN), for high-resolution spectroscopy,*" Applied Physics B-Lasers and Optics **67** (6), 753-756 (1998).

[66] Y. S. Lee, T. Meade, V. Perlin, H. Winful, T. B. Norris, and A. Galvanauskas, "*Generation of narrow-band terahertz radiation via optical rectification of femtosecond pulses in periodically poled lithium niobate,*" Appl. Phys. Lett. **76** (18), 2505-2507 (2000).

[67] H. Ito, T. Hatanaka, S. Haidar, K. Nakamura, K. Kawase, and T. Taniuchi, "*Periodically poled $LiNbO_3$ OPO for generating mid IR to terahertz waves,*" Ferroelectrics **253** (1-4), 651-660 (2001).

[68] T. J. Edwards, D. Walsh, M. B. Spurr, C. F. Rae, M. H. Dunn, and P. G. Browne, "*Compact source of continuously and widely-tunable terahertz radiation,*" Opt. Express **14** (4) (2006).

[69] *Lasers and Electro-Optics, Fundamentals and Engineering*, C. C. Davis, Cambridge University Press, Cambridge, 2000).

[70] *Nonlinear Optics*, R. W. Boyd, Academic Press, Inc., 1992).

[71] R. C. Eckardt and J. Reintjes, "*Phase matching limitations of high efficiency second harmonic generation,*" IEEE Journal of Quantum Electronics **QE-20** (10), 1178-1187 (1984).

[72] L. E. Myers, R. C. Eckardt, M. M. Fejer, R. L. Byer, and W. R. Bosenberg, "*Multigrating quasi-phase-matched optical parametric oscillator in periodically poled $LiNbO_3$,*" Opt. Lett. **21** (8), 591-593 (1996).

[73] P. E. Powers, T. J. Kulp, and S. E. Bisson, "*Continuous tuning of a continuous-wave periodically poled lithium niobate optical parametric oscillator by use of a fan-out grating design,*" Opt. Lett. **23** (3), 159-161 (1998).

[74] T. Suhara and H. Nishihara, "*Theoretical analysis of waveguide second-harmonic generation phase matched with uniform and chirped gratings,*" Quantum Electronics, IEEE Journal of **26** (7), 1265-1276.

[75] M. A. Arbore, O. Marco, and M. M. Fejer, "*Pulse compression during second-harmonic generation in aperiodic quasi-phase-matching gratings,*" Opt. Lett. **22** (12), 865-867 (1997).

[76] M. A. Arbore, A. Galvanauskas, D. Harter, M. H. Chou, and M. M. Fejer, "*Engineerable compression of ultrashort pulses by use of second-harmonic generation in chirped-period-poled lithium niobate,*" Opt Lett **22** (17), 1341-1343 (1997).

[77] Shi-ning Zhu, Yong-yuan Zhu, and Nai-ben Ming, "*Quasi-Phase-Matched Third-Harmonic Generation in a Quasi-Periodic Optical Superlattice,*" Science **278** (5339), 843-846 (1997).

[78] M. H. Chou, K. R. Parameswaran, M. M. Fejer, and I. Brener, "*Multiple-channel wavelength conversion by use of engineered quasi-phase-matching structures in $LiNbO_3$ waveguides,*" Opt. Lett. **24** (16), 1157-1159 (1999).

[79] A. H. Norton and C. M. de Sterke, "*Aperiodic 1-dimensional structures for quasi-phase matching,*" Opt. Express **12** (5) (2004).

[80] Zhang Chao, Zhu Yong-Yuan, Yang Su-Xia, Qin Yi-Qiang, Zhu Shi-Ning, Chen Yan-Bin, Liu Hui, and Ming Nai-Ben, "*Crucial effects of coupling coefficients on quasi-phase-matched harmonic generation in an optical superlattice,*" Opt. Lett. **25** (7), 436-438 (2000).

[81] Wu Jie, T. Kondo, and R. Ito, "*Optimal design for broadband quasi-phase-matched second-harmonic generation using simulated annealing,*" Journal of Lightwave Technology **13** (3), 456-460 (1995).

[82] Liu Xueming and Li Yanhe, "*Optimal design of DFG-based wavelength conversion based on hybrid genetic algorithm,*" Opt. Express **11** (14) (2003).

[83] Z. W. Liu, S. N. Zhu, Y. Y. Zhu, H. Liu, Y. Q. Lu, H. T. Wang, N. B. Ming, X. Y. Liang, and Z. Y. Xu, "*A scheme to realize three-fundamental-colors laser based on quasi-phase matching,*" Solid State Communications **119** (6), 363-366 (2001).

[84] T. W. Ren, J. L. He, C. Zhang, S. N. Zhu, Y. Y. Zhu, and Y. Hang, "*Simultaneous generation of three primary colours using aperiodically poled $LiTaO_3$,*" Journal of Physics Condensed Matter **16** (18), 3289-3294 (2004).

[85] C. Huang, Y. Zhu, and S. Zhu, "*Generation of three primary colours with a 1064 nm pump wave in a single optical superlattice,*" Journal of Physics Condensed Matter **15** (26), 4651-4655 (2003).

[86] N. G. R. Broderick, G. W. Ross, H. L. Offerhaus, D. J. Richardson, and D. C. Hanna, "*Hexagonally poled lithium niobate: a two-dimensional nonlinear photonic crystal,*" Phys. Rev. Lett. **84** (19), 4345-4348 (2000).

[87] N. Fujioka, S. Ashihara, H. Ono, T. Shimura, and K. Kuroda, "*Group-velocity-mismatch compensation in cascaded third-harmonic generation with two-dimensional quasi-phase-matching gratings,*" Opt. Lett. **31** (18), 2780-2782 (2006).

[88] N. G. R. Broderick, R. T. Bratfalean, T. M. Monro, D. J. Richardson, and C. M. de Sterke, "*Temperature and wavelength tuning of second-, third-, and fourth-harmonic generation in a two-dimensional hexagonally poled nonlinear crystal,*" Journal of the Optical Society of America B-Optical Physics **19** (9), 2263-2272 (2002).

[89] M. De Sterke, S. M. Saltiel, and Y. S. Kivshar, "*Efficient collinear fourth-harmonic generation by two-channel multistep cascading in a single two-dimensional nonlinear photonic crystal,*" Opt. Lett. **26** (8), 539-541 (2001).

[90] Jonathan R. Kurz, *"Integrated Optical-Frequency Mixers"* Doctoral Thesis, Stanford, 2003.

[91] G. Imeshev, M. Proctor, and M. M. Fejer, "*Lateral patterning of nonlinear frequency conversion with transversely varying quasi-phase-matching gratings,*" Opt. Lett. **23** (9), 673-675 (1998).

[92] J. R. Kurz, X. P. Xie, and M. M. Fejer, "*Odd waveguide mode quasi-phase matching with angled and staggered gratings,*" Opt. Lett. **27** (16), 1445-1447 (2002).

[93] M Baudrier-Raybaut, R Haidar, Ph Kupecek, Ph Lemasson, and E Rosencher, "*Random quasi-phase-matching in bulk polycrystalline isotropic nonlinear materials,*" Nature **423** (7015), 374 (2004); SE Skipetrov, "*Disorder is the new order,*" Nature **432**, 285 (2004).

[94] R. Fischer, S. M. Saltiel, D. N. Neshev, W. Krolikowski, and Yu S. Kivshar, "*Broadband femtosecond frequency doubling in random media,*" Appl. Phys. Lett. **89** (19), 191105-191105-191103 (2006).

[95] R. Fischer, D. N. Neshev, S. M. Saltiel, A. A. Sukhorukov, W. Krolikowski, and Y. S. Kivshar, "*Monitoring ultrashort pulses by transverse frequency doubling of counterpropagating pulses in random media,*" Appl. Phys. Lett. **91** (3), 31101-31104 (2007).

[96] Y. Sheng, J. Dou, B. Ma, B. Cheng, and D. Zhang, "*Broadband efficient second harmonic generation in media with a short-range order,*" Appl. Phys. Lett. **91** (011101) (2007).

[97] M. M. Fejer, G. A. Magel, D. H. Jundt, and R. L. Byer, "*Quasi-phase-matched second harmonic generation: tuning and tolerances,*" IEEE Journal of Quantum Electronics **28** (11), 2631-2654 (1992).

[98] *Laser processing and chemistry, 3rd edition*, Dieter Bauerle, Springer, Berlin, 2000), p.788.

[99] J. Ren, S. S. Orlov, L. Hesselink, H. Howard, and A. J. Conneely, "*Nanosecond laser silicon micromachining,*" Proc. SPIE - Int. Soc. Opt. Eng. **5339** (1), 382-393 (2004).

[100] E. G. Gamaly, A. V. Rode, and B. Luther-Davies, "*Ultrafast ablation with high-pulse-rate lasers. Part I: Theoretical considerations,*" Journal of Applied Physics **85** (8), 4213-4221 (1999).

[101] K. Piglmayer, E. Arenholz, C. Ortwein, N. Arnold, and D. Bauerle, "*Single-pulse ultraviolet laser-induced surface modification and ablation of polyimide,*" Applied Physics Letters **73** (6), 847-849 (1998).

[102] S. I. Anisimov, "*Vaporizaion of metal absorbing laser radiation* " Soviet Physics, JETP **27** (1) (1968).

[103] J. M. Fishburn, M. J. Withford, D. W. Coutts, and J. A. Piper, "*Study of the fluence dependent interplay between laser induced material removal mechanisms in metals: Vaporization, melt displacement and melt ejection,*" Applied Surface Science **252** (14), 5182-5188 (2006).

[104] J. M. Fishburn, M. J. Withford, D. W. Coutts, and J. A. Piper, "*Method for Determination of the Volume of Material Ejected as Molten Droplets During Visible Nanosecond Ablation,*" Applied Optics **43** (35), 6473-6476 (2004).

[105] J. Ren, X. Yin, S. S. Orlov, and L. Hesselink, "*Realtime study of plume ejection dynamics in silicon laser ablation under 5ns pulses,*" Applied Physics Letters **88**, 061111 (2006).

[106] J. H. Yoo, S. H. Jeong, R. Greif, and R. E. Russo, "*Explosive change in crater properties during high power nanosecond ablation of silicon,*" Journal of Applied Physics **88** (3), 1638-1649 (2000).

[107] J. M. Fishburn, M. J. Withford, D. W. Coutts, and J. A. Piper, "*Study of the interplay of vaporisation, melt displacement and melt ejection mechanisms under multiple pulse irradiation of metals,*" Applied Surface Science **253** (2), 662-667 (2006).

[108] C. Porneala and D. A. Willis, "*Observation of nanosecond laser-induced phase explosion in aluminum,*" Applied Physics Letters **89**, 211121 (2006).

[109] A. M. Marsh, S. D. Harkness, F. Qian, and R. K. Singh, "*Pulsed laser deposition of high quality $LiNbO_3$ films on sapphire substrates,*" Applied Physics Letters **62**, 952 (1993).

[110] C. N. Afonso, J. Gonzalo, F. Vega, E. Dieguez, J. C. C. Wong, C. Ortega, J. Siejka, and G. Amsel, "*Correlation between optical properties, composition, and deposition parameters in pulsed laser deposited $LiNbO_3$ films,*" Applied Physics Letters **66** (12), 1452-1454 (1995).

[111] J. A. Chaos, R. W. Dreyfus, A. Perea, R. Serna, J. Gonzalo, and C. N. Afonso, "*Delayed release of Li atoms from laser ablated lithium niobate,*" Applied Physics Letters **76** (5), 649-651 (2000).

[112] F. J. Gordillo-Vazquez, A. Perea, and C. N. Afonso, "*Effect of Ar and O_2 atmospheres on the fundamental properties of the plasma produced by laser ablation of lithium niobate,*" Applied Spectroscopy **56** (3), 381-385 (2002); Y. Shibata, K. Kaya, K. Akashi, M. Kanai, T. Kawai, and S. Kawai, "*Epitaxial growth and surface acoustic wave properties of lithium niobate films grown by pulsed laser deposition,*" Journal of Applied Physics **77** (4), 1498-1503 (1995).

[113] P. Aubert, G. Garry, R. Bisaro, and J. G. Lopez, "*Structural properties of $LiNbO_3$ thin films grown by the pulsed laser deposition technique,*" Applied Surface Science **86** (1-4), 144-148 (1995).

[114] C. H. Bulmer, W. K. Burns, and A. S. Greenblatt, "*Phase tuning by laser ablation of LiNbO 3 interferometricmodulators to optimum linearity,*" Photonics Technology Letters, IEEE **3** (6), 510-512 (1991).

[115] C. C. Chen, H. Forte, A. Carenco, J. P. Goedgebuer, and V. Armbruster, "*Phrase correction by laser ablation of a polarization independentLiNbO$_3$ Mach-Zehnder modulator,*" Photonics Technology Letters, IEEE **9** (10), 1361-1363 (1997).

[116] H. Hakogi and H. Takamatsu, (United States Patent US005283842A, 1994).

[117] G. P. Luo, Y. L. Lu, Y. Q. Lu, X. L. Guo, S. B. Xiong, C. Z. Ge, Y. Y. Zhu, Z. G. Liu, N. B. Ming, and J. W. Wu, "*$LiNbO_3$ phase gratings prepared by a single excimer pulse through a silica phase mask,*" Applied Physics Letters **69**, 1352 (1996).

[118] C. L. Chang and C. F. Chen, (US Patent US005393371A, 1995).

[119] P. Bunton, M. Binkley, and G. Asbury, "*Laser ablation from lithium niobate,*" Applied Physics a (Materials Science Processing) **65** (4-5), 411-417 (1997).

[120] Chong Han-Woo, A. Mitchell, J. P. Hayes, and M. W. Austin, "*Investigation of KrF excimer laser ablation and induced surface damage on lithium niobate,*" Applied Surface Science **201** (1-4), 196-203 (2002).

[121] F. Meriche, E. Neiss-Clauss, R. Kremer, A. Boudrioua, E. Dogheche, E. Fogarassy, R. Mouras, and A. Bouabellou, "*Micro structuring of $LiNbO_3$ by using nanosecond pulsed laser ablation,*" Applied Surface Science **254** (4), 1327-1331 (2007).

[122] J. Greuters and N. H. Rizvi, "*Laser micromachining of optical materials with a 157nm fluorine laser,*" Proc SPIE **4941**, 77-83 (2002).

[123] A. Rodenas, D. Jaque, C. Molpeceres, S. Lauzurica, J. L. Ocana, G. A. Torchia, and F. Agullo-Rueda, "*Ultraviolet nanosecond laser-assisted micro-modifications in lithium niobate monitored by Nd^{3+} luminescence,*" Applied Physics A (Materials Science Processing) **A87** (1), 87-90 (2007).

[124] L. McCaughan and C. M. Staus, (US Patent US006951120B2, 2005).

[125] S. Mailis, G. W. Ross, L. Reekie, J. A. Abernethy, and R. W. Eason, "*Fabrication of surface relief gratings on lithium niobate bycombined UV laser and wet etching,*" Electronics Letters **36** (21), 1801-1803 (2000).

[126] P. T. Brown, S. Mailis, I. Zergioti, and R. W. Eason, "*Microstructuring of lithium niobate single crystals using pulsed UV laser modification of etching characteristics,*" Opt. Mater. (Netherlands) **20** (2), 125-134 (2002).

[127] B. C. Stuart, M. D. Feit, A. M. Rubenchik, B. W. Shore, and M. D. Perry, "*Laser-induced damage in dielectrics with nanosecond to subpicosecond pulses,*" Phys. Rev. Lett. **74** (12), 2248-2251 (1995).

[128] B. C. Stuart, M. D. Feit, A. M. Rubenchik, B. W. Shore, and M. D. Perry, "*Laser-induced damage in dielectrics with nanosecond to subpicosecond pulses,*" Phys. Rev. Lett. **74** (12), 2248-2251 (1995).

[129] B. C. Stuart, M. D. Feit, S. Herman, A. M. Rubenchik, B. W. Shore, and M. D. Perry, "*Nanosecond-to-femtosecond laser-induced breakdown in dielectrics,*" Phys. Rev. B, Condens. Matter **53** (4), 1749-1761 (1996).

[130] B. C. Stuart, M. D. Feit, S. Herman, A. M. Rubenchik, B. W. Shore, and M. D. Perry, "*Optical ablation by high-power short-pulse lasers,*" J. Opt. Soc. Am. B, Opt. Phys. **13** (2), 459-468 (1996).

[131] M. D. Perry, B. C. Stuart, P. S. Banks, M. D. Feit, V. Yanovsky, and A. M. Rubenchik, "*Ultrashort-pulse laser machining of dielectric materials,*" Journal of Applied Physics **85** (9), 6803-6810 (1999).

[132] E. G. Gamaly, A. V. Rode, B. Luther-Davies, and V. T. Tikhonchuk, "*Ablation of solids by femtosecond lasers: Ablation mechanism and ablation thresholds for metals and dielectrics,*" Phys. Plasmas **9** (3), 949-957 (2002).

[133] E. G. Gamaly, A. V. Rode, O. Uteza, V. Kolev, B. Luther-Davies, T. Bauer, J. Koch, F. Korte, and B. N. Chichkov, "*Control over a phase state of the laser plume ablated by femtosecond laser: spatial pulse shaping,*" Journal of Applied Physics **95** (5), 2250-2257 (2004).

[134] S. Preuss, A. Demchuk, and M. Stuke, "*Sub-picosecond UV laser ablation of metals,*" Applied Physics A: Materials Science & Processing **61** (1), 33-37 (1995).

[135] S. I. Anisimov, N. A. Inogamov, A. M. Oparin, B. Rethfeld, T. Yabe, M. Ogawa, and V. E. Fortov, "*Pulsed laser evaporation: equation-of-state effects,*" Applied Physics A (Materials Science Processing) **A69** (6), 617-620 (1999).

[136] B. Rethfeld, V. V. Temnov, K. Sokolowski-Tinten, P. Tsu, D. von der Linde, S. I. Anisimov, S. I. Ashitkov, and M. B. Agranat, "*Superfast thermal melting of solids under the action of femtosecond laser pulses,*" J. Opt. Technol. , 348-352 (2004).

[137] K. Sokolowski-Tinten, J. Bialkowski, A. Cavalleri, D. von der Linde, A. Oparin, J. Meyer-ter-Vehn, and S. I. Anisimov, "*Transient states of matter during short pulse laser ablation,*" Phys. Rev. Lett. **81** (1), 224-227 (1998).

[138] R. Stoian, D. Ashkenasi, A. Rosenfeld, and E. E. B. Campbell, "*Coulomb explosion in ultrashort pulsed laser ablation of Al_2O_3,*" Physical Review B **62** (19), 13167-13173 (2000).

[139] R. Stoian, A. Rosenfeld, D. Ashkenasi, I. V. Hertel, N. M. Bulgakova, and E. E. B. Campbell, "*Surface Charging and Impulsive Ion Ejection during Ultrashort Pulsed Laser Ablation,*" Phys. Rev. Lett. **88** (9), 97603 (2002).

[140] F. Quere, S. Guizard, and P. Martin, "*Time-resolved study of laser-induced breakdown in dielectrics,*" Europhysics Letters **56** (1), 138-144 (2001).

[141] S. S. Mao, F. Quéré, S. Guizard, X. Mao, R. E. Russo, G. Petite, and P. Martin, "*Dynamics of femtosecond laser interactions with dielectrics,*" Applied Physics A: Materials Science & Processing **79** (7), 1695-1709 (2004).

[142] S. Nolte, C. Momma, H. Jacobs, A. Tunnermann, B. N. Chichkov, B. Wellegehausen, and H. Welling, "*Ablation of metals by ultrashort laser pulses,*" J. Opt. Soc. Am. B, Opt. Phys. **14** (10), 2716-2722 (1997).

[143] F. Korte, S. Nolte, B. N. Chichkov, T. Bauer, G. Kamlage, T. Wagner, C. Fallnich, and H. Welling, "*Far-field and near-field material processing with femtosecond laser pulses,*" Applied Physics A (Materials Science Processing) **A69**, 7-11 (1999).

[144] S. I. Anisimov, B. L. Kapeliovich, and T. L. Perel'man, "*Electron-emission from surface of metals induced by ultrashort laser pulses,*" Sov. Phys. JETP **39**, 375-380 (1974).

[145] C. Momma, B. N. Chichkov, S. Nolte, F. von Alvensleben, A. Tunnermann, H. Welling, and B. Wellegehausen, "*Short-pulse laser ablation of solid targets,*" Opt. Commun. (Netherlands) **129** (1-2), 134-142 (1996).

[146] P. Stampfli and K. H. Bennemann, "*Time dependence of the laser-induced femtosecond lattice instability of Si and GaAs: Role of longitudinal optical distortions,*" Physical Review B **49** (11), 7299-7305 (1994).

[147] A. J. Lee, M. J. Withford, and J. M. Dawes, "*Comparative study of UV-laser ablation of PETG under nanosecond and femtosecond exposure,*" Lasers and Electro-Optics, 2005. CLEO/Pacific Rim 2005. Pacific Rim Conference on, 1456-1457 (2005).

[148] S. Nolte, C. Momma, H. Jacobs, A. Tunnermann, B. N. Chichkov, B. Wellegehausen, and H. Welling, "*Ablation of metals by ultrashort laser pulses,*" Journal of the Optical Society of America B-Optical Physics **14** (10), 2716-2722 (1997).

[149] B. H. Christensen, K. Vestentoft, and P. Balling, "*Short-pulse ablation rates and the two-temperature model,*" Applied Surface Science **253** (15), 6347-6352 (2007).

[150] D. C. Deshpande, A. P. Malshe, E. A. Stach, V. Radmilovic, D. Alexander, D. Doerr, and D. Hirt, "*Investigation of femtosecond laser assisted nano and microscale modifications in lithium niobate,*" Journal of Applied Physics **97** (7), 74316-74311-74316-74316-74319 (2005).

[151] H. Chen, X. Chen, Y. Zhang, and Y. Xia, "*Ablation induced by single-and multiple-femtosecond laser pulses in lithium niobate,*" Laser Phys. **17** (12), 1378-1381 (2007).

[152] S. Preuss, M. Spath, Y. Zhang, and M. Stuke, "*Time resolved dynamics of subpicosecond laser ablation,*" Applied Physics Letters **62** (23), 3049-3051 (1993).

[153] A. Rosenfeld, M. Lorenz, R. Stoian, and D. Ashkenasi, "*Ultrashort-laser-pulse damage threshold of transparent materials and the role of incubation,*" Applied Physics A: Materials Science & Processing **69** (7), 373-376 (1999).

[154] N. S. Stoyanov, D. W. Ward, T. Feurer, and K. A. Nelson, "*Terahertz polariton propagation in patterned materials,*" Nature Materials **1** (2), 95-98 (2002).

[155] J. Burghoff, C. Grebing, S. Nolte, and A. Tunnermann, "*Efficient frequency doubling in femtosecond laser-written waveguides in lithium niobate,*" Applied Physics Letters **89** (8), 81108-81101-81108-81108-81103 (2006).

[156] L. Gui, B. Xu, and T. C. Chong, "*Microstructure in lithium niobate by use of focused femtosecond laser pulses,*" Photonics Technology Letters, IEEE **16** (5), 1337-1339 (2004).

[157] R. R. Thomson, S. Campbell, I. J. Blewett, A. K. Kar, and D. T. Reid, "*Optical waveguide fabrication in z-cut lithium niobate (LiNbO) using femtosecond pulses in the low repetition rate regime,*" Applied Physics Letters **88**, 111109 (2006).

[158] Y. L. Lee, N. E. Yu, C. Jung, B. A. Yu, I. B. Sohn, S. C. Choi, Y. C. Noh, D. K. Ko, W. S. Yang, and H. M. Lee, "*Second-harmonic generation in periodically poled lithium niobate waveguides fabricated by femtosecond laser pulses,*" Applied Physics Letters **89**, 171103 (2006).

[159] G. Zhou and M. Gu, "*Anisotropic properties of ultrafast laser-driven microexplosions in lithium niobate crystal,*" Applied Physics Letters **87**, 241107 (2005).

[160] E. G. Gamaly, S. Juodkazis, V. Mizeikis, H. Misawa, A. V. Rode, W. Z. Krolikowski, and K. Kitamura, "*Three-dimensional write–read–erase memory bits by femtosecond laser pulses in photorefractive LiNbO3 crystals,*" Current Applied Physics **8** (3-4), 416-419 (2008).

[161] M. Eyett and D. Bäuerle, "*Influence of the beam spot size on ablation rates in pulsed-laser processing,*" Applied Physics Letters **51**, 2054 (1987).

[162] H. W. Chong, A. Mitchell, J. P. Hayes, and M. W. Austin, "*Investigation of KrF excimer laser ablation and induced surface damage on lithium niobate,*" Applied Surface Science **201** (1-4), 196-203 (2002).

[163] R. I. Tomov, T. K. Kabadjova, P. A. Atanasov, S. Tonchev, M. Kaneva, A. Zherikhin, and R. W. Eason, "*LiNbO3 optical waveguides deposited on sapphire by electric-field-assisted pulsed laser deposition,*" Vacuum **58** (2-3), 396-403 (2000).

[164] J. A. Chaos, A. Perea, J. Gonzalo, R. W. Dreyfus, C. N. Afonso, and J. Perrière, "*Ambient gas effects during the growth of lithium niobate films by pulsed laser deposition,*" Applied Surface Science **154**, 473-477 (2000).

[165] D. Redfield and W. J. Burke, "*Optical absorption edge of LiNbO,*" Journal of Applied Physics **45**, 4566 (2003).

[166] J. Bonse, S. Baudach, J. Krüger, W. Kautek, and M. Lenzner, "*Femtosecond laser ablation of silicon-modification thresholds and morphology,*" Applied Physics A: Materials Science & Processing **74** (1), 19-25 (2002).

[167] J. Bonse, K. W. Brzezinka, and A. J. Meixner, "*Modifying single-crystalline silicon by femtosecond laser pulses: an analysis by micro Raman spectroscopy, scanning laser microscopy and atomic force microscopy,*" Applied Surface Science **221** (1-4), 215-230 (2004).

[168] S. Lee, D. Yang, and S. Nikumb, "*Femtosecond laser micromilling of Si wafers,*" Applied Surface Science **254** (10), 2996-3005 (2008).

[169] A. Borowiec, M. MacKenzie, G. C. Weatherly, and H. K. Haugen, "*Transmission and scanning electron microscopy studies of single femtosecond-laser-pulse ablation of silicon,*" Applied Physics A: Materials Science & Processing **76** (2), 201-207 (2003).

[170] H. O. Jeschke, M. E. Garcia, M. Lenzner, J. Bonse, J. Krüger, and W. Kautek, "*Laser ablation thresholds of silicon for different pulse durations: theory and experiment,*" Applied Surface Science **197**, 839-844 (2002).

[171] A. Cavalleri, K. Sokolowski-Tinten, J. Bialkowski, M. Schreiner, and D. von der Linde, "*Femtosecond melting and ablation of semiconductors studied with time of flight mass spectroscopy,*" Journal of Applied Physics **85**, 3301 (1999).

[172] D. J. Hwang, C. P. Grigoropoulos, and T. Y. Choi, "*Efficiency of silicon micromachining by femtosecond laser pulses in ambient air,*" Journal of Applied Physics **99**, 083101 (2006).

[173] T. H. R. Crawford, A. Borowiec, and H. K. Haugen, "*Femtosecond laser micromachining of grooves in silicon with 800 nm pulses,*" Applied Physics A: Materials Science & Processing **80** (8), 1717-1724 (2005).

[174] N. Bärsch, K. Körber, A. Ostendorf, and K. H. Tönshoff, "*Ablation and cutting of planar silicon devices using femtosecond laser pulses,*" Applied Physics A: Materials Science & Processing **77** (2), 237-242 (2003).

[175] Z. Guosheng, P. M. Fauchet, and A. E. Siegman, "*Growth of spontaneous periodic surface structures on solids during laser illumination,*" Physical Review B **26** (10), 5366-5381 (1982).

[176] Y. Zhang, X. Chen, H. Chen, and Y. Xia, "*Surface ablation of lithium tantalate by femtosecond laser,*" Applied Surface Science **253** (22), 8874-8878 (2007).

[177] B. Yu, P. Lu, N. Dai, Y. Li, X. Wang, Y. Wang, and Q. Zheng, "*Femtosecond laser-induced sub-wavelength modification in lithium niobate single crystal,*" Journal of Optics A: Pure and Applied Optics **10**, 035301 (2008).

[178] P. R. Herman, A. Oettl, K. P. Chen, and R. S. Marjoribanks, "*Laser micromachining of transparent fused silica with 1-ps pulses and pulse trains,*" Proc. SPIE **3616**, 148-155 (1999).

[179] G. D. Miller, *"Periodically poled lithium niobate: modeling, fabrication, and nonlinear-optical performance"* PhD, Stanford University, 1998.

[180] S. Grilli, P. Ferraro, M. Paturzo, D. Alfieri, P. De Natale, M. de Angelis, S. De Nicola, A. Finizio, and G. Pierattini, "*In-situ visualization, monitoring and analysis of electric field domain reversal process in ferroelectric crystals by digital holography,*" Opt. Express **12** (9), 1832-1842 (2004).

[181] V. Y. Shur, "*Kinetics of ferroelectric domains: Application of general approach to LiNbO 3 and LiTaO 3,*" Journal of Materials Science **41** (1), 199-210 (2006).

[182] A. I. Lobov, V. Y. Shur, I. S. Baturin, E. I. Shishkin, D. K. Kuznetsov, A. G. Shur, M. A. Dolbilov, and K. Gallo, "*Field Induced Evolution of Regular and Random 2D Domain Structures and Shape of Isolated Domains in LiNbO 3 and LiTaO 3,*" Ferroelectrics **341** (1), 109-116 (2006).

[183] D. Kasimov, A. Arie, E. Winebrand, G. Rosenman, A. Bruner, P. Shaier, and D. Eger, "*Annular symmetry nonlinear frequency converters,*" Opt. Express **14** (20), 9371-9376 (2006).

[184] S. M. Saltiel, D. N. Neshev, R. Fischer, W. Krolikowski, A. Arie, and Y. S. Kivshar, "*Spatiotemporal toroidal waves from the transverse second-harmonic generation,*" Opt. Lett. **33** (5), 527-529 (2008).

[185] J. P. Meyn, C. Laue, R. Knappe, R. Wallenstein, and M. M. Fejer, "*Fabrication of periodically poled lithium tantalate for UV generation with diode lasers,*" Applied Physics B: Lasers and Optics **73** (2), 111-114 (2001).

[186] V. Y. Shur, E. L. Rumyantsev, S. D. Makarov, and V. V. Volegov, "*How to extract information about domain kinetics in thin ferroelectric films from switching transient current data,*" Integrated Ferroelectrics **5** (4), 293-301 (1994).

[187] V. Y. Shur and E. L. Rumyantsev, "*Kinetics of ferroelectric domain structure: Retardation effects,*" Ferroelectrics **191** (1), 319-333 (1997).

[188] V. Shur, E. Rumyantsev, and S. Makarov, "*Kinetics of phase transformations in real finite systems: Application to switching in ferroelectrics,*" Journal of Applied Physics **84**, 445 (1998).

[189] V. Y. Shur, "*Kinetics of polarization reversal in normal and relaxor ferroelectrics: Relaxation effects,*" Phase Transitions **65** (1), 49-72 (1998).

[190] V. Shur, E. Rumyantsev, R. Batchko, G. Miller, M. Fejer, and R. Byer, "*Physical basis of the domain engineering in the bulk ferroelectrics,*" Ferroelectrics **221** (1), 157-167 (1999).

[191] V. Y. Shur, E. L. Rumyantsev, R. G. Batchko, G. D. Miller, M. M. Fejer, and R. L. Byer, "*Domain kinetics in the formation of a periodic domain structure in lithium niobate,*" Physics of the Solid State **41** (10), 1681-1687 (1999).

[192] V. Y. Shur, E. L. Rumyantsev, S. D. Makarov, N. Y. Ponomarev, E. V. Nikolaeva, and E. I. Shishkin, "*How to learn the domain kinetics from the switching current data,*" Integrated Ferroelectrics **27** (1), 179-194 (1999).

[193] V. Y. Shur, E. L. Rumyantsev, E. V. Nikolaeva, E. I. Shishkin, D. V. Fursov, R. G. Batchko, L. A. Eyres, M. M. Fejer, and R. L. Byer, "*Nanoscale backswitched domain patterning in lithium niobate,*" Appl. Phys. Lett. **76**, 143 (2000).

[194] P. Ferraro and S. Grilli, "*Modulating the thickness of the resist pattern for controlling size and depth of submicron reversed domains in lithium niobate,*" Appl. Phys. Lett. **89**, 133111 (2006).

[195] S. W. Kwon, Y. S. Song, W. S. Yang, H. M. Lee, W. K. Kim, H. Y. Lee, and D. Y. Lee, "*Effect of photoresist grating thickness and pattern open width on performance of periodically poled LiNbO3 for a quasi-phase matching device,*" Optical Materials **29** (8), 923-926 (2007).

[196] L. E. Myers, "*Periodically poled materials for nonlinear optics,*" Advances in Lasers and Applications: Proceedings of the Fifty-second Scottish Universities Summer School in Physics, St. Andrews, September 1998 (1999).

[197] P. Dekker and J. Dawes, "*Twinning and "natural quasi-phase matching" in Yb: YAB,*" Applied Physics B: Lasers and Optics **83** (2), 267-271 (2006).

[198] A. Ganany, A. Arie, and S. M. Saltiel, "*Quasi-phase matching in $LiNbO_3$ using nonlinear coefficients in the XY plane,*" Applied Physics B (Lasers and Optics) **B85** (1), 97-100 (2006).

[199] V. Pasiskevicius, S. J. Holmgren, S. Wang, and F. Laurell, "*Simultaneous second-harmonic generation with two orthogonal polarization states in periodically poled KTP,*" Opt. Lett. **27** (18), 1628-1630 (2002).

[200] Go Fujii, Naoto Namekata, Masayuki Motoya, Sunao Kurimura, and Shuichiro Inoue, "*Bright narrowband source of photon pairs at optical telecommunication wavelengths using a type-II periodically poled lithium niobate waveguide,*" Opt. Express **15** (20), 12769-12776 (2007).

[201] Yuping Chen, Rui Wu, Xianglong Zeng, and Xianfeng Chen, "*Type I quasi-phase-matched blue second harmonic generation with different polarizations in periodically poled LiNbO3,*" Optics & Laser Technology **38** (1), 19-22.

[202] M. Masuda, Y. Yasutome, K. Yamada, S. Tomioka, T. Kudou, and T. Ozeki, in *Proceedings of ECOC 2000, Munich* (2000), Vol. 1, pp. 137-138.

[203] R. DeSalvo, D. J. Hagan, M. Sheik-Bahae, G. Stegeman, E. W. Van Stryland, and H. Vanherzeele, "*Self-focusing and self-defocusing by cascaded second-order effects in KTP,*" Opt. Lett. **17** (1), 28-30 (1992).

[204] M. Sheik-Bahae, A. A. Said, T. H. Wei, D. J. Hagan, and E. W. Van Stryland, "*Sensitive measurement of optical nonlinearities using a single beam,*" Quantum Electronics, IEEE Journal of **26** (4), 760-769 (1990).

[205] S. Saltiel, in *Ultrafast Photonics*, edited by A. Miller, D. T. Reid, and Finlayson D. M. (Institute of Physics, 2002), pp. 73-102.

[206] G. Assanto, "*Transistor Action through Nonlinear Cascading in Type-II Interactions,*" Opt. Lett. **20** (15), 1595-1597 (1995).

[207] Cha Myoungsik, "*Cascaded phase shift and intensity modulation in aperiodic quasi-phase-matched gratings,*" Opt. Lett. **23** (4), 250-252 (1998).

[208] G. Assanto, I. Torelli, and S. Trillo, "*All-optical processing by means of vectorial interactions in second-order cascading: novel approaches,*" Opt. Lett. **19** (21), 1720-1722 (1994).

[209] S. Saltiel, K. Koynov, Y. Deyanova, and Y. S. Kivshar, "*Nonlinear phase shift resulting from two-color multistep cascading,*" Journal of the Optical Society of America B (Optical Physics) **17** (6), 959-965 (2000).

[210] S. M. Saltiel, A. A. Sukhorukov, and Y. S. Kivshar, in *Progress in Optics, Vol 47* (2005), pp. 1-73.

[211] S. Saltiel and Y. Deyanova, "*Polarization switching as a result of cascading of two simultaneously phase-matched quadratic processes,*" Opt. Lett. **24** (18), 1296-1298 (1999).

[212] G. I. Petrov, O. Albert, J. Etchepare, and S. M. Saltiel, "*Cross-polarized wave generation by effective cubic nonlinear optical interaction,*" Opt. Lett. **26** (6), 355-357 (2001).

[213] A. DeRossi, C. Conti, and G. Assanto, "*Mode interplay via quadratic cascading in a lithium niobate waveguide for all-optical processing,*" Optical and Quantum Electronics **29** (1), 53-63 (1997).

[214] S. G. Grechin and V. G. Dmitriev, "*Quasi-phase-matching conditions for a simultaneous generation of several harmonies of laser radiation in periodically poled crystals,*" Quantum Electronics **31** (10), 933-936 (2001).

[215] B. F. Johnston, P. Dekker, M. J. Withford, S. M. Saltiel, and Y. S. Kivshar, "*Simultaneous phase matching and internal interference of two second-order nonlinear parametric processes,*" Opt. Express **14** (24) (2006).

[216] B. F. Johnston, P. Dekker, S. M. Saltiel, Y. S. Kivshar, and M. J. Withford, "*Energy exchange between two orthogonally polarized waves by cascading of two quasiphase-matched quadratic processes,*" Opt. Express **15** (21), 13630-13639 (2007).

[217] C. G. Trevino-Palacios, G. I. Stegeman, M. P. De Micheli, P. Baldi, S. Nouh, D. B. Ostrowsky, D. Delacourt, and M. Papuchon, "*Intensity dependent mode competition in second harmonic generation in multimode waveguides,*" Appl. Phys. Lett. **67** (2), 170-172 (1995).

[218] C. Weiss, G. Torosyan, Y. Avetisyan, and R. Beigang, "*Generation of tunable narrow-band surface-emitted terahertz radiation in periodically poled lithium niobate,*" Opt. Lett. **26** (8), 563-565 (2001).

[219] Y. Sasaki, A. Yuri, K. Kawase, and H. Ito, "*Terahertz-wave surface-emitted difference frequency generation in slant-stripe-type periodically poled LiNbO3 crystal,*" Appl. Phys. Lett. **81** (18), 3323-3325 (2002).

[220] Y. Sasaki, Y. Avetisyan, H. Yokoyama, and H. Ito, "*Surface-emitted terahertz-wave difference-frequency generation in two-dimensional periodically poled lithium niobate,*" Opt. Lett. **30** (21), 2927-2929 (2005).

[221] Y. Sasaki, A. Yuri, K. Kawase, and H. Ito, "*Terahertz-wave surface-emitted difference frequency generation in slant-stripe-type periodically poled LiNbO crystal,*" Appl. Phys. Lett. **81**, 3323 (2002).

[222] K. R. Parameswaran, J. R. Kurz, R. V. Roussev, and M. M. Fejer, "*Observation of 99% pump depletion in single-pass second-harmonic generation in a periodically poled lithium niobate waveguide,*" Opt. Lett. **27** (1), 43-45 (2002).

Appendices

A1. Important considerations for SHG with waveguides

As well as facilitating integration into fibre based optical systems, waveguides offer increased confinement of light within a material over long interaction lengths which is very beneficial for improving the efficiency of nonlinear processes. Waveguides have played a crucial role in enabling c-band nonlinear devices in PPLN at power levels compatible with telecommunications applications. There have also been some fundamental advances made by using waveguides. For example Parameswaran *et al*[222] have demonstrated that careful design and operation of an annealed proton exchange waveguide can result in almost complete conversion from fundamental to second harmonic in PPLN. The goal of this section is to review some of the benefits and issues associated with guided-wave frequency conversion.

The inclusion of waveguides in the nonlinear medium introduces the additional issue of waveguide modes to the frequency conversion process. A simple approach is to consider the plain wave picture to the propagating electric fields and modified it to take into account the transverse profiles of the waveguide modes, the effective refractive indices of the modes, and the overlap and interaction between modes at different frequencies. A simple approach to waveguides which only support a small number of modes (ideally only single mode) at all the frequencies of interest is to include the transverse mode profiles in the description of the propagating fields, and the overlap of these profiles along with the waveguide losses in the coupled field equations. Staying with the prototypical SHG processes, we continue with the approximate plain-wave picture of the electric fields and introduce a transverse profile $f_{\omega,2\omega}(x,y)$

$$\vec{E}_{\omega}(x,y,z) = f_{\omega}(x,y)E_{\omega}e^{-ik_1 z}$$
$$\vec{E}_{2\omega}(x,y,z) = f_{2\omega}(x,y)E_{2\omega}e^{-ik_2 z}$$
$$\frac{dE_{\omega}}{dz} = -i\sqrt{\eta_0}E_{\omega}^{*}E_{2\omega}e^{-i\Delta kz} - \alpha_{\omega}E_{\omega}$$
$$\frac{dE_{2\omega}}{dz} = -i\sqrt{\eta_0}E_{\omega}^{2}e^{-i\Delta kz} - \alpha_{2\omega}E_{2\omega}$$

Here $f_{\omega,2\omega}(x,y)$ is found as an Eigen-mode of the waveguide. We subsequently introduce the term $\sqrt{\eta_0}$ which includes nonlinearities, impedances and the mode overlap, or effective area of the guided wave frequency doubling process, S_{eff},

$$\eta_0 = \frac{2\omega^2}{\varepsilon_0 c^3}\frac{d_{eff}^2}{n_\omega^2 n_{2\omega} S_{eff}}$$

S_{eff} is the ratio of the products of the auto-correlations of each of the waveguide modes to the cross-correlation of the modes (for SHG we have ω+ω→2ω and we consider there to be two contributions from the fundamental mode, even if they are the same field).

$$S_{eff} = \frac{\iint |f_{2\omega}(x,y)|^2 dxdy \left\{\iint |f_\omega(x,y)|^2 dxdy\right\}^2}{\left\{\iint [f_{2\omega}(x,y)]^* [f_\omega(x,y)]^2 dxdy\right\}^2}$$

The transverse profiles, $f_{\omega,2\omega}(x,y)$, will depend on the refractive index profile of the waveguides, of which there are many varieties depending on the waveguide type and its fabrication. The process becomes more complicated when considering waveguides which support several modes, which can couple and evolve the electric field profiles as they propagate. This will generally cause less than ideal efficiencies, as the different mode patterns have varying effective indices and propagation constants, and will experience varying degrees of phase-matching by a periodic grating. A more thorough consideration of the role of waveguides can be made by including the full coupled mode theory, but is beyond the scope of this dissertation. Suffice to say that the Eigen-modes of a waveguide with a transverse refractive index profile $n(x,y)$ are found by solving the scalar Eigen-mode equation (a similar form to the Helmholtz equation, $\nabla^2 U + k^2 U = 0$ for describing time invariant field components);

$$\left(\frac{\partial^2}{\partial x^2} + \frac{\partial^2}{\partial y^2}\right) f(x,y) + \left[n(x,y)^2 - n_{eff}{}^2\right]\left(\frac{\omega}{c}\right)^2 f(x,y) = 0$$

Where n_{eff} is the effective refractive index of the mode, and there maybe many supported in the waveguide. The concern when designing and fabricating waveguides for frequency conversion is that the waveguide supports all wavelengths participating in the process, and ideally remains single mode at all these wavelengths. For a typical refractive index profile of a particular waveguide, in practice determined by the fabrication technique, the issue becomes what area of

the guiding region to aim for. If the guide area is too large the higher frequency fields may become multimoded. If the guide area is too small the lower frequency fields may become radiative and be lossy. If single moded guiding at the fundamental and second harmonic frequencies of a SHG process is achieved in reasonably symmetric guides, the effective area, S_{eff}, is often well approximated experimentally by considering the Gaussian fits to the transverse mode profiles;

$$f(x,y) = e^{(-2x/w_x)^2} e^{(-2x/w_y)^2}$$

Where $w_{x,y}$ are the $1/e^2$ widths of the mode in the *x* and *y* directions. We can find that the value for S_{eff} can be found as,

$$S_{eff} = \frac{\pi}{32}\left[\frac{\left(w_x^{\omega}\right)^2 + 2\left(w_x^{2\omega}\right)}{w_x^{2\omega}}\right]\left[\frac{\left(w_y^{\omega}\right)^2 + 2\left(w_y^{2\omega}\right)}{w_y^{2\omega}}\right]$$

which can be measured experimentally from the Gaussian fits to the observed modes of the fundamental and SH. If the waveguides in question tend to become slightly multimode at the higher frequencies, the modal shapes may be well approximated by higher order functions such as a Hermite-Gaussian (Cartesian symmetry) or Laguerre-Gaussian (radial symmetry) functions. For guides which remain single mode at all frequencies concerned, the value of S_{eff} will still be affected by the dispersion of the guide material, as the higher frequency fields will be confined more strongly in the guide region due to the higher effective refractive index they experience (in the normal dispersion regime). This will result in differing waist sizes ($w_{x,y}$) for the fundamental and second harmonic, effecting the overlap efficiency.

Another factor in waveguide nonlinear conversion performance is the intrinsic propagation loss of the guides. In the bulk optics picture we assume the medium to be reasonably lossless and generally neglect the loss terms $\alpha_{\omega,2\omega}$ from However the propagation losses for the waveguides may be significant and different for the different frequencies. The higher frequency fields will intrinsically be lossier as they experience a higher effective refractive index and are more susceptible to waveguide imperfections and the shorter wavelength results in more efficient scattering from material defects. For SHG this shows up experimentally as a discrepancy between the fundamental depletion and the extracted second harmonic, as seen in the published

results of Parameswaran *et al*. Here it was reported that ~450mW of SH was extracted for an input pump power of 900mW, despite there being a corresponding 99% depletion of the pump.

A2. Laser machining and characterization apparatus.

Light Wave Electronics frequency doubled Nd:YAG

The nanosecond laser used during this project was a Light Wave Electronics (LWE) Q-series system. This laser is a frequency doubled Nd:YAG system which produces ~0.7 W CW and up to 3 mJ Q-switched pulses at rep-rates from 100's Hz to 20 kHz. For the laser processing of interest in this dissertation, this laser was externally frequency doubled again by a focused single pass in a BBO crystal to produce 266 nm pulses with pulse energies up to ~300 μJ. A photograph of the optical layout for this system is shown on the following page. The motion control for this system was a set of XYZ Aerotech stages. The FWHM of the pulses from this system are 15 ns, however the pulse shape was not ideal and the pulse had significant power out to 40 ns.

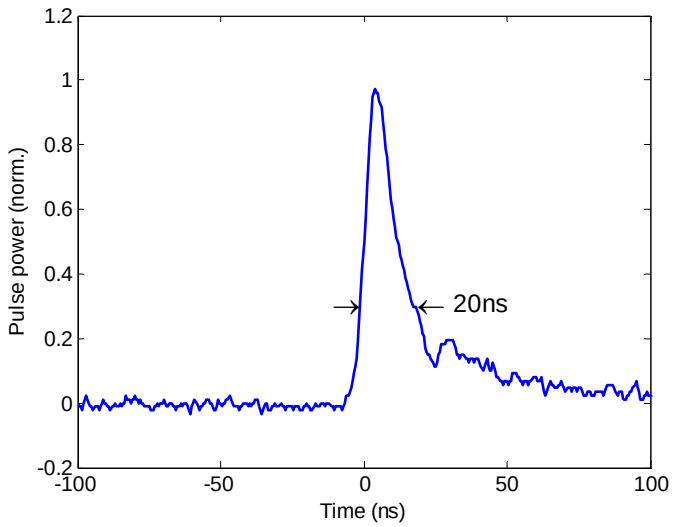

Measured pulse from the LWE nanosecond laser system.

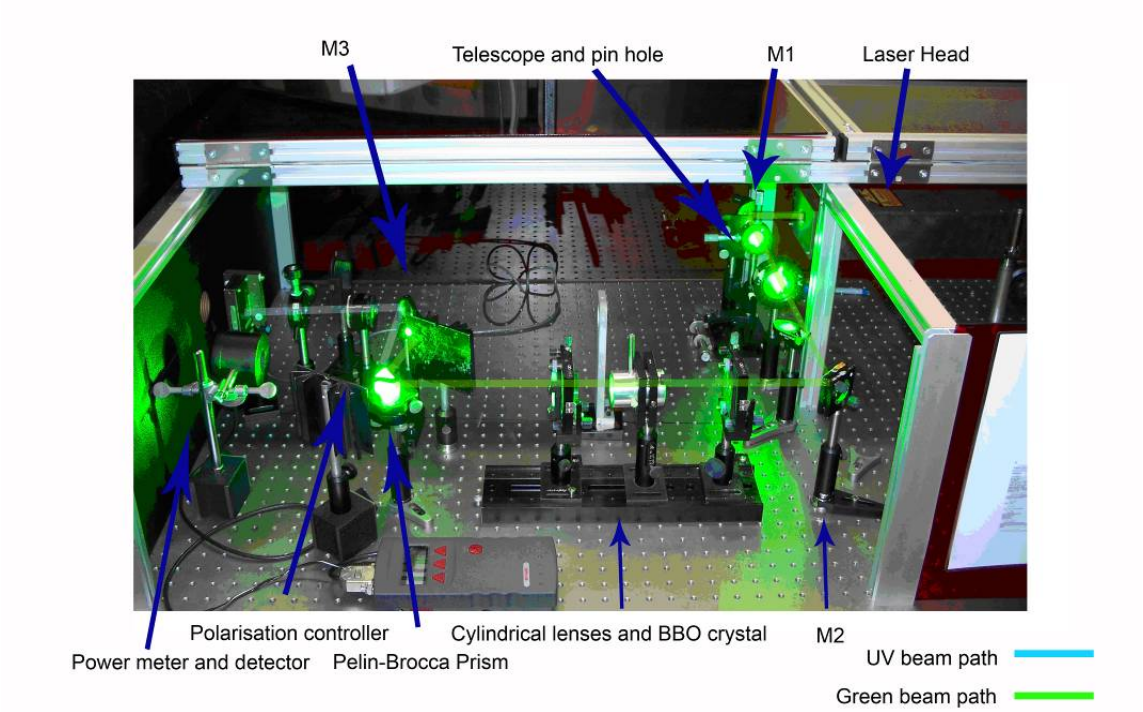

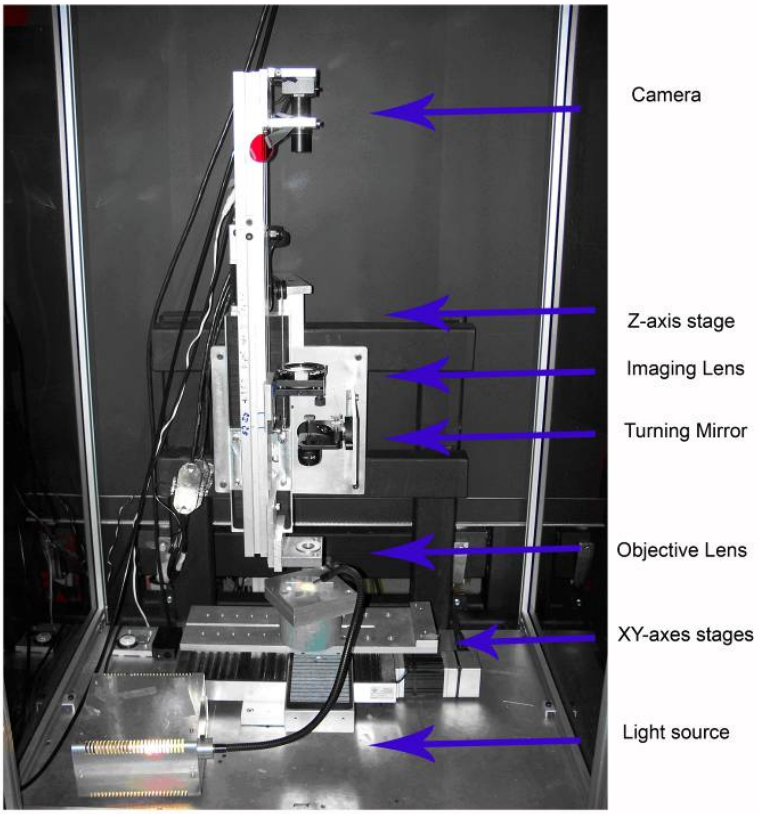

Optical layout and machining head used for the LWE laser system

Spectra-Physics Hurricane Ti:Sapphire 800nm femtosecond system

The ultrafast system used during this project was a Spectra-Physics Hurricane laser. The Hurricane is comprised of the 'Mai-Tai' Ti:Sapphire 80 MHz oscillator and a 1kHz regenerative amplifier. The system produces ~100 fs pulses with up to 1 mJ pulse energy with a pulse repetition rate up to 1 kHz. The optical layout of this system is shown below. The laser beam was characterized with a frequency resolved optical gating (FROG) module and camera beam profiler. The average power was measured using a sensitive thermal detector (Coherent Field Max II). The power on target was controlled by a half-wave plate/ linear polarizer arrangement with the half-wave plate held in a computer controlled rotation stage for careful adjustment of the power. The pulse duration could be controlled to some extent by tuning the pulse compression grating in the stage amplifier of the laser. Pulse durations of 100 fs were typical from this system.

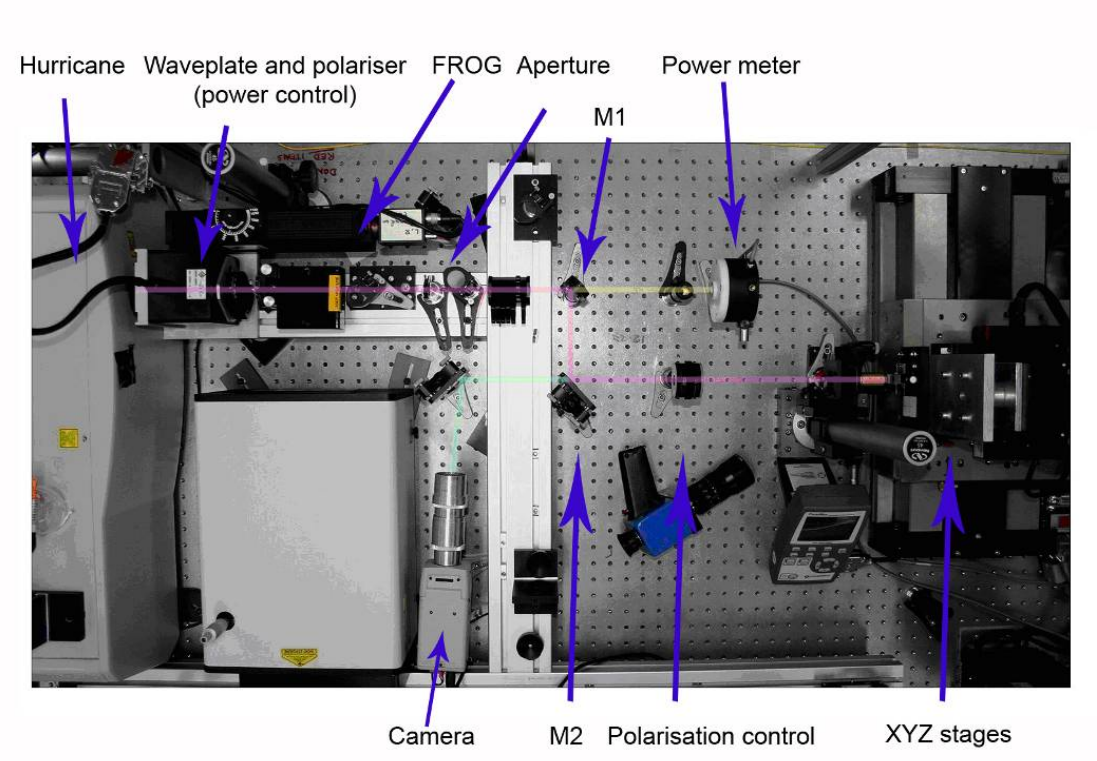

Optical layer for the Hurricane laser system

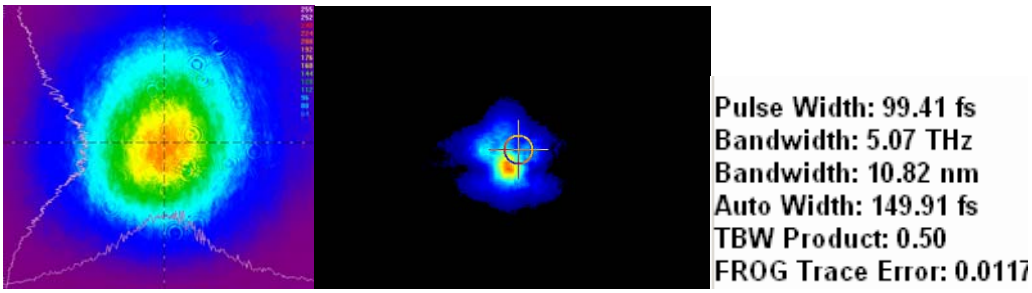

Beam profile and measured pulse duration of the Hurricane laser system, taken with a FROG apparatus

Measurements of the ablated features were carried out using optical profilometry on a Veeco system. While this instrument may not have the resolution of an AFM in all 3 dimensions, the resolution in the direction of the vertical scanning interferometer is ample for ablation studies (on the order on 5-10nm) and its rapid data collection capabilities makes it an ideal tool for looking at large areas of topographical interest. The Veeco instrument is based on Mirau interferometer used in a vertical scanning configuration. The measurements produce 3D data sets and the corresponding surface statistics. A basic schematic of the optics involved in the Veeco optical profiler is shown below.

The Veeco surface optical profilometer at Macquarie University

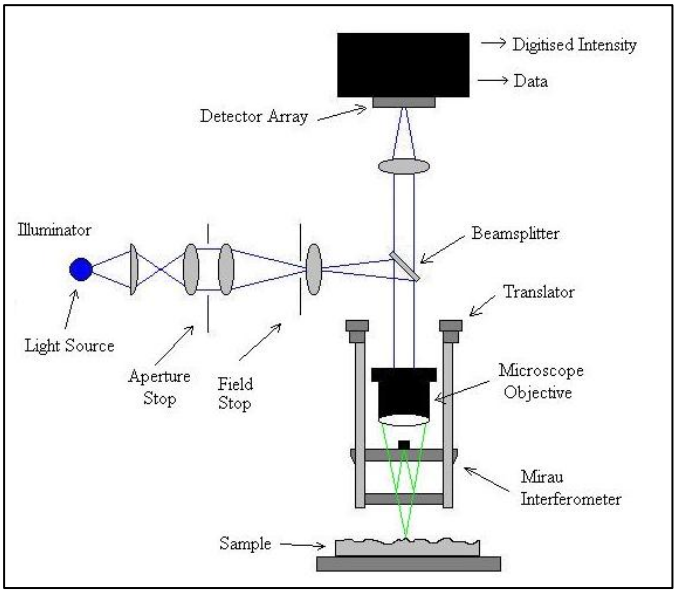

Illustration of the optical layout involved with surface optical profiliomtery

The interferometer has two modes of measurement; phase shifting interferometry (PSI) and vertical scanning interferometry (VSI). PSI mode uses monochromatic light and piezo scanning of the reference mirror to produce a vertical data set of the interference fringes between the surface and the reference arm of the interferometer. These measurements become degenerate for topographical surfaces with peak-to-valley features exceeding $\lambda/4$ so the sample surface needs to be very flat and smooth to begin with. The Veeco instrument used had a PSI wavelength of 645nm so that 160nm peak-to-valley features could be measured unambiguously. PSI mode lends itself well to measuring the quality of polished optical surfaces and thin topographical features such as sputtered metal coatings. On the other hand VSI measurements use white light interferometry to continuously scan the interferometer with scan ranges of µm's to mm's. The fringes produced in the interferometer are dependant on all colours being coherently interfered, which only happens when the image plane of the objective is in the vicinity of the surface of the sample. These measurements are based on the fringe modulation rather than the phase of the fringes. The intensity modulation signal is put through an algorithm which matches pixel values to surface heights. The system is calibrated to a known ~10µm step to an accuracy of 0.05% and accurate measurements of features down to 50nm in the vertical direction can be made. The lateral resolution for both the PSI and VSI modes is ~150nm, dependant on the CCD pixel resolution and the magnification used in the optical column. The laser ablated features being looked at here will range from 10's of nanometers to 10's of micrometers in depth and VSI is the most commonly used method of measurement. The images below show a microscope image of a

single shot ablation crater in silicon from the Hurricane femtosecond system. The 3D image constructed from the optical profile of this ablation is shown in along with the 2D profile across the crater showing a depth of ~85nm. Optical profilometry has been used to characterize the ablation features of various targets throughout the remainder of this chapter.

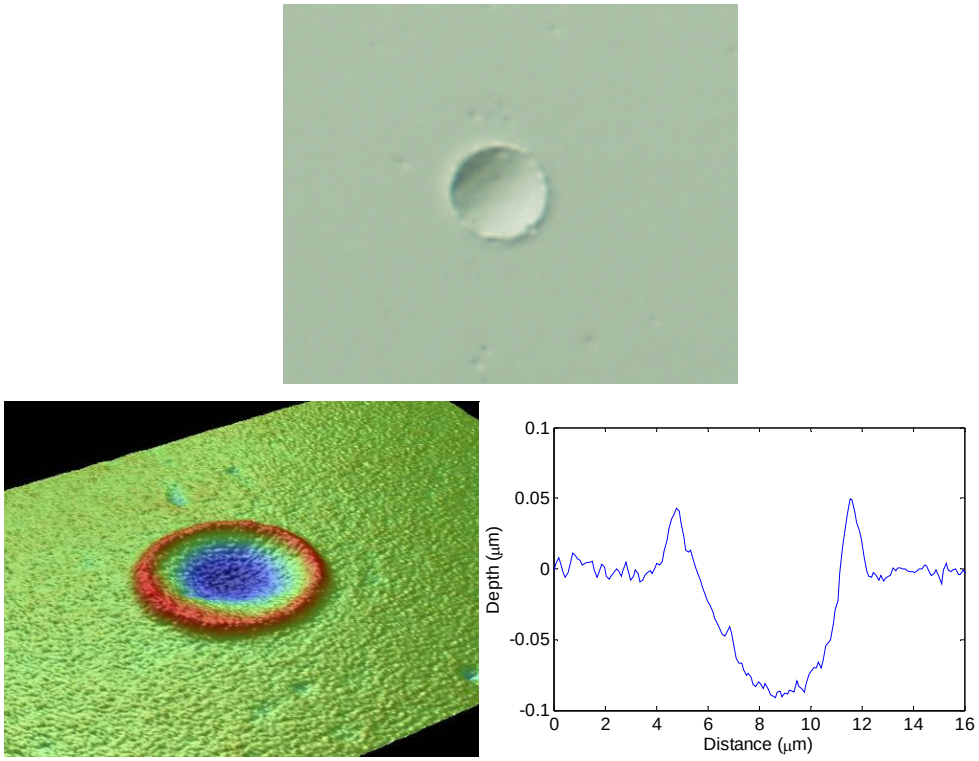

Microscope image (top) and optical profilometry data (bottom) of a single shot ablation crater in silicon

Viewing and photography of samples was carried on an Olympus BX-61 differential interference contrast (DIC) microscope shown in The DIC mode of viewing produces increased contrast based on optical path length and proved to be very useful for viewing small and shallow surface features such as ablation craters and etched crystal domains. This type of microscope imaging is also used for observing refractive index changes within transparent materials. Femtosecond laser induced modification in glasses and crystals has recently been a very active research area for waveguide and grating fabrication, and DIC viewing of such modifications is a convenient method for gleaning qualitative indications of refractive index change. Example DIC images of single mode fibre and laser induced subsurface modifications in lithium niobate are below

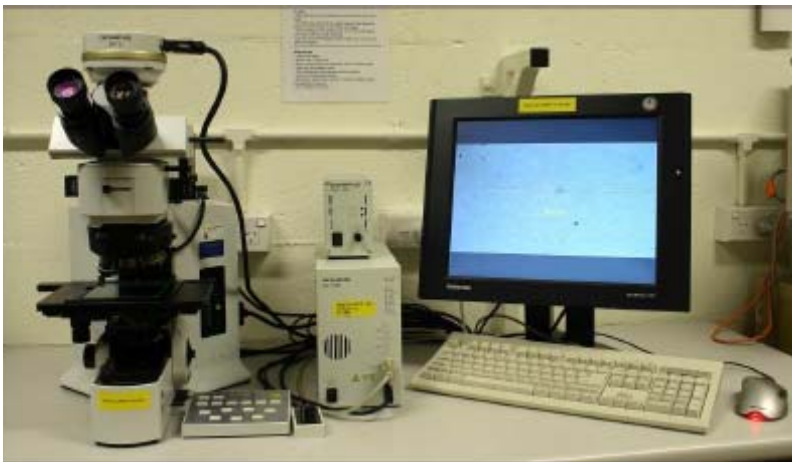

Olympus BX-61 microscope

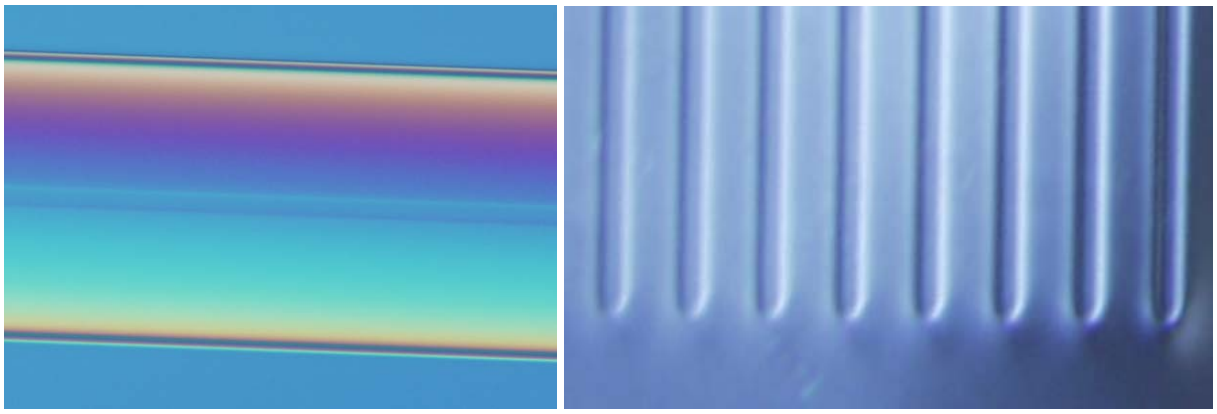

DIC images captured with the BX-61. Left SMF-28 fibre, right: laser induced photorefractive modifications below the surface of lithium niobate.

A3. Visible laser dicing of lithium niobate

Lithium niobate can be a relatively difficult material to handle as it has no natural cleaving planes and is prone to cracking easily from mechanical or thermal stress. During this project a convenient and fast method for crudely sectioning lithium niobate wafers based on visible laser machining with the 532 nm output of the LWE laser system was employed. It was found that certain laser parameters could be used to reliably dice lithium niobate wafers without destructive cracking of the substrate and in much faster times than is possible with a mechanical wafer dicer. This laser dicing method involves both optically damaging the crystal on the surface but also 'percussive' cleaving through the wafer parallel to the incident beam. This technique completely cleaves the crystal so that no mechanical breaking apart of the wafer after machining is required. A cross-section of such a laser cleave is below. The top edge of the crystal is chipped away by

the incident laser pulses and the bottom edge of the crystal has a flat cleave where the percussive breaking has occurred.

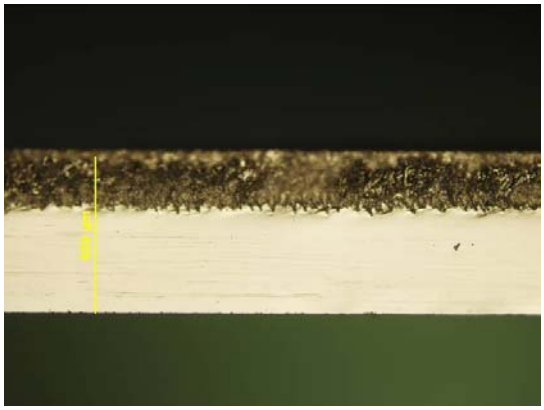

Laser induced cleave of a lithium niobate wafer.

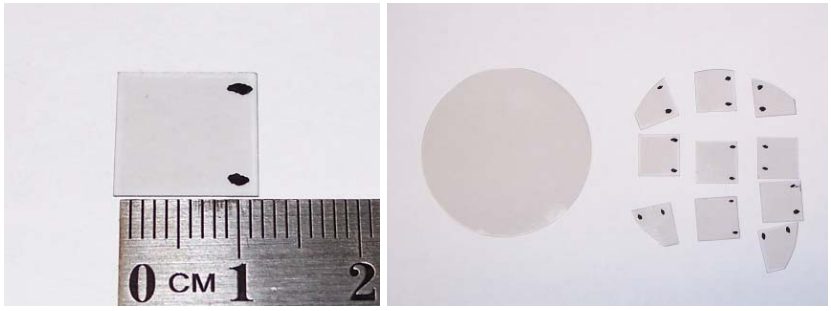

An example of a 2 inch lithium niobate diced into ½ inch squares by laser cleaving. The marks on the diced squares indicate the y-axis flat.

The optimal laser parameters for producing such laser cleaves with the 532nm LWE were found to be pulse fluences of ~5 J/cm^2 with a 1.5 kHz repetition rate (5.12 W average power with a 30µm spot size), and a feed-rate of 100 mm/min. Powers which were in excess of this tended to cause destructive cracking of the wafer beyond the regions of the intended laser guided cleaves. Power much lower than this would result in incomplete cleaving through the wafer, requiring mechanical breaking of the wafer after laser cutting, which despite the laser surface scribes was still unreliable. While not ideal for device fabrication due to the edge chipping generated by the optical damage, rough dicing of lithium niobate wafers using this technique was a convenient method for dicing typical 2 and 3 inch lithium niobate wafers into experimental samples for the laser machining and poling experiments carried out during this project.

Publications

Journal articles

B. F. Johnston and M. J. Withford, "*Dynamics of domain inversion in LiNbO poled using topographic electrode geometries,*" Appl. Phys. Lett. **86**, 262901 (2005).

We report results of an investigation studying the domain inversion kinetics of lithium niobate when electric field poling using laser-machined topographical electrodes. Inversion is shown to begin witha single nucleation spike and the domains evolve in a unique fashion governed by the topographical structure. We also demonstrate control of the resulting domain widths when poling using this technique. The results presented have implications for rapid prototyping of chirped and aperiodic domain structures in lithium niobate.

B. F. Johnston, P. Dekker, M. J. Withford, S. M. Saltiel, and Y. S. Kivshar, *"Simultaneous phase matching and internal interference of two second-order nonlinear parametric processes,"* Opt. Express 14 (24) (2006).

We demonstrate the simultaneous generation and internal interference of two second-order parametric processes in a single nonlinear quadratic crystal. The two-frequency doubling processes are Type 0 (two extraordinary fundamental waves generate an extraordinary secondharmonic wave) and Type I (two ordinary fundamental waves generate an extraordinary second-harmonic wave) parametric interactions. The phasematching conditions for both processes are satisfied in a single periodically poled grating in $LiNbO_3$ using quasi-phase-matching (QPM) vectors with different orders. We observe an interference of two processes, and compare the results with the theoretical analysis. We suggest several applications of this effect such as polarization-independent frequency doubling and a method for stabilizing the level of the generated second-harmonic signal.

B. F. Johnston, P. Dekker, S. M. Saltiel, Y. S. Kivshar, and M. J. Withford, *"Energy exchange between two orthogonally polarized waves by cascading of two quasi-phase-matched quadratic processes,"* Opt. Express 15 (21), 13630-13639 (2007).

We demonstrate energy exchange between two orthogonally polarized optical waves as a consequence of a two-color multistep parametric interaction. The energy exchange results from cascading of two quasi-phase-matched (QPM) second-harmonic parametric processes, and it is intrinsically instantaneous. The effect is observed when both the type-I (ooe) second-harmonic generation process and higher QPM order type-0 (eee) second-harmonic generation processes are phase-matched simultaneously in a congruent periodically-poled lithium niobate crystal. The two second-harmonic generation processes share a common second-harmonic wave which couple the two cross-polarized fundamental components and facilitate an energy flow between them. We demonstrate a good agreement between the experimental data and the results of numerical simulations.

Conference papers

Benjamin Johnston, Michael Withford. "*Laser-based direct-write techniques for electrode patterning of quasi phasematching media."* Proceedings of the 1st Pacific International Conference on Application of Lasers and Optics. MNUFC Session 5. Laser institude of America (2004).

B. Johnston and M. J. Withford. "*Laser machined topographical structures for poling ferroelectrics".* Proceedings of the 7th Australasian conference on optics lasers and spectroscopy. AOS (2005).

Benjamin Johnston and Michael Withford. *"Topographical electrodes for poling lithium niobate."* Proceedings of the 1st Pacific International Conference on Application of Lasers and Optics. pp 348. Laser institude of America (2006).

B. F. Johnston, M. J. Withford, S. M. Saltiel, and Y. S. Kivshar *"Simultaneous SHG of orthogonally polarized fundamentals in single QPM crystals"* LASE, Photonics West 2007. Proc. of SPIE Vol. 6455, 64550Q, (2007) ·

B. F. Johnston, P. Dekker, S. M. Saltiel, Y. S. Kivshar, and M. J. Withford, "*Energy exchange between orthogonally polarized waves by cascaded quasi-phase-matched processes"* Microelectronics, MEMS, and Nanotechnology, Canberra 2007. Proceedings of the SPIE, Vol. 6801, pp. 680116 (2008).